Vertical wind gust profiles

Inaugural-Dissertation
zur
Erlangung des Doktorgrades
der mathematisch-naturwisschenschaftlichen Fakultät
der Universität zu Köln

vorgelegt von

Julian Steinheuer
aus Andernach

Köln
2023

Bericherstatter:	Prof. Dr. Ulrich Löhnert
Gutachter:	Prof. Dr. Susanne Crewell

Tag der mündlichen Prüfung: 13. April 2023

Erklärung zur Dissertation

gemäß der Promotionsordnung vom 12. März 2020

„Hiermit versichere ich an Eides statt, dass ich die vorliegende Dissertation selbstständig und ohne die Benutzung anderer als der angegebenen Hilfsmittel und Literatur angefertigt habe. Alle Stellen, die wörtlich oder sinngemäß aus veröffentlichten und nicht veröffentlichten Werken dem Wortlaut oder dem Sinn nach entnommen wurden, sind als solche kenntlich gemacht. Ich versichere an Eides statt, dass diese Dissertation noch keiner anderen Fakultät oder Universität zur Prüfung vorgelegen hat; dass sie - abgesehen von unten angegebenen Teilpublikationen und eingebundenen Artikeln und Manuskripten - noch nicht veröffentlicht worden ist sowie, dass ich eine Veröffentlichung der Dissertation vor Abschluss der Promotion nicht ohne Genehmigung des Promotionsausschusses vornehmen werde. Die Bestimmungen dieser Ordnung sind mir bekannt. Darüber hinaus erkläre ich hiermit, dass ich die Ordnung zur Sicherung guter wissenschaftlicher Praxis und zum Umgang mit wissenschaftlichem Fehlverhalten der Universität zu Köln gelesen und sie bei der Durchführung der Dissertation zugrundeliegenden Arbeiten und der schriftlich verfassten Dissertation beachtet habe und verpflichte mich hiermit, die dort genannten Vorgaben bei allen wissenschaftlichen Tätigkeiten zu beachten und umzusetzen. Ich versichere, dass die eingereichte elektronische Fassung der eingereichten Druckfassung vollständig entspricht."

Teilpublikationen:

J. Steinheuer and P. Friederichs (2020). "Vertical profiles of wind gust statistics from a regional reanalysis using multivariate extreme value theory". In: *Nonlinear Processes in Geophysics* 27.2, pp. 239–252. DOI: 10.5194/npg-27-239-2020

J. Steinheuer, C. Detring, F. Beyrich, U. Löhnert, P. Friederichs, and S. Fiedler (2022). "A new scanning scheme and flexible retrieval for mean winds and gusts from Doppler lidar measurements". In: *Atmospheric Measurement Techniques* 15.10, pp. 3243–3260. DOI: 10.5194/amt-15-3243-2022

Datum, Name und Unterschrift

Köln, 27. Januar 2023

Julian Steinheuer

Abstract

Wind gusts are usually available for a height of 10 m above ground level, either through the standard wind measurement network or also as a diagnostic variable in numerical weather prediction (NWP). They are relevant for many applications and represent the variable that best characterizes severe wind situations, since they quantify the strongest winds. Mostly, high wind gust peaks recorded at 10 m are related to stronger winds at the heights above, and also, their origin is usually located here. However, high-resolution profiling of the wind is lacking, so only a limited amount of observations exist to study the processes that transport wind gusts or reveal much about their vertical structure. Wind profiles can be recorded at meteorological towers, but these are only found at very few sites because they are costly to operate and then they can only cover the lower few hundred meters of the atmosphere. A wind gust is a short-lived wind spike and represents a phenomenon too small-scale to be resolvable in common weather models. Hence, the gusts are parameterized and derived from other diagnostic variables. However, this is usually done only for the wind gust peak in 10 m. Therefore, there is a lack of wind gust profiling opportunities in both the NWP and the observations.

The present thesis addresses both weather models and new observational methods to generate wind gust profiles. A statistical post-processing is developed that is able to generate a distribution function of gust profiles in the entire lower 250 m of the atmosphere using other atmospheric variables. The post-processing is based on measurements from the weather mast in Hamburg for an observation period of 11 years and uses variables of the regional reanalysis COSMO-REA6 as predictors for a generalized extreme value distribution specifying the occurrence probabilities of hourly gust peaks. This post-processing is not only able to improve the existing gust diagnostics in 10 m of the reanalysis, but also to provide a suitable prediction for heights up to 250 m including intermediate heights without gathered observations.

The second part of the thesis explores the possibilities to obtain wind gust profiles with a Doppler wind lidar (DWL). A comparative study provides a DWL configuration - the quick continuous scanning mode - which allows to acquire about 11 measurements of the Doppler velocity in about 3.4 s, allowing to generate wind vector profiles with high temporal resolution. For this purpose a retrieval is developed, that can provide wind gust peaks, which agree excellently with the standard gust measurements of a sonic anemometer. Furthermore, the high-resolution time-series can reflect the variability in wind profiles in such a detail that individual case studies of high-impact weather events can be illuminated. In the field experiment on sub-mesoscale spatio-temporal variability in Lindenberg (FESSTVaL), the DWL using this new measurement configuration combined with the developed retrieval has demonstrated that it can profile the wind gusts associated with cold fronts and cold pools at such a high-resolution up to about 1500 m. Therefore, DWLs can contribute in future significantly to understanding of the underlying processes, as small-scale variabilities and wind transports can be made observable.

Contents

Chapter 1

Introduction

1.1 Motivation: Difficulties in capturing wind gusts in observations and models

Modern numerical weather prediction (NWP) exploits the computing power of current supercomputers. Both the weather models and the computers are improved continuously and therefore each weather model has its golden age and is replaced, after a given time, by the next generation of models. In the middle of the 20th century, John van Neumann pioneered the first NWP model (see Charney et al., 1950), which was subsequently subject to ongoing refinements. The NWP has benefited enormously from the reduction in computing time, which, according to Bauer et al. (2015), caused the number of possible computational operations to increase tenfold every five years from 1980 onwards. In this evolution, spatial and temporal resolution of the model increase, and a broader range of operational observations can be accessed to determine more accurately the *as-is* state of the atmosphere. Both a higher resolution and more observations to define the initial state of a model run cost computational time and must be matched to the capacity of the computers. And neither will necessarily improve weather forecasting, because previous weather models were tuned to their respective resolution, while an observation always includes errors and may not be representative for the volume of a grid cell.

Many processes occur on scales too small to be resolved by a model grid. In modeling, this is addressed by *parameterization*. Specifically, a certain variable is not directly predicted, but diagnosed from other prognostic variables according to a physical or empirical rule. If a new model generation would allow the direct prediction of some variables that were previously parameterized, it must first be shown whether the forecast skill is actually improved. Even this is only sufficient if the additional gain is substantial compared to the increased computational effort. And how can this be adequately assessed? It must be considered what is a

suitable reference that can be compared with the model, i.e., what is the most trustworthy state of the atmosphere and how should an evaluation be conducted. Assuming that a variable could be observed precisely, could it not also be passed to the model and thus the initial situation of a model-run is represented more realistically? However, with all innovations, one should not forget that the finding of Lorenz (1963) is still valid: weather acts chaotically and small changes in the atmospheric initial situation can cause considerable differences in the subsequent course of the weather. Consequently, while the aim is to constantly improve the weather forecast the ultimate goal of a perfect forecast cannot be achieved.

There are many aspects of how a meteorologist can try to assess the quality of the NWP. Whether it is model evaluation or modification, observations of atmospheric variables will always play a crucial role in advancing research. The present work is dedicated to wind gusts, and thus certainly only addresses a nuance of the meteorological goal of providing an accurate representation and an reliable prediction of the weather. Nevertheless, wind gusts are well suited to understand the fundamental problem of weather model development, as they occur precisely at the edge of observable and predictable phenomena that next-generation models will have to tackle (Yano et al., 2018). Convection starts to appear in the models at scales below a few kilometers and is a *sub-scale* phenomenon for coarser resolutions. At scales between hundreds of meters and a few kilometers, convection emerges partially but not completely, which is why this range is often called the *grey zone* (Vergara-Temprado et al., 2020) of convection. Nowadays it is assumed that at a grid spacing finer than 4 km, deep convection is partly resolved (according to Weisman et al., 1997 or Hohenegger et al., 2008). The global models like *IFS* with 9 km (ECMWF, 2021) or *ICON global* with 13 km (Reinert et al., 2020) are close to this threshold, while regional models like *ICON-D2* (Reinert et al., 2020) with 2 km resolution have already crossed it and include larger convective cells in the forecasts. Gusts also originate from turbulence in the atmosphere (Schreur and Geertsema, 2008) and likewise here, refinements in grid resolution will resolve more accurately the gust creating processes. It is currently the transition phase in which convection and turbulence will soon be able to be directly resolved in global models as well, and also its peripheral phenomena, such as wind gusts, appear in the calculations.

Wind gusts are a relevant issue for weather forecast users. They are responsible for major damage affecting transportation infrastructure, energy supply and buildings. Whole areas of land can be deforested in strong winds, and cropland as well as livestock are exposed to great danger. The winter storm *Lothar* in 1999 caused the highest timber losses in the last decades in Germany and led to studies on wind gust induced deforestation (Jung et al., 2016, Schindler et al., 2016). More than 50 people lost their lives and the total material damage amounted to tens of billions of Euros (Wernli et al., 2002). Winter storms are the main hazard over Central Europe (Pantillon et al., 2018), but summer thunderstorms can locally be even more devastating and much more unexpected. In the context of climate change,

more intense summer convective events are expected (Kunz et al., 2009). Early warnings help to take precautionary action and, in particular, prepare people to protect themselves adequately. Any improvement in the representation of wind gusts is hence of great value for society.

A wind gust is by definition a short-lived wind spike that lasts only a few seconds and is stronger than the mean wind. Usually it is determined from in situ observations close to the Earth's surface, e.g. by using sonic anemometers with 10 – 20 Hz resolution to measure the wind signal. According to the recommendation by the World Meteorological Organization (2018), a wind gust is defined as a 3 s averaged wind speed which is above the mean (e.g. the hourly averaged) wind. The wind gust peak is then the maximum wind gust in a given time interval (such as 10 minutes or 1 hour, both of which is considered below). Conventionally, wind gust peaks are specified at 10 m above ground level (agl). This is the common height for ground based wind measurements and accordingly this is also the height of the usual model parameterizations. That means exactly for 10 m agl one has the possibility to make comparisons of observations versus the model output. In such an evaluation it should be considered that a station observation is not necessarily comparable with the grid-point of the model, which is a representative of a broader area, and certainly orographic effects can produce local differences within such a grid area (Haid et al., 2020). Nevertheless, this is one possibility for evaluation as comparable data exists.

The question remains, what happens in the other levels in the atmospheric boundary layer (ABL; also referred to as planetary boundary layer), i.e., in the lower 100 m to a few kilometers of the troposphere, that is in contact with the Earth's surface (Stewart, 1979)? Convective and turbulent processes are responsible for the mixing of the air masses and transport wind gusts downward, thus the origin of the strong winds at 10 m agl is typically in the higher layers. However, the number of gust measurements at altitudes above 10 m agl is very low. Only a few locations have meteorological towers where wind measurements from the lower hundreds of meters above the ground are provided. This is due to the fact that the construction and maintenance of a tower is very expensive and is not carried out at many locations, but is usually limited to exactly one research site of the national meteorological service or a research institution. Such a tower has enormous research potential and can provide information about the structures of gust transport. For example, Suomi et al. (2014) show by measurements from the 100 m tower in Høvsøre, Denmark, that wind gust peaks at 10 m agl are usually preceded by wind maxima from higher layers. Nevertheless, a tower provides only the lower hundred meters above ground and cannot cover the entire ABL, which reaches usually to a height of about 1 – 2 km.

Modern remote sensing instruments can be used to extend the wind observation range vertically. Doppler wind lidars (DWLs) are capable of deriving winds that originate from heights throughout the ABL. For deriving a mean wind, for instance a representative for 10 minutes

or half an hour, they are proven to be reliable measurement instruments (see for instance Schween et al., 2014 or Päschke et al., 2015). However, they are hardly used yet to determine wind gusts, because the resolution of short-lived wind peaks requires new approaches for operating the DWL. As many measurements as possible must be completed in a relatively short time, which then need to provide an accurate high-resolution time-series of the wind from which gusts can be determined. This indeed poses a challenge for the devices' hardware, and new algorithms for the retrieval software are needed as well. Nevertheless, if successfully implemented, a DWL could add a new aspect to field campaigns and serve as a proof of concept to understand how the transport of gusts to the Earth's surface actually happens, e.g. whether it can be explained predominantly by downward momentum transport as in Brasseur (2001). High-resolution wind measurements might even teach us about unknown physical processes, as they would represent a novelty in the field of observations. A more extensive operational use of DWLs could, in the long run, increase the data set of wind gusts and allow for more significant inferences to be made about their profiles. A small, compact, and affordable instrument that basically requires only a power supply, has the potential to provide profiles in continuous operation and from remote locations, and thus could complement the existing observation network by towers for both wind and wind gusts.

And this only outlines the first step of how a DWL can contribute to NWP. For at the same time, the models need to be further refined so that they can resolve the winds with higher temporal resolution and thus capture gusts directly and also at model levels above 10 m agl. In a very simplified form, the absence of wind gusts in higher layers can be addressed by *post-processing* model data, i.e., enabling the prediction of gust profiles retrospectively from given model variables. This procedure requires observational data and can up to now only be performed at sites with a meteorological tower. On the one hand, a post-processing is suitable to individually improve parameterizations of an already diagnosed variable, but on the other hand, it is able to provide an empirical starting point for parameterizations at higher altitudes.

1.2 Research objectives: Post-processing and remote sensing

Usually wind gusts are divided into convective and turbulent gusts (see e.g. for the *COSMO model* Schulz, 2008). Assuming that the gust is not only a measure of the variability of the wind signal, this subdivision results from the causal process that transports air parcels with stronger wind speeds from high layers down to the surface. A turbulent gust is formed by eddies that mix the air within the ABL and create downdrafts that still have the stronger momentum of the wind from higher layers. Hence, based on the atmospheric stability arising from the temperature stratification and on the vertical wind profile, it can be diag-

nosed whether this transport will actually happen and how strong such a turbulent gust will be (Schreur and Geertsema, 2008).

In a convective cell, similarly, air is vertically exchanged causing warm moist air near the ground to be lifted and air masses from higher layers to be transported downward along with their horizontal momentum, i.e., just as in the turbulent case. If rain falls into the downward driven air, evaporative cooling intensifies the negative buoyancy and accelerates the descending air masses. Near the ground, it must then, maintaining its momentum, deflect its complete motion into a horizontal orientation. So, the parameterization applies the conservation of energy, combines the rain mixing ratio and the temperature deficit due to evaporative cooling to calculate the negative buoyancy, which is then fully converted into the acceleration of the wind speed (Nakamura et al., 1996). Thus, compared to a turbulent gust, the convective gust has the potential to achieve higher wind speeds than the prevailing air masses above have.

Sheridan (2011) reviews the common methods of how wind gusts are parameterized in different NWP models. Non-convective gusts and convective gusts are described. If both are calculated, the model output for the wind gust peak can be determined as the maximum of these two values (Schulz, 2008). However, the formulations based on physical assumptions, such as conservation of energy and momentum, also reach their limits especially if orographic effects like for instance channeling effects in mountain valleys play a role, which a model grid does not resolve (Haid et al., 2020). And if there are problems with the representation of temperature or wind profiles, it is also not possible to correctly diagnose whether and which wind can reach the Earth's surface as a gust. To improve the representation of gusts in models, statistical methods that are data-driven modifications of the predictions are useful. This requires observations of wind gusts for training the model, i.e., to generate a prediction depending on given model variables. It cannot be denied that this approach is somewhat inelegant compared to a coherent physical model that is able to explain where a gust comes from. However, the desired goal is to better represent the observation, and if an improved agreement through a statistical method can be obtained, it should be used as a tool! This way there is also the possibility to address some phenomena that have an influence on the gusts but are not included in the diagnostic and also to correct any systematic model under- or overestimation. In the NWP the subsequent variable adjustment has a tradition even if it makes the results non-physical. Many national weather services use *Model Ouput Statistics* (MOS; attributable to Glahn and Lowry, 1972) to improve the model predictions through long-term observation series (e.g. with the *MOSMIX* at the *German Weather Service*). There are various post-processings for wind gust peaks, since they are the key value for forecasting the impact of storms and are of relevance also for users other than weather model developers. However, most of the approaches focus on the 10 m agl gust only.

Consequently, the first objective of the present thesis is the development of a post-processing that can provide wind gusts in the lower layers of the ABL. The starting point is a reanalysis, i.e., not directly a weather forecast, but the output of an NWP model computed retrospectively with included observations from its entire time span to provide an approximation of the past state of the atmosphere. The reanalysis is regional and covers Europe (Bollmeyer et al., 2014), and was created using the weather model COSMO (Baldauf et al., 2011). Not involved are the observations from the *Hamburg Weather Mast* (Brümmer et al., 2012) so that the wind gust measurements up to 250 m can be used independently for an overlap period from 2004 to 2014 to establish a gust post-processing that covers this lower part of the atmosphere. Included in the reanalysis output is an hourly wind gust peak that is parameterized at 10 m agl and is intended to be both improved and expanded vertically by a post-processing. The approach is based on the fact that, from a mathematical point of view, a gust is an extreme value that can be explained by *extreme value theory* (EVT; which is, for instance, nicely introduced by Coles, 2001) and for which the distributions can be approximated by the *generalized extreme value* (GEV) distribution (Fisher and Tippett, 1928; Gnedenko, 1943). Steinheuer (2018) is addressing this and serves as a basis for the refinement of gust peak predictions throughout the entire 250 m of the lowest part of the atmosphere.

The second objective of the thesis is an assessment about the capability of a DWL to derive wind gusts. Suomi et al. (2017) presented a two day case study in which it is shown that wind gust peaks can be derived by a DWL in high agreement with measured wind gust peaks at a 100 m high meteorological tower. Within the *field experiment on sub-mesoscale spatio-temporal variability in Lindenberg* (FESSTVaL) different sub-scale phenomena are investigated, among which wind gusts are one of the main research topics. This provided the opportunity to test different measurement configurations of a DWL regarding their ability of measuring gusts. In addition to common measurement methods, a method for continuous measuring (see Smalikho and Banakh, 2017) is modified allowing many measurement points to be generated in a short period of time. With respect to the next-by meteorological tower in Falkenberg, it can then be determined which strategy is most suitable for profiling wind gusts.

Furthermore, the scanning strategy thereby identified is intended to be a cornerstone contributing to the success of the FESSTVaL campaign as a whole. Together with wind gusts, the investigation of boundary layer structures and cold pools (CPs) are the main research topics, and all three are to be addressed simultaneously by a dense network of in situ and remote sensing observations. CPs are the events of major interest to all stakeholders and also relevant to this thesis, as they are the convective driver of summer wind gusts. Thus, the third objective of the thesis is to examine the processes that generate wind gusts via high-resolution monitoring of the wind. Due to the availability of multiple DWLs during the

intensive observation period (IOP) in summer 2021, there is the opportunity to evaluate how representative a single wind gust peak can be of its surroundings and when local differences occur.

The thesis is structured in such a way that it is guided by the three objectives. In chapter 2 the wind gust peak post-processing is described (2.1) with a short introduction to EVT (2.2) and the specific application (2.3) to a reanalysis and gust observations (2.4). This is followed in chapter 3 by the introduction of the Doppler wind lidar (3.1), the reasons for a new configuration (3.2), and flexible retrieval to derive wind gusts (3.3) that needs to cope with specific features (3.4), and a description of the FESSTVaL campaign (3.5). Chapter 4 summarizes the results of the work (4.1, 4.2, 4.3), which are published (see in appendices A and B) or available as manuscript and prepared for submission (appendix C). Chapter 5 gives concluding remarks (5.1) and provides an outlook (5.2).

1.3 Findings: List of publications

Part of the results obtained in this thesis are already published in the following peer-reviewed publications:

- J. Steinheuer and P. Friederichs (2020). "Vertical profiles of wind gust statistics from a regional reanalysis using multivariate extreme value theory". In: *Nonlinear Processes in Geophysics* 27.2, pp. 239–252. DOI: 10.5194/npg-27-239-2020

- J. Steinheuer, C. Detring, F. Beyrich, U. Löhnert, P. Friederichs, and S. Fiedler (2022). "A new scanning scheme and flexible retrieval for mean winds and gusts from Doppler lidar measurements". In: *Atmospheric Measurement Techniques* 15.10, pp. 3243–3260. DOI: 10.5194/amt-15-3243-2022

Another manuscript is included in the thesis and is prepared for journal submission:

- J. Steinheuer and U. Löhnert (2023). "High-resolution profiling of wind gust patterns measured by Doppler wind lidars during the FESSTVaL campaign". In: *Preparation for Quarterly Journal of the Royal Meteorological Society*

While chapter 4 gives summaries of the articles, they are given in the appendices A, B, and C.

The wind and wind gust retrieval from DWL observation can be obtained from:

- J. Steinheuer, C. Detring, F. Beyrich, U. Löhnert, P. Friederichs, and S. Fiedler (2021a). "JSteinheuer/DWL_retrieval: DWL retrieval". Version V1.0. In: *Zenodo code*. DOI: 10.5281/ZENODO.5780949

Used DWL data are accessible:

- J. Steinheuer, C. Detring, M. Kayser, and R. Leinweber (2021b). "Doppler wind lidar wind and gust data from FESTVAL 2019/2020". Version 01. In: *ICDC*. DOI: 10.25592/uhhfdm.9758

- C. Detring, F. Beyrich, J. Steinheuer, M. Kayser, R. Leinweber, U. Löhnert, and E. Päschke (2023). "Ultrasonic anemometer and doppler lidar wind and gust data products during FESSTVAL 2021". In: *ICDC*. DOI: 10.25592/UHHFDM.11227

An overview article on the FESSTVaL campaign with contributions to the determination of wind gusts is currently under review:

- C. Hohenegger, F. Ament, F. Beyrich, U. Löhnert, H. Rust, J. Bange, T. Böck, C. Böttcher, J. Boventer, F. Burgemeister, M. Clemens, C. Detring, I. Detring, N. Dewani, I. B. Duran, S. Fiedler, M. Göber, C. van Heerwaarden, B. Heusinkveld, B. Kirsch, D. Klocke, C. Knist, I. Lange, F. Lauermann, V. Lehmann, J. Lehmke, R. Leinweber, K. Lundgren, M. Masbou, M. Mauder, W. Mol, H. Nevermann, T. Nomokonova, E. Päschke, A. Platis, J. Reichardt, L. Rochette, M. Sakradzija, L. Schlemmer, J. Schmidli, N. Shokri, V. Sobottke, J. Speidel, J. Steinheuer, D. D. Turner, H. Vogelmann, C. Wedemeyer, E. Weide-Luiz, S. Wiesner, N. Wildmann, K. Wolz, and T. Wetz (2023). "FESSTVaL: the Field Experiment on Submesoscale Spatio-Temporal Variability in Lindenberg". In: *Preparation for Bulletin of the American Meteorological Society*

Part of the public representation of FESSTVaL are two explanatory videos about CPs, for which illustrative material was contributed, the speech script was co-authored, and the German video was performed as the actor:

- F. Ament, U. Löhnert, H. Rust, and J. Steinheuer (2023). "What Are Cold Pools and What Can They Teach Us?" In: *Latest Thinking*. DOI: 10.21036/ltpub101065

- J. Steinheuer, F. Ament, U. Löhnert, and H. Rust (2023). "Was sind Cold Pools and was können wir von ihnen lernen?" In: *Latest Thinking*

Chapter 2

Post-Processing

This chapter provides the basics for the statistical post-processing on wind gust peaks. It overlaps with the sections 2 and 3 of Steinheuer and Friederichs (2020), although describing the method in much more detail. Section 2.1 gives an overview on statistical post-processings and section 2.2 introduces extreme value theory. It is the mathematical basis that gives the potential distribution functions for extrema. In section 2.3 the application for wind gust peaks is described: from a modified likelihood function the regression parameters are determined that give the most likely combinations of observations and model variables. The data used, to estimate these regression parameters, are introduced in section 2.4. These are wind gust peaks from the Hamburg Weather Mast and model variables from the regional reanalysis COSMO-REA6.

2.1 Statistical post-processing

Statistical post-processing is nowadays a crucial component in the prediction chain for meteorological forecasts. Post-processing ties in with the results of the NWP models and is the subsequent data-driven procedure to improve the output of the meteorological variables. Thereby, the model output should be shifted as close as possible to the observations in the limits of underlying uncertainty. Furthermore, over the long term, the distribution of the post-processed variable is aimed to correspond to the climatology of the observations. The statistics of the predicted variables and the actual observations should thus be rendered indistinguishable. The post-processing can eliminate systematic biases caused by a faulty model, false initial conditions, or incorrect boundary conditions.

There are a number of different post-processing techniques that can be used and applied for different variables. Vannitsem et al. (2021) gives an overview of the state-of-the-art methods. Conventionally, a distinction is made between parametric and non-parametric approaches, i.e., those where a certain framing is given by a predefined family of distributions

and those that are free of such constraints. Parametric methods require some prior knowledge of the distribution function. The model data – the predictors – are then used for regressions, i.e., the determination of the coefficient parameters of a distribution to identify a model-observation relationship. While this allows for simple one-way bias corrections, it also enables complex corrections based on correlations to other variables that are already captured by the model. Functions that represent certain scorings are optimized, such as minimizing the differences between point prediction and point observation. The same functions can be used to optimize the non-parametric approaches, but with no or only limited restrictions on the distribution to be achieved. Depending on the variable to be optimized or the type of events to be captured even more accurately, it may also be appropriate to develop the method for subsets of data only (see, for instance, *quantile regression* in Bremnes, 2004 to account only for higher values). The transitions between parametric and non-parametric approaches are blurred and in particular new methods are emerging around machine learning techniques that can process large amounts of data (i.e., with neural networks in Rasp and Lerch, 2018).

The probabilistic formulation of a post-processing has the advantage that confidences can be specified, and, if required, also point predictions can be generated. For the establishment of the post-processing, optimization functions similar to those that should likewise be applied for the evaluation of probabilistic predictions are suitable. According to Gneiting and Raftery (2007), these are *proper scoring rules* or even *strictly* proper scoring rules, of which there is a comprehensive overview in Wilks (2005). Post-processing can be performed specifically on single variables or at dedicated sites, allowing for individual optimizations to emerge. Unlike a pure NWP model, which consists of the implementation of the physical equations and parameterizations, post-processing is solely data-driven and is not subject to the limitations of a consistent model. This means that situations that cannot be adequately represented by an NWP model can still be corrected afterwards, even though it does not conform to the mechanisms of the model. Undoubtedly, the physical limits are appropriate for considering the complete model output, but for some variables the subsequent adjustment is advantageous. Thus, these constraints can be circumvented to selectively tune certain variables.

Wind gusts are sub-scale in the NWP and therefore their parameterization is necessary. Parameterization can be understood in a broader sense as an implemented post-processing: an unresolvable variable is derived from prognostic variables according to a given rule. If one assumes empirical causality linking different NWP variables, post-processing can become a precursor for parameterization, because it can at best reveal these connections. The variables that constitute a severe weather event and tend to occur less frequently can be addressed efficiently with post-processing. Extremes are often difficult to cover appropriately in NWP models, as they occur very rarely. However, weather extremes such as heavy precipitation,

high flood levels, or strong wind gust peaks are of great importance for the users of the forecasts. Post-processing provides an opportunity to add weight to such situations.

Different approaches are addressing the post-processing of wind gusts. To improve the risk assessment for offshore wind farms off the west coast of North America, Patlakas et al. (2017) gives a deterministic post-processing method based on polynomial Kalman filtering. Staid et al. (2015) also broach gusts in the offshore domain and indicate some simple Gaussian models for the peak wind. A probabilistic gust speed prediction using a non-homogeneous regression with a truncated Gaussian distribution is developed in Thorarinsdottir and Johnson (2012). Part of current research is devoted to machine learning methods for post-processing wind gusts, an overview of which is provided by Schulz and Lerch (2022). In the work of Friederichs et al. (2009) different distributions such as gamma, log-normal, and GEV are compared against each other for fitting to wind gusts from the observation network in Germany. It is shown that a GEV distribution is best suited for estimating wind gusts. The GEV distribution results from EVT and, from a mathematical perspective, is most appropriate for modelling extremes, as it defines the family of all distributions for maxima of arbitrary random variables that are not degenerated. In the following, Friederichs and Thorarinsdottir (2012) designed a Bayesian GEV model for wind gusts with an evaluation method for predictive GEV distributions. Subsequently, in Oesting et al. (2017) and Friederichs et al. (2018) a post-processing for wind gusts is expanded using EVT with included spatial dependencies. In the thesis, this research is continued and a post-processing is built on EVT, the basic principles of which are presented in the following section before applying the theory to wind gust peaks. In Steinheuer (2018) the groundwork is laid for the present chapter and Steinheuer and Friederichs (2020), included in appendix A, use the same data to create a post-processing at different heights based on EVT.

2.2 Extreme value theory

In the following, the core of extreme value theory is given by the *extreme value theorem*, which provides the family of distribution functions for the post-processing. Wind gusts represent maxima of the wind, and this theorem covers the complete variety of potential distribution functions for maxima in the asymptotic limit case. Relationships to other variables are possible by making the parameters of the extreme value distribution dependent on these variables.

For a sequence of independent and identically distributed random variables $X_1, \ldots, X_n$, the random variable

$$M_n = \max\{X_1, \ldots, X_n\} \tag{2.1}$$

is called the *block maximum*. Given a known joint *cumulative distribution function* (CDF) F of the variables X_i, the probability that an X_i has a value not greater than y

is $Pr\{X_i \leq y\} = F(y)$, and for M_n it follows that

$$Pr\{M_n \leq y\} = F^n(y). \tag{2.2}$$

Let F^* be the asymptotic limit of F^n, i.e.,

$$F^* := \lim_{n\to\infty} F^n. \tag{2.3}$$

Without adjustments, F^* would degenerate to a step function (i.e., for values equal to or higher than the upper endpoint of the distribution, it would be equal to 1 and zero otherwise).

Extreme value theorem (Fisher and Tippett, 1928; Gnedenko, 1943): *If there exist sequences of constants* $\{a_n > 0\}$ *and* $\{b_n\}$ *such that*

$$Pr\{(M_n - b_n)/a_n \leq y\} \to G(y) \quad as \quad n \to \infty, \tag{2.4}$$

where G *is a non-degenerate CDF, then* G *is a member of the generalized extreme value family with*

$$G(y;\mu,\sigma,\xi) = \exp\left\{-\left[1+\xi\left(\frac{y-\mu}{\sigma}\right)\right]^{-1/\xi}\right\}, \tag{2.5}$$

defined on $\{y : 1+\xi(y-\mu)/\sigma > 0\}$*, where* $-\infty < \mu < \infty$*,* $\sigma > 0$ *and* $-\infty < \xi < \infty$*.*

The proof can be found in Gnedenko (1943), while a brief sketch of it is given in Coles (2001). Leadbetter et al. (1983) extend the theorem to stationary series X_1, X_2, ... from which the M_n is derived, which are allowed to be dependent to some extent, i.e., neighbor dependencies are allowed but need to vanish as n grows. The CDFs of the GEV family (also refereed to as Fisher-Tippett distributions) are defined by the parameters for location μ, scale σ, and shape ξ. The shape ξ is the crucial parameter defining the tail behavior of the CDF, meaning the probabilities of the higher values. For $\xi = 0$, the theorem and Eq. (2.5) must be read as satisfying the convergence function, i.e.,

$$G(y;\mu,\sigma,0) = \lim_{\xi\to 0} G(y;\mu,\sigma,\xi) = \exp\left\{-\exp\left[-\left(\frac{y-\mu}{\sigma}\right)\right]\right\}, \tag{2.6}$$

which is the *Gumbel* distribution (Gumbel, 1935) of the GEV family. In the cases of a positive or negative shape parameter, the CDFs are known as *Frechét* (Fréchet, 1927) and *Weibull* (Weibull, 1951) distribution, respectively. The Frechét distribution starts from a lower endpoint y_- and the Weibull distribution ends at an upper endpoint y_+, that are the solutions of

$$1 + \xi(y-\mu)/\sigma = 0. \tag{2.7}$$

Figure 2.1 is adapted from Steinheuer (2018) and gives probability density functions for the three different GEV-members, i.e., for different values of ξ. All three members are important in the context of the thesis and both Weibull and Gumbel distributions can be

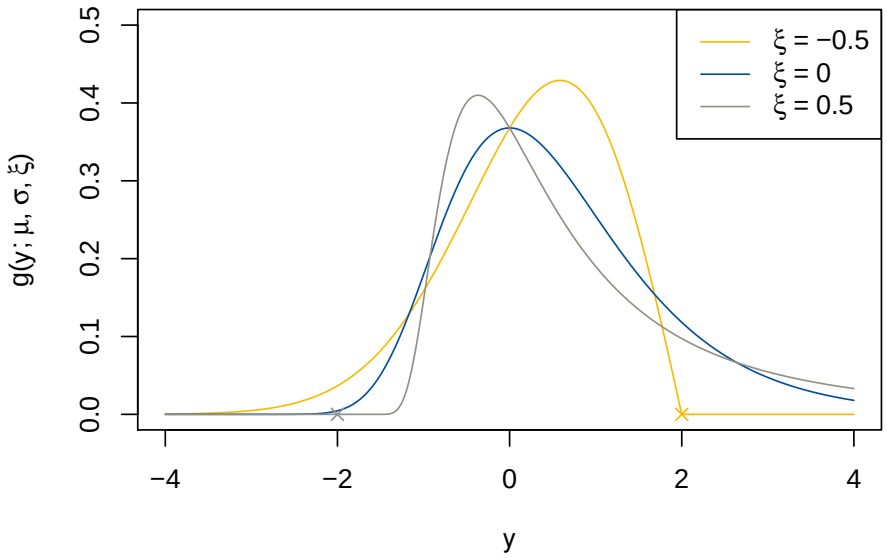

Figure 2.1: Adapted Fig. 2.1 from Steinheuer (2018) with its description: *Densities of the GEV family with parameters* $\mu = 0$, $\sigma = 1$ *and* $\xi = 0.5$ *(Frechét),* $\xi = 0$ *(Gumbel),* $\xi = -0.5$ *(Weibull), respectively. Corresponding endpoints are marked.*

used as candidate distributions for wind gust peaks. The Frechét distribution can be used to describe dependence structures of different distributions (e.g., for simultaneous gusts at different heights, see for more Steinheuer et al., 2022).

In application, the search for the explicit sequences $\{a_n\}$ and $\{b_n\}$ is redundant, since a rescaling of μ and σ results in another member of the GEV family (Coles, 2001). Therefore, the effort to describe a variable with an assumed GEV distribution can be devoted to the determination of the three parameters alone. In meteorological settings, the assumption of stationarity for the distribution of an atmospheric variable is never fulfilled. If the CDF is described purely by three constants, no connection to other variables can be achieved, that undergo time-dependent changes. Therefore, it is useful, to formulate the CDF defining parameters as time-dependent functions, which can include relations to other time-dependent variables, named *covariates*. In this thesis a linear function is chosen for the location parameter, an exponential function with linear argument for the scale parameter, because this guarantees always a positive value, and a constant value for the shape parameter, i.e.,

$$\mu(t) = \mu_0 + \mu_1 C_1(t) + \mu_2 C_2(t) + \ldots, + \mu_L C_L(t) \tag{2.8}$$

$$\sigma(t) = \exp(\sigma_0 + \sigma_1 C_1(t) + \sigma_2 C_2(t) + \cdots + \sigma_L C_L(t)), \tag{2.9}$$

$$\xi(t) = \xi_0, \tag{2.10}$$

with covariates $C_1(t), C_2(t), \ldots, C_L(t)$ and related coefficient parameters.

2.3 Application to wind gust peaks

So far, the application has not been explicitly aimed at wind gusts, but can be applied to other variables as well. In the following, it is described how wind gust peak observations can be related to covariates from NWP. Further, a calculation method is introduced that allows to determine gust distributions from arbitrary heights within the height-range of given observation data.

For the statistical post-processing in this thesis, it is assumed that the 3 s lasting wind gust peak within one hour can be understood as the realization of a GEV distributed random variable $Y(t)$ whose parameters depend on atmospheric covariates $C_1(t), \ldots, C_L(t)$ by Eq. (2.8) - (2.10). In order to obtain a statistical relationship between wind gust peaks and atmospheric variables, data is needed. The connections are then given by regression coefficients Θ with

$$\Theta = (\mu_0, \ldots, \mu_l, \sigma_0, \ldots, \sigma_l, \xi_0). \tag{2.11}$$

A modified *maximum likelihood estimation* (MLE) is used to estimate Θ. The *likelihood function* gives the *probability density function* (PDF) for given data, namely, for realizations $\{y(t)\}$, i.e., observations, and corresponding sets of covariates $\{C_1(t), \ldots C_L(t)\}$, i.e., model variables, and for the unknown regression coefficients. Maximizing the likelihood function then provides the most likely regression coefficients for the given data. With the GEV family related PDF $g(y; \mu, \sigma, \xi)$ and data of different time stamps $t = T_1, \ldots, T_\tau$, the likelihood function $\mathcal{L}$ yields

$$\mathcal{L}(\Theta) = \prod_{t=T_1}^{T_\tau} g\big(y(t); \Theta, C_1(t), \ldots C_L(t)\big). \tag{2.12}$$

For computational reasons, it is convenient to use the log-likelihood function ℓ instead, i.e.,

$$\ell(\Theta) = \log \mathcal{L}(\Theta) = \sum_{t=T_1}^{T_\tau} \log g\big(y(t); \Theta, C_1(t), \ldots C_L(t)\big). \tag{2.13}$$

The most likely parameters $\tilde{\Theta}$ are the values that maximize $\mathcal{L}$ and thus also ℓ.

It is reasonable to question whether one hour is sufficient to assume block maxima that have reached the asymptotic limit of the GEV distributions. Obviously, the larger the block sizes, the better this assumption is, and one hour seems rather short. Nevertheless, the GEV family appears appropriate already here as research indicates. The GEV distribution is better suited than other distributions to specify the CDF of wind gust peaks (Friederichs and Thorarinsdottir, 2012), and one hour is a sufficiently long time interval to obtain reasonable results (Oesting et al., 2017). However, there are certain weather situations in which very weak winds and corresponding weak wind gust prevail and in which describing the hourly wind gust peak as an extreme value is an inappropriate assumption. An adequate model for such low wind situations is not the goal of the post-processing. On the contrary, the aim is to

identify weather situations with the potential for very strong gusts and to be able to indicate correspondingly high probabilities for high wind gust peaks.

In order to take both into account, i.e., less relevance for low gusts and more relevance for stronger ones, the MLE approach is adjusted and the wind gust peaks exceeding a certain threshold are given stronger influence on the parameter estimation. Let u be this threshold. For wind speeds below, only the information that the threshold is not exceeded is to be included, not how far it is below u. This is achieved by following the method of Scheuerer (2013) and censoring the CDF at u, i.e.,

$$G_u(y;\mu,\sigma,\xi) = \begin{cases} 0, & \text{if } y < u, \\ G(y;\mu,\sigma,\xi), & \text{if } y \geq u. \end{cases} \tag{2.14}$$

Thus, the CDF is a step function that jumps to the value of $G(u;\mu,\sigma,\xi)$ at u and is named *censored GEV* (cGEV). In order to use this modified function G_u for the MLE, all observations $y < u$ need to be raised to u so that they fall within the permitted definition range, because according to Eq. (2.14) they appear with a probability of 0 in G_u. For convenience, let the time-series of wind gust peaks be sorted, i.e., say the $T_1, \ldots, T_R$ leading time stamps belong to y-values below u and the $T_{R+1}, \ldots, T_\tau$ following timestamps belong to y-values of at least u. The modified log-likelihood function ℓ_u is then given by

$$\ell_u(\Theta) = \sum_{t=T_1}^{T_R} \log G\big(u;\Theta,C_1(t),\ldots C_L(t)\big) + \sum_{t=T_{R+1}}^{T_\tau} \log g\big(y(t);\Theta,C_1(t),\ldots C_L(t)\big), \tag{2.15}$$

with PDF g same as in Eq. (2.12). The parameters $\tilde{\Theta}$ maximizing Eq. (2.15) are actually the sought quantities.

The influence of the covariates on the distribution can be identified from the estimated regression coefficients. For this purpose, the covariates must be standardized, i.e., in the data set for the determination of $\tilde{\Theta}$ they must average to 0 and have a standard deviation of 1. Through this linear transformation, the estimated regression coefficients directly quantify the influence of the covariates. Thus, values close to zero signal little contribution. However, if a covariate indeed has no contribution, the estimate of the corresponding parameters will not be exactly zero. In addition, there are potential correlations between the covariates, so that two covariates might have a significantly higher contribution to the GEV distribution if the other would not be included in the set of covariates. A model with fewer covariates is often easier to optimize and can produce better results if useless covariates are eliminated. Overall, it is therefore not trivial to decide which covariates are meaningful and should eventually be included in the post-processing from the pool of potential candidates. Therefore, the *least-absolute-shrinkage-and-selection-operator* (LASSO) is used, which was introduced by Tibshirani (1996) and provides decision support. In this work, the LASSO is applied by

introducing a penalty term into the log-likelihood function of the Eq. (2.15) towards

$$\ell_{u,\lambda}(\Theta) = \ell_u(\Theta) - \lambda \sum_{\theta \in \Theta \setminus \{\mu_0, \sigma_0\, \xi_0\}} |\theta|, \tag{2.16}$$

with λ the penalization. The constant parameters μ_0, σ_0, and ξ_o are not penalized, so for sufficiently high λ, maximizing Eq. (2.16) leads to an estimate $\tilde{\Theta}$ that yields zero for all regression coefficients of the covariates and ends in estimates for a constant GEV distribution. Varying the penalty value λ indicates which covariates are relevant, namely when they obtain non-vanishing regression coefficients despite the penalty term, and which contribute little to maximizing the likelihood, thus resulting in zero coefficients for rather moderate penalization.

Not only are distributions of wind gust peaks at 10 m agl to be post-processed, but profiles reaching higher into the vertical are also to be constructed. Therefore, another modification is introduced, namely that the regression coefficients are height variable. The height dependence is modeled with linear combinations of *Legendre polynomials* (Legendre, 1785) up to the order K, i.e.,

$$\begin{aligned} P_0(\eta) &= 1, \\ P_1(\eta) &= \eta, \\ P_2(\eta) &= 1/2(3\eta^2 - 1), \\ &\dots \end{aligned} \tag{2.17}$$

where $\eta \in [0, 1]$ is a generalized height. Each parameter $\mu_l(z)$ and $\sigma_l(z)$ in Θ for $l = 0, \dots, L$ is modulated as

$$\mu_l(z) = \sum_{k=0}^{K} \mu_{lk} P_k(\eta(z)), \tag{2.18}$$

$$\sigma_l(z) = \sum_{k=0}^{K} \sigma_{lk} P_k(\eta(z)). \tag{2.19}$$

Substituting Eq. (2.18) and (2.19) into Eq. (2.16) then yields the ultimately used likelihood function, which is to be used for parameter determination of the post-processing. In principle, realizations, i.e., observations of wind gust peaks, from different heights and from different times can now contribute equally in the likelihood. However, it is allowed that u is set to be height-dependent resulting in different G_u.

The use of Legendre polynomials not only allows to generate CDFs for the heights at which observations exist, but also at the intermediate heights, since η can take all values between 0 and 1. The shape parameter is not influenced by covariates, remains constant in height, and is further fixed at $\xi = 0$. This reduces the family of the GEV distribution to CDFs of the Gumbel type from Eq. (2.6). Friederichs and Thorarinsdottir (2012) indicate that fits of the wind gust peaks in GEV distributions tend to yield Weibull CDFs, i.e., with slightly negative shape parameter, but the principle of allowing distributions that can have lower or upper endpoints results in computational difficulties: the numerical optimization routines

become unstable if impossible values are imposed. This can occur in the estimation routine that maximizes Eq. (2.16) if the parameters are varying in such a way that an observation falls outside the allowed range. One value alone can crash the routine and only the Gumbel-CDFs contains no range-restriction.

2.4 Profiles of wind gust distributions in Hamburg

The observations used here are the hourly 3 s lasting wind gust peaks measured at the Hamburg Weather Mast, which is operated by the meteorological institute of the University of Hamburg in partnership with the Max Planck Institute for Meteorology. The measurement site is located in Hamburg, Germany, with winds from the heights $z = 10,\ 50, 110, 175,$ and 250 m agl recorded by sonic anemometers in a temporal resolution of 20 Hz (Brümmer et al., 2012). The post-processing is based on data acquired in the period from the beginning of 2004 to the end of 2014.

At the *Hans-Ertel Center for Weather Research* (HErZ, Simmer et al., 2016), the regional reanalysis COSMO-REA6 of the *German Weather Service* (DWD) was developed (Bollmeyer et al., 2014) that provides the set of potential covariates for this thesis. The reanalysis is based on the NWP model COSMO (Baldauf et al., 2011) and covers broadly Europe with a horizontal grid of 0.055° (about 6 km) resolution. In the vertical, the reanalysis covers 40 layers from the surface to 40 hPa. The temporal resolution for the 3 dimensional output-fields is 1 hour, and model variables from the 25 grid columns that lie around the weather mast are assumed to be potentially relevant for the wind gust peak distributions. The preselected covariates from the reanalysis variables can be found in Table 1 in Steinheuer and Friederichs (2020).

The cGEV distribution requires threshold values u per altitude. At each altitude, the median of the observed wind gust peaks from the eleven years of observations is chosen, which are at 5.79, 7.40, 8.65, 9.69, and 10.54 m/s, respectively, for increasing altitude levels. For the height-dependent modeling of the regression coefficients, only the first three Legendre polynomials are used, i.e., exactly those given in Eq. (2.17). Thus, height-dependent differences in the CDF are possible by linear and quadratic terms. To evaluate the post-processing, a *cross-validation* (Stone, 1974) method is used for parameter determination and independent validation: for the determination of the parameters, one year of data is omitted and these observations then serve as the basis for a validation. Similarly, observations from one specific altitude are omitted to validate how well the post-processing is able to provide predictions at unobserved altitudes, i.e., the procedure is actually a double cross-validation.

The variability of the regression coefficients already gives an indicator for the suitability of certain covariates. The decision which covariates are used in the post-processing, however, is based on the LASSO approach by solving the Eq. (2.16). The final post-processing then

uses these covariates but determines the regression coefficients without penalization, following the Eq. (2.15).

Chapter 3

Doppler Wind Lidar

In this chapter, the important aspects of the DWL relevant for this thesis are gathered, though some of this information also appears in the articles Steinheuer et al. (2022) and Steinheuer and Löhnert (2023): section 3.1 gives fundamental DWL information, and sections 3.2 and 3.3 describe in more detail what is introduced in section 3 of Steinheuer et al. (2022). Features of the quick scanning mode are discussed in section 3.4 but also in section 3.2 and appendix of Steinheuer and Löhnert (2023). Also, section 3.5 overlaps with the FESSTVaL information from both articles.

3.1 Principle of operation

Scanning coherent Doppler wind light-detection-and-ranging (lidar) systems are proven to be powerful instruments for both research purposes and commercial applications to acquire wind measurements. In recent decades, they have found extensive use in field campaigns (CCIE, see Soderholm et al., 2016; XPIA, see Choukulkar et al., 2017; Perdigão experiment, see Letson et al., 2019; PIANO, see Haid et al., 2020), in surveys of wind power plants (González-Longatt et al., 2012; Bossanyi et al., 2014; Scholbrock et al., 2016; Pichault et al., 2021), and at sites for ground-based long-term observations of the atmosphere (Lindenberg, see Päschke et al., 2015; Jülich, see Schween et al., 2014; Cabauw, see Knoop et al., 2021). Usually, and thus hereafter, a Doppler wind lidar refers to *pulsed* DWL, which, in contrast to a *continuous-wave* DWL (sometimes named *windranger*), emits the light in packets (instead of continuously) and can distinguish measurements from different distances. The determination of the distance results from the different arrival times of the backscattered light within the short break following transmission enabling the profiling of the wind.

A DWL emits light in the infrared frequencies (with wavelengths around 1.5 µm, where the infrared wavelength range is between 780 nm and 1 mm). The light is backscattered by the aerosols and experiences a frequency shift due to their relative motion with respect to the

line-of-sight of the DWL. The DWL receives from a variety of backscatterers and from many transmitted pulses (about 3000 – 30000 pulses per line-of-sight, depending on the configuration) a distribution of different frequency shifts – the spectrum of Doppler shifts – which are assigned to one beam segment (i.e., the beam is divided into equidistant segments separated by so-called *range gates*, and each measurements is assigned to one *center-of-range gate* depending on the segment to which it is attributed to, due to its travel time). The spectrum of Doppler shifts coincides with a spectrum of Doppler velocities from which distribution a mean Doppler velocity is calculated, for instance by a Gaussian filter. This is based on the assumption that the Doppler shifts can be considered as approximately normally distributed with a background contribution of noise in the bandwidth of the receivable velocities, i.e., the *Nyquist-velocity* range. Further, the Doppler shift spectrum can be used to assess how representative the determined mean Doppler velocity is. The noise component behaves like a zero-mean Gaussian random process (for details see Frehlich, 1994) whose contribution to the specified Doppler velocity is aimed to be low. The ratio of signal from backscattering particles to noise, i.e., the signal-to-noise ratio (SNR), is the parameter to asses the quality of the determined Doppler velocity and commonly used to filter measurements. If the SNR is too low, as it is often the case above the ABL or in very clear atmospheric conditions, the measurement of the Doppler velocity is less precise. From SNR, and from the width of the signal spectrum, a theoretical standard deviation of the measured Doppler velocity spectrum can be derived, which can also be used for filtering (see Rye and Hardesty, 1993 or also Barlow et al., 2011).

The DWL obtains information of the wind field by measuring radial velocities along different beam directions. The directions can be set and are defined by azimuth (θ; usually measuring clockwise from north which is 0°, then pointing east at 90°, etc.) and elevation angle (α; or represented by the zenith angle ϕ, which adds up with α to 90°). Assuming a perfect measurement, i.e., along a beam segment there is a unique wind $\mathbf{v} = (u \;\; v \;\; w)^T$ and its radial projection corresponds to the measured Doppler velocity d that is given by

$$d = \mathbf{a}^T \mathbf{v}, \tag{3.1}$$

with $\mathbf{a} = (\sin(\theta)\cos(\alpha) \quad \cos(\theta)\cos(\alpha) \quad \sin(\alpha))^T$ the unit vector in the direction of orientation. Since the wind vector is a 3 dimensional quantity, it cannot be derived from one Doppler velocity measurement alone. The orientation of the beam determines the contribution of the three wind vector components to the Doppler velocity. Therefore, the Doppler velocity must be measured at least at three different orientations to determine the wind vector. Figure 3.1 displays beam orientations and exemplary one projection of the wind along a line-of-sight, that is the geometric illustration of Eq. (3.1).

A single DWL views into a different air volume when the orientation changes and cannot provide one vector without further assumptions. The conventional assumption is that

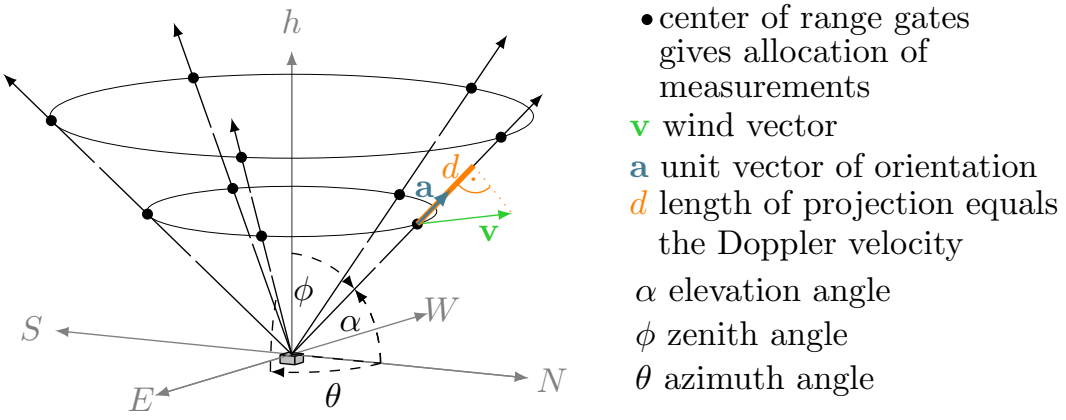

Figure 3.1: Overview of the DWL's mechanism of operation. The orientation is given by azimuth and elevation (or zenith). The Doppler velocity corresponds to the projection length of the wind vector (more precisely: the velocity of the backscattering aerosols in the beam segment) along the unit vector of the orientation. The measurement is allocated to the centre of range gates.

the wind field is *homogeneous* at a given height and for some time. Thus, for n different temporally sequential measurements, a uniform wind vector $\mathbf{v}$ is assumed, leading to

$$d_i = \mathbf{a}_i^T \mathbf{v}, \qquad for \quad i \in 1, \ldots, n. \tag{3.2}$$

From the linear system of equations with n rows, one can then determine $\mathbf{v}$. This can be done by different retrieval methods, the most common of which is the *velocity-azimuth display* (VAD) technique. The name is almost self-explanatory and originates from Browning and Wexler (1968): the measured Doppler velocities are displayed against their azimuth and, if the wind field is sufficiently homogeneous, show a sinusoid behaviour into which a sine function can be fitted. From the three fit parameters amplitude, phase shift, and offset, one can determine u, v, and w. This is then carried out accordingly for all heights so that the wind profile is determined.

The VAD is particularly suitable for determining the mean wind from a large number of measurements and is commonly used to obtain the 10 minute or 30 minute wind. The DWL is operated at a certain elevation angle and realigned by azimuthal steps, resulting in, for example, 24 measurements evenly distributed over 360°, requiring 2 minutes. However, the aim is to resolve wind gusts and so a much higher temporal resolution needs to be achieved. Therefore, the VAD technique is not directly attractive. In order to determine all three wind components quickly, the *Doppler beam swinging* (DBS) technique could be applied (Frehlich et al., 1998; Suomi et al., 2017) which uses five different orientations: one pointing perpendicular to the zenith, i.e., vertically pointing, to measure the w-component directly, and four pointing inclined in the cardinal directions. From the beams inclined to the north and south v can

be determined, from those inclined to the west and east u. The name derives from the principle that the beams then swing back and forth between these few alignments instead of being laboriously moved into position. There are also devices designed to measure exclusively in DBS and that are optimized for this purpose. For instance, if the option of free alignment is dispensed with, wear-intensive orientation components can be eliminated, thereby also reducing the device costs.

Suomi et al. (2017) propose a method for determining wind gusts from a DWL in the DBS configuration. The wind vector is derived every 3.8 s from the five beams and gust peaks are calculated from the time-series and scaled down to 3 s lasting gust peaks. Their successful study, based on two days, was the inspiration to aim for measurements over a longer time and to test other configurations that provide research potential for deriving wind gusts. However, the most important criterion for a suitable configuration is to create a time-series of the wind with the highest possible temporal resolution. The duration of a measurement cycle, i.e., the time until the measurement orientations of the DWL are repeated, is therefore crucial, because it is intended to create a wind vector from the measurements collected during one full cycle. Theoretically, it is possible to calculate the wind vector from three measurements alone, e.g. from three adjacent beam directions, but such a fit is error-prone for those wind components in which direction the DWL was hardly oriented. Hence, in this thesis, no determination of the wind from only parts of the 360° measurement cycle is included.

Figure 3.2: A StreamLine DWL, manufactured by Halo Photonics, that was used in this study and within the FESSTVaL campaign. The author made the photo on July 22, 2020 at the Boundary Layer Field site in Falkenberg, Germany.

With a rotating DWL that precisely drives different azimuth alignments, the cycle time is composed of the measurement intervals and the alignment movements. For the alignment travel time, the distance of the crossed azimuth step is less important, as the acceleration and deceleration of the DWL head mainly consumes the time between two measurements. With the DWLs used, this is about 2-3 s, so there is a strong constraint to derive an only 3 s lasting gust. Also the DBS cannot be conducted in 3.8 s as in Suomi et al. (2017), because instead of using flappable mirrors, its five single alignments are achieved by DWL head moving and the full rotation cycle needs around 28 s. The available equipment therefore prohibits a direct reproduction of their approach. The DWLs used in the thesis are *StreamlLine* devices manufactured by *Halo Photonics* (see Fig. 3.2) and, instead of a temporal optimization, their feature is a high degree of flexibility in their configuration.

3.2 The new scanning scheme

The StreamLine DWLs can be operated in step-stare mode, i.e., precise combinations of angles are driven and repeated after one cycle. One possible configuration is to use 24 different azimuth angles, thus covering the sky's different directions with a step width of 15°. A common configuration is to have further an elevation angle of 75° and additionally one vertically pointing measurement at the end of the cycle. For instance, this *24Beam* configuration is used operationally in Lindenberg and Jülich (Päschke et al., 2015; and Schween et al., 2014). If one reduces the number of beams to six, the namely the *6Beam* method by Sathe et al. (2015), one still has enough measurements to determine the Reynolds stress tensor per cycle, i.e., in addition to the wind, turbulence can be derived. Using only measurements from exactly three directions – the *3Beam* – is the most rudimentary method of deriving the 3 element wind vector. As already mentioned, however, it is not the individual measurement that is time-consuming, but rather the steering of exact alignments.

The *continuous scanning mode* (CSM) saves this time and can perform the measuring cycle faster. Smalikho and Banakh (2017) used this method to determine the turbulent kinetic energy (TKE). Their primary objective was not to use the quickest possible configuration, but to record as many different directions as possible so that the averaged variance of the radial Doppler velocities can be considered as meaningful representative for the measuring circle. By choosing the elevation angle at 35.3°, this variance is directly proportional to the TKE (calculations in Eberhard et al., 1989). For geometric reasons, a flatter angle results in higher resolution profiles vertically, but with a reduced total vertical extent due to the DWL's limited range. And in general, deciding on an elevation angle is always a trade-off consideration: the flatter the alignment, the more directly the horizontal wind is measured, but with a larger volume of air from which the distant measurements of one height originate. Hence, the validity of homogeneity is potentially more compromised. An elevation

angle of 35.3° as used by Smalikho and Banakh (2017) is relatively flat and already provides measurements at 1 km altitude from the edge of a circle with a diameter of about 2.8 km, while for the 75° of the 24Beam this diameter is only of about 500 m. Frequently used for DBS configuration (as in Suomi et al., 2017) are elevation angles of 62°, as here the circle diameter is approximately equal to its originating height. Time can be saved by keeping the number of pulses per measurement as low as possible, as tests with the 3Beam method with a differing number of pulses show, namely by emitting 10000 instead of 30000 pulses the total time for measuring the three beams is reduced to 18 s instead of 24 s (Steinheuer et al., 2022). By combining continuously measuring while driving with only 3000 pulses per measurement, a complete measurement cycle can be completed in 3.4 s, producing 11 measurements assigned to azimuth angles that differ from each other by about 33° – 35°. The exact angles do not repeat at each measurement cycle, but drift slightly, so that a beam in a new cycle differs by about 20° from the beam of the previous cycle. This also has the consequence that there are cycles with 10 or 12 targeted alignments. However, the usual number of emitted light pulses is about ten times higher (e.g., 30000 in Schween et al., 2014 and Päschke et al., 2015), so this new scanning scheme yields a much poorer signal with lower SNR values.

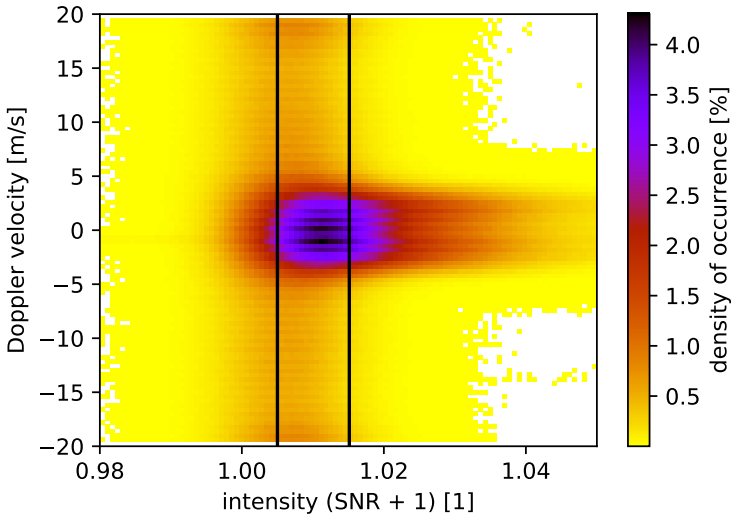

Figure 3.3: Figure 4 from Steinheuer et al. (2022) with a Nyquist velocity range from -19.4 to 19.4 m/s and its description: *Intensities (SNR + 1) vs. Doppler velocities on September 2, 2019 for all center-of-range gates during a 24 h observation period. The DWL is operated in CSM2 with* 62° *elevation angle and it produced 25 million measurements on that day. The area is divided into* 100×100 *bins and the colors indicate the density of occurrence. The left vertical line corresponds to an SNR value of* -23 *dB and the right to* -18.2 *dB.* Note that *CSM2* refers to the quick CSM with approximately 11 measurements in 3.4 s per one measuring cycle.

A low SNR value does not necessarily mean that a Doppler velocity is erroneous, but simply that the signal is weak compared to the noise. However, common filtering methods are based on filtering in advance those Doppler velocities that fall below a particular SNR threshold. A relatively strict threshold is -18.2 dB, as used by Schween et al. (2014) and Päschke et al. (2015), so that a rather large number of observations is filtered out. From the manufacturer's side, the rather moderate threshold of -23 dB is used (see Pearson et al., 2009), so that more values (all with higher SNR) are allowed. Figure 3.3 is copied from Steinheuer et al. (2022) and provides a 2 dimensional histogram for the complete measurements of one day and from all heights which were performed by the quick CSM configuration with the low number of 3000 pulses per measurement. On this day, moderate wind speeds prevailed throughout the ABL (fair backscatter from up to 1500 m height), not exceeding about 10 m/s on the mean, resulting in expected maximum Doppler velocities of 4.7 m/s (when exactly aligned along the horizontal wind direction at an elevation angle of 62°) and, conversely, minima of -4.7 m/s (when aligned against the wind direction). Most of the acquired Doppler velocities are in the range between -5 and 5 m/s. The two filter thresholds are indicated by vertical lines. Even the moderate threshold (of -23 dB on the left) would filter many reasonable observations (reddish area left of -23 dB between -5 and 5 m/s). Conversely, it is evident that even the strict threshold (-18.2 dB on the right) cannot fully guarantee that only trustworthy Doppler velocities are obtained (yellow areas on the right of -18.2 dB). It is negligent to assume here authentic Doppler velocities and to interpret them as wind gust peaks, since this would lead to unrealistic high values.

3.3 A flexible retrieval

Fixing on an SNR threshold and implementing a filtering as described above, is completely absent in the new retrieval: instead, a method is created that initially takes all measurements into account, performs a wind vector fit, and successively removes those measurements that deviate too much from the fit, updating the fit in the process. Herein Eq. (3.2) is followed, but with assuming an individual wind vector $\mathbf{v}_i$ per measurement, which is considered for all i the realization of a normally distributed wind $\mathbf{v_0}$, i.e.,

$$\mathbf{v}_i \sim \mathcal{N}(\mathbf{v}_0, \Sigma)\,. \tag{3.3}$$

Thus, all n individual winds have a common expectation value v_0 and are assumed as independent realizations. Moreover, it is included that each measurement can be erroneous, with an error ϵ_i, which is also assumed to be the realization of a normally distributed random variable with

$$\epsilon_i \sim \mathcal{N}(0, \sigma_\epsilon^2)\,. \tag{3.4}$$

This results in $i = 1, \ldots, n$ Doppler velocities

$$d_i = \mathbf{a}_i^T \mathbf{v}_i + \epsilon_i \,. \tag{3.5}$$

Being the sum of two normally distributed random variables, each Doppler velocity d_i is another normally distributed random variable with

$$d_i \sim \mathcal{N}(\mathbf{a}_i^T \mathbf{v}_0,\, \mathbf{a}_i^T \Sigma \mathbf{a}_i + \sigma_\epsilon^2). \tag{3.6}$$

Next, it is necessary to set up a formula for Σ that describes the variability of the wind field at the particular altitude from which the observations originates. Here, the simple formulation is assumed, that the wind field is isotropically distributed. That is, the probability of a realization $\mathbf{v}_i$ depends solely on the absolute value of its difference from the expected wind $\mathbf{v}_0$ and not on the direction of the difference. Refinements would be conceivable, e.g. a lower deviation probability in the vertical (lower variability of the w component) or higher probabilities for wind strength variability compared to directional changes. The Σ would have to be adjusted accordingly. The assumption of isotropy implies

$$\Sigma = \sigma_v^2 \mathcal{I}_3 \tag{3.7}$$

with only one necessary parameter σ_v, where $\mathcal{I}_3$ denotes the 3 dimensional unit matrix. This simplifies the variance of d_i as

$$\mathbf{a}_i^T \Sigma \mathbf{a}_i = \sigma_v^2 \tag{3.8}$$

for all directions $\mathbf{a}_i$. With n measured Doppler velocities, the likelihood function L can be formulated as

$$L(d_1, \ldots, d_n; \mathbf{v}_0, \sigma^2) = \prod_{i=1}^{n} f(d_i; \mathbf{a}_i^T \mathbf{v}_0, \sigma^2), \tag{3.9}$$

where $\sigma^2 = \sigma_v^2 + \sigma_\epsilon^2$ is total variance and $f(x; \mu, \sigma^2)$ is the PDF of a normal distributed random variable of expectation μ and variance σ^2. From this, the most likely underlying vector $\hat{\mathbf{v}}_0$ can now be determined which is the target variable of the retrieval algorithm. This is the particular wind vector maximizing L for the given d_i. In the formulation it yields that

$$\hat{\mathbf{v}}_0 = (A^T A)^{-1} A^T \mathbf{d}, \quad \text{for} \quad n \geq 3, \tag{3.10}$$

where A is the matrix containing the alignments a_i row by row and with $A^T A$ invertible for $n \geq 3$ and the n beams are not co-planar. The estimate $\hat{\mathbf{v}}_0$ is independent of σ, since σ determines the width of the normal distribution and, in the isotropic formulation, has no effect on the determination of the maximum. Equation (3.10) is equivalent to the approach of calculating least squares errors $\epsilon^T \epsilon$ from Eq. (3.5) with ϵ the vector containing ϵ_i as i-th entry. However, to assess the goodness of fit an estimate of σ^2 is needed. If maximizing the likelihood for σ^2, one obtains

$$\hat{\sigma}^2 = \frac{1}{n} \sum_{i=1}^{n} (d_i - \mathbf{a}_i^T \mathbf{v}_0)^2, \quad \text{for} \quad n > 3. \tag{3.11}$$

For this estimation $\mathbf{v}_0$ is needed, so the estimator $\hat{\mathbf{v}}_0$ is inserted and instead of the quotient $\frac{1}{n}$ the quotient $\frac{1}{n-3}$ is used, since this is the unbiased estimator, i.e., accounting for the fact that this second estimate is based on another estimate for which already three degrees-of-freedom (DOFs; the three components of $\hat{\mathbf{v}}_0$) are used. One finds

$$\hat{\sigma}^2 = \frac{1}{n-3}\sum_{i=1}^{n}(d_i - \mathbf{a}_i^T\hat{\mathbf{v}}_0)^2, \quad \text{for} \quad n > 3. \tag{3.12}$$

The estimate of the standard deviation (the root of the variance) is identical to the (unbiased) root mean squared error between fit projections (i.e., $\mathbf{a}_i^T\hat{\mathbf{v}}_0$) and the measurements d_i. This analogy indicates that the estimate $\hat{\sigma}$ is an appropriate measure to evaluate the fit. Therefore, the proposed algorithm targets this estimate and judges the fit as not sufficiently good, i.e., too many noisy measurements are suspected, if $\hat{\sigma}$ is too high.

At this point, a decision to determine when a fit can be evaluated as reliable enough must be made. A threshold value cannot be avoided which handles this. If the standard deviation is too high (say above u_1), the complete fit is not discarded, but single measurements are eliminated, which cause the estimated standard deviation to be too high. These are Doppler velocities which are not in agreement with the projected radial wind, i.e., with highest deviation from the sinusoid in the actual display of velocity versus azimuth (highest values of $|d_i - \mathbf{a}^T\hat{\mathbf{v}}_0|$). Since they have simultaneously biased the estimate of $\hat{\mathbf{v}}_0$, a new fit is computed after discarding them. In general, this approach allows flexibility for a given number of observations to compute a fit that discards measurements (r per iteration) until the estimate sufficiently good. To avoid any over-fitting, a second criterion is that a certain fraction of the original amount of measurements must be included in the fit (at least a fraction of q). During the development of the algorithm it was noticed that it can lead to improvement if u_1 is kept relatively low to allow an improvement of the fit when still enough observations can be discarded. If then the threshold of maximum observations to discard is reached (i.e., $1 - q$), a tolerant threshold (u_2 with $u_2 \geq u_1$) can still be used to judge the fit as acceptable. This idea is implemented in Steinheuer et al. (2022) and different parameters r, q, u_1, and u_2 should be chosen depending on the required time interval for which the wind is to be determined. The mean wind from observations within a 10 minute window has correspondingly more moderate thresholds than the wind determined from a single DWL cycle, where only a few outliers are acceptable. Figures 5 and 6 from Steinheuer et al. (2022) illustrate the fit method.

For the retrieval applied on the 11 measurements of one DWL cycle, it is required that a wind is computed from at least 66 % of data, with an estimated standard deviation of no more than 1 m/s. This is the core for the later results. From these winds, the 10 minute gust peaks are generated, and the complete time-series of the receiving winds can be analyzed to explain the development of wind gusts. In order to evaluate the estimate and provide a

measure of uncertainty of the derived wind, the covariance of $\hat{\mathbf{v}}_0$ can be estimated with

$$Cov\left[\hat{\mathbf{v}}_0\right] = (A^T A)^{-1}\sigma^2. \tag{3.13}$$

If $\hat{\sigma}$ from Eq. (3.12) would be used here, only the measurements that remain after the elimination process contribute and the uncertainty is significantly underestimated. However, including all the measurements would in contrast overestimate the uncertainty. Either the noise values would distort the estimation or the tails of the distributions are too truncated to still show the true width of the distribution. To account for the eliminated observations, it is assumed that the remaining ones represent the truncated part of a normal distribution. That means all eliminated values are assumed to lay in the shrunken tail regions. Therefore, the estimated variance from the non-eliminated observations has to be modified accordingly by multiplying with the factor

$$\left[1 + \frac{2\Phi^{-1}(p/2)\phi(\Phi^{-1}(p/2))}{1-p}\right]^{-1}, \tag{3.14}$$

whereby p is the percentage of discarded measurements, Φ is the CDF and ϕ the PDF for the standard normal distribution (i.e., $\phi(x) = f(x;1,0)$ and $\Phi(x) = \int_{-\infty}^{x}\phi(t)\,\mathrm{d}t$). The scaling originates from Johnson et al. (1994). Combined Eqs. (3.12), (3.13) and (3.14) thus provide

$$Cov\left[\hat{\mathbf{v}}_0\right] = (A^T A)^{-1}\hat{\sigma}^2\left[1 + \frac{2\Phi^{-1}(p/2)\phi(\Phi^{-1}(p/2))}{1-p}\right]^{-1}. \tag{3.15}$$

However, an evaluation shows that it is not sufficient to use just this modification for the estimation. By $\hat{\mathbf{v}}_0$ and $Cov\left[\hat{\mathbf{v}}_0\right]$ the retrieval provides a prediction of parameters of a normal distribution. From this, wind strength and its standard deviation can be determined, which likewise are parameters of a normally distributed random variable. Inserting an actual measurement (wind strength from sonic anemometer measurements at 90.3 m agl) in the normally distributed CDF with these two parameters (also at 90.3 m agl) gives a probability. On average, the values of such evaluated CDFs should be equally distributed. The histogram for the CDF values is known as *rank histogram*, and these show to be too distorted with the formulation of Eq. (3.15). The assumption that the n measurements are independent and $n-3$ is the DOF is the doubtful assumption that needs to be reconsidered: since the DOFs are not known, the actual DOFs are derived by improving the rank histograms. For the quick CSM configuration, with the approximately 11 measurements per cycle at 3.4 s, an effective CDF of $n_{ef} = 2$ is derived and per 10 minutes interval of $n_{ef} = 12$. Scaled with this and scaled reciprocally by the overestimated CDF of $n-3$ gives

$$Cov\left[\hat{\mathbf{v}}_0\right] = \frac{n-3}{n_{ef}}(A^T A)^{-1}\hat{\sigma}^2\left[1 + \frac{2\Phi^{-1}(p/2)\phi(\Phi^{-1}(p/2))}{1-p}\right]^{-1}. \tag{3.16}$$

The rank histograms can be checked in Figure 12 of Steinheuer et al. (2022). For the quick CSM, the two specified DOFs are each the integer that generates the lowest maximum occurring frequencies based on three months of observations. For other configurations or time intervals of interest n_{ef} has also to be determined accordingly.

3.4 Special features of the quick continuous scanning mode

The DWL is forced to the limits of its hardware with the quick CSM configuration. If a faster rotation than in 3,4 s would have been possible, it would have been tested. From the manufacturer, there was the advise to use this experimental mode with caution, because the device is not designed for such fast rotations (personal information from J. Eacock to R. Leinweber) and may cause higher wear. Accordingly, when it was used, some of the features implied by the mode were discovered for the first time.

By measuring while turning the DWL head, a large number of measurements is generated, approximately one for every 0.31 s. The direct DWL software output is a text file in which each measurement is logged and can be identified with a running integer representing the counter in the instrument software, which is continuously incremented during the operation. At the beginning of the experiments with the CSM, there were some software crashes of the DWL which resulted in the interruption of the recordings. It was assumed that this was due to the internal counter which experienced an integer overflow and thus caused the shutdown. To counteract this, the measurement configuration was rearranged such that the direction of the DWL head rotation changed every half-hour, which was aimed to force the counter to run backwards. The exact configuration therefore works like this: at the beginning of a full hour, the DWL head moves counterclockwise, decelerates after half an hour, then accelerates clockwise and moves until just before the full hour, to stop and stare vertically upwards for a short time until it starts measuring again in the new hour. This heuristic approach was able to prevent the crashes and ensured continuous operation of the DWL both in the summer of 2020 and with multiple DWLs in the summer of 2021.

Operating by alternating the direction of rotation resulted in interesting artifacts that allowed for better understanding the DWL, and which were noticed only because of the half-hourly turn-direction changes. Figure 3.4 top shows the 10 minute horizontal wind barbs for June 12, 2021. The wind directions are rather similar in the vertical at any time, but every 30 minutes they jump about 20-30°. On the hour, this jump is counterclockwise, and on the half-hour, it is clockwise. The actual wind directions are in between, as the control with tower measurements reveals. The reason for this directional shift is an incorrect assignment of the azimuth angle by the DWL which is present on all days. The azimuth is saved before the emission of the light pulses starts. However, since the DWL rotates continuously, it continues to rotate for a short period of time after the azimuth saving but before the light pulses are transmitted and received. Transmitting and receiving of the pulses happens then almost instantaneously, because the measurements are conducted with the speed of light. Hence, the determined Doppler velocity originates from one particular azimuth direction (and is not from a range of directions), that is saved incorrectly and has to be determined. The continuous scanning mode is actually a continuously moving, but no permanently sending/receiving

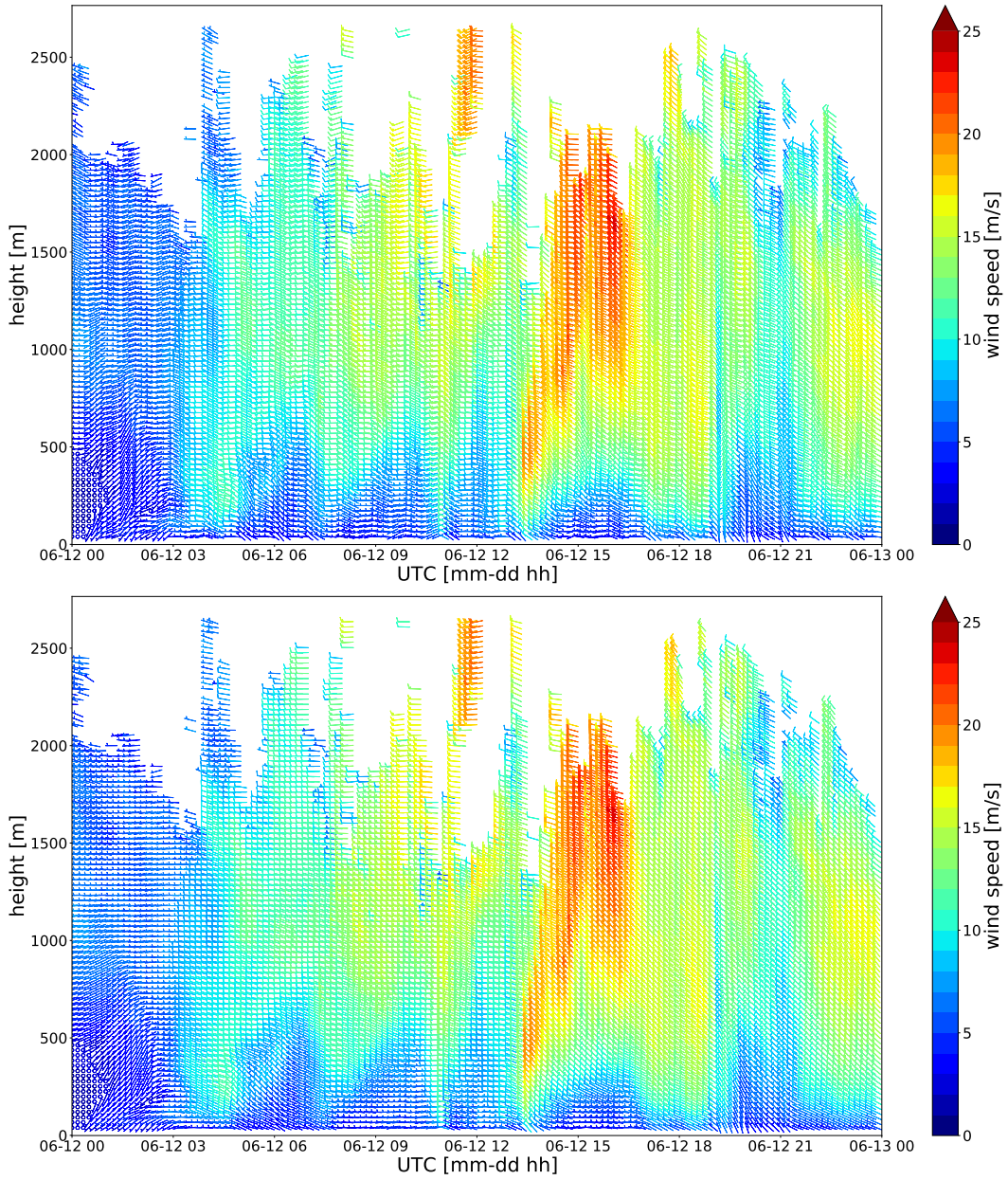

Figure 3.4: Color-coded wind barbs for the 10 minutes mean wind on June 12, 2021 from the DWL operated in the quick CSM. *Top*: Results without an azimuth correction and half-hourly wobbling of wind direction. *Bottom*: Results with azimuth shift to the consecutive recorded azimuth according to Eq. (3.17).

mode. To determine a constant bias would cause problems in the acceleration and deceleration phases (because at slower rotation speeds more measurements are performed within the cycle). The correct azimuth lies between the erroneously determined value (start-value of azimuth window) and the azimuth of the next measurement (end-value of azimuth window). This interval is traveled by the line-of-sight while the measurement takes place in between. In the three summer months of 2020 the quick CSM was almost in permanent operation. From the

statistics of the wind direction jumps every half-hour the correct azimuth for a measurement is determined to be shifted by 40% to the azimuth of the subsequent measurement, i.e.,

$$\theta_{i,update} = 0.6\ \theta_i + 0.4\ \theta_{i+1}, \tag{3.17}$$

for all consecutive measurements $i = 1, \ldots, n$. This adjustment yields the corrected 10 minute horizontal wind barbs of Fig. 3.4 bottom. Figure 3.5 shows the distribution of the 10 minutely wind shifts after the correction between the minutes 00-10 and previous minutes 50-00 in panel a, and between minutes 20-30 and 30-40 in panel b for all the measured hours in summer 2020. The mean values of the shifts are close to 0° and hence less than the accuracy of the wind direction (because the alignment to north of a DWL is done manually). The azimuth correction is thus about +/-10° in magnitude, which implies that the measurement actually is done about 0.3 s after the azimuth has been saved. The correction is based on a StreamLine DWL and could be different for other DWL.

When analyzing the measurements from summer 2021, another feature depending on the direction of rotation was noticed: every half-hour the vertical velocity alternately jumps by about 0.27 m/s. Figure 3.6 is copied from Steinheuer and Löhnert (2023) and gives an example of the derived w-component in the quick CSM for June 29, 2021 (panel a). Especially in the morning hours (until about 7 UTC) a change of the half-hourly vertical motions is visible in the ABL (about up to 1000 m), which jumps around 0 m/s (yellowish for rising air and bluish for sinking). Panel b provides measurements from a DWL that measures pure vertically staring, i.e., directly captures the vertical velocity as Doppler velocity. It is evident that in

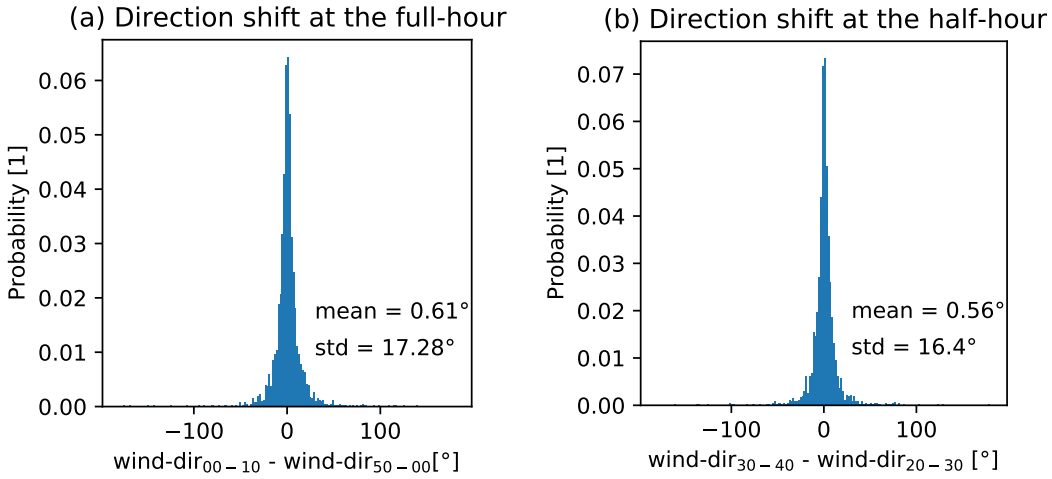

Figure 3.5: Histogram of the 10 minutes horizontal wind direction shift after the correction of Eq. (3.17). (*a*): Results for the shift at the full hour, i.e., distribution of the difference between the wind from the first ten minutes of an hour and the wind from the last ten minutes of the previous hour. (*b*): As in (*a*) but shifted by 30 minutes. Mean and standard deviation (std) of the distribution are given.

the morning hours the vertical motion varies little and the jump-pattern is another artifact which has to be corrected.

The half-hourly offset is independent of altitude, which is why one correction to all layers is applied. The mean vertical wind of the sonic anemometer at 90.3 m agl in Falkenberg is the calibration reference for this purpose. Also, the mean 10 minutes vertical wind of a DWL from 90.3 m agl is determined for all times measured clockwise and counterclockwise, respectively. The difference from the mean of the corresponding sonic anemometer vertical winds (all near 0 m/s) is the offset that is subtracted in all layers for the DWL vertical winds in each case corresponding to the direction of rotation. Panel c shows the vertical

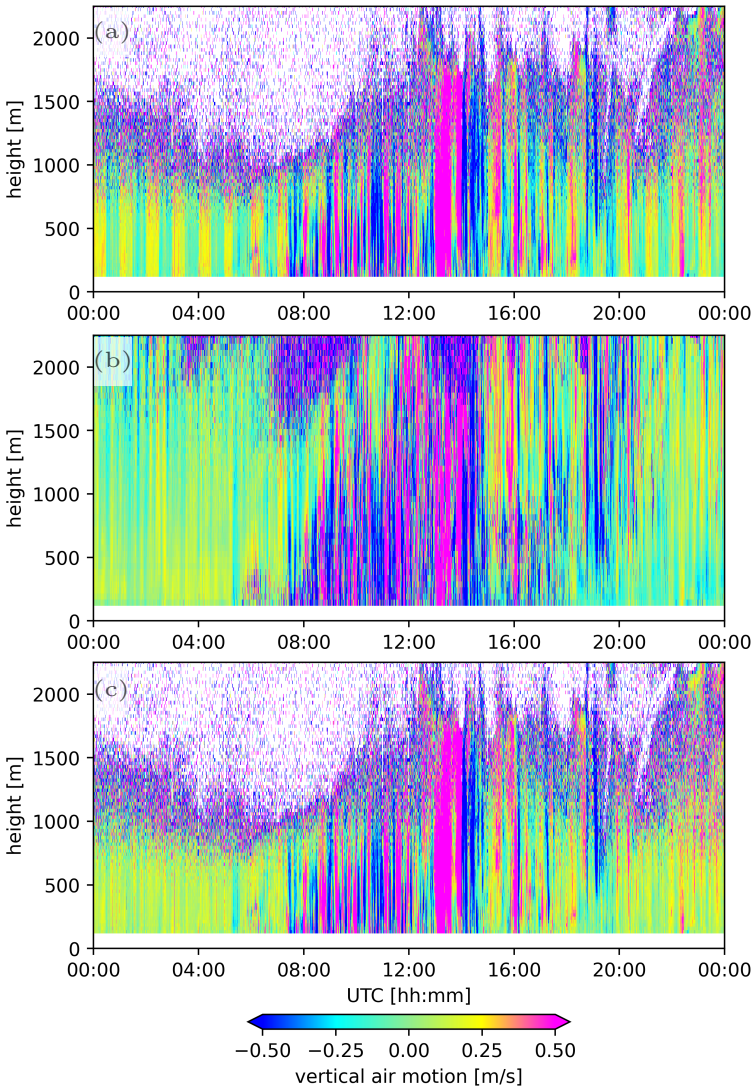

Figure 3.6: Figure 13 from Steinheuer and Löhnert (2023): *Vertical air motion at Falkenberg on June 29, 2021. Panel (a) gives the time-series (∼3.4 s resolution) for the raw w-component of the CSM; panel (b) the Doppler velocity of the vertical pointing DWL (∼3.1 s); and panel (c) the bias-corrected time-series of the CSM (correction of panel (a)).*

wind corrected out of panel a, which now corresponds distinctly in the lower ABL to the profile from panel b. In the manuscript there is a statistic on the differences of the vertical wind in the quick CSM and the vertical stare, which validates the correction (Steinheuer and Löhnert, 2023, Fig. 4). The mean difference is close to 0 m/s up to approximately 1000 m and the standard deviation increases with increasing altitude, which is not surprising since the vertical wind in smaller turbulent eddies can no longer be detected by the CSM (due to the increasing measurement circle diameter).

In the summer of 2021, different DWLs were used that were deployed at different locations up to 6 km away from Falkenberg, but which nevertheless were all calibrated with the sonic anemometer at Falkenberg. Table 2 in Steinheuer and Löhnert (2023) provides the specific rotational direction-dependent offsets. The offset-ranges are all on the order of 0.27 m/s and some offset-pairs are symmetrically distributed around the 0 m/s (0.13 – 0.15 m/s deviation for rotations against the direction of rotation and -0.14 – -0.12 m/s for with the direction of rotation). It is hypothesized that the rotational direction-dependent offset arises because the relative velocity of the rotating DWL head is added to or subtracted from the Doppler velocity for each measurement. This is not systematically investigated, however, an estimate supports the hypothesis, because the DWL mirror distance (exit and entry point of the laser beam) from the rotation axis is 14 to 15 cm, and with a rotation time of 3.4 s and elevation angle of 62°, this leads to Doppler velocity offsets around 0.13 to 0.14 m/s. Asymmetry of the two offsets then indicate another, software-internal miss-calibration of the Doppler velocity, but this is incidentally eliminated by the proposed correction.

3.5 Field Experiment of Sub-mesoscale Spatio-Temporal Variability in Lindenberg

Nowadays, NWP models operate with grid spacing of a few kilometers, where deep convection starts to become resolvable and its representation needs to be verified. However, the kilometer-scale range is usually not covered by standard observations with an operational monitoring network that is too wide-meshed. Therefore, FESSTVaL aimed to illuminate this blind spot by observing ABL variability on the hectometer- to kilometer-scale, focusing on CPs, ABL evolution, and wind gusts. The measurement campaign was initiated by HErZ and conducted by the involved universities, the DWD and external institutions. With the focus on measuring wind gusts, the testing of different measurement configurations of the DWL already started in autumn 2019 in order to determine an appropriate configuration for the campaign. The main observation period was originally planned for summer 2020, but was then postponed by one year due to the COVID-19 pandemic. Instead, a series of sub-campaigns, i.e., three so-called *FESST@home* campaigns, were launched in 2020 that were organized by individual FESSTVaL groups but only had some of the measurement

infrastructure and addressed only sub-aspects of the campaign's focus. By this time, the quick CSM was identified as the most successful configuration and was therefore operated for the full period of three summer months (*FESST@MOL*; Steinheuer et al., 2022). Meanwhile, in Hamburg, low-cost self-developed *autonomous CP loggers* (APOLLOs) were tested with respect to the ability to observe CPs in a dense network (*FESST@HH*, Kirsch et al., 2022). In southern Germany, it was investigated how the measurement campaign could benefit from citizen science (*FESST@Bayern*). Then, in summer 2021, FESSTVaL could actually take place in the area around the *Meteorological Observatory in Lindenberg – Richard-Aßmann Observatory* (MOL-RAO) with many included observation devices, some of which are shown in Fig. 3.7. About 150 self-built and low-cost instruments were stationed in the vicinity within a radius of 15 km. This network recorded ground level pressure and temperature through 80 APOLLOs, 19 weather stations (WXTs; which additionally measured wind, relative humidity, and rain rate), and 70 home-built weather stations (which additionally measured relative humidity and radiation) operated by citizens. Boundary layer and upper air observations were provided by 9 DWLs (air movement), 4 *microwave radiometers* (MWRs; thermodynamic profiles), a *micro rain radar* (MRR; rain profile), and an X-band radar (rain field) at three super-sites. Supplementary measurements were provided by an unmanned aircraft, multicopters, and a small radiation grid during a four-week IOP (July 2021). The three super-sites are Lindenberg (at the MOL-RAO), Falken-

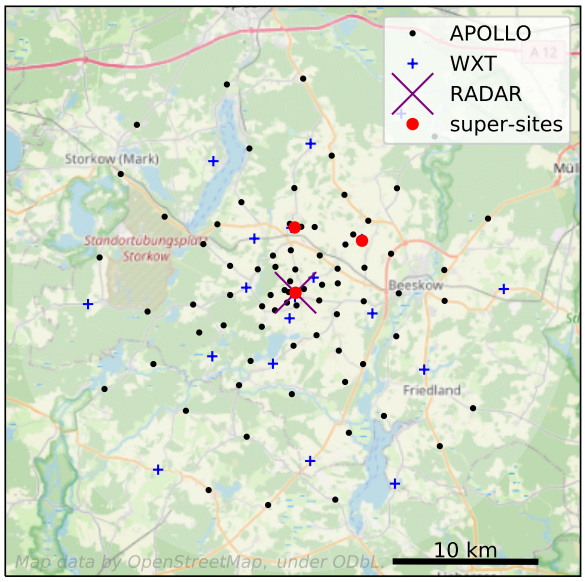

Figure 3.7: Figure 1 from Steinheuer and Löhnert (2023): *The campaign area is located in the northeastern part of Germany in flat terrain with predominantly cropland (yellowgreen), forrests (green), and some lakes (blue). The three FESSTVaL super-sites with DWLs are located about 6 km apart: Lindenberg in the north, Birkholz in the northeast and Falkenberg in the center (red markers).*

berg (at the boundary layer measurement field of the MOL-RAO, Neisser et al., 2002), and Birkholz (at *Gut Hirschau* on a deer meadow, purpose-built temporary site). They are located about 6 km apart and each is equipped with a DWL which was measuring in the quick CSM. This triangle constellation provided measurements in the 3rd dimension from sides close enough to detect the spatial variability in the vertical profile within high-impact weather events (Steinheuer and Löhnert, 2023). An overview article on the FESSTVaL campaign was recently submitted (Hohenegger et al., 2023).

Chapter 4

Summary of Results

This chapter briefly summarizes the main findings of the two publications and the manuscript, which are included completely in the appendices A and B, and C, respectively.

4.1 Vertical profiles of wind gust statistics from a regional reanalysis using multivariate extreme value theory

Wind gust data are required for a number of applications at very different altitudes of the atmosphere. For example, wind farm operators are interested in wind and gust forecasts at the hub height of their turbines, which today can have heights of 150 m but are expected to reach higher altitudes in the future. However, the NWP models usually only give parameterizations for wind gust peaks at the standard measurement height of 10 m agl, and do not provide a quantification of the uncertainty. The article presents a statistical post-processing to obtain a conditional distribution for peak hourly wind gusts as a function of height. By providing a distribution, the prediction can be evaluated in terms of its uncertainty (e.g., the standard deviation), but it can also be reduced to a point prediction (e.g., the mean). The conditioning variables that determine this distribution are obtained from the regional reanalysis COSMO-REA6. The post-processing is created using observations of wind gust peaks from five levels between 10 and 250 m from the Hamburg Weather Mast, recorded between beginning of 2004 and ending of 2014.

The statistical post-processing is based on a censored GEV (cGEV) distribution with inhomogeneous parameters for location and scale conditional on the reanalysis, but constant shape parameter at zero (i.e., Gumbel distributed). The GEV distribution is the theoretical limit distribution for maxima of arbitrary distributions and a commonly used distribution to approximate weather extremes. The censoring is applied to tune the achieved distribution especially to better represent the higher wind gust peaks. For each height, the censoring

threshold is chosen to represent the median of the wind gust peaks for the 11 years. All observations that fall below this threshold are used only to train the post-processing to produce an estimated GEV distibution for similar situations with an exceedance probability of less than 50% for that threshold. To evaluate the quality of the post-processing, a cross-validation is performed: the impacts of the predictors are estimated using 10 years of data and evaluated for the remaining year. This allows for eleven independent judgments of the method. Furthermore, to assess the performance of the prediction in intermediate layers, double cross-validation is performed, i.e., the observations of the layer to be predicted are additionally omitted in the parameter estimation. An MLE then provides, for given time-series of observations and corresponding reanalysis variables, the most likely parameters, which are the regression coefficients that quantify the influence of the variables on the distribution. The determined regression coefficients are relatively similar and differ only slightly with respect to the eleven estimates for each eliminated year.

The LASSO is used to select only the most informative variables for the post-processing and not include those with little impact. Vertical variations of the cGEV parameters are approximated by height-dependent Legendre polynomials so that predictions can also be generated for any desired layer that is at unobserved intermediate height. The important variables, i.e., the final predictors for the wind gust peak distribution, are the 10 m agl gust diagnostic, the barotropic and baroclinic modes of absolute horizontal wind speed, the mean absolute horizontal wind at 700 hPa, the surface pressure tendency, and the lifting index. In contrast, the surface temperature at 2 m, the tendency of convective available energy (CAPE), and the shear of the wind speed (calculated between 6 and 1 km altitude) have less impact, and therefore are not selected by the LASSO (compare to Table 2 in Steinheuer and Friederichs, 2020). The verification is conducted with proper scoring rules (Gneiting and Raftery, 2007), that evaluate the distributional predictions at the respective observations. Compared to climatology, i.e., the constant empirical distribution of all observations, the post-processing shows improvements of up to 60 %, especially at higher altitudes. There is hardly any difference if the model is estimated layer by layer or for the entire set of layers using the Legendre polynomials. Also, the prediction works on intermediate layers whose observations have been completely omitted. Extrapolating to both 10 m and 250 m does not yield good results and should not be used. To improve the 10 m gust peak of the reanalysis, it is advisable to use the mean of the cGEV distribution, as evidenced by the distribution of their differences to the observations, because the bias is eliminated and the standard deviation is reduced compared to the reanalysis 10 m gust diagnostic.

A high-impact weather event is discussed, the storm Emma between February 29 and March 1, 2008, where the highest gusts of the entire 11 years are measured with 28.07 m/s at 10 m (compare to Fig. 3 in Steinheuer and Friederichs, 2020). Like the reanalysis, the post-processing approach does not hit this highest gust on March 1, 2008, although the

post-processed forecast has quite high uncertainties, thus providing at least an indicator of a weather situation that is difficult to forecast. A more accurate prediction is provided by the post-processing method for February 29, 2008, where the too high reanalysis gusts are corrected by the post-processing (i.e., with a distribution shifted towards lower values with respect to the point forecast). To evaluate the dependencies between gusts at different heights, the bivariate Pickands dependence function is used (Pickands, 1981). The more stably stratified the ABL is, the more independent are the gusts in the individual layers and the information of the predictors reduces dependencies between the gust distributions of the individual layers in all situations.

The post-processing model estimated for the Hamburg Weather Mast should be transferable in principle to other sites as well, but could differ locally due to topographic effects. This can be tested using observations from other weather towers in the model region, but these are very sparse and limited in height. Therefore, it is advisable to also consider other measurement concepts that can observe gusts from higher layers.

4.2 A new scanning scheme and flexible retrieval for mean winds and gusts from Doppler lidar measurements

DWLs allow the determination of wind profiles with high vertical resolution and offer an alternative to classic meteorological tower observations, since they can be flexibly deployed at any electrified location and, moreover, they receive signals from higher altitudes. However, these profiles are usually with a rather coarse temporal resolution, because several measurements are required to calculate a mean wind with conventional retrievals. The large number of measurements allows for stable results and adequate estimates of the uncertainties. In contrast, retrieving wind gusts from a DWL is nontrivial because a monostatic DWL provides only one radial velocity per line-of-sight, i.e., only one information of a 3 dimensional wind vector, and measurements in at least three linearly independent directions are required to derive the full wind vector. Therefore, conventional retrievals and slow DWL scanning schemes cannot deliver a wind gust, which by definition is a short-lived wind peak. In this article, the question of whether and how wind gust peaks can be derived from DWL observations is investigated.

The characterization of wind gusts is one central topic of the FESSTVaL measurement campaign besides the investigation of CPs and ABL structures. In the framework of the campaign, many DWLs could be accessed and different DWL configurations could already be tested in advance. Thus, standard configurations (24Beam, DBS), previously investigated (slow CSM, 6Beam), as well as experimental ones (3Beam, quick CSM) have been tested with respect to both capturing 10 minutes mean wind and the wind gust peaks. All measurements were performed at the *Boundary Layer Field site* in Falkenberg (belonging

to MOL-RAO) next to a meteorological tower, whose sonic anemometer at 90.3 m agl serves as the validation reference for the wind. To cope with the multitude of different configurations as well as the requirement to derive the wind from a single DWL full rotation, a new retrieval is developed that can be flexibly adapted to different scan patterns and measurement intervals. The core of the retrieval is the absence of SNR filtering, as this rigorously eliminates measurements that often could be judged reliable. Instead, all measured Doppler velocities are initially used to create a wind vector fit, then the fit is checked if it is too uncertain, and if so, those measurements that do not match the wind vector fit are removed. This process is iterated, i.e., that successively the fit becomes more confident and only a part of the unsuitable observations are eliminated in each step. The iteration procedure follows the concept that the mismatching observations do not represent true recordings of the projected wind speed, but noise, and the iterative updating removes that noise contribution.

All tested configurations are able to reliably monitor the 10 minutes mean wind at 90.3 m agl by the new retrieval: no systematic biases are detected, the data availability is high and almost all root mean squared error (RMSE) values fall below 0.5 m/s (except the comparison for the 24Beam that yields higher values, because the steep elevation angle of 75° leads to partially erroneous Doppler velocities at 90.3 m as the measurements are too close to the DWL and transmitter and receiver field of view do not completely overlap; compare to Fig. 7 in Steinheuer et al., 2022). The 10 minutes wind gust peak is determined from the time-series of wind speeds per DWL cycle, which exhibit varying temporal resolution. These are determined as the peak of the time-series from the DWL, ignoring maxima that are too high (over 1 m/s higher than the closest smaller gust) and also requiring that at least 50 % of the wind vectors have been retrieved. The quick CSM, obtaining about 11 measurements in one cycle within 3.4 s, is best suited to observe the wind gust peaks as measured by the sonic anemometer. In particular for a winter storm event (storm Sabine on February 9 – 11, 2020) even very high wind gust peaks can be accurately recorded (compare to Fig. 9 in Steinheuer et al., 2022). During the summer of 2020, the quick CSM was able to reliably record 10 minutes mean wind and wind gust peak during a three month period of continuous operation, providing wind outputs at nearly all times. Concerning the wind gust peaks, the comparison to the sonic anemometer at 90.3 m exceeds expectations, as the bias is at only 0.32 m/s (very slight overestimation by the DWL on average), the RMSE at 0.8 m/s, and the coefficient of determination with 0.93 close to 1 (compare to Fig. 11 in Steinheuer et al., 2022). The abundance of data made it possible to adjust the uncertainty estimate by determining the effective DOF for the wind in 10 minutes and individual wind gusts, respectively.

The article presents the retrieval and provides the algorithm (Steinheuer et al., 2021a) for deriving different wind products. It shows the usefulness of the quick CSM to observe wind gust peaks. Also, it is demonstrated that the combination of retrieval and CSM is suitable to

determine gust peaks within a storm, i.e., for the kind of events which are of high interest for wind profiling. This raises the question of whether the DWL can be used to perform more detailed case studies for high-impact weather as the derived high-resolution time-series of the wind is not discussed.

4.3 High-resolution profiling of wind gust patterns measured by Doppler wind lidars during the FESSTVaL campaign

The evolution of wind gusts is difficult to track because gusts are short-lived and occasionally very small-scale phenomena. They are an integral part of certain weather such as fronts and CPs, and can vary greatly locally. To observe their propagation, the analysis of an in situ ground level time-series is not sufficient, since their origin is usually in the higher layers. With respect to 10 minutes wind gust peaks, which are the commonly measured and predicted quantity, a high-resolution time-series should be investigated that can visualize the propagation structures. Also, there is the question whether individual gust observations can be considered representative of their surroundings or whether significant differences can already be seen at at scales of few kilometer, i.e., at scales that are sub-scale in common weather models. In FESSTVaL, various phenomena in the ABL were investigated with a variety of instruments during the summer of 2021, including wind gusts as a major research focus. For this purpose, three DWLs were deployed in a triangle configuration at a distance of 6 km to each other to observe wind gusts and detect local differences in the prevailing wind field. These DWLs were operated in the quick CSM, providing time-series of the wind with a temporal resolution of 3.4 s and, depending on atmospheric conditions, were capable of profiling the entire ABL, i.e., ranging approximately up to 1000 – 1500 m altitude and providing values every 30 m vertically. In addition, the investigations benefits from the broad network of observational instruments that constitutes FESSTVaL: thermodynamic profiles by MWRs and cloud base heights by ceilometers are acquired at the three sites; rain rates are observed by a mobile X-band radar and an MRR; and at ground level, APOLLOs and WXTs provide about 100 stations for measurements of pressure and temperature in the surrounding area of 15 km radius around Lindenberg.

The results are based on the high-resolution time-series of the 3 dimensional wind vector from the DWLs. The vertical wind shows an offset which depends on the direction of rotation regardless of the altitude. For its correction, the sonic anemometer at 90.3 m agl on the Falkenberg weather tower is used as the calibration instrument for all three locations so that the mean vertical winds are on average in agreement. Essentially, there are little differences in the wind speeds above the three sites, although there are local variations in some of the highest observed wind gust peaks during high-impact weather events. Two of these are discussed where stronger wind gust peaks were measured. The first example is a cold front

on June 12, 2021, which represents a large-scale event that passes through all locations with slightly different timing. The cold front is first observed near the surface with amplified wind speeds, which then spread out increasingly over the entire observable range. Due to the thermally stable stratification at the back of the front, this area of amplified winds is detached from surface and forms a pronounced wedge formation in the time-height plot with the near-surface arrival of the front as the apex (compare to Fig. 8 in Steinheuer and Löhnert, 2023). By simultaneously recording the vertical air movement, the prefrontal lifting that precedes the onset of rain can be depicted. The falling velocities of the raindrops are superimposed on the vertical air movements and the rain immediately behind the front is thereby detectable by the DWLs.

The second example is a CP event on June 29, 2021 whose effects are locally very different: in the eastern observation area, a rain area moves northwards with the area of lowest temperatures, the CP center, passing over Birkholz (compare to Fig. 11 in Steinheuer and Löhnert, 2023). Falkenberg and Lindenberg experience the outflow of cold air through a deep gust front, which induces significant vertical movements in Falkenberg. Nevertheless, Falkenberg remains dry and only impact of the edge of the CP is observable. Lindenberg receives a small shower as it is only slightly touched by the edge of the rain field before this rain area is pushed northeast by the upper-level flow and out of the observation area. The CP has a vertical extent of 1000 to 1500 m which can be determined relatively precisely at the distinctive shear line of the horizontal winds that is defined by near-surface strong winds originating from the outflow of the area with the highest precipitation, and by overlying air masses of weaker momentum (see Fig. 12 in Steinheuer and Löhnert, 2023). Overall, the CP shows the different characteristics of a schematic CP (see Fig. 10 in Steinheuer and Löhnert, 2023) and, furthermore, in the area of the dry outflow in Falkenberg, even motion at the CP edge line (the wind shear line) to the overlying air can be detected, which has an oscillating height. It is assumed that Kelvin-Helmholtz-waves can be observed here.

The examples show the potential of DWLs to detect highly relevant small-scale features ($\sim$5 s, $\sim$30 m) of winds during high-impact weather. Air mass boundaries, areas and origins of strong winds, updrafts and shear can be detected. In both examples, gust fronts were present, starting close to the ground and causing strong winds only afterwards aloft. The work provides a new proposal for future observation campaigns, which can be crucially supplemented by DWL.

Chapter 5

Conclusion and Perspective

5.1 Concluding remarks

Users of NWP models have to accept that wind gusts are provided only for the height of 10 m above the Earth's surface. The wind gust peaks are parameterized for this height and derived from other prognostic variables. Their direct representation is not yet possible despite improvements in computational capabilities. In order to forecast wind gusts at other model heights, knowledge of their appearance at other heights is required. However, the number of observations available there is very limited, since only tall meteorological towers equipped with in situ anemometers can provide long-time measurements for the time being. The present work proposes a post-processing that allows gust predictions also at higher altitudes and is based on observations made at such a meteorological tower. The larger part of the thesis is dedicated to the DWL with the goal to establish this promising technology in the arsenal of gust measuring instruments and explore a new possibility of high-resolution wind profiling.

Chapter 2 provides the mathematical background and a more detailed theory of the post-processing that is published in Steinheuer and Friederichs (2020) and given in the appendix A. Wind gust peaks, as maxima of the wind signal, can be considered as an extreme value distributed random variable. From a preselected set of variables, the atmospheric predictors are identified that determine the parameters of the hourly wind gust peak distribution in the lower 250 m of the ABL. Not surprisingly, the wind field around the meteorological tower provides crucial predictors for the GEV distribution. The uncertainty of the predicted distribution is increased with the temporal variability of the 10 m gust peak diagnostic. Hence the post-processing incorporates timing problems of the reanalysis. Pressure changes increase the probability of stronger wind gust peaks but also the width of the predicted distribution of the post-processing. In the preselection of potentially influential variables, there were some

whose influence is not significant or possibly nonlinear and therefore are not included in the post-processing. For instance, the wind shear or the CAPE tendency does not have a statistical impact on the wind gust peak distributions, although this would indeed be relevant in summer thunderstorms. Here, however, the exact interpretation is always rather difficult, because if, for example, the 10 m gust diagnostic already provide accurate wind gust peaks in such cases (it is a high-impact predictor at 10 m and above), there is no reason for the statistical model to learn impact from other variables. For the example of a high-impact weather event, the winter storm Emma in 2008, it is demonstrated that the 10 m gust prediction of the reanalysis can be improved by the post-processing. The use of Legendre polynomials proves to be appropriate and allows a seamless prediction of the hourly wind gust peak distributions in all layers between 10 and 250 m.

Based on the idea of Suomi et al. (2017) the research is directed towards the profiling of wind gusts by DWL. Chapter 3 provides the relevant information about the DWL mechanism, the quick CSM, and the new retrieval which is also included in the two articles Steinheuer et al. (2022) or appendix B and Steinheuer and Löhnert (2023) or appendix C. Two adjustments to correct the azimuth and Doppler velocity are introduced because the quick turning of the DWL head leads to systematic offsets in both quantities. The present thesis and the results (Steinheuer et al., 2022; Steinheuer and Löhnert, 2023) are based on measurements of two summers (2020, 2021), a 10 day test phase (autumn 2019), and 3 days around a storm event (Sabine in February 2021) and thus include significantly more measurement days than the idea-generating work of Suomi et al. (2017) with its only 2 days. Initially driven by the necessity of not being able to implement a DBS in 3.8 s per cycle, different DWL configurations were tested and a new configuration with the quick CSM is proposed, that is capable of observing wind gust peaks of similar quality to the observations of a sonic anemometer. Direct comparisons of the wind gust peak against the sonic anemometer measurement at 90.3 m agl on the meteorological tower in Falkenberg result in RMSEs of only 0.8 m/s in summer 2020 and 0.68 m/s in summer 2021. The abundance of measurements collected and the absence of scaling exceeds the expectations making this configuration preferable to a quick DBS, as more measurements are collected (11 instead of 5) in a shorter time. This is only possible by lowering the quality of the single measurements, i.e., fewer light pulses are emitted/received from which Doppler spectra and then Doppler velocities are determined. Rigorous filtering with SNR thresholds becomes inappropriate and would result in hardly enough measurements remaining to determine a wind vector from the leftover measurements of a single DWL cycle. Therefore, a new retrieval is created that only returns wind vectors from measurements that are consistent and iteratively eliminates mismatching measurements that are considered noisy.

In Steinheuer and Löhnert (2023), the interpretation of the high-resolution time-series is addressed. After the direction-dependent bias correction, the vertical wind proves to be a

meaningful parameter for detecting updrafts and rain. Two specific case studies are discussed, illustrating the passage of a cold front and a CP event. Both cases are associated with stronger gusts and are the kind of events that the DWL should be able to record in order to provide a reliable alternative to in situ wind mast observations. In the cases discussed, this has proven successful and has even been surpassed by the profiling of the wind throughout the entire ABL. The cold front presents itself as a large-scale event that is similar at all three FESSTVaL super-sites, with a pronounced cone-shaped area in the time-height plot showing the enhanced winds after the arrival of the front. The CP is a much more local event that produces very individual wind structures at the three sites. The three profiles match the schematic concept of a CP that has radial cold air outflows starting from a central rain field and propagating with a gust front.

5.2 Future research

The limited research years of a PhD project are not nearly enough to illuminate all facets of wind gusts and to investigate the many aspects in adequate detail. The thesis approaches the topic in two different ways – post-processing and remote sensing – and could have done it in more detail or from different perspectives in either case.

The post-processing model is estimated for the location of the Hamburg Weather Mast, but should in principle be transferable to other places. The parameter estimates could be different there, since the local topography could play an important role, which is different in the flat coastal region of Hamburg than in a hilly inner-European area. Nevertheless, it is reasonable to assume that post-processing essentially corrects systematic errors and introduces the influence of other atmospheric variables on wind gusts, which are already included in the reanalysis but not intertwined with the parameterization. As Sheridan (2011) points out, there are different approaches for parameterization, and, accordingly, post-processing for other NWP models might differ. However, the proposed approach has shown that there are predictors that can improve the gust prediction and that are not included in common parameterization schemes and therefore could improve other models as well. It is assumed that meaningful variables are found which can be used for new parameterization approaches.

Other reanalyses or NWP models also lack predictions of wind gust peaks above 10 m. In general, the goal would be an improved and extended gust forecast covering the complete lower model domain. Unfortunately, research seems to be rather far away from this goal today, because there are so few gust observations at higher layers than 10 m which could provide the necessary observations for the model development. As a first next step, the data of the weather towers from Cabauw (Netherlands), Karlsruhe or Falkenberg (both Germany) could be evaluated, but these towers are different in their heights and partly not equipped with sonic anemometers, so both instrument peculiarities (inertial cup anemometers for example

in Karlsruhe) and the lower vertical availability of data (only the 99 m tower in Falkenberg) have to be tackled. And above all, there is the hope that in the future there will be enough wind gust profiles from DWLs to have enough data for statistical models.

If one concentrates exclusively on the wind gust peaks near the ground, one has a much larger measurement network at disposal. For example, the DWD observation network comprises 139 stations in Germany, which record the hourly wind gust peaks in 10 m. Friederichs et al. (2009) used these gust observations to fit a GEV distribution. However, what is still missing is a 2 dimensional model that also models the correlations and generates predictions for locations without observations. Smith (1990) presents a proposal on how spatial extremes can be represented by *max-stable processes*. Max-stable processes are a multi-dimensional extension of EVT. Individual locations have extreme value marginal distributions, thus the method could be integrated and extended by the two horizontal dimensions (for instance as proposed in Friederichs et al., 2018). This will potentially lead to a comprehensive multi-dimensional gust model.

These ideas were not followed any further, because with FESSTVaL a unique opportunity arose to explore how wind gust data can be collected from the DWL. The flexible retrieval is able to create time-series of the wind from which the wind gust peaks can be derived. True to the motto '*a retrieval is never finished*', there is still potential for improvement. The retrieval needs threshold values, which are set, but which could also be chosen differently. Further, situations are encountered where there are unrealistic winds. If there are short shifts in wind direction or high jumps in speed in the time-series, this is usually caused by noisy data, which is, however, consistent in terms of the retrieval and thus included in the wind product. Here, one could adjust the thresholds or consider adding classic wind time-series filters that check the time-series for consistency. This could also include checking for consistency with vertical neighbours of the time-series, i.e., whether the profile is coherent at given points in time.

In general, it is possible to clearly determine the quick CSM as the most suitable configuration for deriving wind gusts and high-resolution time-series of the wind. Especially the comparisons in 90.3 m agl with the sonic anemometer are convincing. The 3 s wind gust peaks of the sonic anemometer coincide with the maximum of the wind time-series from the 3.4 s long lasting individual cycles. At first glance, there is a discrepancy in the gust duration here. In fact, the approximately 11 measurements of the single cycle originate from approximately 3 s, because the travel time between the final measurement of one cycle and the first measurement of the following cycle can be subtracted. The high direct agreement gives no reason to consider scaling, as discussed for instance in Suomi et al. (2017), where a scaling from 3.8 s long lasting gusts to 3 s gusts is conducted. Nevertheless, there is still potential in such a scaling approach and especially the other configurations (Steinheuer et al., 2022) could also be scaled to more matching gusts as their weak agreement arise mostly due to their long cycle duration.

Furthermore, the optimal elevation angle is not systematically determined. The 62° inclination angle is already used (Suomi et al., 2017) and is eventually adopted, partly because the shallower tested angle of 35.3° results in lower vertical range. Further research could ensue here, however, as it is possible that the high-resolution wind time-series and the gusts in the higher ABL layers are of less interest and that a configuration that simultaneously provides TKE measurements (for which the 35.3° angle is useful) is more desirable. Other angles are also conceivable and ultimately the trade-off problem between, on the one hand, a flatter and more direct line-of-sight along the horizontal wind, but, on the other hand, an increasingly weaker homogeneity assumption with increasing altitude, is not resolved. The aim of this work is to create profiles. Homogeneity is assumed, but certainly the horizontal wind field shows variability's that can contradict this assumption, especially in gusty situations. If one chooses very flat elevation angles so that the viewing directions are just above the horizon, namely a low-level plan-position indicator (PPI) configuration, the horizontal wind field close to the ground can be resolved relative to the DWL. Pichault et al. (2022) reveals that gusts occur in patches that are transported through the wind field as areas of increased wind speed. They present a detection algorithm for the PPI to track these. The FESSTVaL data set also includes some DWL measurements in PPI that can be analyzed for such gust patches.

There are cases where the new retrieval has difficulties in distinguishing correctly between noise and actual wind signals. This is mainly associated with the mean wind from the slow CSM configuration, which is ultimately irrelevant to the gust determination and only occurred on one particular device, but still needs to be investigated: there is too often a retrieved wind near 0 m/s in higher layers. The reason for this is that the noise here is not uniformly distributed in the Nyquist-velocity range, but occurs more frequently around the Doppler velocity of 0 m/s. The retrieval reads this accumulation as a wind signal and delivers mean winds of 0 m/s accordingly. This effect is enhanced when the actual wind speeds are indeed very low, because then the true signal and near-zero noise overlap and it is impossible to distinguish between calm and low winds. The cause of this noise characteristic is not yet clear and to solve it is subject of ongoing research at the MOL-RAO (by E. Päschke, C. Detring, and F. Beyrich). Nevertheless, the concept of sending fewer pulses per individual measurement, but achieving a higher number of total measurements in return, can be practical. It should be further investigated whether the mean wind can be generated with a CSM with only 3000 pulses per measurement in really comparable quality to the widely used 24Beam with 30000 pulses. If such results are encouraging, the CSM should be used routinely and thus high-resolution wind and the wind gust peaks could also be routinely acquired.

The quick CSM introduces unforeseen features, which are fixed. Modifying vertical wind and azimuth afterwards is admittedly rather inelegant, but nevertheless it is necessary. This shows that the CSM must still be classified as an experimental mode that needs further

research. Consequently, azimuth and Doppler velocity offset should be modified in advance by the manufacturer software with reference to the direction and speed of rotation of the DWL. Whether this is exactly the same for other CSM configurations as in the particular approach remains to be investigated.

Finally, it remains to be emphasized that a huge potential lays in the quick CSM for conducting case studies. The quick CSM combined with the flexible retrieval provides a new tool for high-resolution profiling of the wind. The FESSTVaL data set has not fully been analyzed yet, but several wind structures that are far too small-scale to have been resolved by

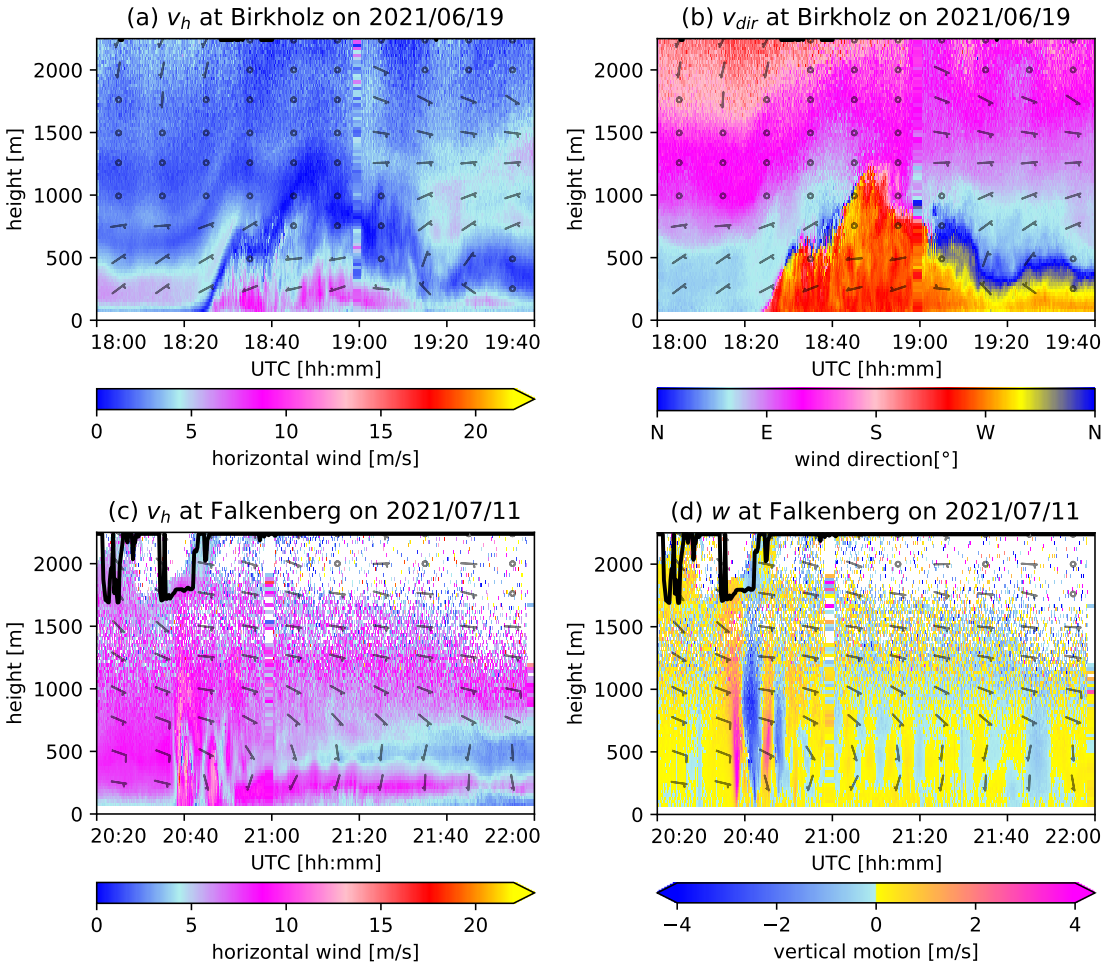

Figure 5.1: Profiles of horizontal wind speed (panel a) and wind direction (panel b) from June 19, 2021 at Birkholz; and profiles of horizontal wind speed (panel c) and vertical air motion (panel d) from July 11, 2021 at Falkenberg. Wind barbs showing wind direction are included every 250 m/10 minutes and the lowest cloud base height recorded by a ceilometer is indicated as a thick black line. Cloud base heights exceeding the image section (which is up to 2250 m) are indicated by a horizontal line at the top of the panel.

common methods are identified. Figure 5.1 provides two examples of such events, which are not yet examined in detail, but might represent attractive wind situations for deeper research. Panels a and b show horizontal wind and wind direction on the evening of June 19, 2021. The wind strength gives little indication for a detailed investigation, as it changes rather slightly and would hardly be noticeable in the mean wind. Their high-resolution time-series shows a slight increase in speed from about 18:30 UTC up to heights of about 500 m, with simultaneous slight decreases in speed above that (slightly darker blue). In the profile of the vertical wind, an uplifting at 18:30 UTC can be detected (not shown). However, the wind direction in panel b is remarkable: it turns dramatically and instead of the prevailing easterly-northeasterly wind direction near the ground, the wind turns to westerly. The observations are from Birkholz, but a similar situation is evident over Falkenberg or Lindenberg. The outflow of a thunderstorm is observed that did not occur in the central part of the FESSTVaL area, but further to the west. The meandering upper boundary of this outflow region, is similar to the discussed case of June 29, 2021 and would hardly be visible in time-series of mean wind. Moreover, it is possible that the outflow area on the other side of the thunderstorm cell could proceed at significantly higher wind speeds, as there the outflow direction and the prevailing flow intensify instead of counteracting each other.

The second example in panels c and d represents horizontal wind and vertical motion over Falkenberg on July 11, 2021. Here, too, the situation is such that a rain cell influences the observations, which itself lies outside the observation area, in this case south of Falkenberg. A rearrangement of the air masses in the evening after 20:30 UTC is apparent, which introduces increased wind speeds close to the ground and changing wind strengths in the vertical (panel c; until about 20:50 UTC). At the same time, there are pronounced vertical movements (panel d) with two changes from updrafts to downdrafts. Due to the absence of rain, the downdrafts can be clearly identified as such. In the aftermath, a wave motion of the air mass boundary in approximately 400 m can be differentiated, which separates the intensified winds close to the ground from the weaker, thus the elevated, winds above it. The boundary line in the horizontal wind is accompanied by an alternation of upward and downward motion. The wave motion is picture-perfect and another example of Kelvin-Helmholtz waves.

Because of such examples, it is clear that case studies of individual events can bring to light fascinating features that have rarely been observed, but for which theories do exist. This is where a link to the NWP is appropriate, because case studies are also common in the evaluation of models. It is not necessarily a question of whether a certain event has the same timing as in reality, but whether the wind situations in comparable weather events turn out likewise. Thus, it could be analyzed whether the wind in the NWP model provides a similar cone structure during the passage of a cold front and whether the air mass boundaries in CP outflows also occur in the wave-like manner. In particular, high-resolution NWP models such

as ICON-D2 could be evaluated with the DWL, but also model runs of *large eddy simulations* or even *direct numerical simulations* could be the subject of future research.

Appendix A

Steinheuer and Friederichs, 2020

Vertical profiles of wind gust statistics from a regional reanalysis using multivariate extreme value theory

Many applications require wind gust estimates at very different atmospheric altitudes, such as in the wind energy sector. However, numerical weather prediction models usually only derive estimates for gusts at 10 m above the land surface. We present a statistical model that gives the hourly wind gust peak. The model is trained based on a weather reanalysis and observations from the Hamburg Weather Mast. Reliable predictions are derived at up to 250 m, even at unobserved intermediate levels.

J. Steinheuer and P. Friederichs (2020). "Vertical profiles of wind gust statistics from a regional reanalysis using multivariate extreme value theory". In: *Nonlinear Processes in Geophysics* 27.2, pp. 239–252. DOI: 10.5194/npg-27-239-2020

Author contributions: Steinheuer and Friederichs jointly developed the concept and methodology for this work. Steinheuer carried out the post-processing and the visualization of the results, and Friederichs supervised the process. Steinheuer was the lead author on the paper with input from Friederichs.

Nonlin. Processes Geophys., 27, 239–252, 2020
https://doi.org/10.5194/npg-27-239-2020

Nonlinear Processes in Geophysics
Open Access
EGU

Vertical profiles of wind gust statistics from a regional reanalysis using multivariate extreme value theory

Julian Steinheuer[1,2] **and Petra Friederichs**[3]

[1]Institute for Geophysics and Meteorology, University of Cologne, Cologne, Germany
[2]Hans Ertel Centre for Weather Research, Climate Monitoring and Diagnostics, Cologne/Bonn, Germany
[3]Institute of Geosciences, University of Bonn, Bonn, Germany

Correspondence: Julian Steinheuer (julian.steinheuer@uni-koeln.de)

Received: 29 November 2019 – Discussion started: 16 December 2019
Revised: 16 March 2020 – Accepted: 23 March 2020 – Published: 23 April 2020

Abstract. Many applications require wind gust estimates at very different atmospheric height levels. For example, the renewable energy sector is interested in wind and gust predictions at the hub height of a wind power plant. However, numerical weather prediction models typically only derive estimates for wind gusts at the standard measurement height of 10 m above the land surface. Here, we present a statistical post-processing method to derive a conditional distribution for hourly peak wind speed as a function of height. The conditioning variables are taken from the COSMO-REA6 regional reanalysis. The post-processing method was trained using peak wind speed observations at five vertical levels between 10 and 250 m from the Hamburg Weather Mast. The statistical post-processing method is based on a censored generalized extreme value (cGEV) distribution with non-homogeneous parameters. We use a least absolute shrinkage and selection operator to select the most informative variables. Vertical variations of the cGEV parameters are approximated using Legendre polynomials, such that predictions may be derived at any desired vertical height. Further, the Pickands dependence function is used to assess dependencies between gusts at different heights. The most important predictors are the 10 m gust diagnostic, the barotropic and the baroclinic mode of absolute horizontal wind speed, the mean absolute horizontal wind at 700 hPa, the surface pressure tendency, and the lifted index. Proper scores show improvements of up to 60 % with respect to climatology, especially at higher vertical levels. The post-processing model with a Legendre approximation is able to provide reliable predictions of gusts' statistics at non-observed intermediate levels. The strength of dependency between gusts at different levels is non-homogeneous and strongly modulated by the vertical stability of the atmosphere.

1 Introduction

Severe wind events are one of the main weather hazards for humans and economies. Extreme wind gusts cause damage to buildings, with effects from loose flying objects to uncovering complete roofs. These hazards also affect whole forests, especially those with shallow-rooting trees such as spruce – the most used timber in Germany. For the energy sector, wind prediction is becoming more relevant due to the growing demand in renewable energy, especially in wind power generation. A steady strong wind is most efficient for the power production, as the power produced at wind plants is proportional to the cube of the horizontal wind speed. The wind energy plant rotors react slowly to fluctuations in wind patterns; thus, they are not able to transform the higher energy of wind gusts into electricity. On the contrary, if the shear forces due to gusts are too strong on the rotor, they can lead to the deactivation of the entire wind park. For a stable electricity network, large wind variations are problematic; therefore, forecasts need to capture these variations. The hubs of power plants reach heights above 150 m, and their size is increasing, especially in off-shore parks. Thus, for the planning and operation of wind power plants, accurate estimates and forecasts of wind gusts are of great value and are requested not only near the surface but along their entire vertical extent.

Regional reanalyses provide a consistent retrospective data set of the three-dimensional (3-D) state of the atmosphere.

Published by Copernicus Publications on behalf of the European Geosciences Union & the American Geophysical Union.

They are characterized by the fact that they incorporate observations via data assimilation into a numerical weather prediction (NWP) model. The COSMO-REA6 regional reanalysis (Bollmeyer et al., 2014) represents one such high-resolution (grid spacing of about 6 km) reanalysis for Europe that is currently available for the period from 1995 to 2017[1] and has already provided guidance for renewable energy applications (e.g. Frank et al., 2019). Due to the short-term nature of gusts – following World Meteorological Organization (2018) gusts are defined as the maximum of 3 s averaged wind speeds – their direct simulation is not possible within a NWP model. Therefore, COSMO-REA6 provides a diagnostic of the expected speed of wind gusts at a height of 10 m above the surface (Doms and Baldauf, 2011; Doms et al., 2011). Although this estimate of the gust speed in COSMO-REA6 provides valuable information on the observed gusts (Friederichs et al., 2018), it is only given at a height of 10 m without an uncertainty estimate. Thus, this study is aims to develop a post-processing method for the distribution of wind gusts at any height of a wind power plant based on the COSMO-REA6 regional reanalysis.

Several approaches have been employed for the post-processing of wind and wind gusts. With the aim of applying this to risk assessment for off-shore wind farms, Patlakas et al. (2017) developed a deterministic post-processing method based on Kalman filtering, and Born et al. (2012) compared different gust estimates, including uncertainty measures. Staid et al. (2015) proposed a Gaussian forecast for maximum-value wind for off-shore environments, and Messner and Pinson (2019) used an adaptive lasso vector autoregression for forecasting wind power generation at wind farms. Probabilistic methods employ non-homogeneous regression, e.g. Thorarinsdottir and Johnson (2012) for wind gusts, and Lerch and Thorarinsdottir (2013), Scheuerer and Möller (2015), or Baran and Lerch (2015) for wind speed. Petroliagis and Pinson (2012) connected extreme winds with the ECMWF extreme forecast index in order to generate early wind warnings. Forecasting wind gusts based on an ensemble prediction system was applied on winter storms from 6 years by Pantillon et al. (2018). Friederichs et al. (2009) compared several distributions such as gamma, log-normal, and generalized extreme value distribution (GEV) for wind gusts as obtained from the observational network in Germany. They showed that the GEV is most appropriate to reliably estimate the distribution of wind gusts and is most theoretically consistent. Demonstrating an evaluation method for predictive GEV distributions, Friederichs and Thorarinsdottir (2012) developed a Bayesian GEV model for wind gusts. Finally, post-processing for wind gusts using extreme value theory (EVT) and accounting for spatial dependencies was developed in Friederichs et al. (2018) and Oesting et al. (2017).

[1] https://www.dwd.de/DE/klimaumwelt/klimaueberwachung/reanalyse/reanalyse_node.html (last access: 17 April 2020)

In this study, we propose a post-processing method for the vertical structure of wind gusts at the location of the Hamburg Weather Mast (Brümmer et al., 2012). The statistical model prediction is conditioned on the state of the atmosphere as given by the COSMO-REA6 reanalysis (Bollmeyer et al., 2014). Our post-processing approach provides a predictive distribution at an arbitrary height between 10 m and the top of the Hamburg Weather Mast, which is given in terms of parameters of a generalized extreme value distribution (GEV). Variable selection is performed with the least absolute shrinkage and selection operator (Tibshirani, 1996). We further investigate the bivariate dependence between gusts at different heights using the Pickands dependency function.

The remainder of this article is structured as follows: in Sect. 2, we describe the observations at the Hamburg Weather Mast and the COSMO-REA6 regional reanalysis; Sect. 3 provides the statistical model used for the post-processing and introduces the bivariate Pickands function; the results are discussed in Sect. 4; and we end with a conclusion in Sect. 5.

2 Data

2.1 Hamburg Weather Mast

Our target data are hourly gusts as measured at the Hamburg Weather Mast. The Meteorological Institute at the University of Hamburg, partnered with the Max Planck Institute for Meteorology, operates the measuring site in Hamburg, Germany (tall mast: 53°31′9.0″ N, 10°6′10.3″ E; 10 m mast: 53°31′11.7″ N, 10°6′18.5″ E). The wind is measured at a 20 Hz frequency by a 3-D ultrasonic anemometer (METEK GmbH, formerly USA-1) at heights of $z = 10$, 50, 110, 175, and 250 m. The raw wind data are averaged observations over 3 s (Brümmer et al., 2012) and are used to calculate hourly gusts as the maximum of raw wind data over 1 h. The data cover a period of 11 years from 1 January 2004 to 31 December 2014.

2.2 COSMO-REA6 regional reanalysis

The COSMO-REA6 regional reanalysis of the German Weather Service (DWD) was developed at the Hans Ertel Centre for Weather Research (Bollmeyer et al., 2014) and provides the set of predictive variables. The reanalysis system is based on the COSMO NWP model (Baldauf et al., 2011) and covers the CORDEX EUR-11 domain with a horizontal grid spacing of approximately 6 km (0.055°). Vertically, the reanalysis comprises 40 layers from the surface to 40 hPa. The time output resolution for the 3-D fields is 1 h. The data assimilation scheme uses a continuous nudging. The Hamburg Weather Mast data are not assimilated into COSMO-REA6. We preselect potentially informative covariates over a region of 25 grid-box columns around the Hamburg Weather Mast location (more details in Sect. 3.3).

3 Method

We denote the hourly gust data as $Y(z,t)$, where z is height, and t is time. As they represent maxima of 3 s data over a block of 1 h, a natural distribution to represent such block maxima is the GEV distribution. The extreme value theorem (Fisher and Tippett, 1928; Gnedenko, 1943) proves that under certain conditions the GEV is the limit distribution of the rescaled block maxima when the block size reaches infinity. The asymptotic cumulative distribution function (cdf) G is defined by

$$G(y;\mu,\sigma,\xi) = \begin{cases} \exp\left(-\left[1+\xi\left(\frac{y-\mu}{\sigma}\right)\right]^{-1/\xi}\right) & \xi \neq 0 \\ \exp\left(-\exp\left[-\left(\frac{y-\mu}{\sigma}\right)\right]\right) & \xi = 0, \end{cases} \quad (1)$$

on $\{y : 1+\xi(y-\mu)/\sigma > 0\}$, where $-\infty < \mu < \infty$, $\sigma > 0$ and $-\infty < \xi < \infty$. The parameters are denoted as location for μ, scale for σ, and shape for ξ. In real-world applications, a sensible question is whether the asymptotic limit is already reached in samples of finite block size. In order to avoid biases due to non-asymptotic behaviour and to concentrate on gusts above a certain level, we censor the data at a given threshold u by setting $Y_u = u$ for $Y < u$ and $Y_u = Y$ for $Y \geq u$. $G(y;\mu,\sigma,\xi)$ denotes the cdf of the uncensored variable Y, whereas the censored GEV (cGEV) G_u represents the cdf of Y_u and is given as $G_u(y;\mu,\sigma,\xi) = G(y;\mu,\sigma,\xi)$ if $y \geq u$ and $G_u(y;\mu,\sigma,\xi) = 0$ otherwise. The respective density function has a density mass at u that represents the probability $Pr(Y \leq u) = G_u(u;\mu,\sigma,\xi)$. This procedure is similar to the censored representation of rainfall in Scheuerer (2013) or Friederichs (2010).

3.1 Post-processing and verification

Thus, we assume that $Y(z,t)$ follows a cGEV with $G_u(y;\mu(z,t),\sigma(z,t),\xi(z,t))$, such that the parameters $\mu(z,t),\sigma(z,t),\xi(z,t)$ vary in both height and time. The temporal non-homogeneity (i.e. non-stationarity) is explained through L covariates $C_l(t)$ assuming a linear regression approach

$$\mu(z,t) = \mu_0(z) + \sum_{l=1}^{L} \mu_l(z) C_l(t), \quad (2)$$

and

$$\sigma(z,t) = \exp\left(\sigma_0(z) + \sum_{l=1}^{L} \sigma_l(z) C_l(t)\right). \quad (3)$$

The exponential inverse link function in Eq. (3) guarantees that the scale parameter is always positive. We further assume a Gumbel-type GEV with $\xi = 0$. The reason for this choice is discussed later in Sect. 4. In order to be able to interpolate the parameters vertically, we approximate their height dependence using a linear combination of Legendre polynomials up to the order K, namely $P_0(\eta) = 1$, $P_1(\eta) = \eta$, $P_2(\eta) = 1/2(3\eta^2 - 1), \ldots$, where $\eta \in [0,1]$ is a normalized height equal to 1 at 250 m and 0 at 10 m. Each parameter $\mu_l(z)$ and $\sigma_l(z)$ for $l = 0, \ldots, L$ is modelled as

$$\mu_l(z) = \sum_{k=0}^{K} \mu_{lk} P_k(\eta(z)), \quad (4)$$

and

$$\sigma_l(z) = \sum_{k=0}^{K} \sigma_{lk} P_k(\eta(z)). \quad (5)$$

By including Eqs. (3) and (5) into the density formulation of $G_u(y;\mu,\sigma,\xi)$, we obtain a likelihood function for Y at each level z and time t.

The cGEV parameters are then inferred using a maximum likelihood estimation (MLE) and the conditional independence assumption. In order to avoid overfitting and to assess sampling uncertainty, we apply a cross-validation procedure. For each year in the time sequence, the parameter estimation is performed on a reduced data set, where the respective year of data is left out. Thus, we obtain one set of parameter estimates for each of the 11 years that is independent of the data of the respective year. Further, the variability of the parameter estimates provides a measure of the sampling uncertainty.

The approximation using Legendre polynomials allows for an estimation using the data at all heights simultaneously. This post-processing model is denoted as "Legendre". In order to assess the predictability in the vertical, an additional leave-one-out procedure is applied, where the layer to be predicted is withheld during the estimation procedure; this procedure is denoted as "leave-out". We finally also estimate the parameter for each level independently, denoted as "layerwise", in order to quantify how well the approximation of the vertical variation of the parameter performs using Legendre polynomials.

As the number of covariates L should be restricted, we perform a selection of covariates a priori using the least absolute shrinkage and selection operator (LASSO), as described in Tibshirani (1996). The LASSO penalizes non-zero regression parameters μ_{lk} and σ_{lk}. Depending on the a parameter λ, they are forced to zero unless they are really relevant for maximizing the likelihood. For a given log-likelihood function $l(\Theta)$, where the vector Θ contains all unknown parameters, the LASSO approach maximizes

$$l_\lambda(\Theta) = l(\Theta) - \lambda \sum_{l=1}^{L} \sum_{k=0}^{K} \left(|\mu_{lk}| + |\sigma_{lk}|\right). \quad (6)$$

The larger the λ value, the stronger the penalization, and the more regression parameters become zero. The constant parameters μ_{0k} and σ_{0k} are not penalized, and a large shrinkage parameter λ consequently results in a temporally homogeneous cGEV model.

The verification of the cross-validated predictive distribution is performed using proper scoring rules (Gneiting and

Raftery, 2007). We use the quantile score (QS) for predictive quantiles $q_\tau = \mathrm{cGEV}^{-1}(\tau; \mu, \sigma, \xi)$ of the censored data at the probability τ given as

$$\mathrm{QS}_\tau(q_\tau, y_u) = \tau\,(q_\tau - y_c)\,I_{y_u \le q_\tau} + (\tau - 1)\,(q_\tau - y_u)\,I_{y_u > q_\tau}, \quad (7)$$

following Friederichs and Hense (2007) and its decomposition (Bentzien and Friederichs, 2014). The observation y_u is also censored with $y_u = y$ for $y \ge u$ and $y_u = u$ otherwise. We further use the Brier score (BS, Brier, 1950) and the continuous ranked probability score (CRPS, Hersbach, 2000) for the cGEV. The CRPS is proportional to the integral of the QS over all probabilities τ (Gneiting and Raftery, 2007) or the BS over all thresholds (Hersbach, 2000). Skill measures are provided as the percentage improvement of the scores with respect to a reference forecast. Our reference is the cGEV with constant parameters estimated using the observed gusts at each mast level individually, referred to as climatology. All scores are evaluated using censoring. Proper scoring rules can be decomposed into contributions related to reliability and resolution. We use the decomposition for the QS as developed in Bentzien and Friederichs (2014).

For the calculations, we used the R statistical programming language (R Core Team, 2016) with modified routines from the "ismev" (for estimation; Heffernan and Stephenson, 2016) and "verification" (for validation; NCAR – Research Applications Laboratory, 2015) packages.

3.2 Residuals and spatial dependence

Residuals of the gust observations are derived using the cross-validated cGEV parameter estimates to transform the data to a standard GEV (e.g standard Gumbel with $\mu = 0$, $\sigma = 1$, $\xi = 0$). No censoring is applied to calculate the residuals, i.e. we assume that the GEV using the fitted cGEV parameters also represent the gust values below the threshold u. A quantile–quantile plot (Q–Q plot) is used to assess the validity of this assumption.

Another assumption that is explicitly used in the MLE is the conditional independence of the gust observations at the different mast levels. Although this assumption mainly concerns the uncertainty of the parameter estimates, conditional dependence will become relevant if one would like to draw realizations of the vertical gusts or derive aggregated measures (e.g. the probability of observing a gust at any level of the mast). To assess the dependence of the gusts between different height levels, we use the bivariate Pickands dependence function (Pickands, 1981). The bivariate extreme value distribution for standard Fréchet variables ($\mu = \sigma = \xi = 1$) has the following form:

$$G(y_1, y_2) = \exp\left(-\left(\frac{1}{y_1} + \frac{1}{y_2}\right) A(\omega)\right), \quad (8)$$

with $\omega = y_2/(y_1 + y_2)$ and, hence, $\omega \in [0, 1]$. The Pickands dependence function $A(\omega)$ describes the dependency of a pair of random variables (Y_1, Y_2) with standard Fréchet margins. A non-parametric estimate of $A(\omega)$ is given in Pickands (1981) with

$$A_m^{\mathrm{P}}(\omega) = m\left[\sum_{i=1}^{m} \min\left(\frac{1}{y_{1,i}\omega}, \frac{1}{y_{2,i}(1-\omega)}\right)\right]^{-1}, \quad (9)$$

for m pairs of observations. Here we use a modification to approach convexity by Hall and Tajvidi (2000):

$$A_m^{\mathrm{HT}}(\omega) = m\left[\sum_{i=1}^{m} \min\left(\frac{\overline{y}_1}{y_{1,i}\omega}, \frac{\overline{y}_2}{y_{2,i}(1-\omega)}\right)\right]^{-1}, \quad (10)$$

with $\overline{y}_j = m(\sum_{i=1}^{m} 1/y_{i,j})^{-1}$. $A_m^{\mathrm{HT}}(\omega)$ is used as a limiting function. A convex and, therefore, valid Pickands dependence function is given by the convex minorant $A_m^{\mathrm{HT,c}}$ of $A_m^{\mathrm{HT}}(\omega)$ (i.e. the largest convex function on [0, 1] that has no values exceeding $A_m^{\mathrm{HT}}(\omega)$). The "evd" R package (Stephenson, 2018) provides the routines to estimate the function.

3.3 Preparation of covariates

We consider the following variables as covariates: the wind gust diagnostic at 10 m (VMAX_10M), the vertical profile of the horizontal wind speed at mast levels, the horizontal (Vh_700) and vertical (W_700) wind speed at 700 hPa, surface pressure tendency (d_t P), the lifted index (LI), total water content (TWATER), atmospheric temperature at a height of 2 m (T_2M), tendency in convective available potential energy (d_t CAPE), vertical shear of horizontal wind between 6 and 1 km (Vh_SHEAR), the temporal variance of VMAX_10M (VAR_t VMAX_10M), and the phase of the annual cycle. For a summary of the covariates, see Table 1. All covariates are standardized before they enter the cGEV regression model.

The gust diagnostic in COSMO-REA6 is probably the most informative variable, as it aims as an estimate of the potential strength of a gust near the surface. On the one hand, gusts are generated by turbulent deflection of upper air wind to the surface (Brasseur, 2001) and, on the other hand, they are generated by convective downdraughts (Nakamura et al., 1996). The turbulent gust diagnostic in COSMO-REA6 is given by an empirical relation to the 10 m wind velocity and the surface drag coefficient for momentum (Schulz and Heise, 2003; Schulz, 2008). The convective gust diagnostic depends on the downdraught formulation in the convection scheme (Schulz and Heise, 2003) and includes the height and the kinetic energy of the downdraught. VMAX_10M is the maximum of the turbulent and convective gust diagnostic. The differences between the observed gusts at a height of 10 m at the Hamburg Weather Mast and the COSMO-REA6 gust diagnostics are displayed in Fig. 1. The differences have a negative bias of about $-1.03\,\mathrm{m\,s^{-1}}$, i.e. COSMO-REA6 slightly overestimates the strength of the gusts. The standard deviation amounts to about $1.8\,\mathrm{m\,s^{-1}}$. We also include the

Table 1. List of preselected covariates from the COSMO-REA6 reanalysis.

Acronyms	Variable	Description
VMAX_10M	Wind gust diagnostic at 10 m	Grid value
VAR_t VMAX_10M	Temporal variance of VMAX_10M	Variance of five consecutive ($\pm$2 h) grid values
Vh_EOF1	Barotropic mode of absolute horizontal wind at lowest layers	Principal component of first eigenvector of covariance matrix from wind time series (11 years) at lowest 300 m (six layers)
Vh_EOF2	Baroclinic mode of absolute horizontal wind at lowest layers	Principal component of second eigenvector of covariance matrix from wind time series (11 years) at lowest 300 m (six layers)
$\mathrm{Mean_h}$ Vh_700	Mean absolute horizontal wind at 700 hPa	Mean of 25 mast-surrounding grid values at layer 23
$\mathrm{SD_h}$ Vh_700	Standard deviation of absolute horizontal wind at 700 hPa	Standard deviation of 25 mast-surrounding grid values at layer 23
$\mathrm{Mean_h}$ W_700	Mean vertical wind at 700 hPa	Mean of 25 mast-surrounding grid values at layer 23
$\mathrm{SD_h}$ W_700	Standard deviation of vertical wind at 700 hPa	Standard deviation of 25 mast-surrounding grid values at layer 23
d_t P	Surface pressure tendency	Mean difference between current and previous surface pressure from mast-surrounding grid values
LI	Lifted index	Difference between the temperature at 500 hPa (layer 18) and the temperature of an adiabatically lifted surface air parcel
TWATER	Water content	Water content of the mast-including grid column
d_t CAPE	CAPE tendency	Difference between current and previous CAPE of the mast-including grid column
Vh_SHEAR	Horizontal wind shear	Difference between absolute horizontal wind in 6 km (layer 17) and 1 km (layer 30)
T_2M	Temperature at 2 m	Grid value
AC_COS	Annual cosine cycle	Cosine oscillation with 1-year period
AC_SIN	Annual cosine cycle	Sine oscillation with 1-year period

variance of VMAX_10M over the period from 2 h before to 2 h after the respective analysis time (Var_t VMAX_10M) as a covariate.

As gusts are naturally related to mean wind speed, we include the horizontal velocities at the station location. COSMO-REA6 has a staggered grid, so the wind velocity is given as the absolute velocity of the centred zonal and meridional velocities. To represent the state of the local vertical profile of the horizontal wind velocity in a height-independent variable, we use a principal component analysis. A principal component analysis of the wind velocity at the different heights reveals that most variability (about 92 %) is explained by a mode of variability where all wind anomalies have the same sign, with a slight increase in variability at higher levels. The second mode of variability, which explains about 6 % of the total variability, represents a dipole (i.e. baroclinic) structure with positive anomalies in the upper two levels and corresponding negative anomalies in the lowest three levels. The latter mode is called the baroclinic wind mode (Vh_EOF2), whereas the former – although not completely barotropic – is called the barotropic wind mode (Vh_EOF1).

An important index to capture vertical instability is the lifted index (LI, e.g. Bott, 2016). It is defined as the difference between the temperature at 500 hPa and the temperature of an air parcel that is adiabatically lifted up from the surface

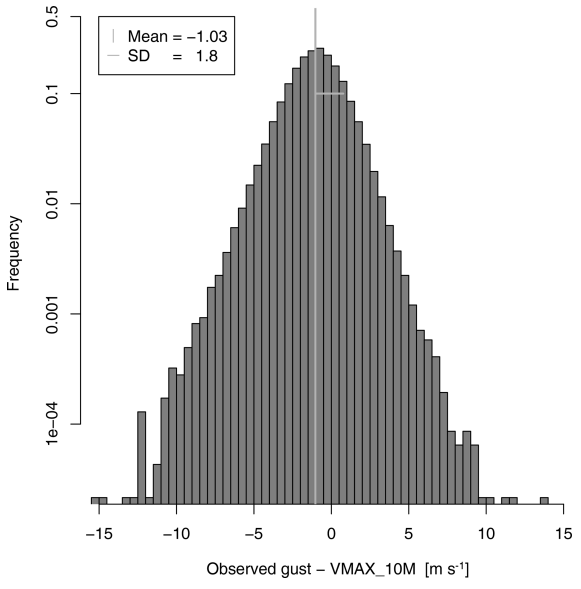

Figure 1. Histogram of differences between observed gusts at 10 m and the COSMO-REA6 10 m gust diagnostic.

to 500 hPa. Negative values indicate a potentially unstable atmosphere, which could lead to convection and, hence, gusts. If convection takes place, CAPE is consumed and a tendency in CAPE is seen in the reanalysis data. Thus, we include the tendency of CAPE (d_t CAPE) over 1 h as a covariate. We also use the total water content (TWATER) of the column that includes the location of the Hamburg Weather Mast. All of these covariates are calculated for the vertical column of the grid point closest to the mast location.

We further include information on the atmospheric circulation above the boundary layer at 700 hPa surrounding the Hamburg Weather Mast. The wind velocities at the closest 25 grid cells are used to calculate an averaged horizontal (Mean_h Vh_700) and vertical (Mean_h W_700) wind speed as well as the respective standard deviations over that region SD_h Vh_700, and SD_h W_700 respectively. Another possible indicator for gust activity is the tendency of pressure at the surface over 1 h within the area surrounding the weather mast. The pressure tendency d_t P is again an averaged tendency over the 25 nearest grid points.

The annual cycle is represented by a linear combination of a sine and cosine function with a period of 1 year (AC_COS and AC_SIN).

4 Results

Several decisions are needed before setting up the post-processing approach. The first concerns the threshold for censoring. We choose the 50 % quantile of the observations at each level respectively, which corresponds to 5.79 m s^{-1} (at a hight of 10 m), 7.40 m s^{-1} (at 50 m), 8.65 m s^{-1} (at 110 m), 9.69 m s^{-1} (at 175 m), and 10.54 m s^{-1} (at 250 m). We further decide to fix the shape parameter ξ to zero for the two abovementioned reasons. First, studies of wind gusts often reveal a negative ξ for the fitted GEV (e.g. Friederichs et al., 2009), i.e. a Weibull-type GEV with an upper end point. Any future gust above this end point would have predictive probability zero, which would results in a very bad forecast. Therefore, a Gumbel-type GEV reduced the risk of missing an extreme gust. The second reason is the stability of the maximum likelihood optimization. The estimation of ξ introduces large uncertainties. Particularly with a large number of parameters (i.e. covariates), the optimization procedures is often stuck in a local maximum. This is particularly critical, if the domain of the distribution is restricted, as is the case for a Weibull-type GEV. Finally, to approximate the vertical variation of the cGEV parameters we use the first three Legendre polynomials P_0 (constant), P_1 (linear), and P_2 (quadratic). Higher-order polynomials did not provide any added value (not shown).

4.1 Model selection

The next step is the selection of the most important predictors. The variable selection is performed using the LASSO approach including cross-validation, providing 11 sets of penalized regression coefficients. The value of λ is determined by analysing the cross-validated LASSO path, which describes the changes in the regression parameters with respect to λ. The LASSO approach is very sensitive to λ. We chose $\lambda = 0.02 \times m$, where m is the number of observations, as a larger λ leads to an excessive penalization, whereas a smaller λ accepts almost all covariates as relevant. As the covariates are standardized, the absolute value of each related coefficient is proportional to the importance of the covariate. We select a covariate if at least one of its three Legendre coefficients is consistently below or above zero for all 11 cross-validation samples. If a covariate is selected, we allow for full flexibility in the vertical including all three Legendre polynomials, as the higher-order polynomials, in particular, are very sensitive to the penalization.

Table 2 represents the regression coefficients obtained for the Legendre model with the selected covariates but without penalization. The parameters that resisted the penalization are displayed using bold numbers. If no regression coefficient is given in Table 2, the covariate was not selected. For the location parameter μ, the most informative covariates are generally the barotropic wind mode (Vh_EOF1) and the gust diagnosis (VMAX_10M). The averaged horizontal wind (Mean_h Vh_700) provides some additional information. The pressure tendency (d_t P) is similarly important, with a positive pressure tendency (e.g. a passing cold front) being related to an increase in gust activity and TWATER with a negative regression coefficient.

The influence of the covariates on σ is generally weaker than on μ. Here, the most informative covariate is indeed VMAX_10M, leading to an increase in σ if VMAX_10M is large. The variance of the predictive cGEV is significantly increased if Var_t VMAX_10M is large. We discuss the influence of Var_t VMAX_10M later in this section. Vh_EOF1 was not selected by the LASSO approach, but some additional information is provided by the baroclinic wind mode (Vh_EOF2). The weak influence of AC_COS indicates a slight increase in gust activity during summer, which is not explained by the other covariates.

The interpretation of the role of the covariates is not straightforward, as the selected covariates are correlated. This is particularly the case for the 10 m gust diagnostic and the barotropic wind mode. Therefore, the omission of one would lead to a modified role of the other. The most important covariates, notably the wind covariates, roughly reveal that stronger winds results in increased μ and σ parameters of the cGEV. Further, there is a remarkable influence of integrated water content and the pressure tendency. A positive pressure tendency is associated with stronger wind gusts, and one may argue that the probability of gusts is increase dur-

Table 2. Estimates of the regression coefficients using the Legendre model with $K = 2$. Estimates are derived without penalization including the selected covariates. Mean and standard deviation are derived from the 11 estimates using cross-validation. Bold text indicates the parameters that resisted the LASSO penalization. No value is given if the variable is not included in the Legendre model.

Covariates	$P_0(\eta) \sim$ constant		$P_1(\eta) \sim$ linear		$P_2(\eta) \sim$ quadratic	
	μ_{l0}	σ_{l0}	μ_{l1}	σ_{l1}	μ_{l2}	σ_{l2}
VMAX_10M	$\mathbf{1.23 \pm 0.01}$	$\mathbf{0.22 \pm 0.00}$	-0.45 ± 0.01	-0.02 ± 0.00	0.02 ± 0.01	0.00 ± 0.00
Var$_t$ VMAX_10M		$\mathbf{0.11 \pm 0.00}$		$\mathbf{-0.03 \pm 0.00}$		0.00 ± 0.00
Vh_EOF1	$\mathbf{2.16 \pm 0.01}$		$\mathbf{1.11 \pm 0.01}$		-0.29 ± 0.00	
Vh_EOF2	0.00 ± 0.01	$\mathbf{0.10 \pm 0.00}$	$\mathbf{0.40 \pm 0.01}$	0.03 ± 0.00	0.04 ± 0.00	0.00 ± 0.00
Mean$_h$ Vh_700	$\mathbf{0.44 \pm 0.02}$	$\mathbf{0.07 \pm 0.00}$	$\mathbf{0.26 \pm 0.01}$	-0.01 ± 0.00	-0.00 ± 0.00	-0.01 ± 0.00
SD$_h$ Vh_700						
Mean$_h$ W_700						
SD$_h$ W_700		$\mathbf{0.04 \pm 0.00}$		0.02 ± 0.00		-0.01 ± 0.00
d$_t$ P	$\mathbf{0.41 \pm 0.01}$	$\mathbf{0.04 \pm 0.00}$	0.09 ± 0.00	-0.02 ± 0.00	-0.06 ± 0.00	0.00 ± 0.00
LI		$\mathbf{-0.03 \pm 0.00}$		0.02 ± 0.00		0.00 ± 0.00
TWATER	$\mathbf{-0.41 \pm 0.01}$		0.03 ± 0.00		0.06 ± 0.00	
d$_f$ CAPE						
Vh_SHEAR						
T_2M						
AC_COS	-0.34 ± 0.01	$\mathbf{-0.07 \pm 0.00}$	-0.06 ± 0.01	0.00 ± 0.00	0.09 ± 0.00	0.02 ± 0.00
AC_SIN	0.02 ± 0.01	0.01 ± 0.00	-0.09 ± 0.00	-0.01 ± 0.00	0.01 ± 0.00	0.01 ± 0.00

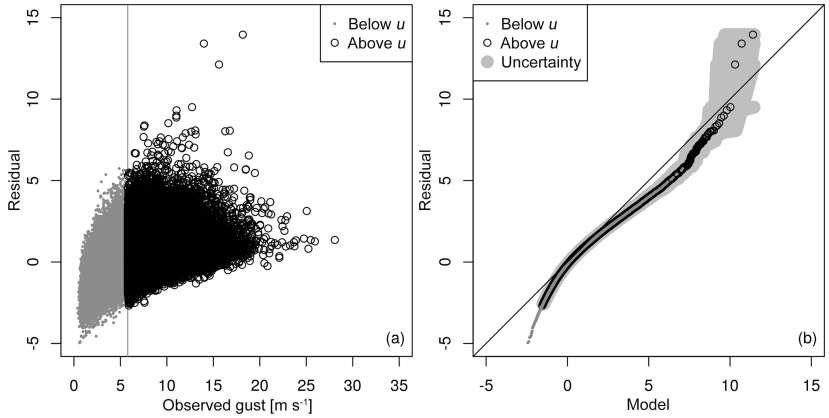

Figure 2. Diagnostics for Legendre model without VAR$_t$ VMAX_10M and with a threshold of $u = 5.79\,\mathrm{m\,s^{-1}}$ at 10 m: **(a)** scatter plot of the standard Gumbel residual against observed gusts, and **(b)** Q–Q plot of the residuals against the standard model. Uncertainty is given in light grey as the range of a 100-member bootstrap sample generated with blocks of 10 consecutive days.

ing the passage of a cold front. The role of TWATER is less obvious at first. TWATER shows a pronounced annual cycle, as the warmer atmosphere during summer has a larger water vapour capacity. Likewise, gusts are stronger during winter than during summer on average. The mean 10 m wind gust at the Hamburg Weather Mast is about $6.3\,\mathrm{m\,s^{-1}}$ in winter and $5.78\,\mathrm{m\,s^{-1}}$ in summer. Thus, one should be careful interpreting this result, as the negative relation between TWATER and gustiness may only be a consequence of the annual cycle and should not be interpreted as a causal relation.

The covariate Var$_t$ VMAX_10M was not included in an earlier version of the Legendre model. Figure 2a shows the residuals using the Legendre model without Var$_t$ VMAX_10M against the observed gusts. The highest gusts above $20\,\mathrm{m\,s^{-1}}$ are well captured, as the residuals are generally small with values between -1 and 4. However, the Q–Q plot in Fig. 2b indicates three outliers that are not well captured by the model. The outliers correspond to gusts of about 15 to $20\,\mathrm{m\,s^{-1}}$ and are therefore of relevance. Two of the outliers occur on 26 August 2011. Figure 3a shows the model predictions on 26 August 2011. The predictive quantiles are calculated using a GEV with the Legendre estimates of the cGEV. The outliers are observed at 18:00 and 20:00 CET respectively and well exceed

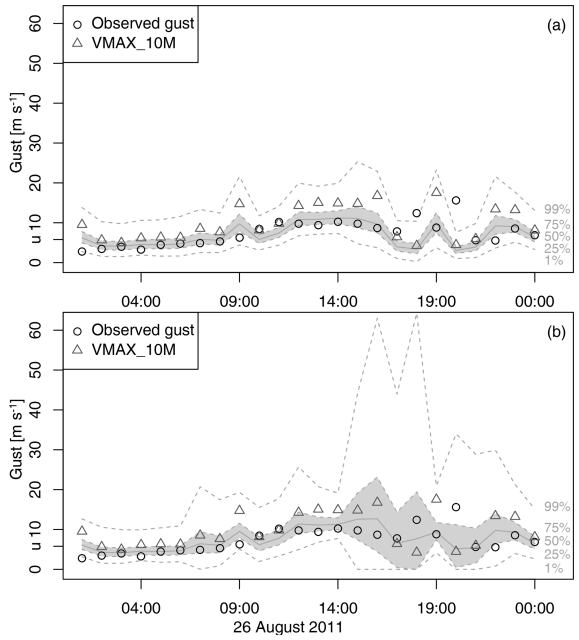

Figure 3. Post-processing of gusts on 26 August 2011 at 10 m: **(a)** Legendre model without VAR_t VMAX_10M; **(b)** Legendre model. Shading indicates the predictive interquartile range, the grey line indicates the median, and dashed lines indicate the 1 % and 99 % quantiles respectively. The observed gust are shown as circles, and the 10 m gust diagnostic is shown as triangles.

the predictive 99 % quantiles, whereas COSMO-REA6 diagnoses a gust of about 20 m s^{-1} at 19:00 CET. The observed gusts are related to two convective storms that passed over Hamburg. The COSMO-REA6 analysed a convective cell over Hamburg but with incorrect timing. The adjusted prediction including VAR_t VMAX_10M is shown in Fig. 3b. We now see an increase in the predicted range of the gusts such that the observed gusts are within the 99 % range of the prediction. The Q–Q plot of the Legendre model including VAR_t VMAX_10M (Fig. 4a) shows that the two outliers on 26 August 2011 are now eliminated; however, this occurs at the cost that the Legendre model now slightly overestimates the high quantiles. With the inclusion of the temporal variability of the 10 m gust diagnostic, we improved the post-processing model mainly by increasing the σ parameter when gustiness in the reanalysis strongly varies over time. Thus, the role of this covariate is to account for timing errors in the reanalysis, which might be particularly large for weather situations that favour small convective cells. This method successfully eliminates two of the three outliers. Figure 4b shows the Q–Q plot at 110 m. The remaining outlier is also present at a higher level, but the overestimation of the high quantiles is much weaker than at 10 m.

4.2 Verification

The post-processing method is assessed using proper verification skill scores. We first assess the effect of the Legendre approximation. Figure 5a–c show skill scores of the layer-wise model with climatology as a reference. The 99 % QSS indicates remarkable improvements of about 45 % to 60 % with respect to climatology. The BSS evaluates the predictive probability of exceeding a threshold defined as the 99 % quantile of the observations at each level respectively. The respective thresholds are given in the caption of Fig. 5. The BSS is smaller than the QSS with values ranging from about 10 % in the lowest level to 40 % at 250 m. The CRPSS ranges between 40 % and 50 %. Ideally, an approximation of the vertical variation of the cGEV parameters by Legendre polynomials should not decrease the skill scores. Figure 5d–f show the skill score of the Legendre model with the layer-wise model as reference. The reduction in skill is not larger than 7 % and is largest in the QSS and BSS at the 10 m level. We conclude that the Legendre model represents an appropriate model for all layers.

The advantage of the Legendre model is the possibility to provide predictions at levels where no observations are available. Figure 6a–c represent the skill score for the leave-out model with climatology as a reference. All skill scores show a strong decrease in skill at 10 and 250 m. At 10 m, the BSS even shows negative skill. In Fig. 6d–f, the direct comparisons show that, except for at the lowest and highest level, the loss in skill is only of about 10 % at the most when compared to what is obtained with the layer-wise model. The decomposition of the QSS of the 99 % quantiles at 10 and 110 m shows that the loss in predictive skill is mainly due to the reliability term, while the resolution remains almost constant; it also shows that the reliability is particularly bad for the leave-out model at a height of 10 m. Thus, the interpolation of the cGEV parameters is applicable, whereas an extrapolation to the 10 and the 250 m levels fails to provide a reliable predictive distribution.

The post-processing method aims at an improved 10 m wind gust diagnostic. In order to compare the post-processed gust distribution with the COSMO-REA6 gust diagnostic, we calculate the median of a GEV using the cGEV parameters of the layer-wise model. Figure 8 shows the histogram of differences between the observations and the mean at 10 m. Compared with the gust diagnostic of COSMO-REA6 in Fig. 1, we see an improvement as the bias almost vanishes and the standard deviation of the differences is reduced to 1.57 m s^{-1}. Large differences still occur in situations where the reanalysis is not able to simulate small-scale convective cells correctly in terms of timing or location.

4.3 Application and bivariate dependency

To illustrate the post-processing using the Legendre model, we have a closer look at storm Emma between 29 February

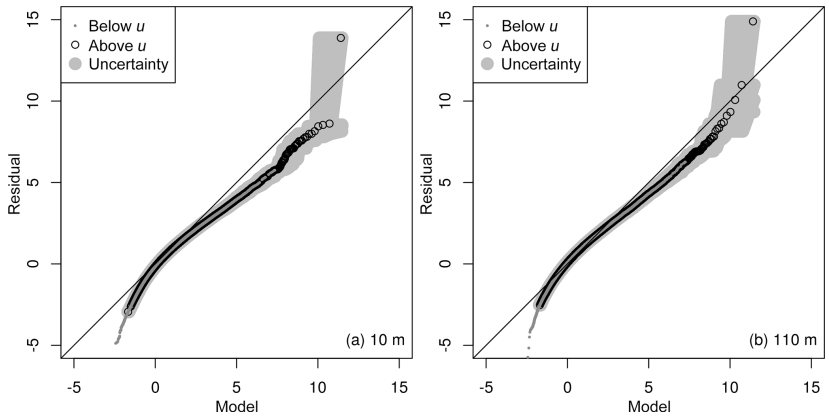

Figure 4. Q–Q plots for the Legendre model **(a)** at 10 m and **(b)** at 110 m with bootstrap uncertainty, as in Fig. 2.

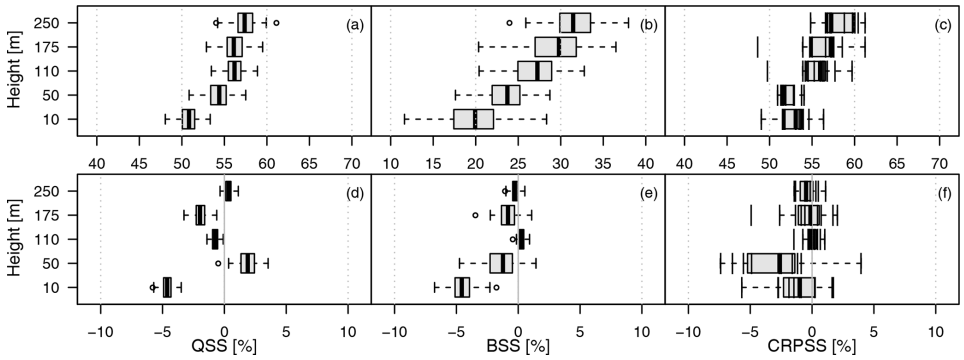

Figure 5. Verification skill scores for the Legendre model against climatology **(a–c)** and against the layer-wise model **(d–f)**. The QSS is given for the predictive $\tau = 99\,\%$ quantile in **(a)** and **(d)**; the BSS for thresholds corresponding to the observations' 99 % quantile ($u = 14.8\,\mathrm{m\,s^{-1}}$ at 10 m, $u = 19.26\,\mathrm{m\,s^{-1}}$ at 50 m, $u = 21.01\,\mathrm{m\,s^{-1}}$ at 110 m, $u = 22.55\,\mathrm{m\,s^{-1}}$ at 175 m, and $u = 23.97\,\mathrm{m\,s^{-1}}$ at 250 m) in **(b)** and **(e)**; and the CRPSS in **(c)** and **(f)**. For QSS and BSS, the box and whiskers represent the 100-member bootstrap sample, with the box giving the interquartile range. The range of the whiskers is a maximum of 1.5 times the width of the box. For the CRPSS, the boxes represent the 11 cross-validated estimates.

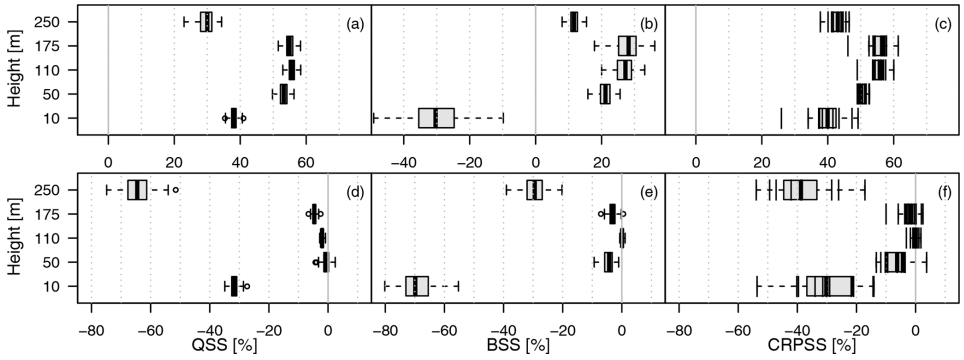

Figure 6. Same as in Fig. 5 but for **(a–c)** the leave-out model against climatology and **(d–f)** against the layer-wise model.

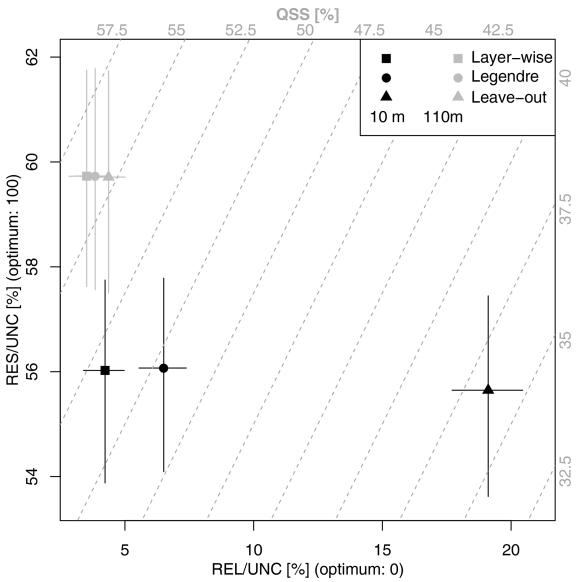

Figure 7. Decomposition of the QSS of the predictive 99 % quantile at 10 m (black) and 110 m (grey) into scaled resolution (RES/UNC) and scaled reliability (REL/UNC) for the layer-wise, Legendre, and leave-out models. The crosses show the range of the 100-member bootstrap samples. The grey dashed lines indicate the QSS. The QSS amount is given on the upper and the right axes (grey numbers).

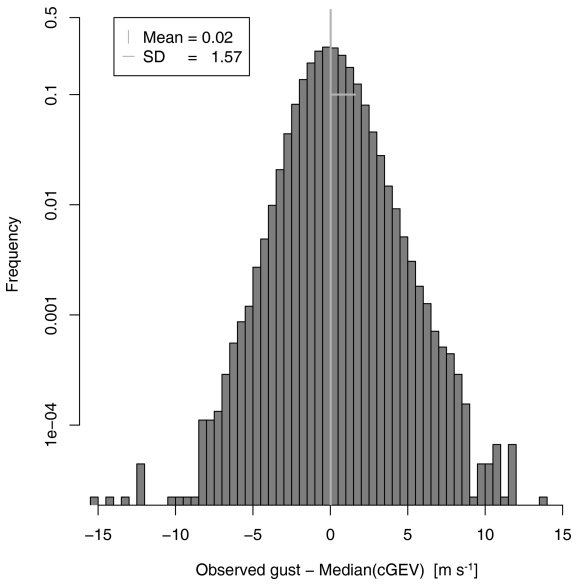

Figure 8. Histogram of differences between observed gusts at 10 m and the GEV median prediction at 10 m.

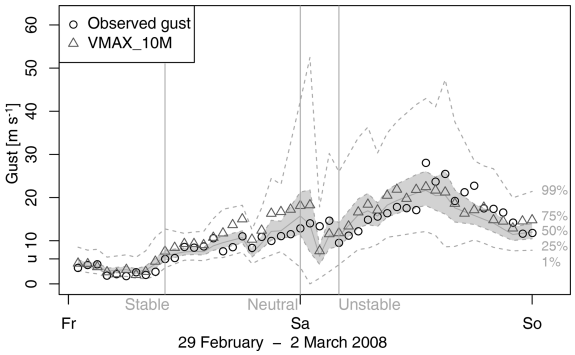

Figure 9. Post-processing of gusts on 29 February and 1 March 2008 at 10 m. Shading indicates the predictive interquartile range, the grey line indicates the median, and dashed lines indicate the 1 % and 99 % quantiles respectively. The observed gust are shown as circles, and the 10 m gust diagnostic is shown as triangles. The vertical lines indicate times with stable (LI of 8.7 K), neutral (LI of 2.4 K), and unstable (LI of −3.1 K) conditions.

and 1 March 2008. During Emma, we observe the largest gusts at 10 m over the whole observation period of the Hamburg Weather Mast, with 28.07 m s^{-1} on 1 March 2008 between 12:00 and 13:00 CET. The storm hit a large region in Europe. In Hamburg, a storm surge also flushed parts of the city. COSMO-REA6 has difficulties precisely capturing the evolution of the storm over Hamburg (Fig. 9). As in the reanalysis, the post-processing approach misses the highest gusts on Saturday, 1 March 2008, although the prediction is provided with reasonably high uncertainties. A better prediction is generated by the post-processing method on Friday, 28 February 2008. By way of example, we selected 3 h that represent differently stratified atmosphere, as indicated by vertical lines in Fig. 9. According to Bott (2016), we characterize the atmosphere as stable if LI ≥ 6 K, as neutral if $6\,\mathrm{K} \geq \mathrm{LI} \geq -2\,\mathrm{K}$, and as unstable if $-2\,\mathrm{K} \geq \mathrm{LI}$. Figure 10 shows the corresponding vertical profiles of the predictive GEV distribution. In all cases, the median prediction is in good agreement with the observations. On 29 February 2008 at 10:00 CET (stable atmosphere), the observed gusts are within the interquartile range of the predictive GEV and slightly below the censoring threshold. The variance of the predictive GEV is small. On 1 March 2008 at 01:00 CET (neutral atmosphere), the interquartile range is larger, and the vertical variation of the gusts is also larger and well captured by the predictive GEV. On 1 March 2008 at 04:00 CET, the atmosphere is highly unstable. The observed gust are very close to the median of the predictive GEV. Note that the LI only influences the cGEV scale parameter and that the regression coefficient is small (see Table 2).

Figure 10 suggests that the gusts do not vary independently of each other. In order to investigate the height dependency, we calculate the bivariate Pickands dependency function fol-

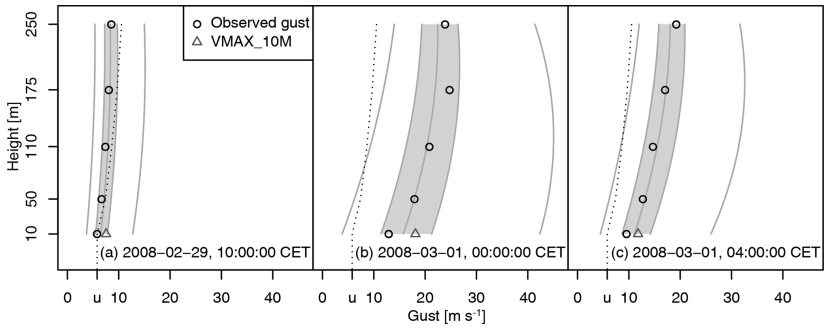

Figure 10. Vertical post-processing of gusts using the Legendre model for times highlighted in Fig. 9. The grey solid lines indicate the conditional quantiles using a GEV at probabilities 1 %, 25 %, 50 %, 75 %, and 99 %. The dotted line represents the censoring threshold.

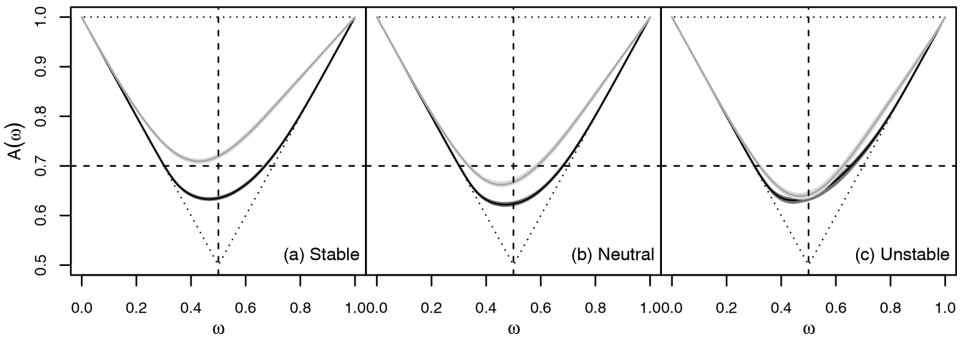

Figure 11. Pickands dependence function of 10 and 110 m for the Legendre model (light grey) and climatology (dark grey). According the LI, the data are classified into 53 % stable **(a)**, 36 % neutral **(b)**, and 11 % unstable **(c)** cases. Uncertainty is derived using block bootstrapping. A horizontal line at 0.7 is displayed for visualization purpose only. The dotted lines indicate complete independence with $A(\omega) = 1$ as well as complete dependence.

lowing Eq. (10). Transformation to standard Fréchet is performed using the parameters for the climatological cGEV (i.e. assuming a homogeneous marginal cGEV independently at each height) and from the Legendre model (i.e. accounting for non-homogeneity by post-processing). Figure 11 shows the estimated Pickands dependence function between the gust residuals at 10 and 110 m respectively for the stable, neutral, and unstable cases. Using homogeneous marginals, the dependence between the gusts at the two levels is strong and seems independent of the stability of the atmosphere. Post-processing strongly reduces vertical dependencies in the residuals. The weakest dependence is observed in a stable atmosphere, whereas dependence for the post-processed residuals is almost as strong as for the climatological residuals in an unstable atmosphere. Variation in the dependency structure is reasonable, as the more unstable the atmosphere, the more vertical mixing is induced.

The dependence between residual gusts at 10 m and higher levels decreased with distance in the vertical, as indicated by the value of the Pickands dependency function at $\omega = 1/2$ in Fig. 12a. Again, for the climatological residuals, dependence is strong and decreases less with distance compared with the post-processed residuals. The decrease in dependence with distance is largest during cases with a stable atmosphere. A simple relation between the strength of the dependency and the distance between layers is not given, as e.g. the dependence between gusts at 110 and 250 m is stronger than between gusts at 110 and 10 m (Fig. 12b).

5 Conclusions

This study presents a post-processing approach for hourly wind gusts at different vertical heights from observations at the Hamburg Weather Mast. The post-processing model is based on a conditional censored Gumbel-type GEV distribution. The censoring threshold is defined as the 50 % quantile of the observations at each mast level respectively. The censoring approach performs well and leads to a good representation of the larger gusts.

A LASSO approach is used to select the most informative covariates. The selected variables are the COSMO-REA6 wind gust diagnostic at 10 m and its temporal variance, the

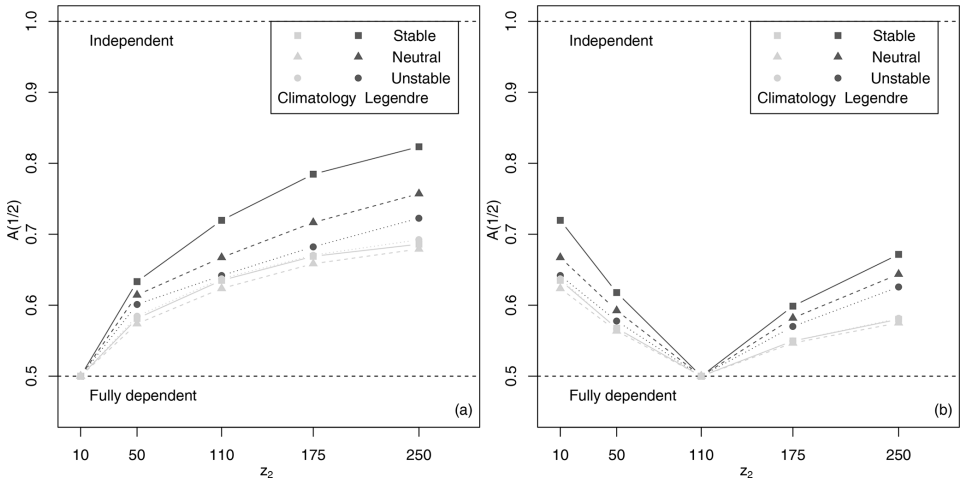

Figure 12. Pickands dependence function at $\omega = 1/2$ between gusts (grey) and residuals (black) at all layers as well as **(a)** $z_1 = 10\,\mathrm{m}$ and **(b)** $z_1 = 110\,\mathrm{m}$ for stable, neutral, and unstable case, as in Fig. 11.

barotropic and baroclinic mode of absolute horizontal wind speed, the mean absolute horizontal wind at 700 hPa, the pressure tendency, the lifted index, and the grid column water content. The predictive cGEV median provides an improved gust estimate compared with the reanalysis gust diagnostic at 10 m.

Vertical variations of the cGEV parameters are approximated using the three lowest-order Legendre polynomials. Although the best scores are obtained if the post-processing is performed for each level independently, the unified description only results in a slight degradation of skill at the intermediate layers. The unified description induces a small bias at 10 m, with gusts being slightly overestimated. Extrapolation of the cGEV parameters towards the 10 m level and the uppermost level generates large biases and thereby degrades skill. In contrast, interpolation towards intermediate levels is very successful, as the degradation in terms of predictive skill is barely significant when excluding the model level. Therefore, the post-processing method not only provides calibrated predictive distributions of gusts at the observed levels but also at arbitrary heights of the weather mast.

Our post-processing strategy is applicable to NWP forecasts without relevant changes, except for the selection of the covariates. Particularly, if applied to ensemble forecasts, additional predictors such as the predictive uncertainty, quantiles, or probabilities for threshold exceedances as derived from the ensemble may be considered. For an example of how to include ensemble statistics into the post-processing approach, see Wahl (2015). In Friederichs et al. (2018), a similar approach is applied to COSMO-DE-EPS forecasts to predict 6-hourly maxima of 10 m wind gusts. Although not really comparable, i.e. hourly maxima in this study but 6-hourly maxima in the above-mentioned study and a variety of covariates as predictors in this study but wind variables only in Friederichs et al. (2018), they obtain a BSS for a $14.8\,\mathrm{m\,s^{-1}}$ threshold and a QSS for the 99 % quantile of about 40 %. The forecast lead time in their study is between 12 and 18 h. This suggests that forecast errors at lead times of about 1 d for 6-hourly maxima are small enough to obtain reasonable skill. The respective skill scores at the 10 m level in this study amount to about 24 % for the BSS and about 53 % for the QSS. The skill scores are comparable and suggest that similar skill scores may be obtained at higher levels.

The strength of the spatial dependency of gusts is assessed using the Pickands dependence function. The gusts at the different heights are highly dependent. Conditioning the gusts on the COSMO-REA6 covariates reduces the dependency of the residuals between heights. This reduction in dependence is significantly modulated by the stability of the atmosphere as given by the lifted index in the sense that an unstable atmosphere increases mixing and, therefore, dependency. Dependency is not simply a function of distance. For a full spatial model description of the gusts, dependency needs to be modelled as a function of atmospheric condition as well as height.

The post-processing model as estimated for the Hamburg Weather Mast should, in principle, be transferable to other locations. This may be tested using observations from other weather masts in the model region. However, difficulties may arise because observations from different masts might be processed differently or made with different instruments. Furthermore, different topography or other local parameters could introduce systematic biases. Moreover, at other locations, only measurements of the 10 m are available; however it would be of interest to assess how well gust statistics that are only based on observations at 10 m would be estimated

at higher levels. The ultimate goal of this work would be to provide estimates of vertical gust statistics at any location in the COSMO-REA6 reanalysis domain.

Data availability. The wind gust observations from the Hamburg Weather Mast were provided by Ingo Lange from the Meteorological Institute of the University of Hamburg (further information and contact: https://wettermast.uni-hamburg.de, last access: 20 April 2020). The COSMO-REA6 data are stored at the DWD and are accessible via ftp://opendata.dwd.de/climate_environment/REA/ (last access: 20 April 2020). For further information, see https://www.dwd.de/DE/klimaumwelt/klimaueberwachung/reanalyse/reanalyse_node.html (last access: 20 April 2020).

Author contributions. JS and PF jointly developed the concept and methodology for this work. JS carried out the post-processing and the visualization of the results, and PF supervised the process. JS was the lead author on the paper with input from PF.

Competing interests. The authors declare that they have no conflict of interest.

Special issue statement. This article is part of the special issue "Advances in post-processing and blending of deterministic and ensemble forecasts". It is not associated with a conference.

Acknowledgements. We are grateful to Ingo Lange and the Meteorological Institute at the University of Hamburg for the provision of the wind data from the Hamburg Weather Mast. Special thanks go to Sebastian Buschow for helpful discussions and valuable ideas. We wish to thank Stéphane Vannitsem and the two anonymous reviewers for their constructive comments.

Financial support. This work has been conducted in the framework of the Hans Ertel Centre for Weather Research funded by the German Federal Ministry for Transportation and Digital Infrastructure (grant no. BMVI/DWD 4818DWDP5A).

Review statement. This paper was edited by Stéphane Vannitsem and reviewed by two anonymous referees.

References

Baldauf, M., Seifert, A., Förstner, J., Majewski, D., Raschendorfer, M., and Reinhardt, T.: Operational Convective-Scale Numerical Weather Prediction with the COSMO Model: Description and Sensitivities, Mon. Weather Rev., 139, 3887–3905, https://doi.org/10.1175/MWR-D-10-05013.1, 2011.

Baran, S. and Lerch, S.: Log-normal distribution based Ensemble Model Output Statistics models for probabilistic wind-speed forecasting, Q. J. Roy. Meteor. Soc., 141, 2289–2299, https://doi.org/10.1002/qj.2521, 2015.

Bentzien, S. and Friederichs, P.: Decomposition and graphical portrayal of the quantile score, Q. J. Roy. Meteor. Soc., 140, 1924–1934, https://doi.org/10.1002/qj.2284, 2014.

Bollmeyer, C., Keller, J. D., Ohlwein, C., Wahl, S., Crewell, S., Friederichs, P., Hense, A., Keune, J., Kneifel, S., Pscheidt, I., Redl, S., and Steinke, S.: Towards a high-resolution regional reanalysis for the European CORDEX domain, Q. J. Roy. Meteor. Soc., 141, 1–15, https://doi.org/10.1002/qj.2486, 2014.

Born, K., Ludwig, P., and Pinto, J. G.: Wind gust estimation for Mid-European winter storms: towards a probabilistic view, Tellus A, 64, 17471, https://doi.org/10.3402/tellusa.v64i0.17471, 2012.

Bott, A.: Synoptische Meteorologie, Springer Spektrum, 2016.

Brasseur, O.: Development and Application of a Physical Approach to Estimating Wind Gusts, Mon. Weather Rev., 129, 5–25, https://doi.org/10.1175/1520-0493(2001)129<0005:daaoap>2.0.co;2, 2001.

Brier, G. W.: The Statistical Theory of Turbulence and the Problem of Diffusion in the Atmosphere, J. Meteorol., 7, 283–290, https://doi.org/10.1175/1520-0469(1950)007<0283:tstota>2.0.co;2, 1950.

Brümmer, B., Lange, I., and Konow, H.: Atmospheric boundary layer measurements at the 280 m high Hamburg weather mast 1995-2011: mean annual and diurnal cycles, Meteorol. Z., 21, 319–335, https://doi.org/10.1127/0941-2948/2012/0338, 2012.

Doms, G. and Baldauf, M.: A description of the non-hydrostatic regional model LM – Part I: Dynamics and numerics, Tech. rep., Deutscher Wetterdienst, Offenbach, Germany, available at: http://www.cosmo-model.org/content/model/documentation/core/cosmoDyncsNumcs.pdf (last access: 17 April 2020), 2011.

Doms, G., Förster, J., Heise, E., Herzog, H. J., Mironov, D., Raschendorfer, M., Reinhardt, T., Ritter, B., Schrodin, R., and Vogel, J. P. S. G.: A description of the non-hydrostatic regional model LM – Part II: Physical Parameterization, Tech. rep., Deutscher Wetterdienst, Offenbach, Germany, available at: http://www.cosmo-model.org/content/model/documentation/core/cosmoPhysParamtr.pdf (last access: 17 April 2020), 2011.

Fisher, R. A. and Tippett, L. H.: On the estimation of the frequency distributions of the largest or smallest member of a sample, Math. Proc. Cambridge, 24, 180–190, 1928.

Frank, C. W., Pospichal, B., Wahl, S., Keller, J. D., Hense, A., and Crewell, S.: The added value of high resolution regional reanalyses for wind power applications, Renew. Energ., 148, 1094–1109, https://doi.org/10.1016/j.renene.2019.09.138, 2019.

Friederichs, P.: Statistical downscaling of extreme precipitation events using extreme value theory, Extremes, 13, 109–132, https://doi.org/10.1007/s10687-010-0107-5, 2010.

Friederichs, P. and Hense, A.: Statistical Downscaling of Extreme Precipitation Events Using Censored Quantile Regression, Mon. Weather Rev., 135, 2365–2378, https://doi.org/10.1175/MWR3403.1, 2007.

Friederichs, P. and Thorarinsdottir, T. L.: Forecast verification for extreme value distributions with an application to probabilistic peak wind prediction, Environmetrics, 23, 579–594, https://doi.org/10.1002/env.2176, 2012.

Friederichs, P., Göber, M., Bentzien, S., Lenz, A., and Krampitz, R.: A probabilistic analysis of wind gusts using extreme value statistics, Meteorol. Z., 18, 615–629, https://doi.org/10.1127/0941-2948/2009/0413, 2009.

Friederichs, P., Wahl, S., and Buschow, S.: Postprocessing for Extreme Events, in: Statistical Postprocessing of Ensemble Forecasts, Elsevier, 127–154, https://doi.org/10.1016/b978-0-12-812372-0.00005-4, 2018.

Gnedenko, B.: Sur La Distribution Limite Du Terme Maximum D'Une Serie Aleatoire, Ann. Math., 44, 423, https://doi.org/10.2307/1968974, 1943.

Gneiting, T. and Raftery, A. E.: Strictly Proper Scoring Rules, Prediction, and Estimation, J. Am. Stat. Assoc., 102, 359–378, https://doi.org/10.1198/016214506000001437, 2007.

Hall, P. and Tajvidi, N.: Distribution and Dependence-Function Estimation for Bivariate Extreme-Value Distributions, Bernoulli, 6, 835–844, https://doi.org/10.2307/3318758, 2000.

Heffernan, J. E. and Stephenson, A. G.: ismev: An Introduction to Statistical Modeling of Extreme Values, available at: http://ral.ucar.edu/~ericg/softextreme.php (last access: 17 April 2020), 2016.

Hersbach, H.: Decomposition of the Continuous Ranked Probability Score for Ensemble Prediction Systems, Weather Forecast., 15, 559–570, https://doi.org/10.1175/1520-0434(2000)015<0559:dotcrp>2.0.co;2, 2000.

Lerch, S. and Thorarinsdottir, T. L.: Comparison of non-homogeneous regression models for probabilistic wind speed forecasting, Tellus A, 65, 21206, https://doi.org/10.3402/tellusa.v65i0.21206, 2013.

Messner, J. W. and Pinson, P.: Online adaptive lasso estimation in vector autoregressive models for high dimensional wind power forecasting, Int. J. Forecasting, 35, 1485–1498, https://doi.org/10.1016/j.ijforecast.2018.02.001, 2019.

Nakamura, K., Kershaw, R., and Gait, N.: Prediction of near-surface gusts generated by deep convection, Meteorol. Appl., 3, 157–167, https://doi.org/10.1002/met.5060030206, 1996.

NCAR – Research Applications Laboratory: verification: Weather Forecast Verification Utilities, available at: https://cran.r-project.org/web/packages/verification/verification.pdf (last access: 17 April 2020), 2015.

Oesting, M., Schlather, M., and Friederichs, P.: Statistical post-processing of forecasts for extremes using bivariate Brown-Resnick processes with an application to wind gusts, Extremes, 20, 309–332, https://doi.org/10.1007/s10687-016-0277-x, 2017.

Pantillon, F., Lerch, S., Knippertz, P., and Corsmeier, U.: Forecasting wind gusts in winter storms using a calibrated convection-permitting ensemble, Q. J. Roy. Meteorol. Soc., 144, 1864–1881, https://doi.org/10.1002/qj.3380, 2018.

Patlakas, P., Drakaki, E., Galanis, G., Spyrou, C., and Kallos, G.: Wind gust estimation by combining a numerical weather prediction model and statistical post-processing, Enrgy. Proced., 125, 190–198, https://doi.org/10.1016/j.egypro.2017.08.179, 2017.

Petroliagis, T. I. and Pinson, P.: Early warnings of extreme winds using the ECMWF Extreme Forecast Index, Meteorol. Appl., 21, 171–185, https://doi.org/10.1002/met.1339, 2012.

Pickands, J.: Multivariate extreme value distributions, Bull. Inst. Internat. Statist, 49, 859–878, 894–902, 1981.

R Core Team: R: A Language and Environment for Statistical Computing, R Foundation for Statistical Computing, Vienna, Austria, available at: http://R-project.org/ (last access: 17 April 2020), 2016.

Scheuerer, M.: Probabilistic quantitative precipitation forecasting using Ensemble Model Output Statistics, Q. J. Roy. Meteor. Soc., 140, 1086–1096, https://doi.org/10.1002/qj.2183, 2013.

Scheuerer, M. and Möller, D.: Probabilistic wind speed forecasting on a grid based on ensemble model output statistics, Ann. Appl. Stat., 9, 1328–1349, https://doi.org/10.1214/15-AOAS843, 2015.

Schulz, J.-P.: Revision of the Turbulent Gust Diagnostics in the COSMO Model, COSMO Newletter, 8, 17–22, available at: http://cosmo-model.org/content/model/documentation/newsLetters/newsLetter08/cnl8_schulz.pdf (last access: 17 April 2020), 2008.

Schulz, J.-P. and Heise, E.: A New Scheme for Diagnosing Near-Surface Convective Gusts, COSMO Newletter, 3, 221–225, available at: http://cosmo-model.org/content/model/documentation/newsLetters/newsLetter03/cnl3-chp9-15.pdf (last access: 17 April 2020), 2003.

Staid, A., Pinson, P., and Guikema, S. D.: Probabilistic maximum-value wind prediction for offshore environments, Wind Energy, 18, 1725–1738, https://doi.org/10.1002/we.1787, 2015.

Stephenson, A.: evd: Functions for Extreme Value Distributions, available at: https://cran.r-project.org/web/packages/evd/evd.pdf (last access: 17 April 2020), 2018.

Thorarinsdottir, T. L. and Johnson, M. S.: Probabilistic Wind Gust Forecasting Using Nonhomogeneous Gaussian Regression, Mon. Weather Rev., 140, 889–897, https://doi.org/10.1175/MWR-D-11-00075.1, 2012.

Tibshirani, R.: Regression Shrinkage and Selection Via the Lasso, J. R. Stat. Soc. Ser. B Methodol., 58, 267–288, https://doi.org/10.1111/j.2517-6161.1996.tb02080.x, 1996.

Wahl, S.: Uncertainty in mesoscale numerical weather prediction: probabilistic forecasting of precipitation, Dissertation, Rheinischen Friedrich-Wilhelms-Universität Bonn, 2015.

World Meteorological Organization: Measurement of surface wind, Guide to Meteorological Instruments and Methods of Observation, 8, 196–213, available at: https://library.wmo.int/index.php?lvl=notice_display&id=12407 (last access: 20 April 2020), 2018.

Appendix B

Steinheuer et al., 2022

A new scanning scheme and flexible retrieval for mean winds and gusts from Doppler lidar measurements

Doppler wind lidars allow the determination of wind profiles with high vertical resolution and thus provide an alternative to meteorological towers. We address the question of whether wind gusts can be derived since they are short-lived phenomena. Therefore, we compare different Doppler wind lidar configurations and develop a new method applicable to all of them. A quick continuous scanning mode that completes a full observation cycle within 3.4 s is found to be the best-performing configuration.

J. Steinheuer, C. Detring, F. Beyrich, U. Löhnert, P. Friederichs, and S. Fiedler (2022). "A new scanning scheme and flexible retrieval for mean winds and gusts from Doppler lidar measurements". In: *Atmospheric Measurement Techniques* 15.10, pp. 3243–3260. DOI: 10.5194/amt-15-3243-2022

Author contributions: Löhnert and Beyrich, together with others, planned the FESSTVaL campaign. Beyrich and Detring were responsible for logistics on the site and performed the measurements. Steinheuer and Detring developed the retrieval methodology with idea contributions from all others. Steinheuer coded the retrieval. Steinheuer, Löhnert, and Fiedler planned and structured the paper. Steinheuer and Friederichs developed the uncertainty methodology of the retrieval. Steinheuer drafted the manuscript. Steinheuer, Detring, Beyrich, Löhnert, Friederichs, and Fiedler reviewed it iteratively.

Atmos. Meas. Tech., 15, 3243–3260, 2022
https://doi.org/10.5194/amt-15-3243-2022

Atmospheric Measurement Techniques
Open Access
EGU

A new scanning scheme and flexible retrieval for mean winds and gusts from Doppler lidar measurements

Julian Steinheuer[1,2], **Carola Detring**[3], **Frank Beyrich**[3], **Ulrich Löhnert**[1,2], **Petra Friederichs**[2,4], and **Stephanie Fiedler**[1,2]

[1]Institute for Geophysics and Meteorology, University of Cologne, Cologne, Germany
[2]Hans-Ertel Centre for Weather Research, Climate Monitoring and Diagnostics, Cologne/Bonn, Germany
[3]Deutscher Wetterdienst, Meteorological Observatory Lindenberg – Richard Aßmann Observatory, Lindenberg, Germany
[4]Institute of Geosciences, University of Bonn, Bonn, Germany

Correspondence: Julian Steinheuer (julian.steinheuer@uni-koeln.de)

Received: 17 December 2021 – Discussion started: 26 January 2022
Revised: 6 May 2022 – Accepted: 11 May 2022 – Published: 30 May 2022

Abstract. Doppler wind lidars (DWLs) have increasingly been used over the last decade to derive the mean wind in the atmospheric boundary layer. DWLs allow the determination of wind vector profiles with high vertical resolution and provide an alternative to classic meteorological tower observations. They also receive signals from altitudes higher than a tower and can be set up flexibly in any power-supplied location. In this work, we address the question of whether and how wind gusts can be derived from DWL observations. The characterization of wind gusts is one central goal of the Field Experiment on Sub-Mesoscale Spatio-Temporal Variability in Lindenberg (FESSTVaL). Obtaining wind gusts from a DWL is not trivial because a monostatic DWL provides only a radial velocity per line of sight, i.e., only one component of a three-dimensional vector, and measurements in at least three linearly independent directions are required to derive the wind vector. Performing them sequentially limits the achievable time resolution, while wind gusts are short-lived phenomena. This study compares different DWL configurations in terms of their potential to derive wind gusts. For this purpose, we develop a new wind retrieval method that is applicable to different scanning configurations and various time resolutions. We test eight configurations with StreamLine DWL systems from HALO Photonics and evaluate gust peaks and mean wind over 10 min at 90 m a.g.l. against a sonic anemometer at the meteorological tower in Falkenberg, Germany. The best-performing configuration for retrieving wind gusts proves to be a fast continuous scanning mode (CSM) that completes a full observation cycle within 3.4 s. During this time interval, about 11 radial Doppler velocities are measured, which are then used to retrieve single gusts. The fast CSM configuration was successfully operated over a 3-month period in summer 2020. The CSM paired with our new retrieval technique provides gust peaks that compare well to classic sonic anemometer measurements from the meteorological tower.

1 Introduction

Extreme wind situations are responsible for many weather-related hazards. The most important weather parameter for the amount of associated damage is the peak wind gust (e.g., Pasztor et al., 2014; Jung et al., 2016; Schindler et al., 2016). This is generally considered in both the standard observational network and in the diagnostic of numerical weather forecasts at 10 m above ground level (World Meteorological Organization, 2018; Brasseur, 2001; Schreur and Geertsema, 2008; Sheridan, 2011). Information on wind gusts from higher altitudes is therefore less frequently available. However, vertically available information about wind gusts would help to better predict wind-related hazards and to identify vulnerable locations in this context, which is useful, for example, for the design of larger buildings or wind turbines.

The short-term nature of wind gusts makes them difficult to observe accurately. In addition, there are different definitions of wind gusts. According to the World Meteorological Organization (2018), a wind gust is a short-lived sig-

Published by Copernicus Publications on behalf of the European Geosciences Union.

nificant increase in wind speed that lasts at least 3 s. Wind gust peak, or briefly gust peak, refers to the maximum wind gust in a given time window, e.g., within 10 min. A measuring device must therefore resolve the wind speed with high temporal resolution. The most advanced instruments are sonic anemometers that measure wind at sampling frequencies of up to 100 Hz, whereas typical sampling rates for routine wind measurements at national meteorological services are 1–4 Hz. The advantage is that these are in situ measurements. However, the instruments must be attached to taller structures, so these can strongly influence the measurements, such as can be observed in the wake of wind turbines (González-Longatt et al., 2012). Long-term gust observations above 10 m are collected at meteorological tower sites equipped with sonic anemometers. The installation of a meteorological tower site is expensive and requires regular maintenance afterwards. Usually, this effort is carried out by research institutions and national meteorological services at only a few sites, e.g., at Hamburg, Karlsruhe, and Cabauw (Brümmer et al., 2012; Kohler et al., 2017; Bosveld et al., 2020). Accordingly, the spatial coverage with such observations is sparse. Moreover, the height of such towers is limited to about 300 m, and hence no long-term observations can be made above this height.

The use of Doppler wind lidars (DWLs) overcomes some of the limitations of meteorological towers, as they are remote sensing devices. These have become increasingly important in recent decades, in part because they have become less expensive (Emeis et al., 2007). Further, DWLs are portable instruments that can be set up with considerably less effort than a tower. They provide reliable vertical profiles of mean wind in the lower atmospheric boundary layer under most conditions (Päschke et al., 2015). However, it is unclear whether they are suitable for retrieving highly fluctuating gusts. A DWL measures Doppler velocities along different beam directions to determine the three-dimensional wind vector. Therefore, a DWL must observe a larger volume of air to infer the wind vector. As a result, unlike an in situ instrument, a DWL cannot provide a high-resolution time series of wind vectors at a specific point in space. Accordingly, small-scale wind variations may be noticeable only in certain regions of the sampled air volume, and not all determined Doppler velocities may be affected the same way. For the strongest gust peaks, we assume that they also occur over a larger area by realizing that the air parcels with increased velocities travel a longer distance in a given time interval. Thus, we assume that strong gusts influence the measured Doppler velocities to a sufficient extent over the whole sampling volume. However, a fast measurement configuration for the DWL is required to obtain gust peak estimates comparable to measurements by a sonic anemometer of wind peaks lasting 3 s.

Suomi et al. (2017) propose a method for determining wind gusts using WindCube V2 DWL measurements. The DWL they considered operated for 2 d in a Doppler beam

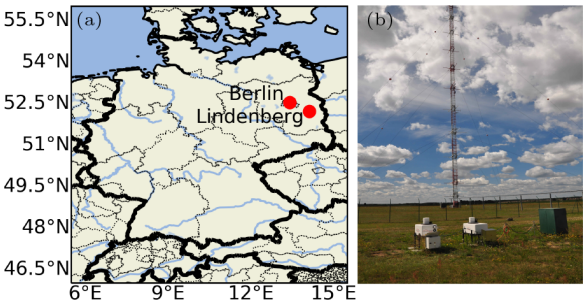

Figure 1. Measurement site. **(a)** The MOL-RAO is situated in the northeastern part of Germany, approximately 65 km southeast of Berlin. **(b)** Two Doppler wind lidars in front of Falkenberg meteorological tower (27 July 2020, author's photo); Falkenberg is approximately 5 km south of Lindenberg.

swinging (DBS) mode that provides measurements of five beams per one configuration cycle in 3.8 s. Wind vectors are derived from each set of five measurements, and gust peaks are obtained from them. The approach includes a scaling method for the detected 3.8 s gusts to infer 3 s gusts. This way, the results agree well with 3 s gust peaks as measured by a nearby sonic anemometer on a meteorological tower. The considered observation period is very short, and it remains open whether another measurement configuration is also suitable.

Within the Field Experiment on Sub-Mesoscale Spatio-Temporal Variability in Lindenberg (FESSTVaL, Fig. 1a), different sub-mesoscale phenomena in the atmospheric boundary layer are investigated. These include various observations and high-resolution modeling. Both address phenomena such as the evolution of the diurnal boundary layer, taking into account its turbulent nature, and the evolution of wind gusts. For this purpose, multiple institutions gathered a variety of measuring devices in order to create a comprehensive observation network. A number of DWLs are involved, which were deployed at the boundary layer field site in Falkenberg next to a 99 m high meteorological tower. The tower is equipped with sonic anemometers, which routinely provide wind and turbulence information.

In this study, we will focus on the deployed DWLs and their ability to retrieve wind gusts. Up to three colocated DWLs are used to test different measuring configurations in parallel. The available DWL devices, StreamLine from HALO Photonics, cannot achieve the DBS scanning configuration in 3.8 s, but they are very flexible when it comes to setting up other measurement configurations. The results are compared with measurements from the sonic anemometer at 90.3 m. When exploring different DWL scan configurations, it turns out that a fast continuous scanning mode (CSM) is capable of completing a single revolution of the scanning head within 3.4 s. This configuration is thus closest to the gust definition and is therefore tested over an extended period during

the 3 summer months of 2020. For the calculation of the wind vectors, we develop a new retrieval scheme that can be used flexibly for different scanning configurations, for any number of observations, and for any desired time interval down to the duration of a single sampling cone. All results are derived from the new retrieval, which, in addition to calculating the gust peaks, is also used to determine the 10 min mean wind, since a practical configuration must also correctly capture the mean wind.

In Sect. 2, we first provide an overview of the wind measuring devices, from which the data were obtained during FESSTVaL. Here we also describe in more detail the different tested DWL configurations. Section 3 introduces the new retrieval with an integrated iterative noise filtering. Section 4 provides the results and is structured in three parts that report on the test campaign in 2019–2020, demonstrate the capabilities of the new retrieval scheme during the extratropical cyclone Sabine in February 2020, and give 3-month statistics on the DWL performance with the CSM in summer 2020. The paper is concluded in Sect. 5 with prospective plans for the evaluation of further FESSTVaL observations.

2 Wind measurements

The measurements analyzed here are part of the FESSTVaL campaign. Originally, the FESSTVaL campaign was planned for 2020, but it had to be postponed to 2021 as a result of the Covid-19 pandemic, and its evaluation is not part of the presented work. Here, we will evaluate the 2019 test campaign and the reduced 2020 campaign, called FESST@MOL, in which fewer measurements were made than initially planned but with DWL observations involved. In the 2019 test campaign, different configurations were investigated with up to three DWLs. In 2020, one of these DWLs was in operation when extratropical cyclone Sabine passed in February and during the 3 summer months.

All instruments were operated at the boundary layer field site (in German: Grenzschichtmessfeld, GM) at Falkenberg (52°10′ N, 14°07′ E, 73 m above mean sea level). The GM Falkenberg is operated by the Meteorological Observatory Lindenberg – Richard Aßmann Observatory (MOL-RAO) and is located about 5 km south of the Lindenberg observatory site, which is approximately 65 km southeast of Berlin, Germany (Fig.1a). The measurement field is situated in flat terrain and surrounded by agricultural land. There is a 99 m high meteorological tower at the field site, where sonic anemometers regularly measure wind and turbulence. Further information is given in Sect. 2.1. The DWLs were deployed at about 70 m of distance from the meteorological tower (Fig.1b). Further information on the general measuring principle and the different configurations of the DWL is given in Sect. 2.2 and 2.3.

2.1 Sonic wind anemometer measurements

The meteorological tower at the GM Falkenberg site is equipped with two sonic anemometers at 50.3 and 90.3 m height. These ultrasonic wind anemometers are manufactured by Metek (factory version USA-1) and resolve the wind vector with a high temporal resolution of 20 Hz. Since the first usable DWL measurements are above 50.3 m, the measurement height of 90.3 m is taken as the reference for validation. To ensure data quality of the sonic anemometer measurements three main steps of operational data quality control are realized: filter nonphysical and constant values, detect spikes, and replace them by interpolating the neighboring points. Constant values can occur when the sonic anemometer is not working properly; for instance, when it is frozen for a short time and sends the last measured value until a new measurement is available. Unrealistic spikes are detected following Vickers and Mahrt (1997) and replaced by a linear interpolation of the neighboring values. Despiking is very rarely used, and strong gusts are not removed by the procedure because they are characterized by a persistent signal in successive measurements that are technically not spikes. The filtered and corrected time series are used to calculate the 10 min mean and the 3 s gust peak, which is derived from a moving average over 60 single measurements within each 10 min interval. Thus, the sonic anemometer gust peak represents a high-resolution reference for the DWL validation. The sonic anemometer at 90.3 m is located on a boom pointing towards the south from the tower. The distance to the tower construction is 4 m. Due to shadowing effects caused by the meteorological tower itself, measured values from wind directions of 0–50° are disturbed and must be discarded in a fair evaluation. These are winds from the north-northeast and thus not from a very frequently occurring direction in Falkenberg. For the comparisons of the sonic anemometer and the DWL measurements, only data from a wind direction sector between 50 and 360° are therefore analyzed.

2.2 Doppler wind lidar measurements

A DWL measures radial wind velocities along the beam direction of emitted light in the near-infrared part of the electromagnetic spectrum. The emitted laser pulses are backscattered by aerosols and received with a shifted frequency since the aerosols move with the wind. The range allocation of the backscattered signal follows from the traveling time. The Doppler shift in the light frequency enables the determination of the radial velocity, which is therefore referred to as the Doppler velocity. Figure 2 schematically illustrates the measurement principle. Each beam direction is determined by an elevation angle and an azimuth angle. The latter is counted clockwise from the north; i.e., 0° equals north and 90° equals east. The beam is divided into a series of range gates. Each received Doppler velocity is assigned to the cen-

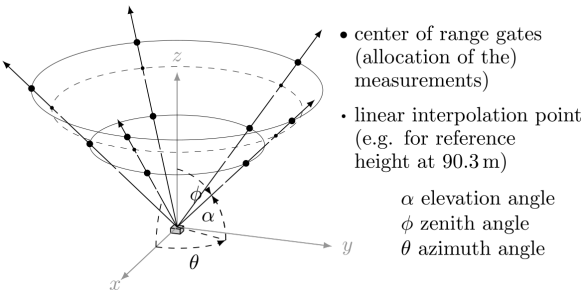

Figure 2. The DWL observation principle is shown here with five beams per cycle. Each beam consists of several thousand laser pulses, and the backscattered signal is affiliated with a discrete series of range gates depending on the length of a single laser pulse and the traveling time. The resulting Doppler velocities are assigned to center-of-range gates. In order to obtain comparable results at intermediate heights, a linear interpolation between the two neighboring measurements along each beam is performed.

ter of a range gate. The corresponding height of the center of the range gates depends on its distance to the sensor and on the inclination of the beam. To allow comparison with the sonic anemometer, we linearly interpolate for each beam a virtual Doppler velocity at 90.3 m from the retrieved Doppler velocities at the two nearest range gates. The wind retrieval presented in the following section is then also applied to the interpolated Doppler velocities.

Three HALO Photonics DWLs have been part of the comparative test campaign – two of them (DWL 78 and DWL 177) are owned by the German Weather Service (in German: Deutscher Wetterdienst, DWD) and one is owned by the Technical University Berlin (DWL 143). A summary of their technical details is given in Table 1. The DWLs are flexible in setting up individual configurations. This involves the number of pulses per ray, the number of radial measurements required by the DWL to complete a single measurement cycle before repeating the configuration, and the elevation and azimuth of the beam direction. By using a smaller number of laser pulses per ray, a shorter duration to complete one measurement cycle is achievable. However, the accuracy of a single Doppler velocity may be reduced by using too few pulses. Typically, a DWL is operated in a step-stare mode; i.e., the DWL moves to an exact angular position, measures, and moves again, including acceleration and deceleration time. This time can be saved by setting up a continuous scanning mode wherein acceleration and deceleration are omitted and measurements are taken during motion of the DWL scan head. Here, the azimuth covers a specific window, and each Doppler velocity is assigned to an azimuth representative of that window.

Table 1. Instrument parameters of the three HALO Photonics StreamLine DWL systems.

	DWL 78 & DWL 177	DWL 143
Instrument type	StreamLine	StreamLine XR
Wavelength	1.5 µm	1.5 µm
Pulse width	180 ns	352 ns
Range gate length	30 m	30 m
Pulse repetition frequency	10 kHz	10 kHz
Resolution of Doppler velocity	$\pm 0.038\,\mathrm{m\,s^{-1}}$	$\pm 0.076\,\mathrm{m\,s^{-1}}$
Telescope focus	2000 m	6535 m
Sampling frequency	50 MHz	100 MHz
Nyquist velocity	$19.4\,\mathrm{m\,s^{-1}}$	$38.8\,\mathrm{m\,s^{-1}}$
Number of FFT points	1024	1024

2.3 Doppler wind lidar configurations

We present eight different configurations that are tested for their suitability for retrieving gusts. Figure 3 illustrates the configurations with the corresponding panels as in the following itemized list.

a. *CSM1* (75 s) is conducted in continuous scanning mode, completing one DWL cycle in 75 s with a 35.3° elevation angle. One measurement is performed with 3.000 pulses, and each cycle consists of about 210 beams, giving a relatively high spatial coverage. Smalikho and Banakh (2017) propose measuring continuously to determine the turbulent kinetic energy (TKE). The rather flat elevation angle of 35.3° is based on considerations by Eberhard et al. (1989), as this enables a convenient calculation of TKE.

b. *24Beam* (120 s) is conducted in step-stare mode in 120 s with a 75° elevation angle. One measurement is performed with 30 000 pulses, and each cycle consists of 24 beams of exactly 15° azimuth steps to each other. This configuration is a popular mode for mean wind measurements with a relatively steep elevation angle to obtain observations from higher altitudes. At Lindenberg, for instance, there is another DWL that has been operated in this configuration for several years (Päschke et al., 2015). Similar to the CSM1, the 24Beam is not fast, but it is worth testing in terms of its widespread usage.

c. *DBS* (28 s) is conducted in Doppler beam swinging in 28 s with a 62° elevation angle. One measurement is made with 30 000 pulses, and each cycle consists of four beams pointing north, east, south, and west as well as one vertical beam. This configuration was proposed by Suomi et al. (2017) for measuring wind gusts but originally with 3.8 s per cycle for the system used in their study. However, our HALO Photonics StreamLine

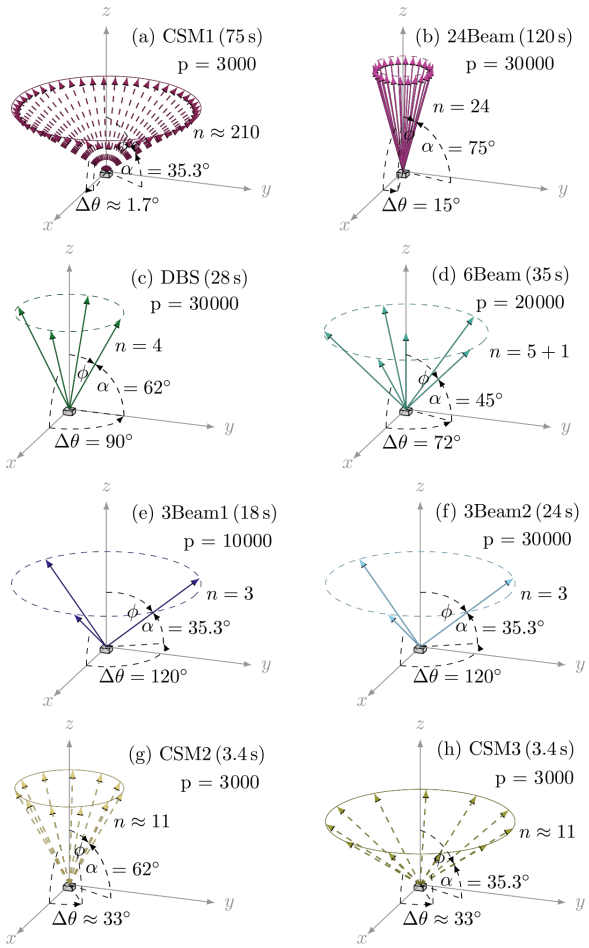

Figure 3. The different tested DWL configurations with corresponding averaged cycle time (in parentheses), the total number of averaged pulses per measured Doppler velocity (p), their elevation angle (α) and azimuth step angle ($\Delta\theta$), and the number of beams per cycle (n; for the continuous modes this is an approximated value).

DWLs do not reach this temporal resolution but require 28 s to complete one cycle. Thus, although the study of Suomi et al. offers a promising way to retrieve wind gusts, it is not directly implementable here, and it is questionable whether we can achieve comparable results and hence validate their approach.

d. *6Beam* (35 s) is conducted in step-stare mode with six beams in 35 s with a 45° elevation angle. One measurement is made with 20 000 pulses, and each cycle consists of five symmetrically arranged beams having an azimuth angle difference of $\Delta\theta = 72°$ with respect to each other, as well as one vertical beam. Sathe et al. (2015) propose using this configuration to measure turbulence with a DWL. Six different measurements allow the estimation of the Reynolds stress tensor since it consists of six independent entries. Their approach uses an optimal elevation angle of $\alpha = 45°$ for the inclined beams.

e. *3Beam1* (18 s) is conducted in step-stare mode with three beams in 18 s with a 35.3° elevation angle. One measurement is made with 10 000 pulses, and each cycle consists of three beams having an azimuth angle difference of $\Delta\theta = 120°$ with respect to each other. A relatively short temporal resolution can be achieved by using only three beams for a DWL cycle and a relatively small number of pulses for a step-stare mode. Note that when using only three measurements, the calculation of the wind vector uncertainty is not possible and the result is prone to error, so a rather smaller elevation angle is chosen to measure the horizontal wind more directly.

f. *3Beam2* (24 s) is conducted in step-stare mode with three beams in 24 s with a 35.3° elevation angle. One measurement is made with 30 000 pulses, and each cycle consists of three beams having an azimuth angle difference of $\Delta\theta = 120°$ with respect to each other. Using only three beams but 30 000 pulses per beam gives this configuration a duration of 24 s. It can be seen that tripling the transmission pulse rate from 10 000 to 30 000 pulses per ray does not increase the total cycle time significantly; or, expressed differently, no time resolution close to a 3 s gust duration can be achieved with the devices when they are operating in the step-stare modes. In this mode most time is spent accelerating the scan head, moving it to the new position, and slowing down again to zero rotation speed.

g. *CSM2* (3.4 s) is conducted in continuous scanning mode in 3.4 s and with a 62° elevation angle. The configuration uses 3000 pulses per measurement, which are assigned to an azimuth range and no longer directly to a defined constant beam direction. The measurement is identified with a mean azimuth, and a complete cycle usually consists of 11 measurements, although due to the fact that the azimuth ranges drift 10 or 12 counted measurements may also occur for some cycles. The high temporal resolution of 3.4 s is achieved when the beams are measured while the azimuth angle is continuously changing, and this mode of operation clearly outperforms step-stare methods with respect to the cycle time.

h. *CSM3* (3.4 s) is conducted in continuous scanning mode in 3.4 s and with a 35.3° elevation angle. One measurement is made with 3000 pulses, and each cycle consists of roughly 11 beams. This fast continuous scanning mode uses a flat elevation angle of 35.3°. The determination of an optimal elevation angle is not trivial. A higher elevation angle achieves larger measurement heights with a smaller scanning cone cross section. With a smaller elevation angle the horizontal wind can be

measured more directly and the propagation of the measurement error can be reduced, but with the larger scanning cone cross section the assumption of wind field homogeneity can already be violated at smaller heights. This last configuration is therefore in contrast to CSM2. The quick CSM can be challenging for DWL hardware due to the rapid rotation.

The configurations were operated as illustrated in Table 2. The test campaign began in late summer 2019 and continued through autumn 2019. Extratropical cyclone Sabine in February 2020 is the most significant event in our observation period. Although this event falls in 2020, it is likewise considered part of the test campaign in the later analysis. The number of days shown does not exactly reflect the observation period, as the configurations were switched during the day and also some observations in the daily files were truncated at the beginning or end of the day. As the sonic anemometer does not provide valid observations for north-northeast winds, these situations are missing in the comparison.

2.4 Noise filtering

Typically, a DWL wind retrieval begins with a preprocessing of the observations that filters out noise. There are several approaches that use the signal-to-noise ratio (SNR) to separate useful and noisy measurements (e.g., Pearson et al., 2009; Barlow et al., 2011; Schween et al., 2014; Päschke et al., 2015). By comparing Doppler velocities with their SNR values, these approaches yield an SNR threshold below which measurements should be discarded. The threshold is given at the highest SNR value at which the Doppler velocities start to behave uniformly distributed over the entire range of theoretically measurable Doppler velocities, i.e., for our measurements roughly in the range of $[-20\,\mathrm{m\,s^{-1}}, 20\,\mathrm{m\,s^{-1}}]$ whereby $20\,\mathrm{m\,s^{-1}}$ denotes the approximate Nyquist velocity. This change in the distribution behavior is most significant for direct measurements of vertical velocities because they usually take values close to zero.

However, we have found that filtering by an SNR threshold is not useful for some of our DWL configurations, especially for the quicker continuous scanning modes. Here, a high number of observations is achieved by emitting a relatively small number of pulses, which are then, however, associated with lower signal-to-noise ratios. If a threshold were introduced and only the observations with SNR values below it could be assumed to be noise-free, many measurements would be discarded. Nevertheless, noisy values can also be observed for the CSMs over the entire SNR range, which is why a rigid threshold value does not seem appropriate. In addition, threshold filtering always has the problem that too many measurements with reasonable Doppler velocities are eliminated.

As an example, Fig. 4 illustrates all SNR values measured with CSM2 on 2 September 2019 against their Doppler velocities. Here, it should be noted that the elevation angle is 62° so that the vertical wind is not measured directly. One can assume, however, that the very high absolute Doppler velocities correspond to noise. In this case, it is appropriate to detect noise by absolute values that are above about $5\,\mathrm{m\,s^{-1}}$. The two vertical lines in Fig. 4 are examples for which an SNR threshold could be set, e.g., at −23 dB as done by Pearson et al. (2009) or at −18.2 dB as done by Päschke et al. (2015). Nevertheless, at any reasonable or calculable threshold, noise would still be present in the measurements filtered this way, even if we filtered at an even stricter threshold, i.e., at a vertical line that would be further to the right in Fig. 4. Conversely, it can be seen that a large proportion of the measurements are in a region where the SNR thresholds suggest unreliable values (purple region).

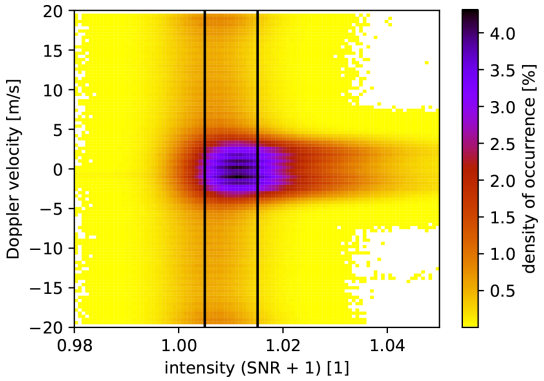

Figure 4. Intensities (SNR + 1) vs. Doppler velocities on 2 September 2019 for all center-of-range gates during a 24 h observation period. The DWL is operated in CSM2 with a 62° elevation angle, and it produced 25 million measurements on that day. The area is divided into 100 × 100 bins, and the colors indicate the density of occurrence. The left vertical line corresponds to an SNR value of −23 dB and the right to −18.2 dB.

Instead of filtering the measurements in advance, we develop a method that initially includes all measurements but then iteratively filters out those measurements that deviate significantly compared to an intermediate fit solution such that they are detected as noise. This ensures that enough data are available to derive wind, in particular, gusts, which are in fact based on very few measurements. Simultaneously, the iteration incorporates thresholds that terminate the retrieval procedure if the set of measurements is too inconsistent and conditions prevail under which the wind vector cannot be derived. The complete iteration procedure is explained in more detail in the next section, as it is integrated in the retrieval.

3 Retrieval

The following calculations can be made for measurements performed during a specific time window, such as a 10 min

Table 2. Configuration time schedule (in day/month/year) for the DWLs used.

	CSM1	24Beam	DBS	6Beam	3Beam1	3Beam2	CSM2	CSM3	Days
15/8/19–21/8/19	DWL 78								7
22/8/19–26/8/19	DWL 78		DWL 177						5
29/8/19–5/9/19	DWL 78	DWL 143					DWL 177		8
7/9/19–17/9/19	DWL 78		DWL 177						11
18/9/19–22/9/19	DWL 78								5
23/9/19–30/9/19	DWL 78	DWL 143						DWL 177	8
1/10/19–7/10/19	DWL 78				DWL 177	DWL 143			7
19/11/19–12/12/19	DWL 78			DWL 177					24
9/2/20–11/2/20 (Sabine)							DWL 177		3
Days test campaign	75	16	16	24	7	7	11	8	
1/6/20–31/8/20							DWL 177		92
Days FESST@MOL							92		

interval, or based on measurements during a single DWL cycle. The number of single measurements per DWL cycle depends on the configuration used.

3.1 Wind vector fit

A measured Doppler velocity d_i is the projection of the wind vector $\boldsymbol{v}_i$ along the measuring beam direction $\boldsymbol{a}_i$ and satisfying the relation

$$d_i = \boldsymbol{a}_i^T \boldsymbol{v}_i + \epsilon_i, \tag{1}$$

with $\boldsymbol{a}_i = (\sin(\theta_i)\cos(\alpha_i), \cos(\theta_i)\cos(\alpha_i), \sin(\alpha_i))^T$, where α_i is the elevation and θ_i the azimuth angle of the ith of $i = 1 \ldots n$ consecutive Doppler velocity observations at a certain height. The instrument-induced observation errors are ϵ_i, which are assumed to be independent and normally distributed with zero mean and variance σ_ϵ^2. The different Doppler velocities d_i all originate from different beams and thus from different wind vectors $\boldsymbol{v}_i$. Since the measurements are made sequentially with changing azimuth angle, there is not only a spatial but also a temporal difference, which is reflected in the $\boldsymbol{v}_i$. However, we assume that the wind field is homogeneous and each $\boldsymbol{v}_i$ in the given time window, i.e., including the single DWL cycle, is the realization of one multivariate normally distributed random variable:

$$\boldsymbol{v}_i \sim \mathcal{N}(\boldsymbol{v}_0, \boldsymbol{\Sigma}), \tag{2}$$

with mean wind vector $\boldsymbol{v}_0$ and three-dimensional covariance matrix $\boldsymbol{\Sigma}$. The homogeneity assumption may be violated over complex terrain or during long time intervals. The different $\boldsymbol{v}_i$ are assumed to be independent, which is another strong assumption and should be scrutinized by a DWL user as it ignores spatial and temporal correlations.

With different realizations $\boldsymbol{v}_i$, i.e., with consecutive measurements at different viewing angles θ_i and α_i in a certain time window, the underlying values $\boldsymbol{v}_0$ and $\boldsymbol{\Sigma}$ could be estimated. The Doppler velocities d_i then are the linearly transformed wind vectors (i.e., projection on beam direction in Eq. 1), with an error variance that represents the observation error ϵ_i as well as the projected wind vector variability. They are normally distributed according to

$$d_i \sim \mathcal{N}\left(\boldsymbol{a}_i^T \boldsymbol{v}_0, \boldsymbol{a}_i^T \boldsymbol{\Sigma} \boldsymbol{a}_i + \sigma_\epsilon^2\right). \tag{3}$$

We now assume that the wind vector variability is isotropic, i.e., the deviations of the individual $\boldsymbol{v}_i$ from $\boldsymbol{v}_0$ are identically distributed in all spatial directions. Then the projection of the covariance matrix is independent of the direction $\boldsymbol{a}_i$ and

$$\boldsymbol{a}_i^T \boldsymbol{\Sigma} \boldsymbol{a}_i = \sigma_v^2. \tag{4}$$

The variance of d_i is thus a combination of the measurement error and the projected wind variability, i.e., the representation error. The likelihood function L for $i, \ldots, n$ measured Doppler velocities d_i then reads

$$L(d_1, \ldots, d_n; \boldsymbol{v}_0, \sigma^2) = \prod_{i=1}^{n} f(d_i; \boldsymbol{a}_i^T \boldsymbol{v}_0, \sigma^2), \tag{5}$$

where $\sigma^2 = \sigma_v^2 + \sigma_\epsilon^2$ is the combined variance and $f(x; \mu, \sigma^2)$ is the probability density function of a Gaussian distribution with expectation μ and variance σ^2. Storing the n different beam directions $\boldsymbol{a}_i$ row-wise in a $n \times 3$ matrix $\mathbf{A}$ and the Doppler velocities in an n-dimensional vector $\boldsymbol{d}$ yields the maximum likelihood estimate (MLE) for $\hat{\boldsymbol{v}}_0$, which is

$$\hat{\boldsymbol{v}}_0 = (\mathbf{A}^T \mathbf{A})^{-1} \mathbf{A}^T \boldsymbol{d}, \quad \text{for} \quad n \geq 3. \tag{6}$$

Thus, $\hat{\boldsymbol{v}}_0$ is the least-squares fit over all measurements n within one single DWL cycle or within a respective time window. Note that we need at least three independent beam directions for the inversion of $\mathbf{A}^T \mathbf{A}$. The residuals $e_i = d_i - \boldsymbol{a}^T \boldsymbol{v}_0$ can be used to estimate σ^2. For this, we use the unbiased estimator, i.e., the denominator $n - 3$ instead of n to account for the degrees of freedom used to estimate the components of $\hat{\boldsymbol{v}}_0$, which leads to

$$\hat{\sigma}^2 = \frac{1}{n-3} \sum_{i=1}^{n} (d_i - \boldsymbol{a}_i^T \hat{\boldsymbol{v}}_0)^2, \quad \text{for} \quad n > 3. \tag{7}$$

In the case of exactly three measurements the estimation of the variance $\hat{\sigma}^2$ is not possible. The corresponding standard deviation $\hat{\sigma}$ is equivalent to the root mean squared error (RMSE) and gives a measure of the fit performance.

3.2 Distribution of the estimator $\hat{\boldsymbol{v}}_0$

With all the assumptions, the residuals are Gaussian-distributed with zero mean and variance σ^2. The latter results from the assumption that the variability of the wind vector $\boldsymbol{v}_i$ and the Gaussian observation errors ϵ_i are independent. Under the assumptions above, the distribution of the estimator $\hat{\boldsymbol{v}}_0$ is multivariate Gaussian-distributed. The expected value of $\hat{\boldsymbol{v}}_0$ is given as

$$E\left[\hat{\boldsymbol{v}}_0\right] = \boldsymbol{v}_0. \tag{8}$$

The expectation value estimator is therefore unbiased. The variance of $\hat{\boldsymbol{v}}_0$ is

$$\mathrm{Cov}\left[\hat{\boldsymbol{v}}_0\right] = (\mathbf{A}^T\mathbf{A})^{-1}\sigma^2. \tag{9}$$

Both moments are derived in detail in Appendix A. Note that $\mathbf{A}^T\mathbf{A} = \sum_{i=1}^{n} \boldsymbol{a}_i \boldsymbol{a}_i{}^T$ and the number of rows increases proportionally with n. One important assumption behind the covariance estimate of $\hat{\boldsymbol{v}}_0$ is that $\boldsymbol{v}_i$ and $\boldsymbol{v}_0$ are independent of each other and the number of independent observations (i.e., degrees of freedom, DOFs) is $n-3$. This is definitely not the case, since the number of effective DOFs n_{ef} is much smaller than $n-3$, and therefore σ represents a lower bound of uncertainty. If we now assume that the estimate is based on substantially fewer independent measurements, we need to introduce a correction factor and estimate the covariance matrix $\hat{\boldsymbol{\Sigma}}_{\hat{\boldsymbol{v}}_0}$ with an effective n_{ef} instead of $n-3$, reading

$$\hat{\boldsymbol{\Sigma}}_{\hat{\boldsymbol{v}}_0} = \frac{n-3}{n_{\mathrm{ef}}}(\mathbf{A}^T\mathbf{A})^{-1}\hat{\sigma}^2. \tag{10}$$

Here, the estimate $\hat{\sigma}^2$ in Eq. (7) is used, and the n_{ef} needs to be specified depending on the desired time window of the retrieval.

3.3 Iterative retrieval update

Our retrieval aims at the estimation of two variables v_{m} and v_{g}. The 10 min mean wind velocity v_{m} is estimated according to Eq. (6) over all n_{10} beams within a 10 min interval. The wind gust peak of a 10 min interval v_{g} is the maximum of wind estimates, each derived from measurements along a single DWL cycle with n_{c} observations, again using Eq. (6).

As discussed before, the noise in DWL measurements is uniformly distributed over the measurable Doppler velocity range and therefore distorts the estimation of $\hat{\boldsymbol{v}}_0$. This is the case when $\hat{\sigma}$ is particularly large. For example, pure noise with uniformly distributed observations within $[-20\,\mathrm{m\,s^{-1}}, 20\,\mathrm{m\,s^{-1}}]$ would yield an estimate of $\hat{\sigma} \approx 11.6\,\mathrm{m\,s^{-1}}$. Our retrieval procedure aims to filter out the Doppler velocity measurements d_i that are dominated by noise in an iterative process. To this end, we define a threshold u_1 for $\hat{\sigma}$ at which the $\hat{\boldsymbol{v}}_0$ is assumed to be dominated by noise, as well as a minimum number q of measurements d_i that should be included in the estimation of $\hat{\boldsymbol{v}}_0$. If $\hat{\sigma} > u_1$, then $\hat{\boldsymbol{v}}_0$ is not accepted and the r measurements with the largest absolute residuals e_i are removed. Provided that the number of remaining d_i is not less than q, $\hat{\boldsymbol{v}}_0$ is estimated again. Otherwise $\hat{\boldsymbol{v}}_0$ should be regarded as dominated by noise and set to not available (n.a.). However, we introduce a second threshold u_2, which is more tolerant and accepts $\hat{\boldsymbol{v}}_0$ if $\hat{\sigma} \le u_2$ even though $\hat{\sigma} > u_1$. This second threshold is a higher bound at which sufficient confidence in the result has already been achieved, and the first threshold is a lower threshold that allows further improvement of the estimate when enough data are available. Note that the parameters u_1, u_2, r, and q are different for the two wind variable estimates v_{m} and v_{g}.

The iteration procedure is displayed in Fig. 5. In the upper right, the parameters are displayed for both v_{m} and v_{g}. The termination criterion u_1 is $\hat{\sigma} \le 1\,\mathrm{m\,s^{-1}}$ in both cases. For v_{m} the second threshold is $u_2 = 3\,\mathrm{m\,s^{-1}}$. Since the single-cycle estimates of $\boldsymbol{v}_0$ rely only on very few d_i, we do not let u_2 be more tolerable, i.e., $u_2 = u_1 = 1\,\mathrm{m\,s^{-1}}$. We in turn require that at least 66 % of the measurements are included for the single-cycle iteration, while $q = 50\,\%$ is sufficient for the 10 min mean wind. The number r of discarded measurements per iteration is 5 % for the 10 min wind and one for the single-cycle estimates. The set thresholds are intended to provide a clear distinction between observations that are too noisy and those which are usable. Nevertheless, it is possible to tune these values, but this is beyond the scope of this work.

Figure 6 illustrates the principle of the iteration procedure. Figure 6a to c illustrate different iteration steps for the estimation of a 10 min mean wind and Fig. 6d to f for the estimation of a wind of one single cycle. In the upper panels, the iteration runs for 10 complete iterations, discards 50 % of measurements, and ends with $\hat{\sigma}$ that falls between 1 and $3\,\mathrm{m\,s^{-1}}$. Hereby, Fig. 6b shows the first intermediate state in which the retrieval would already accept the estimate because $\hat{\sigma}$ falls below $3\,\mathrm{m\,s^{-1}}$, but then continues improving until less than 50 % of measurements are used, as in Fig. 6c, or the more rigorous threshold $u_1 = 1\,\mathrm{m\,s^{-1}}$ would be reached. In the lower panels, one measurement is discarded in each iteration and the retrieval only returns a result that falls below $1\,\mathrm{m\,s^{-1}}$, as in Fig. 6f, since the $\hat{\sigma}$ values in Fig. 6d and e are both too high.

Combined, the retrieval then provides the 10 min mean and a sequence of cycle-based individual winds within 10 min. The gust peak can then be determined from the cycle-based winds. Here another check is included to prevent susceptibility to unrealistic outliers. Those cycle-based winds that deviate in absolute speed by more than $1\,\mathrm{m\,s^{-1}}$ from all others within the 10 min sequence are removed. This affects outliers of the two bounds, so both the strongest and weakest gusts are checked. If at least 50 % of the cycle-based winds still exist and also the 10 min wind is not n.a., the gust peak is then determined to be the maximum of all remaining cycle-

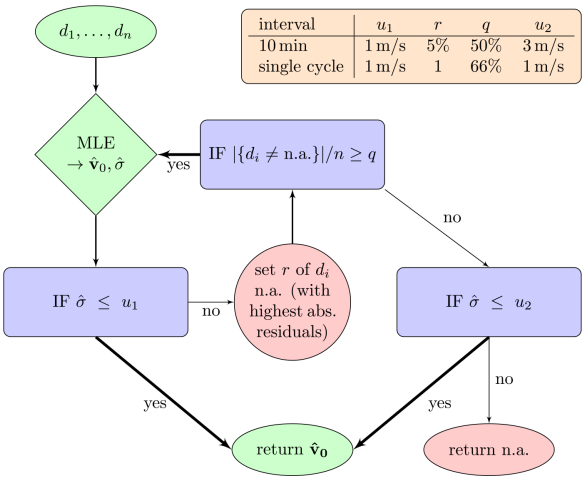

Figure 5. Schematic flowchart of the DWL retrieval with the main steps to determine the wind vector estimate $\hat{\mathbf{v}}_0$. All measurements $d_1, \ldots, d_n$ from a given height and in a given time interval pass through the iteration loop. "If" statements (blue) use thresholds (u_1, u_2, and q) to decide whether to set n.a. values (red) or pass wind-fit data (green). The thresholds depend on whether the time interval is 10 min or consists only of the measurements of a single DWL cycle (see orange box).

based winds within 10 min (and the minimum is defined as the minimum of the cycle-based winds).

3.4 Estimation of uncertainty

The covariance estimate $\hat{\mathbf{\Sigma}}_{\hat{\mathbf{v}}_0}$ in Eq. (10) includes the estimated value $\hat{\sigma}^2$. If $\hat{\sigma}^2$ is derived from the residuals that remain after the iteration process to estimate $\hat{\mathbf{v}}_0$, then the uncertainty is greatly underestimated. However, the inclusion of all measurements would overestimate the uncertainty. To account for uncertainty in the eliminated observations that is consistent with our statistical model, we assume that these residuals represent the truncated part of a normal distribution. Therefore, the variance $\hat{\sigma}^2$ estimated from the non-eliminated measurements must be corrected accordingly. Let p be the percentage of discarded measurements, i.e., truncated values. If p is the fraction of two-sided truncated values at symmetric thresholds a and b, then the threshold a and b are given by $(a-\mu)/\sigma_S = \Phi^{-1}(p/2) = \gamma$ and $(b-\mu)/\sigma_S = \Phi^{-1}(1-p/2) = \beta$, i.e., the $p/2$ and $1-p/2$ quantiles, respectively, where Φ is the cumulative distribution function and ϕ the probability density function for the standard normal distribution of the original (non-truncated) values with parameters μ and σ_S^2. Following Johnson et al. (1994), the relation between the variance of the truncated variable σ_T^2 and non-truncated σ_S^2 is

$$\sigma_T^2 = \sigma_S^2\left[1 + \frac{2\gamma\phi(\gamma)}{\Phi(\gamma) - \Phi(\beta)}\right] = \sigma_S^2\left[1 + \frac{2\Phi^{-1}(p/2)\phi(\Phi^{-1}(p/2))}{1-p}\right]. \quad (11)$$

This can be used to re-scale $\hat{\sigma}$ and approximate a corrected covariance matrix towards

$$\mathrm{Cov}\left[\hat{\mathbf{v}}_0\right] = \frac{n-3}{n_{\mathrm{ef}}}(\mathbf{A}^T\mathbf{A})^{-1}\hat{\sigma}^2 \times \left[1 + \frac{2\Phi^{-1}(p/2)\phi(\Phi^{-1}(p/2))}{1-p}\right]^{-1}. \quad (12)$$

We use the corrected covariance matrix as the estimate of the wind uncertainty for both the 10 min mean wind and the wind of a cycle. The uncertainty of the gust peak is associated with the covariance matrix of the corresponding maximum. Determining n_{ef} is discussed in Sect. 4.3.

4 Results

The results in Sect. 4.1 are obtained from DWLs operated in different configurations from the end of summer 2019 to the beginning of winter 2019–2020, with additional consideration of 3 d of cyclone Sabine in February 2020. Moreover, cyclone Sabine is the subject of Sect. 4.2. Based on these results, we performed measurements in the fast CSM2 over several weeks in summer 2020, for which performance statistics were derived and are presented in Sect. 4.3.

4.1 Comparative test study

Figure 7 shows scatterplots of the 10 min mean horizontal wind from the sonic anemometer versus the DWL retrieval for the eight configurations in Fig. 3. In order to measure the quality of the retrieval, we use the RMSE, the bias, and the coefficient of determination R^2 between DWL retrieval and sonic measurement. All eight configurations produce only minor biases ranging from -0.13 to $0.14\,\mathrm{m\,s^{-1}}$. The CSM1 in Fig. 7a is based on a large sample since it has been tested almost continuously. Apart from some underestimations at low wind speeds, here the wind is observed with small RMSE ($0.41\,\mathrm{m\,s^{-1}}$), high R^2 (0.97), and negligible bias ($0.04\,\mathrm{m\,s^{-1}}$). For the 24Beam in Fig. 7b, some DWL outliers can be recognized, which can be explained by the relatively steep elevation angle. The outliers result from the fact that the linear interpolation of the Doppler velocities fails at 90.3 m because the involved Doppler velocities of the lowest range gate centers are too close to the DWL. Close to the DWL, the transmitter and receiver field of view do not completely overlap. Therefore, the Doppler velocities originating from the lowest range gates should be discarded and those of the following ones are at least noisier. The amount

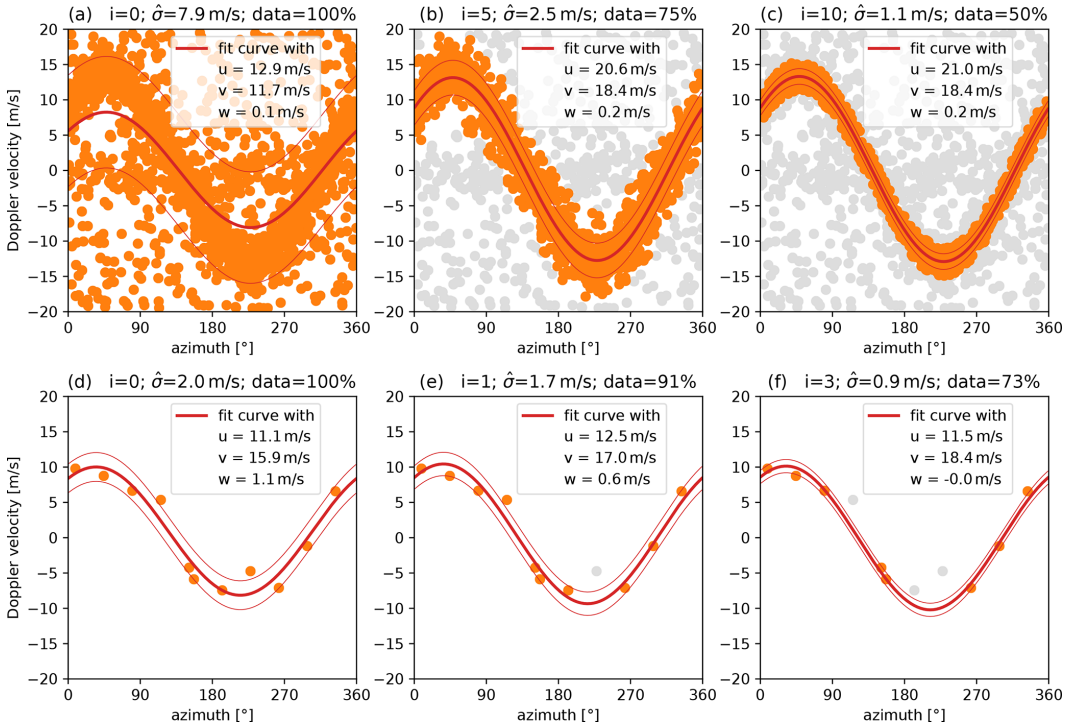

Figure 6. Different steps (i) of the retrieval for 10 min mean wind **(a–c)** and for the wind of a single DWL cycle **(d–f)**. The sinusoidal projection (fit curve with) of the fitted wind vector (u, v, and w) is shown in thick red, with a standard deviation tube around it ($\pm\hat{\sigma}$, red). Observations used for the displayed wind vector fit are orange, and omitted observations are grey. Panels **(c)** and **(f)** display the fits that are finally returned. The examples are from a DWL operated in CSM2 on 10 February 2020 and from measurements at 808 m **(a–c)** and 225 m **(d–f)**.

of full overlap is instrument-dependent, and the obvious outliers show that the Doppler velocities cannot always be considered reliable at 75 m of radial distance from the DWL, i.e., at 72 m a.g.l. for 75° elevation, which corresponds to the distance to the third center-of-range gate. In fact, a comparison with the results of range gates centered at 101 m a.g.l. (fourth center-of-range gate) would give a better result (not shown). These outliers lead to a higher RMSE (1.12 m s^{-1}) and a lower R^2 (0.8). DBS in panel (c) and 6Beam in panel (d) both exhibit low RMSE values (0.29 and 0.34 m s^{-1}, respectively) and R^2 values close to 1 (both 0.98), indicating a low scattering between sonic anemometer measurement and DWL retrieval. The 3Beam configurations in Fig. 7e and f perform very similarly, and the scatterplots are based on parallel measurements in October 2019. The quicker configuration actually performs slightly better in terms of diagnostic variables (RMSE with 0.38 m s^{-1} < 0.48 m s^{-1} and bias with $|0.0\,\mathrm{m\,s^{-1}}| < |-0.11\,\mathrm{m\,s^{-1}}|$), although this is mainly due to the one high DWL outlier at low sonic anemometer wind in Fig. 7f. The two fast continuous measurement modes CSM2 and CSM3 yield narrow scatterplots in Fig. 7g and h, respectively, with low RMSE (0.43 and 0.34 m s^{-1}), little bias (−0.1 and 0.12 m s^{-1}), and low variation in terms of R^2 (0.98 and 0.99).

The DWL data availability at 90.3 m is close to 100 % for all configurations. Data availability with height depends mainly on the elevation angle; i.e., the steeper the angle, the higher the amount of retrieved wind data at a certain height. For the same elevation angles, the configuration with more pulses emitted per beam tends to achieve higher data availability for a given height (compare DBS and CSM2 with 3Beam2 and 3Beam1, respectively). The 6Beam has a comparatively low data availability in the vertical profile. However, it should also be mentioned here again that the data are not directly comparable because the observation period and duration are different. The 6Beam observation period fell in November–December, which is a period with different atmospheric conditions, especially more precipitation and more frequent occurrence of low clouds and fog, which can interfere with the DWL observations. All in all, the configurations seem to be able to properly monitor the lowest 1 km above the ground and thus the atmospheric boundary layer.

Figure 8 shows scatterplots of the 10 min gust peaks from the sonic anemometer versus the DWL retrieval for the eight

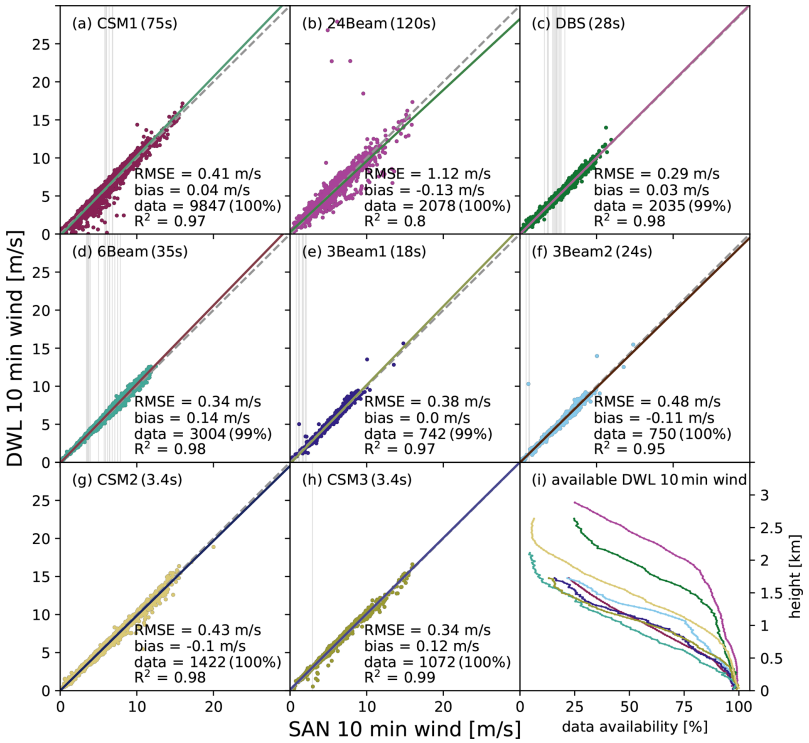

Figure 7. Scatterplots of 10 min mean horizontal wind from the sonic anemometer (SAN) versus DWL for the eight different tested DWL configurations at 90.3 m. Colors and letters **(a)**–**(h)** correspond to the configurations shown in Fig. 3 with the measurement configuration schedule given in Table 1. For each panel, the colored linear fit line, the root mean squared error (RSME), the bias, the involved data, and the coefficient of determination (R^2) are given. The parameter data indicate in parentheses the fraction of situations in which the DWL retrieval returned valid wind values. Grey vertical lines indicate sonic anemometer measurements with missing corresponding DWL results. Panel **(i)** shows the DWL data availability against height with colors per configuration as in panels **(a)**–**(h)**.

configurations. The performance of the configurations depends strongly on the time required per DWL cycle. The two slow configurations, CSM1 and 24Beam, in Fig. 8a and b underestimate the gust peaks (biases of -0.97 and $-1.1\,\mathrm{m\,s^{-1}}$). Here, the CSM1 yields a good coefficient of determination (0.93) and could still be useful with an adequate bias correction, while the 24Beam results appear to be too variable, especially for the highest gust peaks. DBS and 6Beam appear to be quite accurate in Fig. 8c and d, with lower RMSEs (0.69 and $0.86\,\mathrm{m\,s^{-1}}$). However, their observation periods coincide with weak gust peaks, so their performance is not entirely clear. At least the highest gust peaks determined for the 6Beam are below the intersection line, suggesting that more extreme gust peaks tend to be underestimated. Here, a bias correction or rescaling could also provide useful results. Obviously, in too many cases, the 3Beam1 in Fig. 8e fails to detect the actual low gust peaks recorded by the sonic anemometer. In contrast, though, the few actual high gust peaks are detected very well. The parallel-measuring 3Beam2 in Fig. 8f provides only two significant overestimates but is less capable of catching the highest gust peaks, although it still gives reasonable results. Both 3Beam configurations thus provide worse performance values (e.g., RMSEs of 2.29 and $1.36\,\mathrm{m\,s^{-1}}$). The fast CSM configurations are closest to the gust definition of a wind peak lasting at least 3 s since it takes 3.4 s to complete their measurement cycles. The two scatterplots in Fig. 8g and h show very high agreement between the measured gust peaks from the DWL and sonic anemometer. Although the performance values (e.g., biases of 0.14 and $-0.34\,\mathrm{m\,s^{-1}}$) are comparable to DBS and 6Beam, the measurements include gust peaks above $20\,\mathrm{m\,s^{-1}}$. Moreover, for the two elevation angles of 62° and 35.3° studied here, high gust peaks were observed whose points were also close to the intersection line. The linear fit for CSM2 is nearly perfect at the line of intersection, while the flatter CSM3 has a fit with a slightly lower slope. At the steep elevation angle, the observation cone at 90.3 m has a diameter of almost 100 m and at the lower elevation angle a diameter of 255 m. The smaller the studied volume, the more likely one particular gust can be assumed to be detectable in the observation cone. In terms of RSME, the CSM2 provides a lower value ($0.77\,\mathrm{m\,s^{-1}}$ compared to $0.87\,\mathrm{m\,s^{-1}}$).

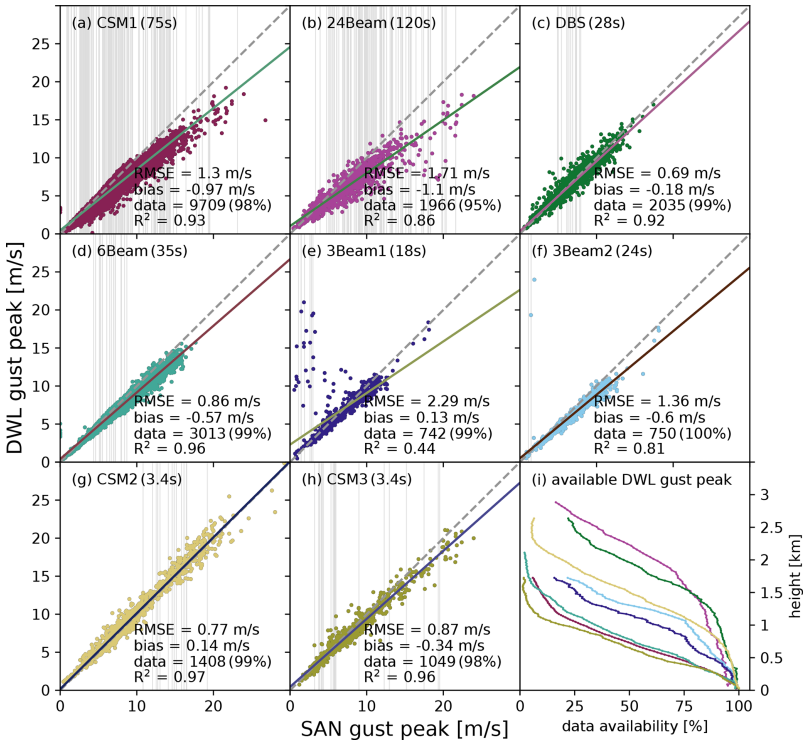

Figure 8. Scatterplots of the sonic anemometer (SAN) gust peak (3 s in 10 min) versus the DWL gust peak (gust duration as indicated per panel in 10 min) for the eight different tested DWL configurations at 90.3 m. The further explanations are the same as in Fig. 7. Panel **(i)** shows the data availability against height with colors per configuration as in panels **(a)**–**(h)**.

The availability of the wind data is generally lower than that of the mean horizontal 10 min wind, but again the same elevation angle dependence is evident; i.e., the higher the elevation angle of the configuration, the more data are available at given height. Consideration of all these factors, combined with relatively good data availability in the vertical for an elevation angle of 62°, leads to the decision to use the CSM2 for the later observation periods.

4.2 Extratropical cyclone Sabine

Storm Sabine was an extratropical cyclone with severe impacts throughout Europe. Gale-force winds led to the collapse of large sections of the transport network in Germany. The highest gust peak in Germany of about 49.1 m s^{-1} was measured at Feldberg in the Black Forest (Haeseler et al., 2020). For Falkenberg's sonic anemometer at 90.3 m, the highest gust peak was observed on 10 February 2020 at 29.3 m s^{-1}, which was the highest value during the observation period of our study.

Figure 9 shows the observations during the 3 d evolution of storm Sabine at 90.3 m in Falkenberg for both a DWL operated in CSM2 and the sonic anemometer. It can be seen that the wind speed increases throughout the day on 9 February, reaching the overall highest values around noon on 10 February 2020. During the following night, the wind intensity decreases, becoming high again on 11 February and decaying afterwards (on 12 February 2020, which is not shown). The complete time series of the sonic anemometer is convincingly reproduced by the DWL in terms of the 10 min mean wind, the wind minima, and the gust peaks. There are three periods when the DWL underestimates the minimum wind and at the same time tends to underestimate the 10 min mean wind. Simultaneously, however, the gust peaks are adequately reproduced. Furthermore, the strongest gust is calculated to be 29.8 m s^{-1}. It deviates by only 0.5 m s^{-1} from the sonic anemometer measurement, thus providing a convincing result. For the other high gust peaks, in some cases larger deviations are registered, although these do not show any systematic underestimation or overestimation. In addition, the horizontal wind values of the individual cycles are shown, which cover the ranges of minimum wind to gust peak. As shown by the discrepancy of some DWL cycle winds and the returned DWL gust peaks or wind minima, the implemented outlier detection works, and mostly unrealistically high or low values are filtered out before peaks and wind minima are determined.

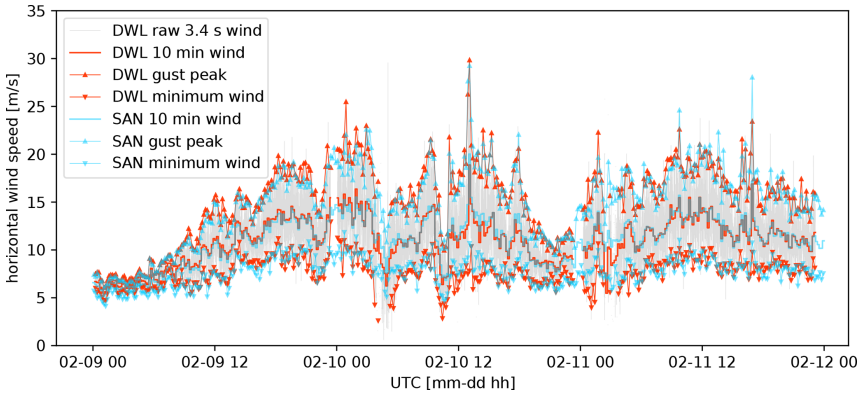

Figure 9. Time series of wind speeds during extratropical storm Sabine on 9–11 February 2020. Both the DWL operated in CSM2 (red) and sonic anemometer (SAN, cyan) winds are shown. The triangles indicate the 10 min gust peaks and wind minima, the thicker step-like lines indicate the 10 min mean horizontal wind, and the light grey line shows the results for all processed DWL cycles. Very good agreement between the data means that markers and lines completely overlap. Note that due to outlier filtering, not all cycle maxima and minima match the gust peak and wind minimum values, respectively.

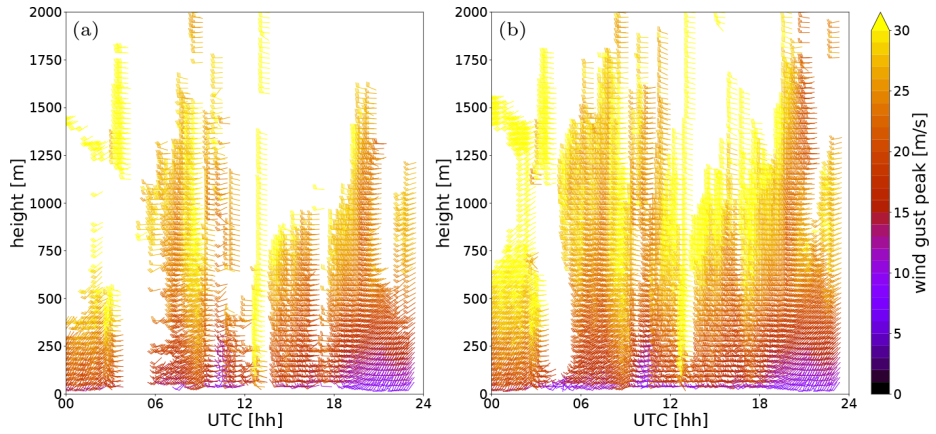

Figure 10. Color-coded wind barbs for gust peaks during extratropical cyclone Sabine on 10 February 2020 from the DWL operated in CSM2. **(a)** Results for a retrieval with classic SNR filtering at −18.2 dB and MLE. **(b)** Results without SNR filtering and iteratively improved MLE as developed in this study. In both approaches, the gust peak per 10 min is only given if at least 50 % of the DWL cycles obtain valid values.

To assess the performance of the retrieval in terms of vertical resolution of gusts, we compare our new retrieval to a classic retrieval exemplified for 10 February 2020 in Fig. 10. A classic retrieval is not designed to derive wind gusts but usually to determine a mean wind, so the filtering can eliminate more measurements. Here, by classic retrieval, we mean classic threshold filtering followed by MLE, which determines the wind vector from the remaining measurements of each DWL cycle. Thus, similar to the new approach, we obtain wind vectors from which wind gusts can be derived. Hence, the calculation is not iterated and all remaining observations are used. The wind gusts in Fig. 10a are from this classic retrieval with the cycle-based MLE for prefiltered Doppler velocities at an SNR threshold of −18.2 dB according to Päschke et al. (2015). For each MLE, 66 % of available Doppler velocities are required, and for the calculation of the 10 min gust peak, at least 50 % of the individual cycles must have been processed (valid for both approaches). This procedure is a classic noise filtering, but with a calculation based on very few observations. Figure 10b shows the result of our proposed retrieval. Both retrievals used the same measured Doppler velocities from a DWL operated in the CSM2 configuration. The new retrieval has significantly higher data availability. The gust peaks indicated by the classic retrieval are very similarly covered by the new retrieval, which shows that the new retrieval eventually uses the same observations that the classic threshold filtering would leave. In Fig. 10b, the additional obtained gust peaks fit coherently

into the overall impression of the storm. This means that the new retrieval does not distort results that are also produced by rigorous filtering. On the other hand, it is also observed that the inclusion of too many observations that are potentially noisy does not disturb the retrieval result.

This example is a satisfactory demonstration of the usefulness of the CSM2 configuration in combination with the new retrieval in terms of data availability of coherent gust peaks. Exactly such extreme events are to be monitored precisely by the DWL. For this reason and because of the statistics from the whole comparative test campaign, we set up a DWL in CSM2 throughout the summer of 2020.

4.3 Summer 2020

We extend the validation to a longer time period to look at a large sample of data. Figure 11 provides the comparative statistics for observations from summer 2020. The 3 months were relatively warm and dry for Brandenburg, while in addition weak winds from the north-northeast prevailed frequently. This is reflected in the data availability for the comparisons, which is reduced by 13 % due to the shading effect of the tower on the sonic anemometer. The DWL, in contrast, conducts wind measurements for almost the entire period. The vertical lines denote the sonic anemometer measurements in which the DWL does not process any winds and which are less than 1 % for both wind products. In particular, neither high mean winds nor strong gust peaks are missing in the processed data of the DWL. The comparison of the 10 min mean winds confirms that the CSM2 is suitable for deriving a mean wind at 90.3 m. Both the appropriate linear fit and the measures of spread, i.e., RMSE ($0.4\,\mathrm{m\,s^{-1}}$) and the coefficient of determination (0.98), emphasize the suitability of the retrieval and the used configuration for retrieving a conventional DWL wind product. The comparison of the gust peaks provides high coincidences. The scatter is larger compared to the mean wind, as a small-scale process is more difficult to capture. As for the discussed test period, the CSM2 does not introduce a systematic error, and larger deviations are rare. Except for 18 cases, gust peaks are calculated for the situations in which the 10 min mean wind is processed. It can therefore be assumed that iterative filtering eliminates noise in a relatively similar way, regardless of whether the mean wind vector or the instantaneous wind value of an individual measurement cycle is considered. Although it may happen that a high gust peak could generate Doppler velocities that are considered noise in the derivation of the mean wind, it is precisely then that it is very practical to filter for both wind products independently. On the one hand, Doppler velocities of an individual gust peak that are significantly different to Doppler velocities belonging to the mean wind are negligible in the mean wind retrieval as these would be only few of the total amount of observations within 10 min. On the other hand, that gust peak is recognized as such in the single cycle-based retrieval, provided it

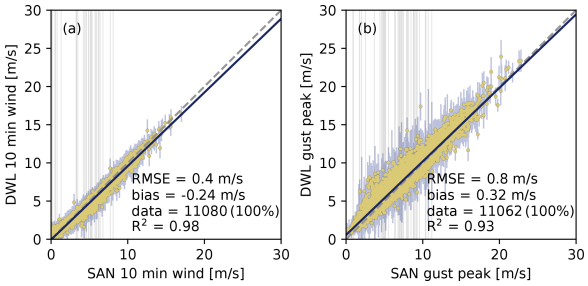

Figure 11. Scatterplots of sonic anemometer vs. DWL wind retrieval during the period 1 June to 31 August 2020 at 90.3 m. **(a)** Scatterplot of 10 min mean horizontal wind from a sonic anemometer (SAN) versus the DWL operated in CSM2. **(b)** Scatterplot of the SAN gust peak (3 s in 10 min) versus the DWL gust peaks (3.4 s) operated in CSM2. The diagnostic numbers are explained in Fig. 7. The estimated DWL standard deviation of the horizontal wind or gust peak is shown with vertical bars derived from the estimated covariance matrix with $n_{\mathrm{ef}} = 12$ **(a)** and $n_{\mathrm{ef}} = 2$ **(b)**, respectively.

is clearly visible in the few measurements within one single DWL cycle. Thus, the noise filtering seems to work effectively with respect to the requested wind product.

The scatterplot includes the uncertainty estimates for the horizontal winds. The standard deviation, shown with two vertical bars for each point, should approximately cover the range by which the observation falls within 68 % probability for normally distributed random variables. The estimation of the uncertainty depends on the choice of the effective DOFs, i.e., n_{ef} from Eq. (12). We set $n_{\mathrm{ef}} = 12$ for the 10 min mean wind and $n_{\mathrm{ef}} = 2$ for the wind of a cycle, which is then also representative for the gust peak. Except for some outliers, the uncertainties for both wind products emphasize the agreement between the DWL and sonic anemometer, and larger deviations between them are usually associated with larger uncertainties. The two effective DOFs used here are a result of tests with different n_{ef}. For that, we used all available results from observations in the CSM2 configuration, i.e., also the measurements of the comparative test study. Figure 12 shows scatterplots for uncertainty estimates against the difference between sonic anemometer and DWL wind, as well as an assessment from a probabilistic point of view with rank histograms, namely for $n_{\mathrm{ef}} = 12$ and $n_{\mathrm{ef}} = 2$. In these rank histograms, the retrieval outcome is understood as expectation and variance parameters of a Gaussian cumulative distribution function (CDF), which is evaluated for the sonic anemometer observation. The histogram illustrates the frequencies of the different CDF values. An equally distributed rank histogram indicates a calibrated forecast, i.e., in which the uncertainty parameters of the distribution are neither underestimated nor overestimated. In Fig. 12a it can be seen that the 10 min mean wind is estimated to be very confident while also deviating relatively little from the sonic anemome-

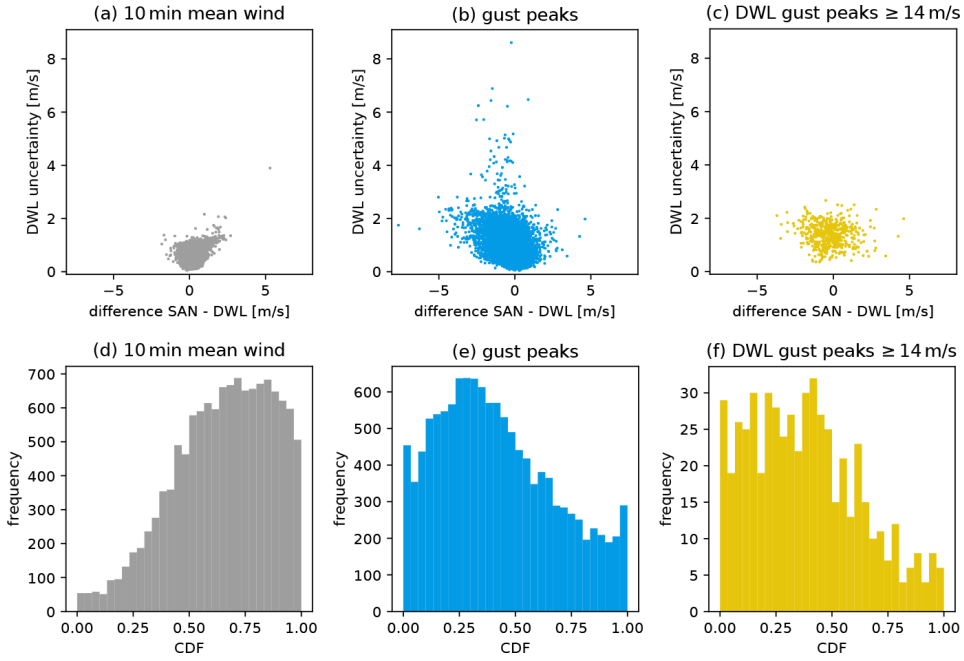

Figure 12. Examination of uncertainty. Panels **(a)**–**(c)** show comparisons for the differences of the sonic anemometer (SAN) and DWL wind values against the estimated DWL uncertainty. Panel **(a)** displays the results for the 10 min mean horizontal wind, panel **(b)** for the gust peaks, and panel **(c)** for only cases in which the DWL gust peaks exceed 14 m s^{-1}. Panels **(d)**–**(f)** show the rank histograms for the retrieved DWL wind and its corresponding uncertainty; panel **(d)** addresses the 10 min mean horizontal wind, panel **(e)** gust peaks, and panel **(f)** the gust peaks exceeding 14 m s^{-1}. Each histogram shows the frequency of the Gaussian wind cumulative distribution function values, evaluated at the sonic anemometer observations. A perfect model would show equally distributed frequencies.

ter observation. Nevertheless, it is also recognizable that tentatively more winds are underestimated than overestimated. Such underestimated winds come with increased DWL uncertainty estimates, which becomes extremely noticeable in the case of one realization (see the upper left corner). Differences and uncertainty estimates are of the same order of magnitude, however. For the mean wind in Fig. 12d it is apparent that the sonic anemometer 10 min mean wind is over-proportionally often higher than the expectation value. Nevertheless, setting the effective degrees of freedom with $n_{ef} = 12$ results in an appropriate order of magnitude for effective independence. Higher values for n_{ef} would reduce the estimates for uncertainty and contribute to a slight flattening of the rank histogram, but also lead to a more frequent occurrence of results around CDF = 1 (i.e., cases of underestimated winds with simultaneously estimated confidence that is too high). Vice versa, a lower n_{ef} would yield uncertainties that are too high, producing a higher peak in the rank histogram. The skewness cannot be fixed with the modification of n_{ef}. Concerning the evaluation for gust peaks in Fig. 12b, it is again noticeable that the differences between the sonic anemometer and DWL are generally larger than for the mean winds. At the same time, however, the estimate for the uncertainty is also larger. Further, it is apparent that gust peaks tend to be overestimated by the DWL. Figure 12e confirms this impression because there are more evaluations of the sonic anemometer observation on the left side of the histogram. With $n_{ef} = 2$ we set a reasonably low value in order not to underestimate the uncertainty. There are not many misunderstood outliers; i.e., there are not too many sonic anemometer gust observations that do not match the retrieval at all and whose CDFs are close to 0 or 1. Since the consideration of extreme gust peaks is of particular relevance, Fig. 12c and f show the assessment for gusts above 14 m s^{-1}. This is the threshold value for the forecast at which warnings of gusts must be issued in Germany. No significant difference to the assessment of all gust peaks can be ascertained here. This confirms once again that strong gusts in our observation period do not present special difficulties for the new retrieval.

5 Conclusions

Within the framework of the FESSTVaL measurement campaign, we investigate various configurations with regard to their ability to observe 10 min mean wind and wind gust peaks. For this purpose, a retrieval is developed that can flexibly quantify wind and associated uncertainty for differ-

ent averaging time intervals. Our noise filtering is meshed in the retrieval and is based on the assumption that noise is distinguishable from real measurements and can be removed iteratively. The retrieval proves to be suitable to process the 10 min mean wind for all tested DWL configurations. Besides the mean wind, the retrieval is used to process the wind of the single DWL cycles. The maxima of the single cycles within 10 min are considered to represent the wind gust peaks. Due to different settings, the tested configurations differ in the time required to complete all measurements of a respective cycle. A quick continuous scanning mode, the CSM2, proves to be successful for deriving gust peaks similar to those of a sonic anemometer at 90.3 m. This CSM2 provides 11 single radial Doppler wind measurements during one revolution of the DWL scan head, which is completed within 3.4 s and from which the wind vector is derived. Measurements with this configuration are performed during the passage of extratropical storm Sabine in February 2020. The strongest gust peak in the whole observation period was measured here and accurately reproduced. Comparison of the new retrieval with a classic approach showed significantly higher vertical data availability for the new retrieval. Although comparative measurements from other heights are missing, the results of this storm day example provide a coherent overall picture of the vertical wind gust profiles. The other configurations require a longer time to complete a measurement cycle and are therefore unsuitable for measuring wind gusts directly. However, it would be possible to scale the retrieved gusts to obtain values that are more comparable to the 3 s sonic anemometer results. In particular, the scaling method of Suomi et al. (2017) could be applied.

During the summer of 2020, we tested the CSM2 for a full 3 months. For both mean winds and gust peaks, we are able to cover almost the entire observation period for which usable sonic anemometer observations exist. Overall, the DWL and sonic measurements agreed with low RMSE ($0.4\,\mathrm{m\,s^{-1}}$ for 10 mean wind and $0.8\,\mathrm{m\,s^{-1}}$ for gust peaks, respectively) and small biases (-0.24 and $0.32\,\mathrm{m\,s^{-1}}$); in addition, there are also no cases of strong gusts that the DWL retrieval has not identified. Finally, the estimated uncertainty of the retrieval is evaluated. The uncertainty estimates for mean wind and gust peaks are of the order of magnitude of absolute error with respect to the sonic anemometer. The mean wind is somewhat too often underestimated by the DWL, while the gust peaks are rather too often detected higher than the sonic anemometer. Apart from this asymmetry, these results are nevertheless satisfactory, because it also shows that the DWL distribution did not describe situations that do not match the sonic anemometer observation too often.

The uncertainty was correctly represented, but the use of an effective DOF is necessary. We have used different DOFs for requested winds, i.e., whether it was cycle-based or within 10 min, but there is still room for improvement. Our aim was to provide a reliable estimate, and its tuning is beyond the scope of this study. In particular, separate DOFs could also be appropriate for different weather situations, as well as for the different configurations, of which we examined only CSM2. We show how useful the CSM2 could be if operated at an elevation angle of 62°. Using an elevation angle 35.3° gives results of similar quality. We have not systematically answered how to choose the optimal angle, which could be investigated further. The general advantage of the suggested fast CSM lies in the fact that it completes one measurement cycle within 3.4 s. To our knowledge, there is no comparable DWL scan configuration that performs a similar number of radial velocity measurements in such a short cycle.

The newly available FESSTVaL data set from summer 2021 offers further opportunities for detailed case studies and comparative studies involving several DWLs and airborne in situ measurements. The airborne measurements provide a reference for the quality of retrieval in higher layers. There are parallel DWL measurements in the same quick CSM configuration but at different locations, so the spatial evolution of gust structures can be analyzed. Here, the high-resolution time series of the wind vector generated with the retrieval offers the potential to study turbulence in detail. Thereby, it has to be shown whether the derived vertical wind is of comparable quality as measurements of a vertically pointing DWL. Steinheuer and Friederichs (2020) show that gust profiles can be derived from reanalysis data. This method can still be tested at various locations, which is now also possible with the means of DWLs. We hope that our retrieval lays the foundation for expanding the monitoring network for high-frequency wind measurements with DWLs for weather research and applications.

Appendix A

The expected value of $\hat{\boldsymbol{v}}_0$ holds the following.

$$E\left[\hat{\boldsymbol{v}}_0\right] = E\left[(\mathbf{A}^T\mathbf{A})^{-1}\mathbf{A}^T\boldsymbol{d}\right] \tag{A1}$$

$$= E\left[(\mathbf{A}^T\mathbf{A})^{-1}\sum_{i=1}^{n}\boldsymbol{a}_i d_i\right] \tag{A2}$$

$$= E\left[(\mathbf{A}^T\mathbf{A})^{-1}\sum_{i=1}^{n}\boldsymbol{a}_i(\boldsymbol{a}_i^T\boldsymbol{v}_i+\epsilon_i)\right] \tag{A3}$$

$$= (\mathbf{A}^T\mathbf{A})^{-1}\sum_{i=1}^{n}\boldsymbol{a}_i(\boldsymbol{a}_i^T\boldsymbol{v}_0+0) \tag{A4}$$

$$= (\mathbf{A}^T\mathbf{A})^{-1}\mathbf{A}^T\mathbf{A}\boldsymbol{v}_0 \tag{A5}$$

$$= \boldsymbol{v}_0 \tag{A6}$$

Equations (A1)–(A3) are obtained by inserting definitions. Then the expectation is applied to $\boldsymbol{v}_i$ and ϵ_i, and the matrices cancel out.

The variance of $\hat{\boldsymbol{v}}_0$ holds the following.

$$\begin{aligned}
\mathrm{Cov}\left[\hat{\boldsymbol{v}}_0\right] &= E\left[\left((\mathbf{A}^T\mathbf{A})^{-1}\mathbf{A}^T\boldsymbol{d} - \hat{\boldsymbol{v}}_0\right)\right. \\
&\quad \left.\times \left((\mathbf{A}^T\mathbf{A})^{-1}\mathbf{A}^T\boldsymbol{d} - \hat{\boldsymbol{v}}_0\right)^T\right] && \text{(A7)} \\
&= E\left[\left((\mathbf{A}^T\mathbf{A})^{-1}\sum_{i=1}^{n}\boldsymbol{a}_i\left(\boldsymbol{a}_i^T\boldsymbol{v}_i + \epsilon_i\right) - \hat{\boldsymbol{v}}_0\right)\right. \\
&\quad \left.\times \left((\mathbf{A}^T\mathbf{A})^{-1}\sum_{i=1}^{n}\boldsymbol{a}_i\left(\boldsymbol{a}_i^T\boldsymbol{v}_i + \epsilon_i\right) - \hat{\boldsymbol{v}}_0\right)^T\right] && \text{(A8)} \\
&= E\left[\left((\mathbf{A}^T\mathbf{A})^{-1}\sum_{i=1}^{n}\boldsymbol{a}_i\left(\boldsymbol{a}_i^T\boldsymbol{v}_i + \epsilon_i - \boldsymbol{a}_i^T\boldsymbol{v}_0\right)\right)\right. \\
&\quad \left.\times \left((\mathbf{A}^T\mathbf{A})^{-1}\sum_{i=1}^{n}\boldsymbol{a}_i\left(\boldsymbol{a}_i^T\boldsymbol{v}_i + \epsilon_i - \boldsymbol{a}_i^T\boldsymbol{v}_0\right)\right)^T\right] && \text{(A9)} \\
&= \sum_{i=1}^{n} E\left[(\mathbf{A}^T\mathbf{A})^{-1}\left(\boldsymbol{a}_i\left(\boldsymbol{a}_i^T(\boldsymbol{v}_i - \boldsymbol{v}_0) + \epsilon_i\right)\right)\right. \\
&\quad \left.\times \left((\mathbf{A}^T\mathbf{A})^{-1}\boldsymbol{a}_i\left(\boldsymbol{a}_i^T(\boldsymbol{v}_i - \boldsymbol{v}_0) + \epsilon_i\right)\right)^T\right] && \text{(A10)} \\
&= \sum_{i=1}^{n}(\mathbf{A}^T\mathbf{A})^{-1}\boldsymbol{a}_i\left(\boldsymbol{a}_i^T\boldsymbol{\Sigma}\boldsymbol{a}_i + \sigma_\epsilon^2\right)\boldsymbol{a}_i^T \\
&\quad \times (\mathbf{A}^T\mathbf{A})^{-1} && \text{(A11)} \\
&= \sum_{i=1}^{n}(\mathbf{A}^T\mathbf{A})^{-1}\boldsymbol{a}_i\sigma_d^2\boldsymbol{a}_i^T(\mathbf{A}^T\mathbf{A})^{-1} && \text{(A12)} \\
&= (\mathbf{A}^T\mathbf{A})^{-1}(\mathbf{A}^T\mathbf{A})\sigma^2(\mathbf{A}^T\mathbf{A})^{-1} && \text{(A13)} \\
&= (\mathbf{A}^T\mathbf{A})^{-1}\sigma^2 && \text{(A14)}
\end{aligned}$$

Equation (A9) arises by supplementing $\boldsymbol{v}_0$ with $(\mathbf{A}^T\mathbf{A})^{-1}\mathbf{A}^T\mathbf{A}$ and rearranging. Then in Eq. (A12) the expectation value calculation is applied, exploiting the fact that observation errors ϵ_i are uncorrelated with each other and with the individual deviations from the mean wind $(\boldsymbol{v}_i - \boldsymbol{v}_0)$.

Code availability. The code is available at https://doi.org/10.5281/zenodo.5780949 (Steinheuer et al., 2021a).

Data availability. The data are available at https://doi.org/10.25592/uhhfdm.9758 (Steinheuer et al., 2021b).

Author contributions. UL and FB, together with others, planned the FESSTVaL campaign. FB and CD were responsible for logistics on the site and performed the measurements. JS and CD developed the retrieval methodology with idea contributions from all others. JS coded the retrieval. JS, UL, and SF planned and structured the paper. JS and PF developed the uncertainty methodology of the retrieval. JS drafted the paper. JS, CD, FB, UL, PF, and SF reviewed it iteratively.

Competing interests. The contact author has declared that neither they nor their co-authors have any competing interests.

Disclaimer. Publisher's note: Copernicus Publications remains neutral with regard to jurisdictional claims in published maps and institutional affiliations.

Special issue statement. This article is part of the special issue "Profiling the atmospheric boundary layer at a European scale (AMT/GMD inter-journal SI)". It is not associated with a conference.

Acknowledgements. We would like to thank Ronny Leinweber (DWD, MOL-RAO) in particular for the installation and maintenance of the Doppler wind lidars. We are grateful to Fred Meier (Technical University Berlin, Institute for Ecology) for providing us with a Doppler wind lidar in autumn 2019. Jan Schween (University of Cologne, Institute for Geophysics and Meteorology) always provided helpful assistance with all DWL-related questions. We thank Markus Kayser (DWD, MOL-RAO) and Ronny Leinweber for providing the Level 1 data. There were useful ideas from Eileen Päschke (DWD, MOL-RAO) and valuable discussions with all mentioned. Also, this work has profited from the scientific exchange within the EU COST Action PROBE (CA18235) and the Hans Ertel Centre for Weather Research. We wish to thank Domenico Cimini and the two anonymous reviewers for their constructive comments.

Financial support. This research has been supported by the Bundesministerium für Verkehr und Digitale Infrastruktur (grant no. BMVI/DWD 4818DWDP5A).

Review statement. This paper was edited by Domenico Cimini and reviewed by two anonymous referees.

References

Barlow, J. F., Dunbar, T. M., Nemitz, E. G., Wood, C. R., Gallagher, M. W., Davies, F., O'Connor, E., and Harrison, R. M.: Boundary layer dynamics over London, UK, as observed using Doppler lidar during REPARTEE-II, Atmos. Chem. Phys., 11, 2111–2125, https://doi.org/10.5194/acp-11-2111-2011, 2011.

Bosveld, F. C., Baas, P., Beljaars, A. C. M., Holtslag, A. A. M., de Arellano, J. V.-G., and van de Wiel, B. J. H.: Fifty Years of Atmospheric Boundary-Layer Research at Cabauw Serving Weather, Air Quality and Climate, Bound.-Lay. Meteorol., 177, 583–612, https://doi.org/10.1007/s10546-020-00541-w, 2020.

Brasseur, O.: Development and Application of a Physical Approach to Estimating Wind Gusts, Mon.

Weather Rev., 129, 5–25, https://doi.org/10.1175/1520-0493(2001)129<0005:daaoap>2.0.co;2, 2001.

Brümmer, B., Lange, I., and Konow, H.: Atmospheric boundary layer measurements at the 280 m high Hamburg weather mast 1995–2011: mean annual and diurnal cycles, Meteorol. Z., 21, 319–335, https://doi.org/10.1127/0941-2948/2012/0338, 2012.

Eberhard, W. L., Cupp, R. E., and Healy, K. R.: Doppler Lidar Measurement of Profiles of Turbulence and Momentum Flux, J. Atmos. Ocean. Technol., 6, 809–819, https://doi.org/10.1175/1520-0426(1989)006<0809:dlmopo>2.0.co;2, 1989.

Emeis, S., Harris, M., and Banta, R. M.: Boundary-layer anemometry by optical remote sensing for wind energy applications, Meteorol. Z., 16, 337–347, https://doi.org/10.1127/0941-2948/2007/0225, 2007.

González-Longatt, F., Wall, P., and Terzija, V.: Wake effect in wind farm performance: Steady-state and dynamic behavior, Renew. Energy, 39, 329–338, https://doi.org/10.1016/j.renene.2011.08.053, 2012.

Haeseler, S., Bissolli, P., Dassler, J., Zins, V., and Kreis, A.: Orkantief Sabine löst am 09./10. Februar 2020 eine schwere Sturmlage über Europa aus, Abteilung Klimaüberwachung, Deutscher Wetterdienst, https://www.dwd.de/DE/leistungen/besondereereignisse/stuerme/20200213_orkantief_sabine_europa.pdf (last access: 1 October 2021), 2020.

Johnson, N. L., Kotz, S., and Balakrishnan, N.: Continuous Univariate Distributions, Volume 1, 2nd edn., Wiley Series in Probability and Statistics, John Wiley & Sons, Nashville, TN, ISBN 978-0-47-158495-7, 1994.

Jung, C., Schindler, D., Albrecht, A., and Buchholz, A.: The Role of Highly-Resolved Gust Speed in Simulations of Storm Damage in Forests at the Landscape Scale: A Case Study from Southwest Germany, Atmosphere, 7, 7, https://doi.org/10.3390/atmos7010007, 2016.

Kohler, M., Metzger, J., and Kalthoff, N.: Trends in temperature and wind speed from 40 years of observations at a 200-m high meteorological tower in Southwest Germany, Int. J. Climatol., 38, 23–34, https://doi.org/10.1002/joc.5157, 2017.

Päschke, E., Leinweber, R., and Lehmann, V.: An assessment of the performance of a 1.5 µm Doppler lidar for operational vertical wind profiling based on a 1-year trial, Atmos. Meas. Tech., 8, 2251–2266, https://doi.org/10.5194/amt-8-2251-2015, 2015.

Pasztor, F., Matulla, C., Zuvela-Aloise, M., Rammer, W., and Lexer, M. J.: Developing predictive models of wind damage in Austrian forests, Ann. For. Sci., 72, 289–301, https://doi.org/10.1007/s13595-014-0386-0, 2014.

Pearson, G., Davies, F., and Collier, C.: An Analysis of the Performance of the UFAM Pulsed Doppler Lidar for Observing the Boundary Layer, J. Atmos. Ocean. Technol., 26, 240–250, https://doi.org/10.1175/2008jtecha1128.1, 2009.

Sathe, A., Mann, J., Vasiljevic, N., and Lea, G.: A six-beam method to measure turbulence statistics using ground-based wind lidars, Atmos. Meas. Tech., 8, 729–740, https://doi.org/10.5194/amt-8-729-2015, 2015.

Schindler, D., Jung, C., and Buchholz, A.: Using highly resolved maximum gust speed as predictor for forest storm damage caused by the high-impact winter storm Lothar in Southwest Germany, Atmos. Sci. Lett., 17, 462–469, https://doi.org/10.1002/asl.679, 2016.

Schreur, B. W. and Geertsema, G.: Theory for a TKE based parameterization of wind gusts, HIRLAM newsletter, 177–188, https://www.researchgate.net/profile/Gertie-Geertsema/publication/242591870_Theory_for_a_TKE_based_parametrization_of_wind_gusts/links/5b7a753e92851c1e12218714/Theory-for-a-TKE-based-parametrization-of-wind-gusts.pdf (last access: 24 May 2022), 2008.

Schween, J. H., Hirsikko, A., Löhnert, U., and Crewell, S.: Mixing-layer height retrieval with ceilometer and Doppler lidar: from case studies to long-term assessment, Atmos. Meas. Tech., 7, 3685–3704, https://doi.org/10.5194/amt-7-3685-2014, 2014.

Sheridan, P.: Review of techniques and research for gust forecasting and parameterisation, Technical report, Met Office Exeter, UK, https://www.researchgate.net/profile/Peter-Sheridan-2/publication/268744498_Review_of_techniques_and_research_for_gust_forecasting_and_parameterisation/links/5474c0b00cf245eb436e0791/Review-of-techniques-and-research-for-gust-forecasting-and-parameterisation.pdf (last access: 24 May 2022), 2011.

Smalikho, I. N. and Banakh, V. A.: Measurements of wind turbulence parameters by a conically scanning coherent Doppler lidar in the atmospheric boundary layer, Atmos. Meas. Tech., 10, 4191–4208, https://doi.org/10.5194/amt-10-4191-2017, 2017.

Steinheuer, J. and Friederichs, P.: Vertical profiles of wind gust statistics from a regional reanalysis using multivariate extreme value theory, Nonlin. Processes Geophys., 27, 239–252, https://doi.org/10.5194/npg-27-239-2020, 2020.

Steinheuer, J., Detring, C., Beyrich, F., Löhnert, U., Friederichs, P., and Fiedler, S.: JSteinheuer/DWL_retrieval: DWL retrieval, Zenodo [code], https://doi.org/10.5281/zenodo.5780949, 2021a.

Steinheuer, J., Detring, C., Kayser, M., and Leinweber, R.: Doppler wind lidar wind and gust data from FESTVAL 2019/2020, ICDC [data set], https://doi.org/10.25592/uhhfdm.9758, 2021b.

Suomi, I., Gryning, S.-E., O'Connor, E. J., and Vihma, T.: Methodology for obtaining wind gusts using Doppler lidar, Q. J. Roy. Meteor. Soc., 143, 2061–2072, https://doi.org/10.1002/qj.3059, 2017.

Vickers, D. and Mahrt, L.: Quality Control and Flux Sampling Problems for Tower and Aircraft Data, J. Atmos. Ocean. Technol., 14, 512–526, https://doi.org/10.1175/1520-0426(1997)014<0512:qcafsp>2.0.co;2, 1997.

World Meteorological Organization: Measurement of surface wind, Guide to Meteorological Instruments and Methods of Observation, 8, 196–213, https://library.wmo.int/index.php?lvl=notice_display&id=12407#.YZz2hiVCdhF (last access: 25 November 2021), 2018.

Appendix C

Steinheuer and Löhnert, 2023

High-resolution profiling of wind gust patterns measured by Doppler wind lidars during the FESSTVaL campaign

The evolution of gusts is difficult to observe as gusts are short-lived phenomena. Within the Field Experiment on Sub-mesoscale Spatio-Temporal Variability in Lindenberg, phenomena in the atmospheric boundary layer are studied, including the observation of the wind field by three Doppler wind lidar at a distance of 6 km of each other. A quick continuous scanning provides the wind vector every 3.4 s. This allows to analyze wind gust causes, such as the passage of a cold front or cold pools.

J. Steinheuer and U. Löhnert (2023). "High-resolution profiling of wind gust patterns measured by Doppler wind lidars during the FESSTVaL campaign". In: *Preparation for Quarterly Journal of the Royal Meteorological Society*

Author contributions: Löhnert planned the FESSTVaL campaign together with others. Steinheuer and Löhnert planned and structured the paper. Steinheuer did coding, visualization and the formal analysis. Steinheuer drafted the manuscript and reviewed it iteratively with Löhnert.

RESEARCH ARTICLE

High-resolution profiling of wind gust patterns measured by Doppler wind lidars during the FESSTVaL campaign

Julian Steinheuer[1, 2] | **Ulrich Löhnert**[1, 2]

[1]Institute for Geophysics and Meteorology, University of Cologne, Cologne, Germany

[2]Hans-Ertel Centre for Weather Research, Climate Monitoring and Diagnostics, Cologne/Bonn, Germany

Correspondence
Julian Steinheuer, Institute for Geophysics and Meteorology, University of Cologne, Cologne, Germany
Email: Julian.Steinheuer@uni-koeln.de

Funding information
This work has been conducted in the framework of the Hans Ertel Centre for Weather Research funded by the German Federal Ministry for Transportation and Digital Infrastructure (grant no. BMVI/DWD 4818DWDP5A)

The evolution of wind gusts is difficult to observe as gusts are short-lived and small-scale phenomena. They are an integral part of certain weather configurations such as fronts, and cold pools, and may differ strongly locally. The question arises if individual gust observations can be considered representative of their surroundings or whether significant differences are already evident at the meso-gamma scale (2-20 km). Within the Field Experiment on Sub-Mesoscale Spatio-Temporal Variability in Lindenberg (FESSTVaL) in summer 2021 different phenomena in the atmospheric boundary layer are studied with a variety of instruments. This involved a set-up of three Doppler wind lidars (DWLs) in a trinagle configuration at a distance of 6 km to capture the local wind field. We use a novel fast continuous scanning mode that completes a full observation cycle within 3.4 seconds and is suitable for deriving high-resolution time series of the full wind vector per each observation cycle. We use this experimental set-up to analyze the spatio-temporal evolution of wind patterns on the sub-mesoscale with unprecedented resolution. Based on this, our work provides a new approach to future high-resolution wind profiling.

KEYWORDS
Doppler wind lidar, wind gust, cold pool, cold front, FESSTVaL

1 | INTRODUCTION

Accurate monitoring of the wind field is one of the most important applications of meteorological measuring instruments. Modern surface-based in-situ measuring instruments are capable of detecting highly fluctuating wind patterns such as gusts. In particular, sonic anemometers are suitable instruments, since they record the 3-dimensional wind vector with a very high resolution on the order of 1 to 20 Hz (Lee et al., 2004). The slower reacting cup anemometers are also sufficient to measure stronger gusts. Suomi and Vihma (2018) estimated that these are able to detect wind speeds above 10 m/s if those last at least 0.2 s, which is sufficient to provide higher wind gusts consistent with the World Meteorological Organization (2018) recommendation i.e., corresponding to a wind speed lasting at least for 3 s. The wind gust peak then denotes the maximum gust of a specific time window such as 10 minutes. Radiosonde ascents play a crucial role for the numerical weather prediction (NWP), as they measure wind profiles with a high vertical resolution and extent. However, this happens only for sporadic locations and regularly only in a six-hour cycle or even less frequently. Accordingly, the vertical coverage of wind observations is very thin and, in particular, the high temporal resolved wind speeds from which gusts are derived are observed exclusively near the surface.

In NWP, the temporal resolution is too coarse to model wind gusts, resulting in only a mean wind being diagnosed. The wind gust peaks are sub-scale and therefore cannot be calculated explicitly but only be parameterized. Usually this is done for 10 m a.g.l. (Brasseur, 2001; Schreur and Geertsema, 2008; Sheridan, 2011) to give a near-surface result that is not too strongly mitigated by surface friction. The parameterization schemes could be evaluated against the existing in-situ measurements at 10 m a.g.l. However, thanks to increased model resolutions as used in large eddy simulations or direct numerical simulations, the wind can also be diagnosed more explicit and there is a need for higher resolution observing systems that could profile the atmospheric boundary layer (ABL). Doppler wind lidars (DWLs) have the potential to provide these wind observations. For instance, Päschke et al. (2015) demonstrated that DWLs are suitability tools for observing the mean wind in the ABL under most atmospheric conditions. In our work, we emphasize that DWLs are also suitable to provide profiles of the 3-dimenional wind vectors at high temporal resolution. In addition to an accurate representation of the wind gust peak within a specific time window, we provide a time series that profiles the entire wind regime in high resolution. This allows to perform special case studies and to observe small scale features like convective rolls or Kelvin-Helmholtz instabilities, but also the complex processes in larger frontal systems or thunderstorms. To our knowledge, this is the first time that wind can be observed in such detail by a DWL.

DWLs are produced by various manufacturers and differ in their properties. To generate high-resolution wind products, devices with scanning patterns that can measure many radial velocities in a short time are needed. Suomi et al. (2017) used a *WindCube V2* DWL in a Doppler beam swinging configuration to obtain wind-vectors with a temporal resolution of 3.8 s. Steinheuer et al. (2022) introduced a quick continuous scanning mode (CSM) that finishes eleven radial velocity measurements in 3.4 s. The used instruments, manufactured by *Halo Photonics* (Worcester, United Kingdom), proved to be very accurate in measuring ten minutes wind gust peaks when compared to observations from a sonic anemometer at 90.3 m. This was the groundwork to determine the most appropriate configuration to observe wind gusts. Therefore, this configuration was operated on three Halo Photonics DWLs in the *Field Experiment on Sub-Mesoscale Spatio-Temporal Variability in Lindenberg* (FESSTVaL) in summer 2021 which data is the basis of this study.

The goal of FESSTVaL is to accurately monitor sub-scale phenomena by establishing a dense network of observing systems. A particular focus is on cold pools (CPs), which are difficult to locate and to resolve accurately with standard weather models. Numerical simulations require grid resolutions much lower than 1 km to resolve a CP (Drager and van den Heever, 2017; Cafaro and Rooney, 2018; Fournier and Haerter, 2019; Drager et al., 2020). Thus, the campaign's ground-based observational network consists of many temperature and pressure measurements (at 120 sites)

and additional relative humidity, wind, and rain rate measurements (at 19 sites) distributed around Lindenberg, Brandenburg, Germany. Within this area are three super-sites (Falkenberg, Lindenberg, Birkholz) that provide additional vertical profiles of major meteorological variables using remote sensing devices, such as the DWLs mentioned above, microwave radiometers (MWRs), micro rain radars (MRRs), and ceilometers. Further, Falkenberg has a mobile X-Band rain radar with a range of 20 km (Lengfeld et al., 2014). Our focus is on the DWLs and the events that lead to strong winds. The triangular arrangement of the DWLs, which are positioned at a distance of 6 km from each other, enables us to detect even small-scale differences in the profiles. In this respect, the CP is worth highlighting not only for the campaign, but also for the presented study

A convection-driven CP is generated from air into which rain falls and which is then cooled by evaporation of the rain. The cooled, dense air descends and spreads at the surface, displacing the warmer surrounding air. The boundary of the cold air is marked by a gust front associated with a distinctive convergence line and accompanied by vertical motions, which could potentially trigger further convection. Whether this is initiated depends on the surface temperature and moisture fields, but also on the wind profiles. For instance, wind shear has a strong influence on the organization of convective squall lines (Grant et al., 2018). The intensity of the rain affects the size of a CP and thus the temperature drop and propagating wind speeds. This can be related to rain rates from radar observations (Kruse et al., 2021) or surface-observed saturation deficits (Kirsch et al., 2021).

Strong winds also occur when weather fronts are passing. Driven by a low-pressure system, air masses of different temperatures shift, with the warmer air rising above the colder air, usually triggering precipitation. The change of air masses is accompanied by a wind shift, which varies depending on whether it is a warm front, i.e. warm air follows cold air and the wind direction changes cyclically, or a cold front, i.e. cold air follows warm air and the wind direction changes anticyclically (Bott, 2016). Also here, the DWL can provide a detailed wind profile image and contribute to an analysis of the air mass change.

Overall, we pursue the three main goals: (1) to generate high-resolution wind profiles in the ABL, (2) to use multiple DWLs to detect sub-mesoscale variability in the wind patterns, and (3) to identify mechanisms leading to extreme wind speeds by fully illuminating the weather situation through a variety of measuring instruments. To achieve, we will present the campaign and the different measuring instruments in section 2. The quality of the retrieved wind from the DWL will be assessed in section 3 and an adjustment of the obtained vertical velocities will be given. The results in section 4 consists of a description of the general wind variability between the three locations and a discussion of two cases, namely the passage of a cold front on June 12, 2021, and a cold pool event on June 29, 2021. We conclude with a summary of all findings in section 5.

2 | OBSERVATIONS

2.1 | FESSTVaL

The field experiment on sub-mesoscale spatio-temporal variability in Lindenberg is a measurement campaign initiated by the *Hans Ertel Center for Weather Research* (HErZ). It took place during the summer months of 2021 at the *Meteorological Observatory Lindenberg – Richard-Aßmann-Observatory* (MOL-RAO) of the *German Weather Service* (DWD), located 65 km southeast of Berlin in Germany. To investigate the sources of sub-mesoscale variability, the measurement campaign focuses on three main aspects: Atmospheric boundary layer structures, cold pools, and wind gusts. The sub-scale refers to the meso-gamma scale, i.e., it ranges from 2 to 20 km, and the campaign aims to capture the phenomena and processes therein with a high spatial coverage. To measure the vertical dimension, radiosondes were launched, unmanned aerial vehicles were flown, and three profiling super-sites were set up at a distance of 6 km of

each other. DWLs are used to measure the wind, thermodynamic profiles of the atmosphere are obtained, and falling precipitation is resolved vertically. The two super-sites Lindenberg and Falkenberg arose from the infrastructure provided by the DWD and were complemented by the site Birkholz to a triangle formation to ensure that transported wind patterns can be observed again regardless of the advection direction. The horizontal dimension is covered by 100 compact weather stations that measure near-surface temperature and air pressure, 19 automatic weather stations that additionally record wind and humidity, energy balance stations, and a precipitation radar. This equipment is complemented by the ground-based remote sensing capabilities of the MOL-RAO. Beyond that, the added value of a citizen-sensing network has been explored, and all measurements are complemented by high-resolution large-eddy simulations. In the following, we will present only the instruments that contribute to the present study. Figure 1 shows the map of the campaign area with three marked super-sites where the profiles were measured. In the center is the DWD boundary layer field site at Falkenberg, where the mobile X-band radar was stationed for the whole campaign. North of this is the MOL-RAO and to the North-east a third profiling site was established at Birkholz. The entire terrain is flat and consists mainly of farmland with some forested areas and a few lakes. The dense network of surface observations consists of the APOLLOs and WXTs presented below.

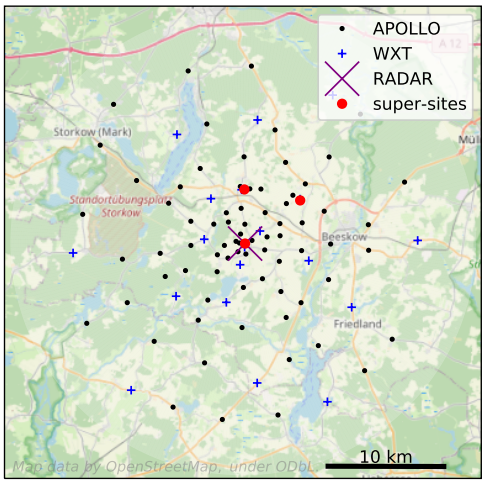

FIGURE 1 The campaign area is located in the northeastern part of Germany in flat terrain with predominantly cropland (yellowgreen), forrests (green), and some lakes (blue). The three FESSTVaL super-sites with DWLs are located about 6 km apart: Lindenberg in the North, Birkholz in the North-East and Falkenberg in the center (red markers).

2.2 | Doppler wind lidar

Key to the presented work are the measurements of the DWLs at the three super-sites. A DWL measures the alongsite Doppler shift of the backscattered near-infrared radiation transmitted at 1.5 µm with pulse repetition frequency of 10 kHz. If a sufficient number of aerosols is available and signal to noise is large enough, the relative velocity – the Doppler velocity – can be derived at different distances from the lidar. In the ABL, there are usually enough backscatterers because there are enough aerosol particles, e.g. that were previously dispersed from the earth's surface. If the air is very clear, e.g. after heavy rain or in higher layers, it is more difficult to retrieve the Doppler velocity accurately because there are fewer backscattering particles. Raindrops are also backscatterers and, depending on rain intensity,

their falling velocities are recorded instead of air movement. Dense clouds scatter so strongly that the light signals do not penetrate into higher layers in order to return Doppler velocities from there, i.e. clouds limit the vertical range of the DWL. Multiple Doppler velocities originating from the same altitude but from different DWL orientations have a different perspective on the wind vector and therefore the three wind components can be reconstructed. All DWLs used are configured in the same way using a continuous scanning mode, i.e. while light is being emitted and received, the transmitting and receiving scan head of the DWL continues to move. By performing this quickly, eleven measurements per scan head rotation are generated in about 3.4 s. Each measurement contains Doppler velocities from about 100 beam segments along changing azimuth angles and at 62° elevation angle. From the measurements of one scan head rotation, a wind vector is calculated for each altitude, assuming that all Doppler velocities are projections of a single vector. The retrieval algorithm is introduced in detail in Steinheuer et al. (2022). In total we use five different DWLs which are all *StreamLine* devices built by Halo Photonics. The triangle configuration was performed during two periods in summer with different DWLs at the super-sites. From June 11 to July 14, 2022, i.e. 34 days, the DWL *RAO 02* was located in Falkenberg, the DWL *KIT 01* in Lindenberg, and the DWL *RA0 03* in Birkholz. From August 10 to August 31, 2022 i.e. on 22 days the DWL *RAO 01* operated in Falkenberg, the DWL *RAO 00* in Lindenberg, and the DWL *KIT 01* in Birkholz. The DWL *RAO 00* is an extended range instrument (*StreamLine XR*) that emits more radiation than the other DWLs and is therefore able to obtain signals at even lower aerosol concentrations and thus can generally obtain more useful Doppler velocities from higher layers (see for detailed instruments specification Table 1 in Steinheuer et al., 2022). Other measurement configurations and DWLs are also involved in the campaign. The DWL *RAO 00* routinely measures at Lindenberg to derive the mean wind (cf. Päschke et al., 2015), and another StreamLine device provide by the *Finnish Meteorological Institute* (DWL *FMI 00*) was located at Falkenberg to measure exclusively the vertical component of the wind. We will use both for comparison.

2.3 | Sonic anemometer

The meteorological tower at the Falkenberg site is equipped with an ultrasonic anemometer manufactured by *Metek* (Meteorologische Messtechnik GmbH, Elmshorn, Germany) at 90.3 m and the device version is *USA-1*), which resolves the wind vector with a temporal resolution of 20 Hz. The data processing is done in the same way as in Steinheuer et al. (2022). Nonphysical values like abrupt peaks are filtered and replaced by interpolations of the neighboring points (following Vickers and Mahrt, 1997). From the filtered time series, both the 10 minute winds are averaged, resulting in mean quantities of all three wind components, and the 3-second lasting wind maximum is determined within the 10 minutes. The sonic anemometer is mounted on a boom directed southward and at a distance of 4 m from the tower. Due to shadowing and wake effects caused by the tower structure, data obtained from wind directions within 0-50° are disturbed and have to be discarded for fair comparisons with other measurements like those from the DWL.

2.4 | Micro rain radar

The Micro Rain Radar (MRR) is a solely vertically oriented frequency modulated continuous wave (FM-CW) Doppler radar operating at K-band (24.1 GHz, 12.4 mm wavelength) and manufactured by Metek. The transmitted radar signal (50mW transmit power, 1.5° beam width) is backscattered by falling hydrometeors such as rain, graupel, snow and received with a 0.5 m diameter antenna. From the Doppler spectra the radar reflectivity factor and the terminal fall velocity distribution can be derived. The range resolution can be varied and is here set to 100 m, which, together with the 30 range gates, gives a maximum altitude of 3100 m. In the case of rain, the Doppler spectra can be used to

derive vertical profiles of microphysical rain properties such as drop size distribution and the rain rate, which is the quantity we are interested in. We use an MRR which is installed at Lindenberg and owned by the MOL-RAO, and measures raing rates with a temporal resolution of 10 s.

2.5 | Microwave radiometer

The microwave radiometer (MWR) is a passively operating remote sensing instrument for determining humidity and temperature profiles (hence also referred to as HATPRO for Humidity And Temperature PROfiler) manufactured by *RPG* (Radiometer Physics GmbH, Meckenheim, Germany). It measures six brightness temperatures around the 22.235 GHz water vapor absorption line (i.e. within the K-band), one in the atmospheric window at 31.4 GHz and seven in the oxygen absorption complex around 60 GHz (i.e. within the V-band). The former being used for water vapor profiling and liquid watrer path, and the latter for temperature profiling. Zenith measurements alternate with off-zenith elevation scans that improve the accuracy of the temperature profiles in the ABL (Crewell and Lohnert, 2007) and which are therefore used here. However, at our three super-sites, this only gives us profiles every 5 minutes (Falkenberg, *SUNHAT* owned by the *University of Cologne*), respectively every 10 minutes (Birkholz, *HAMHAT* by *University of Hamburg*; Lindenberg, *RAOHAT* by MOL-RAO). The data are available in Löhnert et al. (2022).

2.6 | APOLLO/WXT network

The unique characteristic of the FESSTVaL campaign is a dense network of ground-based observations, which was conceived, created, built, and maintained with high efforts by the Hamburg project members. On the one hand, 19 commercial compact weather stations (*Vaisala Weather Transmitter WXT536, hence abbreviated WXT*; from Vaisala Vantaa, Finland) were set up to measure air pressure, temperature, relative humidity, wind speed, wind direction, and precipitation. Additionally, 80 rudimentary stations measuring only air pressure and temperature were spread across the observation domain. By means of this dense observation network (Fig. 1), the near-ground impacts of cold pools can be documented, which is why such a station is named *Autonomous cold POoL LOgger* (APOLLO). Both station types measure with a temporal resolution of 10 s. A detailed description of the instruments and the integrated sensors can be found in Kirsch et al. (2022b) and the data are available in Kirsch et al. (2022a).

2.7 | X-band radar

At Falkenberg, the project partners from Hamburg also deployed a mobile rain radar operating within the X-band (i.e. at 9410 MHz frequency). This non-polarized radar resolves the rain field every 30 s with a fine range resolution of 60 m and a maximum range of 20 km. Measurements are made at an elevation angle of 2.3° and with an azimuth increment of 1°. See Lengfeld et al. (2014), for a detailed description of the radar and the rain rate retrieval and obtain the campaign data from Burgemeister et al. (2022).

2.8 | Ceilometer

At each of the three super-sites, there is a ceilometer to measure the height of the cloud base. A ceilometer emits laser pulses and measures the backscattered light. From the travel time, the distance of the backscattered object can be determined. And from strength and attenuation of the received signal, the backscatter coefficient is calculated. The instrument identifies cloud base by calculating visibility from the backscatter coefficient and indicating the height

above which the ground cannot be seen. If the lower clouds are sufficiently transparent, the device is able to detect up to three different cloud layers. Different ceilometer types are located at the different sites (one *CBME80B* ceilometer from *Eliasson* (Västerås, Sweden) in Birkholz, owned by the *University of Bonn*; two *CHM15k Nimbus* ceilometers from *Jenoptik* (Jena, Germany) in Falkenberg and Lindenberg, owned by the MOL-RAO). When it rains, failures in acquiring the correct cloud base height are possible and the derived cloud base drops abruptly to the ground or the cloud disappears completely.

3 | ASSESSMENT OF THE DWL WIND QUALITY

3.1 | Evaluation of the horizontal wind speed

Steinheuer et al. (2022) examined different measurement configurations and the CSM was best suited to derive wind gust peaks. By measuring continuously, a comparatively large number of observations can be obtained in a comparatively short time. This is possible because the head of the DWL does not have to be driven into exact alignments, but is constantly in motion, which means that the resulting set of azimuth angles per cycle is constantly changing. A relatively small number of laser pulses are emitted per measured interval, so that a full cycle is achieved very quickly. The configuration exploits the capabilities of the hardware and has the fastest possible rotation speed. This reduces the quality of a single measurement and it is reasonable to doubt whether the CSM is suitable for permanent operation and whether it delivers similarly reliable mean winds as established configurations.

During the three summer months, observations were not conducted completely at all three sites, and there were also DWL changeovers. At the beginning of June a different DWL was deployed in Lindenberg, which generally had difficulties to provide a usable Doppler signal and which had to be replaced. In order to systematically determine differences between the devices, a set of comparative measurements of all deployed DWLs was performed. In Falkenberg, these were conducted for 3.5 weeks starting in mid-July with all devices in parallel. Discrepancies were noticed, which are the subject of ongoing investigations and beyond the scope of this paper. However, there were no indications that the CSM was fundamentally a difficult configuration for the devices. Hence, it should be emphasized that during the intended main observation period we measured usable velocities in the CSM with each of the DWLs to deduce the wind values.

To assess the quality of the obtained winds, we rely on the DWL in Lindenberg, which routinely measures in a conventional configuration, and the sonic anemometer at the Falkenberg tower. The former measures in a slow step-stare mode with 24 beams (cf. Päschke et al., 2015) and can thus only be a reference for mean wind. This allows comparisons in higher altitudes. The latter has a high temporal resolution, but is limited to the tower reference altitude. Thus, in addition to the mean wind, wind gust peak comparisons can be conducted. Figure 2 shows these results. Panel (a) provides the scatterplot for Lindenberg for 912 m, during the comparison period from mid-June to mid-July. Except for about 5 outliers, the two DWLs have a fair agreement with minor mean deviation (-0.16 m/s), small RMSD (0.57 m/s), and correspondingly a high coefficient of determination (0.97). In panel (b), the mean wind at 90.3 m above Falkenberg and from the whole triangle-established observation period provides an even higher agreement between the CSM generated wind and the reference sonic anemometer. Low RMSD (0.34 m/s), negligible MD (-0.09 m/s), and high R^2 (0.98), together with very good data availability (96 %) illustrate that the mean wind can be observed very accurately. The present study is intended to demonstrate the potential that the high resolution wind product of the CSM has, i.e. where the wind is derived from each cycle. Here we are particularly interested in retrieving correctly the strong gusts. Panel (c) provides the comparison of DWL versus sonic anemometer for the 10 minute wind gust peaks, also from 90.3 m above Falkenberg. Data availability is insignificantly lower than for

the mean wind (only 64 fewer comparison points) and the spread is rather broad, since a fast-fluctuating quantity is compared (with an RMSD at 0.68 m/s). Low mean deviation (0.2 m/s) and high R^2 value (0.95), however, confirm the results of Steinheuer et al. (2022) that the CSM captures the wind gusts excellently. Therefore, we conclude that in general the cycle-based wind retrieval provides a reliable representation of the horizontal wind in the ABL.

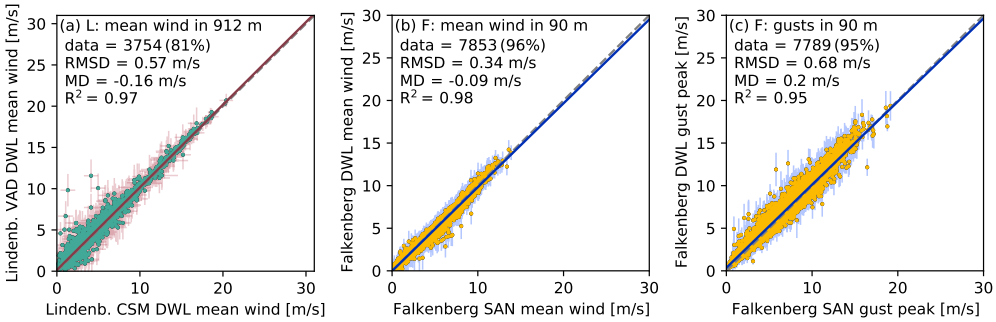

FIGURE 2 Scatterplots comparing the wind from the DWL in the CSM against conventionally measured wind from another DWL and a sonic anemometer. Panel (a) shows the comparison of the 10 min mean wind from the DWL at Lindenberg with the DWL that is routinely measuring in a slow step-stare mode with 24 beams per cycle in 912 m. Panels (b) and (c) show the comparison of the 10 min mean wind and wind gusts, respectively, of DWL at Falkenberg with the sonic anemometer (SAN) of the meteorological tower at 90.3 m. For each plot, the colored linear fit line, root mean square deviation (RMSD), mean deviation (MD), data involved, and coefficient of determination (R^2) are indicated. The numbers in parentheses indicate the fraction of situations in which both instruments provided valid wind values. The estimated standard deviation of the wind value is shown with vertical (y-axis DWL) and horizontal (x-axis DWL only) bars. Only measurements with less then 2 m/s standard deviation are shown.

3.2 | Vertical wind correction for the DWLs

The vertical wind is a fragile variable. Whether the air is descending or ascending will make a significant difference to the weather situation. With the daily formation of the turbulent atmospheric boundary layer, thermal eddies are created that exchange air vertically and are reflected in an alternation of upward and downward movements. A DWL that points solely vertically measures the w-component of the wind directly and therefore the *Vertical Stare* is the preferred DWL configuration when only the vertical air motion is of interest. Nevertheless, we use a measurement configuration that is established primarily to derive the horizontal wind, but also provides the w-component. The retrieval fits the wind vector to different Doppler velocities, and does not explicitly account for the fact that the vertical wind is about an order of magnitude lower than the horizontal wind components. Small deviations in the horizontal wind are acceptable, but in the vertical wind velocity they can make the crucial difference between whether air is rising or descending. In the CSM, the measurements are performed with an elevation angle of 62°, i.e. each Doppler velocity contains an additive contribution of $w\cos(62°)$. Therefore, the vertical wind affects all measurements equally in the sense that upward vertical movements induce larger Doppler velocities and downward vertical movements induce smaller Doppler velocities. Conversely, a systematic offset in the Doppler velocities would affect only the estimation of the w-component. Such an offset could be corrected within the instrument software.

Figure 3 panel (a) shows the distribution of 10 min averaged vertical winds at 90.3 m for DWLs at the three different sites (colored) and the sonic anemometer at the Falkenberg tower (gray). The wind measured at the tower

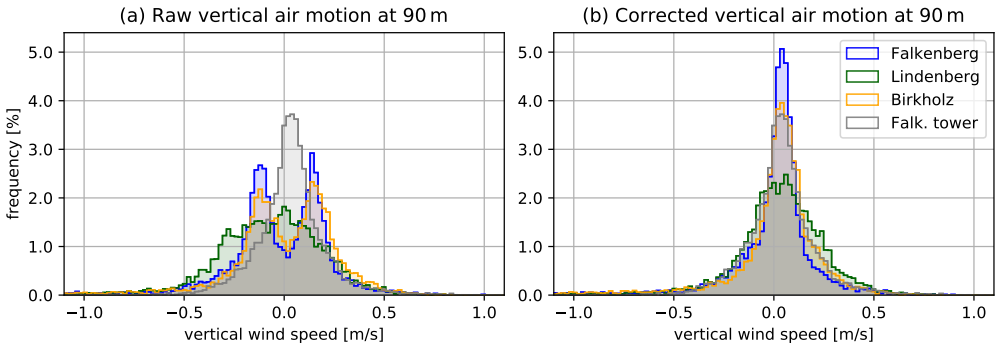

FIGURE 3 Histograms of the raw (a) and the corrected (b) vertical air motion in 90.3 m for the DWLs at the three different sites (Falkenberg in blue, Lindenberg in green, and Birkholz in yellow) and the sonic anemometer at the Falkenberg meteorological tower (Falk. tower in gray). The bin width is 0.02 m/s.

is distributed close to 0 m/s, whereas the three DWL winds show bimodal histograms (Falkenberg and Birkholz) or a broad distribution (Lindenberg). This bimodal distributions results from leaps in the vertical wind that occur every half hour and are illustrated in the appendix for an example day (cf. Fig. 13). The reason for the artificial pattern is the particular configuration of the CSM, which is set for one hour and then recurs. Every full hour, the scan head starts with a counterclockwise rotation, brakes after half an hour and then runs clockwise. Towards the end of the hour, the rotating measurements are stopped and the scan head moves into a vertical stare to remain there until the new hour begins and the pattern repeats. The half-hour rotation change was set up because of some system crashes that occurred during the testing phase and were prevented this way, but is responsible for the jumps in the vertical motion. To remove the artifacts in the statistics and obtain correct w, we apply an alternating bias correction which lead to the satisfactory histograms of Fig. 3 panel (b).

This bias-correction is applied to all vertical winds of the DWLs in the CSM. To determine the DWL offset, we calculate mean values of the vertical winds in 90.3 m for both DWLs used at each of the three locations. A distinction is made between the first half hour and the second half hour of each full hour, so there are two mean values per device and location. Thus we obtain twelve different mean vertical winds from individual observation periods, which are contrasted with the mean values of the same period from the sonic anemometer in 90.3 m. The offsets are obtained from these twelve DWL values minus the respective mean-w of the sonic anemometer. All the sonic anemometer mean-w values are close to 0 m/s and hardly differ (0.02 m/s - 0.04 m/s, cf. Table 1 in the appendix). Therefore, we assume that the different observation periods are long enough to be independent of individual diurnal variations or weather phenomena and can be assumed to be representative in terms of both the DWL offset and the correct mean vertical wind of the sonic anemometer. The error appears independent of altitude (cf. example day in Fig. 13 in the appendix), i.e. we also consider the offset from 90.3 m to be representative for all layers. The sites are 6 km away from each other and differ somewhat topographically. It is conceivable that the summer climatology of vertical wind is slightly different here, but this should be minor. For lack of a better reference, we therefore also correct for the DWL in Lindenberg and Birkholz using the sonic anemometer in Falkenberg.

Figure 4 gives a statistic for the comparison of the corrected vertical wind from the DWLs in the CSM at Falkenberg against the nearby DWL *FMI 00* in the vertical stare (34+22 days). A minutely retrieval resolution was chosen for the CSM, and the Doppler velocities of the vertical stare were linearly interpolated to the heights of the CSM output and averaged minutely. At the DWLs first comparable height above the surface (at 146 m) the distribution of the differences is very narrow (with a mean of 0.04 m/s and a standard deviation of 0.2 m/s) while it widens upwards

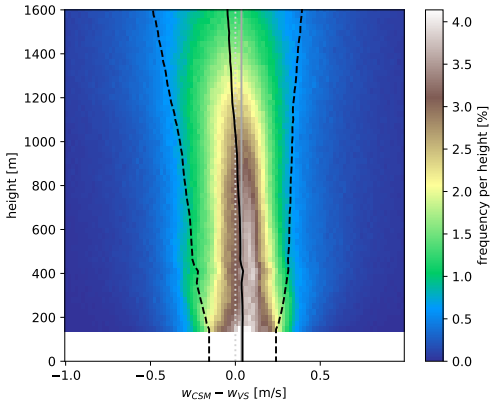

FIGURE 4 Frequency of differences in the 1 min vertical motion of bias-corrected DWL in CSM minus DWL in vertical stare (VS) per height in Falkenberg. The Doppler velocities of the VS are linearly interpolated to the heights of the CSM to be comparable. The solid black line indicates the mean difference, and the dashed lines bound the one-times standard deviation interval around it. Differences of wind speeds with $|w| > 1$ m/s from at least one of the two DWLs are not considered, resulting in used data ranging from 89 % at 146 m to 52 % at 1600 m. The bin width is 0.02 m/s.

and becomes slightly negative in the mean (mean of -0.05 m/s and standard deviation of 0.44 m/s at 1603 m). The slightly positive mean difference in the lower 500 m is of the order of the mean-w measured at the sonic anemometer in 90.3 m. A bias-correction that would shift the mean-w in 90.3 m to 0 m/s would thus improve mean difference in the lower 500 m somewhat. Nevertheless, we remain with the chosen correction, since these differences are small and the histogram shows that the bias-corrected w-component is of sufficient quality to estimate the vertical motion in general and that the bias due to the direction of rotation has been eliminated.

The range of the offset between both rotation directions is roughly constant at 0.27 m/s for all six DWL-site-pairs (cf. to Table 1 in the appendix). The source of the error has not been definitively determined, but we hypothesize that it is related to the fast rotation of the DWL. Accordingly, this could cause the Doppler velocity to be doubly shifted by the relative velocity of the light transmitting/receiving-spot on the DWL head (doubly, since this happens twice when the light is transmitted and received). As the DWL head rotates in the direction of its zenith tilt, the relative velocity of the DWL is positive with respect to the transmitted light and as it reverses, it is correspondingly negative. With an error of 0.13-0.14 m/s (half offset range) and rotation speed of 3.4 Hz it can be estimated that this transmitting/receiving-spot is about 14-15 cm away from the DWL rotation axis, which is approximately correct. If the two rotational offsets are not symmetrically located around 0 m/s, this could indicate a wrong device calibration, which can be prevented by adjusting the software settings accordingly.

4 | RESULTS

4.1 | Wind variability in summer 2021

To get an impression of the wind variability in summer 2021, we checked the winds over the three sites. Wind roses from different heights provided quite similar patterns: In the lower hundred meters of the ABL, a west-southwest component prevails in the wind direction, while at around 1000 m height the dominant westerly wind zone is more pronounced. This is due to the fact that with increasing altitude the influence of the surface roughness decreases,

the wind describes a clockwise rotation and at the same time gains intensity. The three locations hardly differ in their general wind conditions, i.e. neither in strength nor in direction.

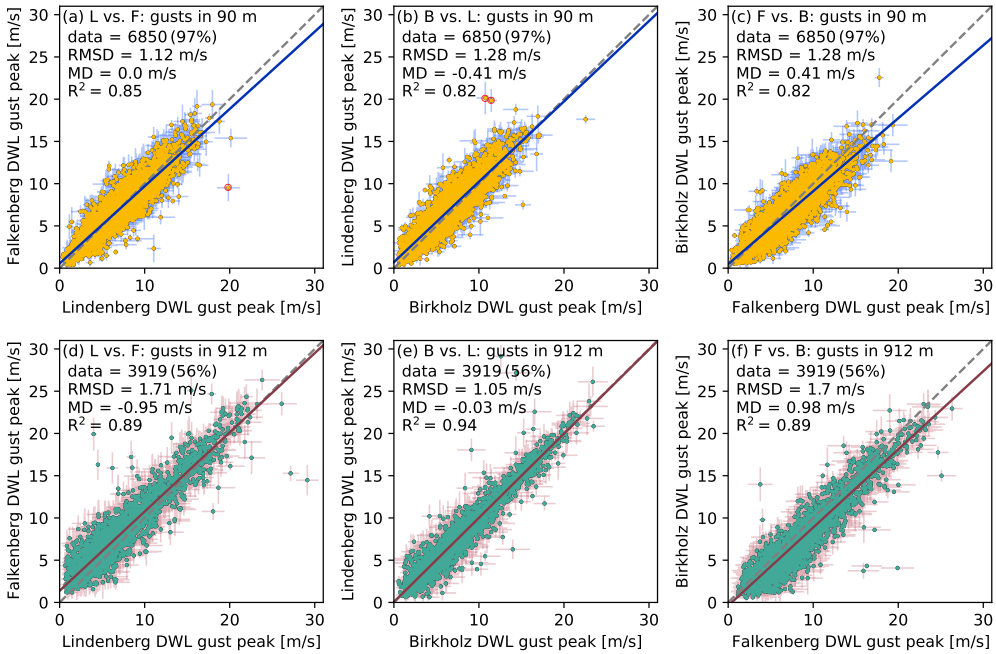

FIGURE 5 Scatterplots comparing the wind gust peaks over each location (L, B, F) with the other two locations. The top row shows the comparison for 90 m and the bottom row for 912 m. The quantities data, RMSD, MD, and R^2 are as in Fig. 2 The estimated standard deviation of the wind gust is shown with vertical (y-axis) and horizontal (x-axis) bars. Only measurements with less then 2 m/s standard deviation are shown. The three highest mismatches at 90 m are indicated by a red circle.

To identify local differences, we directly compare the 10 min wind gust peaks above each site with the other sites, exemplified for the two heights 90 m and 912 m in Fig. 5. Measurements are only visualized if the wind gust was retrieved at each of the three locations. We scatter the maxima against each other because we are interested in joint strong wind velocities. By choosing the time window of 10 minutes, we take into account that an occurring gust pattern needs some time to travel to another location. A direct comparison of the high-resolution time series could not include such transport effects and would yield more scattered plots. The panels show that all three sites are strongly correlated with each other. The coefficient of determination at 90 m ranges from 0.82 to 0.85 and at 912 m from 0.89 to 0.94. In 90 m all three DWL have a high data availability, so that almost the complete observation period can be compared. In contrast to Fig. 2 panel (c), where wind gust peaks in Falkenberg from DWL and sonic anemometer are compared, it can be seen that comparisons between the distant sites results in broader scattering (note that the time period is different, which however does not have a significant influence). The mean deviation in Fig. 5 panels (b) and (c) shows that the wind gusts at Birkholz are somewhat weaker than at the other two sites. We assume this is due to the presence of trees, in the south of super-site Birkholz, which are responsible for greater surface roughness. At 912 m, displayed in panels (d)-(f), the data availability is lower and the differences in surface roughness should not matter. It is noticeable that significantly fewer wind gusts were retrieved, especially in Falkenberg, which accounts for the small amount of data included. While the comparison between Lindenberg and Birkholz in panel (e) yields the lowest variability with a vanishing mean deviation, statistically stronger gusts seem to occur over Falkenberg (with a mean

deviation above the other sides that is 0.95 and 0.98 m/s, respectively). Here we are not sure if this deviation represents actual wind differences or if the DWL in Falkenberg is biased. Nevertheless, there are local differences and we consider the observations from 90 m reliable to address these. Namely, some points are recognizable which deviate clearly from the intersection line of the scatterplots. The two days with highest deviations are August 26 (one gust at Lindenberg is about 10 m/s higher than the corresponding gust at Birkholz (cf. point (11/20) in panel b) and Falkenberg (cf. point (20/10) in panel a), and June 29 (one gust at Lindenberg is about 9 m/s higher than the corresponding gust at Birkholz (cf. second point around (11/20) in panel b).

On August 26, a cold front passed over the observation area, which was accompanied by a strengthening of the wind, appearing at the three locations in a time shifted manner. Instead of analyzing this particular day, we discuss the passage of another cold front, where the temporal development of the wind strengthening in the ABL is more striking, namely on June 12. On June 29, the high differences are attributed to a cold pool that started in the early afternoon. This is analyzed in more detail in the subsection 4.3.

4.2 | Cold Front passing on June 12, 2021

The weather in Central Europe is dominated by the frontal systems of extra-tropical cyclones (described by the Norwegian Bjerknes, 1919 or the Shapiro-Keyser cyclone model Shapiro and Keyser, 1990). They develop along a frontal wave and involve the formation of a warm front followed by a cold front with a warm sector in between. Strong winds can occur along the air mass boundary, which can also be enhanced by incoming stratospheric air (cf. dry intrusion, e.g., Browning, 1997) and become devastating (i.e., sting jets, Clark and Gray, 2018). The higher-level wind jets and cold, warm, and dry conveyor belts determine the exact characteristics of the fronts and result in different vertical profiles of wind and induced convection. These bands can also cause warm air to sink and the cold air to rise if the dry belt is pushing through the jet crosswise to the frontal path. In this case, the front is called Kata-front, while the more frequently observed front is called Ana-front, i.e., when warm air rises and cold sinks (Bergeron, 1937). This classification determines the slope of the front as the plane of separation between warm and cold air and thus how intensely lifting is initiated. The positions of the transport bands and the jet can be detected by satellite imagery and allow the rough categorization of the front. Winds are mainly detected near the surface, so changes in strength and direction are documented very accurately here, although winds from the higher layers determine the characteristics of the front. However, there is a gap between broad-scale satellite imagery and ground-based in situ observation of vertical wind profiles, leaving the individuality of each front vertically poorly studied. Certainly, there are already

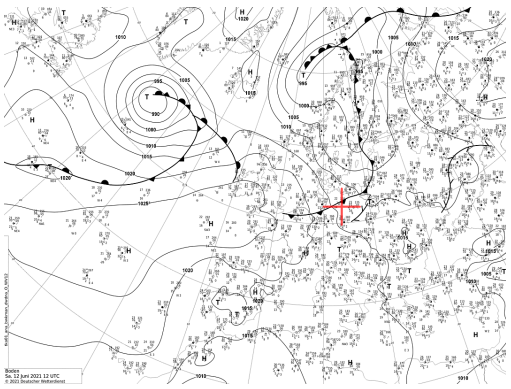

FIGURE 6 Surface pressure map on June 12, 2021 at 12:00 UTC provided by DWD with a red cross at Lindenberg.

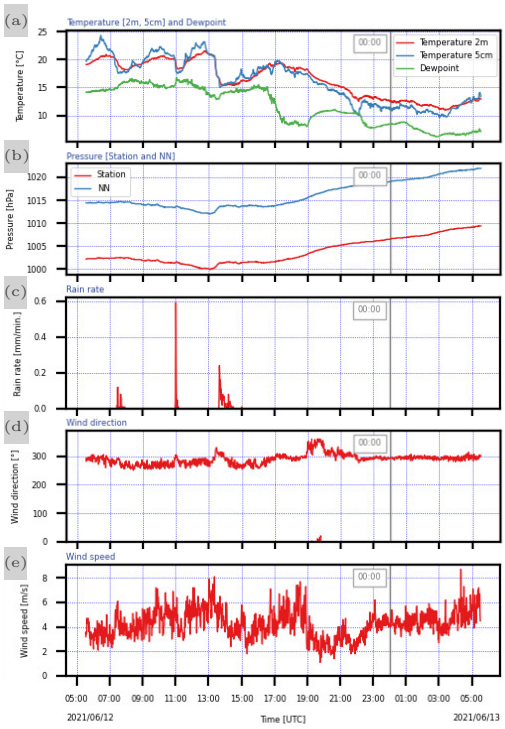

FIGURE 7 Meteorological surface variables in Lindenberg on June 12, 2021. The panels display time series of temperature at 2 m and 5 cm a. g. l. and the dewpoint temperature (panel a), pressure at station height and computed for sea level height (NN; panel b), rain rate (panel c), wind direction and speed (panels d and e). The time series are from the DWD's weather station.

collected observations of gusts along frontal passages from weather towers (e.g. Sinclair et al., 2012), DWLs (Neiman et al., 1988), and wind profilers (e.g. Parton et al., 2009). To our knowledge, there are hardly any high temporal resolution wind profiles covering the entire ABL. In the following, we will analyze the passage of one cold front and show by way of example which features the DWL can see and what value the quick configuration could have for future investigations. With this configuration, it is possible to explicitly resolve the passage of a front as a discontinuity surface of the wind with a resolution of only a few seconds and about 30 m vertically.

On June 12, 2021, a cold front from West-Northwest passed through our observation domain between 13:00 and 14:00 UTC. Figures 6 and 7 show the conventional overview from the DWD's AMDA station (stands for automatic meteorological data acquisition system, similar to WXT), from which one can determine relatively precisely when the front passed over Lindenberg. Figure 6 gives one of the surface pressure maps provided every six hours by the DWD, showing here the situation at 12 UTC. A low pressure system is centered north of Scandinavia and its cold front extends over the Baltic Sea and across northern Germany, so that the observation area is in the region of the warm air sector. The panels in Fig. 7 provide more precise information about the arrival time of the front on site. Thus, it can be detected at about 13:30 to 13:40 UTC, as this is when the temperature drops rapidly (about 5 K in panel a), the pressure rises slightly (panel b), rain commences (panel c), and the wind direction changes (panel d). At this point, the wind strength is already decreasing slightly and had its local peak in the minutes before (panel e). The highest wind speed at 10 m a.g.l. is only about 8 m/s and offers little reason to investigate the case with respect to wind, but stronger gusts were measured at the meteorological tower in Falkenberg (with a wind gust peak of 18.8 m/s at the sonic anemometer in 90.3 m within 13:30 and 13:40 UTC), which indicate the convective activity of the front.

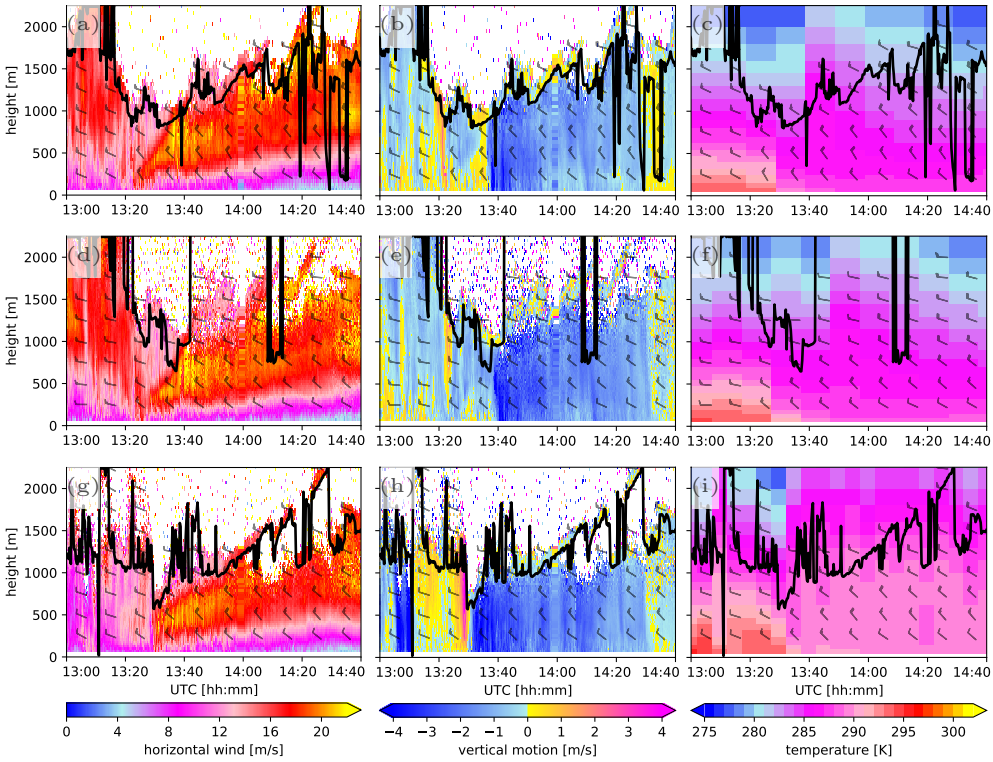

FIGURE 8 Profiles of horizontal wind speed (first column) and vertical motion (second) from DWLs, and temperature (third) from MWRs on June 12, 2021 at 13:00 to 14:40. The profiles are from Lindenberg (top row), Birkholz (middle), and Falkenberg (bottom). Wind barbs showing wind direction are included every 250m/10min and the lowest cloud base height recorded by a ceilometer is indicated as a thick black line. Cloud base heights exceeding the image section (which is up to 2250 m) are indicated by a horizontal line at the top of the panel.

The new retrieval approach adds information about the fine-scale structure of the wind in the ABL and the triangle set-up can demonstrate local differences. Figure 8 shows measurement profiles of horizontal wind, vertical motion and temperature at the three super-sites. The ceilometers additionally indicate the lowest cloud base heights and wind barbs give the 10 min horizontal wind for a few heights. The temperature profiles show that from 13:30 to 13:40 UTC the air masses are exchanged with a sudden temperature drop of 3 to 5 K in the lowest 500 m at all sites (panels c, f, and i). However, we have to be careful with the interpretation after the onset of rain, especially for the Falkenberg MWR the radome was wet due to a faulty heater/blower system. Raindrops on the radome interfere with the measurements, explaining the warmer cloud base temperatures at Falkenberg, compared to the other two stations.

The Falkenberg X-band radar and the MRR at Lindenberg provide information about the rain of the cold front and are given in Fig. 9. Panel (a) shows the accumulated rain just before the onset of area-wide rain, which arrives somewhat staggered rather than within a perfect frontal line. Thus, the rain in Falkenberg starts already at 13:30 UTC, while in Lindenberg and Birkholz it begins a few minutes later. Hence, the low-level change from warm to cold air mass at 13:30 UTC in Lindenberg and Birkholz and at 13:25 UTC in Falkenberg is consistently identified by MWRs before it rains at all three locations until shortly thereafter. Subsequently, the ABL appears to be stably stratified as the constant temperature profile indicates an increase in potential temperature with altitude. Comparing the vertical

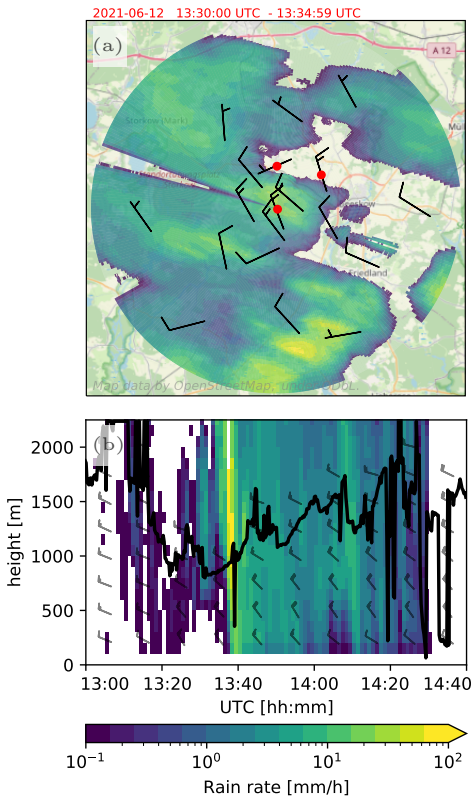

FIGURE 9 Rain on June 12, 2021 within a cold front. Panel (a) shows the rain rate of X-band radar at Falkenberg for 5 min accumulated (13:30 - 13:35 UTC). The wind barbs show the horizontal wind gust peaks from the WXTs within the 5 min. Panel (b) displays minute rain rate profiles from the micro rain radar at Lindenberg for 13:00 to 14:40 UTC. The cloud base height and wind gust peaks are the same as in Fig. 8, first row.

motion (Fig. 8 panel b) with the rain intensity (Fig. 9 panel b) at Lindenberg, it can be seen that the high negative vertical motions correspond to falling rain. Raindrops have a fall velocities that depend primarily on the droplet size and range from a few cm/s (very small drops) to about -10 m/s (for very large drops; e.g. see Serio et al., 2019). At Lindenberg, heavier rain begins at about 13:35 UTC and then continues moderately until about 14:30 UTC. The DWL indicates negative vertical motions exactly in this window with values from -1 m/s to -4 m/s. It should be considered that continuous negative vertical motion alone should not be taken as proof for rain, since downdrafts and fall velocities are superimposed on the observed Doppler spectrum. However, the prominent negative vertical motions in Fig. 8 panels (e) and (h) can be identified confidently as rain. Panel (h) of Fig. 8 shows that rain starts already at 13:30 UTC in Falkenberg, while it begins some minutes later in Lindenberg and Birkholz (panels b and e), which thus agrees with the radar observations (panel a of Fig. 9). It can also be seen that there was a shower in Falkenberg at 13:05 to 13:10 UTC with prominent negative velocities. In addition to rain, pronounced positive vertical motion can be seen in Falkenberg at about 13:25 UTC. Here, the prefrontal lifting of the cold front is visible, which triggers the onset of precipitation. Prefrontal lifting is also recognizable at Lindenberg and Birkholz (13:20 to 13:30 UTC), however somewhat weaker. After the frontal passage, postfrontal downdrafts could onset, but since, as already explained, rain starts from 13:40 UTC, it is difficult to distinguish between the two.

The transition of the air masses along the cold front is marked by a significantly increase in the intensity of the

horizontal winds (Fig. 8 panels a, d and g), which starts near the surface (between 13:20 and 13:30 UTC) and then spreads to the entire ABL. The wind direction is shown only for the 10 min mean wind, but it is evident that the strengthening is accompanied by a right turn of the wind direction. Simultaneously the evolution of the lower cloud base heights indicate an upward lift of the air mass boundary. The strengthened horizontal winds appear in a wedge-shaped area bounded by cloud base height, the surface, and its apex marking the arrival of the front at surface. The highest wind speeds occur vertically in the center of these areas, for example, after a few minutes of the arrival of the front and at about 500 m height (see all three panels). The inclined transition line between weaker wind in the warm air sector and stronger wind in the cold air sector is remarkable and pronounced. Above all three locations, the wind speeds are high in the area below the clouds, whereas they decreases rather quickly in the layers directly above the surface when the warm air is exchanged. The strong winds decouple from the surface, and there is pronounced shear area in the lower 500 m of the ABL. Therefore, it is plausible that individual post-frontal gusts could be transported down to the surface, and this is alluded by the slightly fringy structure in all three panels. In the present case study, however, this does not happen, as the lower part of the ABL is stable stratified. Instead, at all three sites, the DWLs recorded the strongest gusts at the level closest to the surface (17 - 18.4 m/s in 90.3 m) during the initial front passing. Lindenberg and Birkholz show quite similar patterns, with these gusts first observed between 13:20 and 13:30 UTC, and the zone of strong winds then shifting to higher layers. Above Falkenberg, the first front-associated gusts are measured 5 minutes later, with the wind front arriving abruptly and extending to the lowest cloud base height. This is associated with much stronger prefrontal lifting (cf. vertical motion and early precipitation in panel h). If we identify the arrival of the front with the wind gust peak near the surface, i.e. at 90.3 m, we can determine this to within a few seconds. Accordingly, the DWL cycles with the highest horizontal winds are between 13:24 and 13:25 UTC in Birkholz and Lindenberg and between 13:29 and 13:30 UTC in Falkenberg. Altogether, a cold front is clearly a large-scale phenomenon and the commonalities in the vertical profile of wind, rain and temperature predominate. Nevertheless, the fine local differences in the wind situation can be monitored very precisely with the DWLs in the present example.

4.3 | Cold Pool event on June 29, 2021

A primary objective of the FESSTVaL campaign was to study summer convection leading to cold pools. Compared to a cold front, a CP is typically a small-scale phenomenon whose 4-dimensional extent is not adequately documented by routine weather observations, which is why we wanted to observe local with a high-resolution, implying a narrow-meshed observation network of the essential parameters temperature, pressure and wind. The CP refers to the body of relatively cold air that results from evaporative cooling in an area of rain. These areas typically range over a few kilometers, but can also extend over hundreds of kilometers (Zuidema et al., 2017). Temperature drops of up to 10 K are observed (Kirsch et al., 2022b), depending on the size and intensity of the rain area. The drop size distribution of the rain contributes to the cooling, since smaller drops evaporate more effective than larger ones (Seifert, 2008). Soil moisture and the resulting thermodynamic profiles are also relevant, because the drier, the more evaporation and thus cooling is possible (Drager et al., 2020). The expansion of the cold air is accompanied by intensified winds which could induce further convection. For conventional numerical weather prediction, a CP is a difficult phenomenon because the driving processes happen on the sub-grid scale and appropriate parameterization is required to include them (e.g. Suselj et al., 2019). Model resolution should not be coarser than 100 m horizontal and 50 m vertical (in the layers close to the surface) to explicitly resolve a CP (Grant and Heever, 2016), although insightful simulations are possible even at slightly lower resolution (Drager and van den Heever, 2017). In this respect, systematically varying grid sizes in large eddy simulations show the more intense but the less frequent CPs at finer grids (Hirt et al., 2020). However,

at a fine resolution of a few hundred meters, deficiencies in the turbulence representation can occur as some eddies are resolvable while others must be parameterized, often referred to as the *gray zone* of turbulence (Honnert, 2016). In order to advance models, but also generally the process understanding, observational data are key and have been collected in a variety of ways. For instance, Goff (1976) already used meteorological tower data to analyze the vertical structure of CPs. Recent studies relate tower observations to radar measurements, and by extrapolating vertical temperature anomalies, the depths of CPs can be assessed (Kruse et al., 2021). It is evident that the height of the meteorological towers is not sufficient to observe a CP as a whole. Here, airborne measurements offer possibilities (see Terai and Wood, 2013), but are obviously elaborate to perform and do only provide observations from the flight tracks. Broad-equipped measurement campaigns such as for instance the Coastal Convective Interactions Experiment in Australia have great research potential due to a large number of measurement instruments (Soderholm et al., 2016). Here, a DWL was used in a range-height-indicator scanning mode that provide snapshots of relative velocities during CP events. However, this limits the observation to only one component of the wind. High-resolution profiling by a DWL of all wind components, by contrast, gives a more complete picture of air motions above the DWL and is to be demonstrated for one CP on June 29, 2021.

Figure 10 schematically shows the mechanism that constitutes a cold pool and is adapted from figures of Goff (1976). Convection triggers rain, which evaporates as it falls, cooling the air it passes through. The cooled air descends

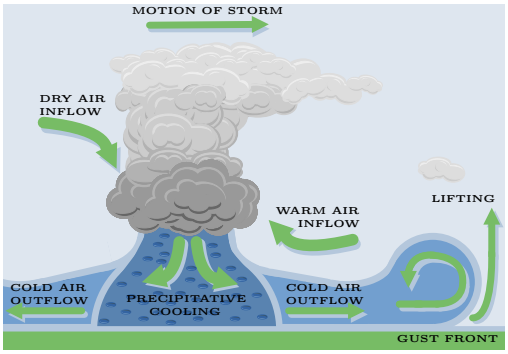

FIGURE 10 Schematic of a Cold Pool according to Goff (1976): Below the clouds, the evaporative cooling of raindrops generates cold air (bluish), which descends outwards. The green arrows indicate the induced motions.

to the surface, then propagates outward and pushes under the environmental warm air. The main characteristic of a CP is a significant drop in temperature, which is measurable not only below the rain cell, but also in the adjacent area. The near-surface propagation of cold air is accompanied by an amplification of the horizontal wind, due to pushing cold air from the rain cell. This amplification extends radially from the CP center and can be observed as a gust front during the transition from warm to cooled air. Warm air that is forced upward by the outflow can then start a chain reaction of thunderstorm formation. Embedded in a large-scale wind situation, the entire storm structure moves and can supply itself via the lifted warm and moist air. In addition, dry air could reinforce the CP by providing a high potential for evaporation when brought into the area of falling rain. The gusty edge of the CP, i.e. the gust front, is characterized by high baroclinicity and is a turbulent transition zone to the warm air. The lifting of the warm air stimulates an internal *secondary circulation*, which also carries cold air backwards in height relative to the expansion of the CP. Because of this, and also because the cold pool outflow behaves like a density current whose magnitude oscillates (cf. Kelvin-Helmholtz-wave, e.g. see Grant and Heever, 2016), this outer boundary region, also referred to as CP head, can extend vertically the intermediate pushing outflow region.

On June 29, 2021, a CP forms around 13:30 UTC in the Southeast of our observation area. Figure 11 shows dif-

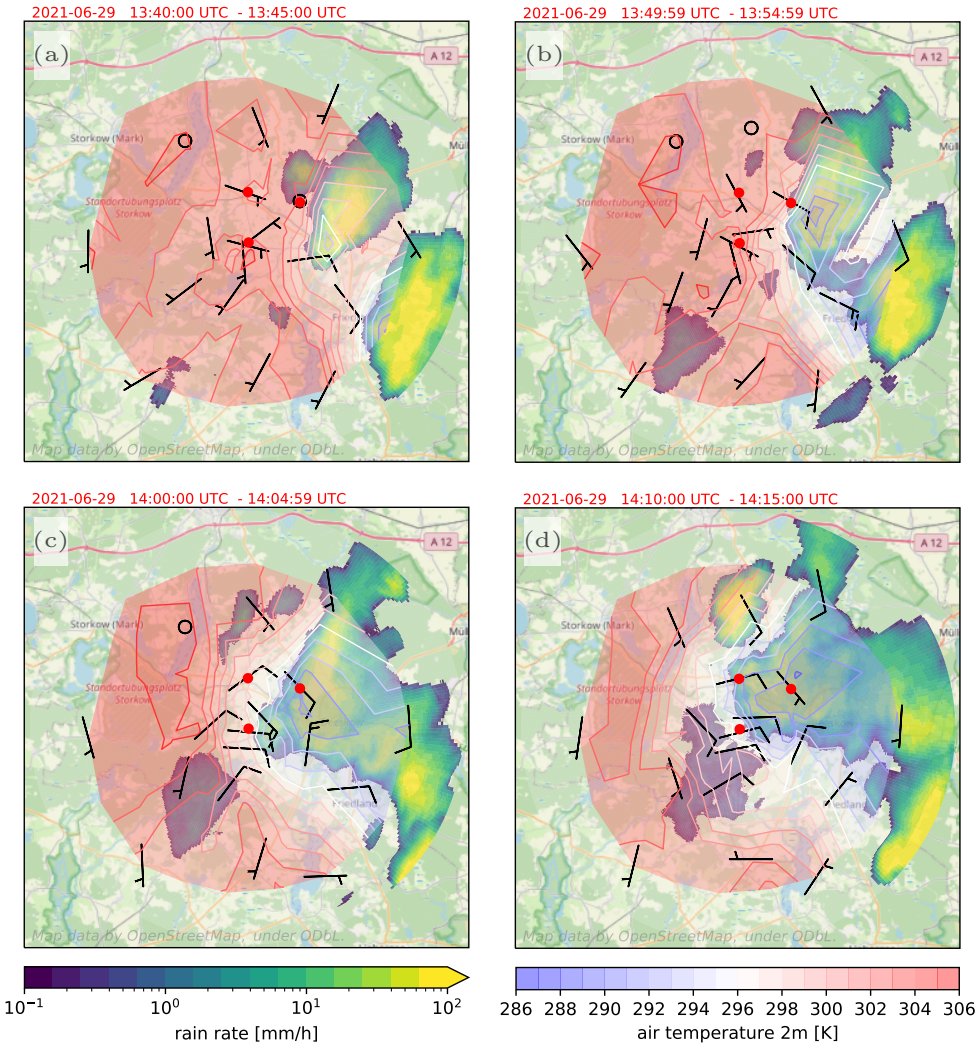

FIGURE 11 Rainfall and temperature on June 29, 2021, as a cold pool forms. Each panel shows the rain rates from the X-band radar at Falkenberg accumulated for 5 min at different times. The wind barbs show the horizontal wind gust peaks at surface from the WXTs within the 5 min span, and overlaid is the surface temperature field that is interpolated from the WXT and APOLLO measurements of the corresponding 5 min end time.

ferent stages of the CP, with the accumulated rain rate of 5 min combined with the temperature field of the respective end time. At 13:45 UTC (panel a), the CP is located south of Birkholz with a pronounced temperature drop near the surface and a rain area extending northeastward above it. Ten minutes later (panel b), the temperature drop is further intensified and the associated rain area has reached Birkholz. Simultaneously, cold air begins to spread westward along the surface. By 14:05 UTC (panel c), significant cooling is observed in Lindenberg and Falkenberg, which are embedded in the cold air spreading easterly from the rain area. The rain area itself loses its isolated shape above the CP core, but merges with another rain cell appearing from the southeast. At 14:15 UTC (panel d), the temperature

drop of the CP is most pronounced (cf. 291 K isoline north of Birkholz) and the rain area reaches Lindenberg. On the other hand, Falkenberg is at the edge of the rain area and experiences the effects of the cold air outflow only. Subsequently, the rain area moves to the northeast (not shown), and Falkenberg remains dry. While Lindenberg receives only a small shower, it rains heavily and persistently in Birkholz. For the sake of discussion, the shower in the southwest (panels b – d) is negligible, as it does not deliver significant amounts of rain and has no effect on surface-level temperatures. When looking at the surface level gusts, two different wind patterns need to be superimposed. First, the overall weather pattern is embedded in a south-southwesterly flow, and second, there are radial winds originating from the CP. Both together result in changing wind directions, however, in the CP edge region, wind gusts run roughly parallel to the temperature gradient, documenting the cold air outflow.

Figure 12 shows the wind and temperature profiles at the three locations in the time window where the CP dominates the weather. Very weak horizontal winds initially prevail over all three supersites throughout the entire

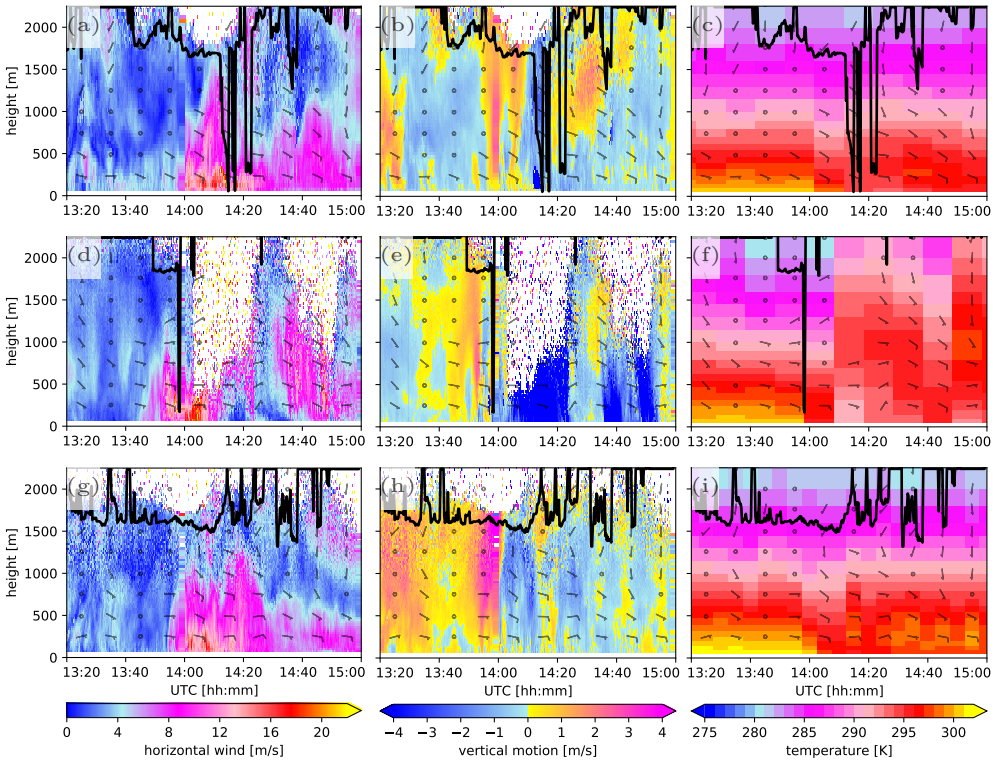

FIGURE 12 Profiles of horizontal wind speed (first column) and vertical motion (second) from DWLs, and temperature (third) from MWRs on June 29, 2021 at 13:40 to 15:20. The profiles are from Lindenberg (top row), Birkholz (middle), and Falkenberg (bottom). Wind barbs showing wind direction are included every 250m/10min and the lowest cloud base height recorded by a ceilometer is indicated as a thick black line. Cloud base heights exceeding the image section (which is up to 2250 m) are indicated by a horizontal line at the top of the panel.

ABL until about 13:40 UTC (panels a, d, and g). In the lower ABL, an easterly flow is evident, which turns with altitude to a southerly flow and even to a slight southwesterly flow (about 1500 m; panels a and g). In Birkholz, at about 13:45 UTC, a strengthening of the horizontal wind starts near the surface, blowing from the direction of the CP. Until about 13:55 UTC, this strengthening is measurable up to an altitude of about 1300 m. In the vertical ve-

locity (panel e) upward motions can be seen at the same time. These abruptly change to negative vertical motions a few minutes before precipitation onset, while the vertical extent of the increased horizontal winds is simultaneously reduced. The abrupt drop in the cloud base height then indicates the actual onset of precipitation. With the occurrence of heavy rain around 14:05 UTC the quality of the DWL signal decreases and the wind profile can only be resolved in the lowest few hundreds of meters. There, very high wind speeds with more than 20 m/s are observed, which happen very close the CP center (compare to Fig. 11 panel c). In Lindenberg the strong winds commence about 10 min later (panel a; note that because of the DWL scanning schedule the last 1–2 minutes of the full hour are not well resolved), whereas here, the impact of the CP on horizontal velocity can be detected up to about 1500 m altitude. It can be clearly seen, that the strong wind speeds (> 10m/s) arrive first close to the surface with a vertical extension of 250 m shortly before 14:00 and reaching up to 1500 m around 14:15 UTC before precipitation sets in, whereby the strongest wind speeds are registered in the lowest levels. Also here, a slight decrease in vertical dimension is apparent around 14:00 to 14:05 UTC, i.e., after the gust front and before the maximum extent preceding the rain cell. The ceilometer shows that the lowest cloud base height then drops to surface level, accompanied by strongly negative vertical motions at about 14:15 UTC (panel b). Both are evidence of the short rain shower that hit Lindenberg. This rain emerges from the CP-generating rain area, but only briefly touches Lindenberg and then moves further north, driven by the large-scale flow, as indicated by the mean wind directions in 1000 m to 2000 m between 14:20 and 14:30 UTC (panels a to c). The gust front reaches Falkenberg at 14:55 UTC and is very precisely resolved, again with a slight slope in the time-height diagram, illustrating once more that the gusts initiate near the surface. It causes a very distinctive lifting (panel h) that extends at least to 1500 m, the height at which clouds prevent the DWL from resolving the winds from higher altitudes. Notably, despite the lifting, no rain is produced that actually reaches the surface. The slightly negative vertical motions at 14:10 UTC suggest that some rain might be triggered, but then evaporates completely before it could reach the surface. In the horizontal wind, the body of the CP is remarkably clearly delineated in the cyan-colored transition of weaker (blue, below 3 m/s, outside) and stronger (magenta to red, above 6 m/s, inside) winds. In the interior, westward propagation is evident, while the large-scale flow above is northward. The transition line has a bumpy shape and indicates the wave characteristic of the CP outflow. This shape (cf. panel g after 14:30 UTC in approximately 500 m) can be explained by a recognizable alternation of upward and downward movements at the boundary surface (cf. panel h after 14:30 UTC with changes of yellow and blue).

Examining at the temperature profiles, the initial situation is similar at all locations with very consistent temperature profiles (panels d, f, and g), beginning at approximately 301 K near the surface and 10 K cooler at about 1 km above, depicting well-mixed conditions. Somewhat delayed to the onset of the gust front, temperatures drop at all locations (note the relatively coarse resolution of the MWR making it hard to define the exact minute). However, the temperature profile in Birkholz after 14:00 UTC has only limited validity, because the heavy rain leaves water on the radome of the MWR and thus corrupts the measurement. Since there is little or no rain in Lindenberg and Falkenberg, respectively, these profiles are not disturbed. At both locations we see the prominent near-surface drop in temperature at 14:00 UTC which is evident up to about 1 km, indicating the vertical extension of the cooler air composing the cold pool. Although there is hardly any change at about 1 km, the temperature drops noticeably in the area below, embedded in easterly winds, i.e. air movement out of the CP. At Lindenberg, the rain shower leaves a wet ground, hence cold temperatures are observed near the surface until it rewarms starting around 14:40 UTC. In contrast, Falkenberg remains dry and only a purely outflow-driven cooling is apparent. Accordingly, the surface temperature recovers more efficiently. Compared to the other two sites, this leaves the lower 500 m of the ABL rather unstable stratified because there is no precipitation-induced cooling at surface and the warm air is still available. The MWR over Falkenberg shows not only this prevailing warmer air masses, but also documents a vertical variation of the temperature stratification in that layers. Although the coarse resolution does not allow us to resolve explicitly

a wave structure, it can be assumed that the same oscillation can be recognized that was found in the shear line of the horizontal wind. Therefore, we assume that we actually encounter Kelvin-Helmholtz waves at the shear surface between stronger and weaker horizontal winds in about 500 m.

In total, a comprehensive picture of the air movements induced by the CP on June 12, 2021 is obtained. While accurate documentation is lacking at the center of the precipitation, as it is an inherent problem for a DWL to resolve wind in rain, the outflow motions and the steep gust fronts are precisely recorded over each of the three super-sites. At the edge of the CP above Falkenberg, the DWL shows pronounced updrafts, which, however, do not trigger new convection here, as the large-scale upper-level flow pushes to the north-northeast. There, new thunderstorm cells subsequently develop, leaving our observation area. The vertical extent of the CP can be sharply differentiated in the horizontal wind by means of the shear line between high, i.e. inner, and weak, i.e. outer, winds at any given time. This also corresponds roughly to the height up to which the two undisturbed MWRs (because they are not wet) show the temperature drops. The highest wind speeds within the CP occur near the surface. Here, the conceptual secondary circulation can be concluded within the CP outflow, as air near the surface overtakes overlying CP air. A second conceptual feature can in fact be observed directly even if it is not very pronounced, namely that the CP head has a slightly larger vertical extent than the outflow region immediately following it. It can be seen that the CP boundary surface varies significantly and the wave character can be noticed, which shows that the CP outflow oscillates like a density current.

5 | CONCLUSIONS

The FESSTVaL campaign provides a broad data set to analyze local summer weather variability. Various observations were collected in summer 2021, using a dense network of ground-based in-situ measurements as well as vertical profiles from remote sensing devices at three super-sites located approximately 6 km apart from each other. The present work focuses on the DWL measurements that provide high-resolution profiles of the wind at these sites. The emphasis is on investigating the variability of the wind within the sub-meso gamma scale, i.e. within scales up to 20 km. The variability is particularly high during high impact weather that causes strong wind gusts.

The DWLs are operated in a quick continuous measurement configuration and from this the wind vector can be resolved for every 3.4 s using the retrieval of Steinheuer et al. (2022). In the vertical motion, the DWLs show a turn direction dependent bias, which is independent of height and has to to be taken into account. It is corrected based on comparison with wind measurements taken in 90 m by a sonic anemometer at the Falkenberg meteorological tower. All three DWL show an offset range of about 0.27 m/s in the mean vertical motion at 90 m regardless of super-site. We assume the offset is related to the quick continuous scanning configuration and reflects the relative velocity of the DWL head to the emitted light. In addition, we assume that the DWLs are not perfectly calibrated and therefore the correction is not always symmetrical. Our bias correction could be improved as we do not differentiate between weather conditions and location. However, in order to see the tendencies in the vertical motion and to eliminate the half-hourly artifacts caused by the change in turn direction, our procedure is sufficient.

We have seen high correlations in the time series of the 10 minute wind gust peaks over the different locations. The largest differences are due to prominent weather events such as cold fronts and cold pools. Hence, we performed two case studies depicting the passage of a cold front on June 12 and the development of a cold pool on June 29. As the front approaches, the wind profiles of the DWLs show the onset of stronger winds close to the surface and a then expanding increase in wind intensity over the entire ABL. The onset appears at different times at the three sides and the high differences in observed wind gust peaks simply reflect the different timing. The vertical motion

can be used as a tracker for rain, according to the comparison with a micro rain radar, because negative values in the order of -1 to -4 m/s reflect measurements of falling raindrops. Without rain, vertical movement can be monitored, which resolves air movements such as the prefrontal lifting. Thus, observations are created that are otherwise only generated by a vertical staring DWL. The cold pool is an event with differences on the meso-gamma scale, as the illustrated example of June 29 shows. There, a major precipitation area passes over Birkholz, while hardly any rain falls over Lindenberg and none over Falkenberg. Using the APOLLO/WXT network for temperature, we could clearly observe the ground-level outflow of cooled air spreading radially from the centre of the cold pool. Along with this, the wind intensifies and appears in the shape of a gust front, the vertical extent of which was made visible in the DWL profiles. The dry edge of the CP showed gust fronts of 1000 m vertical extent and in the interior, close to the rain area even expansions up to the cloud base height, here up to 1500m. The synergy with MWR provides corresponding temperature profiles, demonstrating that the temperature drop is significant in the lower hundreds of metres of the ABL. Particularly over Falkenberg, effects can be observed that originate exclusively from the edge of the CP and developed without local rain. This shows strong updrafts caused by the lifting of cold air, which are known to be able to trigger further convection. The high-resolution profiling of the wind enables us to clearly delineate the cold pool region against the ambient air, since weaker winds prevail there which are also oriented in a different direction. At the interface a wave structure can be recognized, which we interpret as Kelvin-Helmholtz waves.

The present work shows only two examples of case studies of interesting wind situations, but can already demonstrate the potential of the measurement configuration. During the measurement campaign, a total of 42 cold pools were recorded and thus more data exist for further case studies that we are currently analyzing. We draw parallels to existing conceptual models for the shown situations, but we are convinced that the knowledge of the processes can be extended, because certain patterns are now observable for the first time due to the achieved resolution. It is our hope that a DWL in the fast configruation will be included in in future campaigns, or even operationally, to expand the data pool of highly resolved situations. This will also result in research that can look at specific weather phenomena through a more statistical perspective. The data from the FESSTVaL campaign is far from fully exploited and other measurement data can be included that were omitted here. For example, the flights performed can be used to verify the quality of the DWL profiles more completely than we were able to do in this paper. Also the seen wave structure is not comprehensively investigated and other cases have to confirm our hypothesis. We hope that this work will convince researchers to reconsider the use of DWL in remote sensing and see it as a instrument for high-resolution wind observation.

Acknowledgements

Especially we would like to thank Ronny Leinweber (DWD, MOL-RAO) for the installation and maintenance of the Doppler wind lidars. Carola Detring and Frank Beyrich (both DWD, MOL-RAO) helped a lot with with valuable exchange about the fast configuration's features. Jan Schween (University of Cologne, Institute for Geophysics and Meteorology) always provided helpful assistance with all DWL-related questions. We thank Markus Kayser (DWD, MOL-RAO) for providing the Level 1 data. There were useful ideas and valuable discussions with the different FESSTVaL participants. Many thanks to Sebastian Buschow (Institute of Geosciences, University of Bonn) for valuable comments. Also, this work has profited from the scientific exchange within the *EU COST Action PROBE (CA18235)*.

Data availability

Many FESSTVaL data are available at the *Integrated Climate Data Center* (ICDC): The MWR data are available at Löhnert et al. (2022), the APOLLO and WXT data at Kirsch et al. (2022a), and the X-band rain radar data at Burgemeister et al. (2022). The DWL and sonic anemometer data will be published soon.

Code availability

The DWL retrieval is available at (Steinheuer et al., 2021) and will be updated to include the bias correction.

Author contributions

UL planned the FESSTVaL campaign together with others. JS and UL planned and structured the paper. JS did coding, visualization and the formal analysis. JS drafted the manuscript and reviewed it iteratively with UL.

Competing interests

The authors declare that they have no conflict of interest.

references

Bergeron, T. (1937) On the physics of fronts. *Bulletin of the American Meteorological Society*, **18**, 265b–275. URL: https://doi.org/10.1175/1520-0477-18.9.265b.

Bjerknes, J. (1919) On the structure of moving cyclones. *Monthly Weather Review*, **47**, 95–99.

Bott, A. (2016) *Synoptische Meteorologie*. Springer Spektrum.

Brasseur, O. (2001) Development and application of a physical approach to estimating wind gusts. *Mon. Weather Rev.*, **129**, 5 – 25.

Browning, K. A. (1997) The dry intrusion perspective of extra-tropical cyclone development. *Meteorological Applications*, **4**, 317–324. URL: https://doi.org/10.1017/s1350482797000613.

Burgemeister, F., Clemens, M. and Ament, F. (2022) Rainfall rates estimated from x-band radar observations during fesstval 2021. URL: https://www.fdr.uni-hamburg.de/record/10090.

Cafaro, C. and Rooney, G. G. (2018) Characteristics of colliding density currents: A numerical and theoretical study. *Quarterly Journal of the Royal Meteorological Society*, **144**, 1761–1771. URL: https://doi.org/10.1002/qj.3337.

Clark, P. A. and Gray, S. L. (2018) Sting jets in extratropical cyclones: a review. *Quarterly Journal of the Royal Meteorological Society*, **144**, 943–969. URL: https://doi.org/10.1002/qj.3267.

Crewell, S. and Lohnert, U. (2007) Accuracy of boundary layer temperature profiles retrieved with multifrequency multiangle microwave radiometry. *IEEE Transactions on Geoscience and Remote Sensing*, **45**, 2195–2201. URL: https://doi.org/10.1109/tgrs.2006.888434.

Drager, A. J., Grant, L. D. and Heever, S. C. (2020) Cold pool responses to changes in soil moisture. *Journal of Advances in Modeling Earth Systems*, **12**. URL: https://doi.org/10.1029/2019ms001922.

Drager, A. J. and van den Heever, S. C. (2017) Characterizing convective cold pools. *Journal of Advances in Modeling Earth Systems*, **9**, 1091–1115. URL: https://doi.org/10.1002/2016ms000788.

Fournier, M. B. and Haerter, J. O. (2019) Tracking the gust fronts of convective cold pools. *Journal of Geophysical Research: Atmospheres*, **124**, 11103–11117. URL: https://doi.org/10.1029/2019jd030980.

Goff, R. C. (1976) Vertical structure of thunderstorm outflows. *Monthly Weather Review*, **104**, 1429–1440. URL: https://doi.org/10.1175/1520-0493(1976)104<1429:vsoto>2.0.co;2.

Grant, L. D. and Heever, S. C. (2016) Cold pool dissipation. *Journal of Geophysical Research: Atmospheres*, **121**, 1138–1155. URL: https://doi.org/10.1002/2015jd023813.

Grant, L. D., Lane, T. P. and van den Heever, S. C. (2018) The role of cold pools in tropical oceanic convective systems. *Journal of the Atmospheric Sciences*, **75**, 2615–2634. URL: https://doi.org/10.1175/jas-d-17-0352.1.

Hirt, M., Craig, G. C., Schäfer, S. A. K., Savre, J. and Heinze, R. (2020) Cold-pool-driven convective initiation: using causal graph analysis to determine what convection-permitting models are missing. *Quarterly Journal of the Royal Meteorological Society*, **146**, 2205–2227. URL: https://doi.org/10.1002/qj.3788.

Honnert, R. (2016) Representation of the grey zone of turbulence in the atmospheric boundary layer. *Advances in Science and Research*, **13**, 63–67. URL: https://doi.org/10.5194/asr-13-63-2016.

Kirsch, B., Ament, F. and Hohenegger, C. (2021) Convective cold pools in long-term boundary layer mast observations. *Monthly Weather Review*, **149**, 811–820. URL: https://doi.org/10.1175/mwr-d-20-0197.1.

Kirsch, B., Hohenegger, C., Klocke, D. and Ament, F. (2022a) Meteorological network observations by apollo and wxt weather stations during fesstval 2021. URL: https://www.fdr.uni-hamburg.de/record/10179.

Kirsch, B., Hohenegger, C., Klocke, D., Senke, R., Offermann, M. and Ament, F. (2022b) Sub-mesoscale observations of convective cold pools with a dense station network in hamburg, germany. *Earth System Science Data*, **14**, 3531–3548. URL: https://essd.copernicus.org/articles/14/3531/2022/.

Kruse, I. L., Haerter, J. O. and Meyer, B. (2021) Cold pools over the netherlands: A statistical study from tower and radar observations. *Quarterly Journal of the Royal Meteorological Society*. URL: https://doi.org/10.1002/qj.4223.

Lee, X., Massman, W. and Law, B. (eds.) (2004) *Handbook of micrometeorology*. Atmospheric and Oceanographic Sciences Library. Tucson, AZ: Kluwer Academic, 2004 edn.

Lengfeld, K., Clemens, M., Münster, H. and Ament, F. (2014) Performance of high-resolution x-band weather radar networks – the PATTERN example. *amt*, **7**, 4151–4166. URL: https://doi.org/10.5194/amt-7-4151-2014.

Löhnert, U., Knist, C., Böck, T. and Pospichal, B. (2022) Microwave radiometer observations during fesstval 2021. URL: https://www.fdr.uni-hamburg.de/record/10198.

Neiman, P. J., Hardesty, R. M., Shapiro, M. A. and Cupp, R. E. (1988) Doppler lidar observations of a downslope windstorm. *Monthly Weather Review*, **116**, 2265–2275. URL: https://doi.org/10.1175/1520-0493(1988)116<2265:dlooad>2.0.co;2.

Parton, G. A., Vaughan, G., Norton, E. G., Browning, K. A. and Clark, P. A. (2009) Wind profiler observations of a sting jet. *Quarterly Journal of the Royal Meteorological Society*, **135**, 663–680. URL: https://doi.org/10.1002/qj.398.

Päschke, E., Leinweber, R. and Lehmann, V. (2015) An assessment of the performance of a 1.5 μm doppler lidar for operational vertical wind profiling based on a 1-year trial. *amt*, **8**, 2251–2266. URL: https://doi.org/10.5194/amt-8-2251-2015.

Schreur, B. W. and Geertsema, G. (2008) Theory for a tke based parameterization of wind gusts. *HIRLAM newsletter*, 177–188.

Seifert, A. (2008) On the parameterization of evaporation of raindrops as simulated by a one-dimensional rainshaft model. *Journal of the Atmospheric Sciences*, **65**, 3608–3619. URL: https://doi.org/10.1175/2008jas2586.1.

Serio, M. A., Carollo, F. G. and Ferro, V. (2019) Raindrop size distribution and terminal velocity for rainfall erosivity studies. a review. *Journal of Hydrology*, **576**, 210–228. URL: https://doi.org/10.1016/j.jhydrol.2019.06.040.

Shapiro, M. A. and Keyser, D. (1990) Fronts, jet streams and the tropopause. In *Extratropical Cyclones*, 167–191. American Meteorological Society. URL: https://doi.org/10.1007/978-1-944970-33-8_10.

Sheridan, P. (2011) Review of techniques and research for gust forecasting and parameterisation. *Met Office*, **570**.

Sinclair, V. A., Niemelä, S. and Leskinen, M. (2012) Structure of a narrow cold front in the boundary layer: Observations versus model simulation. *Monthly Weather Review*, **140**, 2497–2519. URL: https://doi.org/10.1175/mwr-d-11-00328.1.

Soderholm, J., McGowan, H., Richter, H., Walsh, K., Weckwerth, T. and Coleman, M. (2016) The coastal convective interactions experiment (CCIE): Understanding the role of sea breezes for hailstorm hotspots in eastern australia. *Bulletin of the American Meteorological Society*, **97**, 1687–1698. URL: https://doi.org/10.1175/bams-d-14-00212.1.

Steinheuer, J., Detring, C., Beyrich, F., Löhnert, U., Friederichs, P. and Fiedler, S. (2021) Jsteinheuer/dwl_retrieval: Dwl retrieval. *Zenodo [code]*. URL: https://zenodo.org/record/5780949.

— (2022) A new scanning scheme and flexible retrieval for mean winds and gusts from doppler lidar measurements. *Atmospheric Measurement Techniques*, **15**, 3243–3260. URL: https://amt.copernicus.org/articles/15/3243/2022/.

Suomi, I., Gryning, S.-E., O'Connor, E. J. and Vihma, T. (2017) Methodology for obtaining wind gusts using doppler lidar. *Q. J. R. Meteorol. Soc.*, **143**, 2061–2072.

Suomi, I. and Vihma, T. (2018) Wind gust measurement techniques—from traditional anemometry to new possibilities. *Sensors*, **18**, 1300. URL: https://doi.org/10.3390/s18041300.

Suselj, K., Kurowski, M. J. and Teixeira, J. (2019) A unified eddy-diffusivity/mass-flux approach for modeling atmospheric convection. *Journal of the Atmospheric Sciences*, **76**, 2505–2537. URL: https://doi.org/10.1175/jas-d-18-0239.1.

Terai, C. R. and Wood, R. (2013) Aircraft observations of cold pools under marine stratocumulus. *acp*, **13**, 9899–9914. URL: https://doi.org/10.5194/acp-13-9899-2013.

Vickers, D. and Mahrt, L. (1997) Quality control and flux sampling problems for tower and aircraft data. *J. Atmos. Ocean. Technol.*, **14**, 512–526.

World Meteorological Organization (2018) Measurement of surface wind. *Guide to Meteorological Instruments and Methods of Observation*, **8**, 196–213. URL: https://library.wmo.int/index.php?lvl=notice_display&id=12407#.YZz2hiVCdhF.

Zuidema, P., Torri, G., Muller, C. and Chandra, A. (2017) A survey of precipitation-induced atmospheric cold pools over oceans and their interactions with the larger-scale environment. *Surveys in Geophysics*, **38**, 1283–1305. URL: https://doi.org/10.1007/s10712-017-9447-x.

Appendix

Figure 13 gives the vertical air motion above Falkenberg for June 29, 2021. Panel (a) shows the uncorrected minutely vertical wind from the DWL in the CSM. In the morning hours, a half-hourly change in the sign up to the highest layers (approx. 700 m) is visible, where neither upward nor downward motion is expected. Panel (b) shows the direct measurement of the Doppler velocity from the vertical stare, from which it is evident that the changing pattern is an artefact. Panel (c) displays the corrected vertical motion of the DWL from panel (a) after we have applied the alternating bias-correction. The correction terms needed are given in Table 1

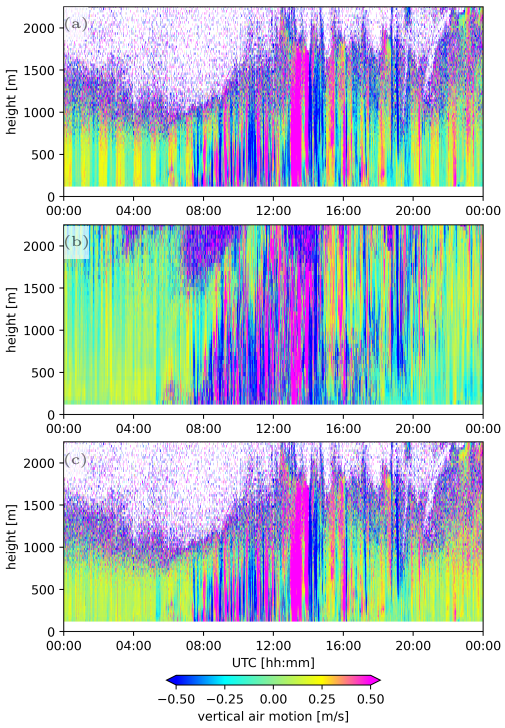

FIGURE 13 Vertical air motion at Falkenberg on June 29, 2021. Panel (a) gives the time series (~3.4 s resolution) for the raw w-component of the CSM; panel (b) the Doppler velocity of the vertical pointing DWL (~3.1 s); and panel (c) the bias-corrected time series of the CSM (correction of panel (a)).

TABLE 1 Vertical air motion correction per site (Falkenberg (F), Lindenberg (L), and Birkholz (B)), DWL, and direction of rotation (counterclockwise (cc) and clockwise (cw)). The w-component of the 10 min mean wind is given for DWL (DWL_{cc} and DWL_{cw}) and same times of the sonic anemometer (SAN_{cc} and SAN_{cw}), and with their differences ($offset_{cc}$ and $offset_{cw}$). The range of the offset is given in the last column. Note that all numbers are rounded and their unit is m/s.

DWL	DWL_{cc}	SAN_{cc}	$offset_{cc}$	DWL_{cw}	SAN_{cw}	$offset_{cw}$	$offset_{range}$
F RAO 02	+0.14	+0.04	+0.10	-0.13	+0.03	-0.17	0.27
F RAO 01	+0.13	+0.03	+0.10	-0.14	+0.02	-0.16	0.27
L KIT 01	+0.08	+0.04	+0.05	-0.19	+0.04	-0.23	0.28
L RAO 00	+0.05	+0.03	+0.02	-0.24	+0.03	-0.26	0.27
B RAO 03	+0.15	+0.04	+0.11	-0.12	+0.04	-0.16	0.27
B KIT 01	+0.17	+0.03	+0.14	-0.10	+0.03	-0.13	0.27

Bibliography

Ament, F., U. Löhnert, H. Rust, and J. Steinheuer (2023). "What Are Cold Pools and What Can They Teach Us?" In: *Latest Thinking*. DOI: 10.21036/ltpub101065.

Baldauf, M., A. Seifert, J. Förstner, D. Majewski, M. Raschendorfer, and T. Reinhardt (2011). "Operational Convective-Scale Numerical Weather Prediction with the COSMO Model: Description and Sensitivities". In: *Monthly Weather Revue* 139.12, pp. 3887–3905. DOI: 10.1175/MWR-D-10-05013.1.

Barlow, J. F., T. M. Dunbar, E. G. Nemitz, C. R. Wood, M. W. Gallagher, F. Davies, E. O'Connor, and R. M. Harrison (2011). "Boundary layer dynamics over London, UK, as observed using Doppler lidar during REPARTEE-II". In: *Atmospheric Chemistry and Physics* 11.5, pp. 2111–2125. DOI: 10.5194/acp-11-2111-2011.

Bauer, P., A. Thorpe, and G. Brunet (2015). "The quiet revolution of numerical weather prediction". In: *Nature* 525.7567, pp. 47–55. DOI: 10.1038/nature14956.

Bollmeyer, C., J. D. Keller, C. Ohlwein, S. Wahl, S. Crewell, P. Friederichs, A. Hense, J. Keune, S. Kneifel, I. Pscheidt, S. Redl, and S. Steinke (2014). "Towards a high-resolution regional reanalysis for the European CORDEX domain". In: *Quarterly Journal of the Royal Meteorological Society* 141.686, pp. 1–15. DOI: 10.1002/qj.2486.

Bossanyi, E. A., A. Kumar, and O. Hugues-Salas (2014). "Wind turbine control applications of turbine-mounted LIDAR". In: *Journal of Physics: Conference Series* 555, p. 012011. DOI: 10.1088/1742-6596/555/1/012011.

Brasseur, O. (2001). "Development and Application of a Physical Approach to Estimating Wind Gusts". In: *Monthly Weather Revue* 129.1, pp. 5–25. DOI: 10.1175/1520-0493(2001)129<0005:DAAOAP>2.0.CO;2.

Bremnes, J. B. (2004). "Probabilistic Forecasts of Precipitation in Terms of Quantiles Using NWP Model Output". In: *Monthly Weather Review* 132.1, pp. 338–347. DOI: 10.1175/1520-0493(2004)132<0338:pfopit>2.0.co;2.

Browning, K. A. and R. Wexler (1968). "The Determination of Kinematic Properties of a Wind Field Using Doppler Radar". In: *Journal of Applied Meteorology* 7.1, pp. 105–113. DOI: 10.1175/1520-0450(1968)007<0105:tdokpo>2.0.co;2.

Brümmer, B., I. Lange, and H. Konow (2012). "Atmospheric boundary layer measurements at the 280 m high Hamburg weather mast 1995-2011: mean annual and diurnal cycles". In: *Meteorologische Zeitschrift* 21.4, pp. 319–335. DOI: 10.1127/0941-2948/2012/0338.

Charney, J. G., R. Fjörtoft, and J. v. Neumann (1950). "Numerical Integration of the Barotropic Vorticity Equation". In: *Tellus* 2.4, pp. 237–254. DOI: 10.1111/j.2153-3490.1950.tb00336.x.

Choukulkar, A., W. A. Brewer, S. P. Sandberg, A. Weickmann, T. A. Bonin, R. M. Hardesty, J. K. Lundquist, R. Delgado, G. V. Iungo, R. Ashton, M. Debnath, L. Bianco, J. M. Wilczak, S. Oncley, and D. Wolfe (2017). "Evaluation of single and multiple Doppler lidar techniques to measure complex flow during the XPIA field campaign". In: *Atmospheric Measurement Techniques* 10.1, pp. 247–264. DOI: 10.5194/amt-10-247-2017.

Coles, S. (2001). *An Introduction to Statistical Modeling of Extreme Values*. Springer London. DOI: 10.1007/978-1-4471-3675-0.

Detring, C., F. Beyrich, J. Steinheuer, M. Kayser, R. Leinweber, U. Löhnert, and E. Päschke (2023). "Ultrasonic anemometer and doppler lidar wind and gust data products during FESSTVAL 2021". In: *ICDC*. DOI: 10.25592/UHHFDM.11227.

Eberhard, W. L., R. E. Cupp, and K. R. Healy (1989). "Doppler Lidar Measurement of Profiles of Turbulence and Momentum Flux". In: *Journal of Atmospheric and Oceanic Technology* 6.5, pp. 809–819. DOI: 10.1175/1520-0426(1989)006<0809:dlmopo>2.0.co;2.

ECMWF (2021). "IFS Documentation CY47R3 - Part III Dynamics and numerical procedures". In: DOI: 10.21957/B18QSX663.

Fisher, R. A. and L. H. Tippett (1928). "On the estimation of the frequency distributions of the largest or smallest member of a sample". In: *Proceedings of the Campridge Philosophical Society* 24, pp. 180–190.

Fréchet, M. (1927). "Sur la loi de probabilité de l'écart maximum". In: *Ann. Soc. Math. Polon.* 6, pp. 93–116.

Frehlich, R. (1994). "Coherent Doppler lidar signal covariance including wind shear and wind turbulence". In: *Applied Optics* 33.27, p. 6472. DOI: 10.1364/ao.33.006472.

Frehlich, R., S. M. Hannon, and S. W. Henderson (1998). "Coherent Doppler Lidar Measurements of Wind Field Statistics". In: *Boundary-Layer Meteorology* 86.2, pp. 233–256. DOI: 10.1023/a:1000676021745.

Friederichs, P., M. Göber, S. Bentzien, A. Lenz, and R. Krampitz (2009). "A probabilistic analysis of wind gusts using extreme value statistics". In: *Meteorologische Zeitschrift* 18.6, pp. 615–629. DOI: 10.1127/0941-2948/2009/0413.

Friederichs, P. and T. L. Thorarinsdottir (2012). "Forecast verification for extreme value distributions with an application to probabilistic peak wind prediction". In: *Environmetrics* 23.7, pp. 579–594. DOI: 10.1002/env.2176.

Friederichs, P., S. Wahl, and S. Buschow (2018). "Postprocessing for Extreme Events". In: *Statistical Postprocessing of Ensemble Forecasts*. Elsevier, pp. 127–154. DOI: 10.1016/b978-0-12-812372-0.00005-4.

Glahn, H. R. and D. A. Lowry (1972). "The Use of Model Output Statistics (MOS) in Objective Weather Forecasting". In: *Journal of Applied Meteorology* 11.8, pp. 1203–1211. DOI: 10.1175/1520-0450(1972)011<1203:tuomos>2.0.co;2.

Gnedenko, B. (1943). "Sur La Distribution Limite Du Terme Maximum D'Une Serie Aleatoire". In: *Annals of Mathemtatics* 44.3, p. 423. DOI: 10.2307/1968974.

Gneiting, T. and A. E. Raftery (2007). "Strictly Proper Scoring Rules, Prediction, and Estimation". In: *Journal of the American Statistical Association* 102.477, pp. 359–378. DOI: 10.1198/016214506000001437.

González-Longatt, F., P. Wall, and V. Terzija (2012). "Wake effect in wind farm performance: Steady-state and dynamic behavior". In: *Renewable Energy* 39.1, pp. 329–338. DOI: 10.1016/j.renene.2011.08.053.

Gumbel, E. J. (1935). *Les valeurs extrêmes des distributions statistiques*. Vol. 5. 2, pp. 115–158.

Haid, M., A. Gohm, L. Umek, H. C. Ward, T. Muschinski, L. Lehner, and M. W. Rotach (2020). "Foehn–cold pool interactions in the Inn Valley during PIANO IOP2". In: *Quarterly Journal of the Royal Meteorological Society* 146.728, pp. 1232–1263. DOI: 10.1002/qj.3735.

Hohenegger, C., F. Ament, F. Beyrich, U. Löhnert, H. Rust, J. Bange, T. Böck, C. Böttcher, J. Boventer, F. Burgemeister, M. Clemens, C. Detring, I. Detring, N. Dewani, I. B. Duran, S. Fiedler, M. Göber, C. van Heerwaarden, B. Heusinkveld, B. Kirsch, D. Klocke, C. Knist, I. Lange, F. Lauermann, V. Lehmann, J. Lehmke, R. Leinweber, K. Lundgren, M. Masbou, M. Mauder, W. Mol, H. Nevermann, T. Nomokonova, E. Päschke, A. Platis, J. Reichardt, L. Rochette, M. Sakradzija, L. Schlemmer, J. Schmidli, N. Shokri, V. Sobottke, J. Speidel, J. Steinheuer, D. D. Turner, H. Vogelmann, C. Wedemeyer, E. Weide-Luiz, S. Wiesner, N. Wildmann, K. Wolz, and T. Wetz (2023). "FESSTVaL: the Field Experiment on Submesoscale Spatio-Temporal Variability in Lindenberg". In: *Preparation for Bulletin of the American Meteorological Society*.

Hohenegger, C., P. Brockhaus, and C. Schär (2008). "Towards climate simulations at cloud-resolving scales". In: *Meteorologische Zeitschrift* 17.4, pp. 383–394. DOI: 10.1127/0941-2948/2008/0303.

Johnson, N. L., S. Kotz, and N. Balakrishnan (1994). *Continuous Univariate Distributions, Volume 1*. 2nd ed. Wiley Series in Probability and Statistics. Nashville, TN: John Wiley & Sons. ISBN: 978-0-471-58495-7.

Jung, C., D. Schindler, A. Albrecht, and A. Buchholz (2016). "The Role of Highly-Resolved Gust Speed in Simulations of Storm Damage in Forests at the Landscape Scale: A Case Study from Southwest Germany". In: *Atmosphere* 7.1, p. 7. DOI: 10.3390/atmos7010007.

Kirsch, B., C. Hohenegger, D. Klocke, R. Senke, M. Offermann, and F. Ament (2022). "Submesoscale observations of convective cold pools with a dense station network in Hamburg, Germany". In: *Earth System Science Data* 14.8, pp. 3531–3548. DOI: 10.5194/essd-14-3531-2022.

Knoop, S., F. C. Bosveld, M. J. d. Haij, and A. Apituley (2021). "A 2-year intercomparison of continuous-wave focusing wind lidar and tall mast wind measurements at Cabauw". In: *Atmospheric Measurement Techniques* 14.3, pp. 2219–2235. DOI: 10.5194/amt-14-2219-2021.

Kunz, M., J. Sander, and C. Kottmeier (2009). "Recent trends of thunderstorm and hailstorm frequency and their relation to atmospheric characteristics in southwest Germany". In: *International Journal of Climatology* 29.15, pp. 2283–2297. DOI: 10.1002/joc.1865.

Leadbetter, M. R., G. Lindgren, and H. Rootzén (1983). *Extremes and Related Properties of Random Sequences and Processes*. Springer New York. DOI: 10.1007/978-1-4612-5449-2.

Legendre, A. M. (1785). "Recherches sur l' attraction des spheroides homogenes". In: *Mémoires de Mathématiques et de Physique, présentés à l'Académie Royale des Sciences, par divers savans, et lus dans ses Assemblées.*

Letson, F., R. J. Barthelmie, W. Hu, and S. C. Pryor (2019). "Characterizing wind gusts in complex terrain". In: *Atmospheric Chemistry and Physics* 19.6, pp. 3797–3819. DOI: 10.5194/acp-19-3797-2019.

Lorenz, E. N. (1963). "Deterministic Nonperiodic Flow". In: *Journal of the Atmospheric Sciences* 20.2, pp. 130–141. DOI: 10.1175/1520-0469(1963)020<0130:dnf>2.0.co;2.

Nakamura, K., R. Kershaw, and N. Gait (1996). "Prediction of near-surface gusts generated by deep convection". In: *Meteorological Applications* 3.2, pp. 157–167. DOI: 10.1002/met.5060030206.

Neisser, J., W. Adam, F. Beyrich, U. Leiterer, and H. Steinhagen (2002). "Atmospheric boundary layer monitoring at the Meteorological Observatory Lindenberg as a part of the "Lindenberg Column": Facilities and selected results". In: *Meteorologische Zeitschrift* 11.4, pp. 241–253. DOI: 10.1127/0941-2948/2002/0011-0241.

Oesting, M., M. Schlather, and P. Friederichs (2017). "Statistical post-processing of forecasts for extremes using bivariate Brown-Resnick processes with an application to wind gusts". In: *Extremes* 20.2, pp. 309–332. DOI: 10.1007/s10687-016-0277-x.

Pantillon, F., S. Lerch, P. Knippertz, and U. Corsmeier (2018). "Forecasting wind gusts in winter storms using a calibrated convection-permitting ensemble". In: *Quarterly Journal of the Royal Meteorological Society* 144.715, pp. 1864–1881. DOI: 10.1002/qj.3380.

Päschke, E., R. Leinweber, and V. Lehmann (2015). "An assessment of the performance of a 1.5 μm Doppler lidar for operational vertical wind profiling based on a 1-year trial". In: *Atmospheric Measurement Techniques* 8.6, pp. 2251–2266. DOI: 10.5194/amt-8-2251-2015.

Patlakas, P., E. Drakaki, G. Galanis, C. Spyrou, and G. Kallos (2017). "Wind gust estimation by combining a numerical weather prediction model and statistical post-processing". In: *Energy Procedia* 125, pp. 190–198. DOI: 10.1016/j.egypro.2017.08.179.

Pearson, G., F. Davies, and C. Collier (2009). "An Analysis of the Performance of the UFAM Pulsed Doppler Lidar for Observing the Boundary Layer". In: *Journal of Atmospheric and Oceanic Technology* 26.2, pp. 240–250. DOI: 10.1175/2008jtecha1128.1.

Pichault, M., C. Vincent, G. Skidmore, and J. Monty (2022). "LiDAR-based detection of wind gusts: An experimental study of gust propagation speed and impact on wind power ramps". In: *Journal of Wind Engineering and Industrial Aerodynamics* 220, p. 104864. DOI: 10.1016/j.jweia.2021.104864.

Pichault, M., C. Vincent, G. Skidmore, and J. Monty (2021). "Short-Term Wind Power Forecasting at the Wind Farm Scale Using Long-Range Doppler LiDAR". In: *Energies* 14.9. ISSN: 1996-1073. DOI: 10.3390/en14092663.

Pickands, J. (1981). "Multivariate extreme value distributions". In: *Bull. Inst. Internat. Statist* 49, pp. 859–878, 894–902.

Rasp, S. and S. Lerch (2018). "Neural Networks for Postprocessing Ensemble Weather Forecasts". In: *Monthly Weather Review* 146.11, pp. 3885–3900. DOI: 10.1175/mwr-d-18-0187.1.

Reinert, D., F. Prill, H. Frank, M. Denhard, M. Baldauf, C. Schraff, C. Gebhardt, C. Marsigli, and G. Zängl (2020). *DWD Database Reference for the Global and Regional ICON and ICON-EPS Forecasting System*. Tech. rep. Research and Development at DWD. Offenbach, Germany: Deutscher Wetterdienst. URL: https://www.dwd.de/SharedDocs/downloads/DE/modelldokumentationen/nwv/icon/icon_dbbeschr_aktuell.pdf?view=nasPublication (visited on 12/06/2022).

Rye, B. and R. Hardesty (1993). "Discrete spectral peak estimation in incoherent backscatter heterodyne lidar. II. Correlogram accumulation". In: *IEEE Transactions on Geoscience and Remote Sensing* 31.1, pp. 28–35. DOI: 10.1109/36.210441.

Sathe, A., J. Mann, N. Vasiljevic, and G. Lea (2015). "A six-beam method to measure turbulence statistics using ground-based wind lidars". In: *Atmospheric Measurement Techniques* 8.2, pp. 729–740. DOI: 10.5194/amt-8-729-2015.

Scheuerer, M. (2013). "Probabilistic quantitative precipitation forecasting using Ensemble Model Output Statistics". In: *Quarterly Journal of the Royal Meteorological Society* 140.680, pp. 1086–1096. DOI: 10.1002/qj.2183.

Schindler, D., C. Jung, and A. Buchholz (2016). "Using highly resolved maximum gust speed as predictor for forest storm damage caused by the high-impact winter storm Lothar in Southwest Germany". In: *Atmospheric Science Letters* 17.8, pp. 462–469. DOI: 10.1002/asl.679.

Scholbrock, A., P. Fleming, D. Schlipf, A. Wright, K. Johnson, and N. Wang (2016). "Lidar-enhanced wind turbine control: Past, present, and future". In: *2016 American Control Conference (ACC)*. IEEE. DOI: 10.1109/acc.2016.7525113.

Schreur, B. W. and G. Geertsema (2008). "Theory for a TKE based parameterization of wind gusts". In: *HIRLAM newsletter*, pp. 177–188.

Schulz, B. and S. Lerch (2022). "Machine Learning Methods for Postprocessing Ensemble Forecasts of Wind Gusts: A Systematic Comparison". In: *Monthly Weather Review* 150.1, pp. 235–257. DOI: 10.1175/mwr-d-21-0150.1.

Schulz, J.-P. (2008). "Revision of the Turbulent Gust Diagnostics in the COSMO Model". In: *COSMO Newletter* 8, pp. 17–22. URL: http://cosmo-model.org/content/model/documentation/newsLetters/newsLetter08/cnl8_schulz.pdf (visited on 10/08/2019).

Schween, J. H., A. Hirsikko, U. Löhnert, and S. Crewell (2014). "Mixing-layer height retrieval with ceilometer and Doppler lidar: from case studies to long-term assessment". In: *Atmospheric Measurement Techniques* 7.11, pp. 3685–3704. DOI: 10.5194/amt-7-3685-2014.

Sheridan, P. (2011). "Review of techniques and research for gust forecasting and parameterisation". In: *Met Office* 570 (Forecasting Research Technical Report).

Simmer, C., G. Adrian, S. Jones, V. Wirth, M. Göber, C. Hohenegger, T. Janjic´, J. Keller, C. Ohlwein, A. Seifert, S. Trömel, T. Ulbrich, K. Wapler, M. Weissmann, J. Keller, M. Masbou, S. Meilinger, N. Riß, A. Schomburg, A. Vormann, and C. Weingärtner (2016). "HErZ: The German Hans-Ertel Centre for Weather Research". In: *Bulletin of the American Meteorological Society* 97.6, pp. 1057–1068. DOI: 10.1175/bams-d-13-00227.1.

Smalikho, I. N. and V. A. Banakh (2017). "Measurements of wind turbulence parameters by a conically scanning coherent Doppler lidar in the atmospheric boundary layer". In: *Atmospheric Measurement Techniques* 10.11, pp. 4191–4208. DOI: 10.5194/amt-10-4191-2017.

Smith, R. L. (1990). "Max-stable processes and spatial extremes". In: *Unpublished manuscript* 205, pp. 1–32.

Soderholm, J., H. McGowan, H. Richter, K. Walsh, T. Weckwerth, and M. Coleman (2016). "The Coastal Convective Interactions Experiment (CCIE): Understanding the Role of Sea Breezes for Hailstorm Hotspots in Eastern Australia". In: *Bulletin of the American Meteorological Society* 97.9, pp. 1687–1698. DOI: 10.1175/bams-d-14-00212.1.

Staid, A., P. Pinson, and S. D. Guikema (2015). "Probabilistic maximum-value wind prediction for offshore environments". In: *Wind Energy* 18.10, pp. 1725–1738. DOI: 10.1002/we.1787.

Steinheuer, J. (2018). "Estimation of Vertical Wind Gust Profiles from a Regional Reanalysis Using Extreme Value Theory". Master's Thesis. Rheinischen Friedrich-Wilhelms-Universität Bonn.

Steinheuer, J., F. Ament, U. Löhnert, and H. Rust (2023). "Was sind Cold Pools and was können wir von ihnen lernen?" In: *Latest Thinking*.

Steinheuer, J., C. Detring, F. Beyrich, U. Löhnert, P. Friederichs, and S. Fiedler (2021a). "JSteinheuer/DWL_retrieval: DWL retrieval". Version V1.0. In: *Zenodo code*. DOI: 10.5281/ZENODO.5780949.

— (2022). "A new scanning scheme and flexible retrieval for mean winds and gusts from Doppler lidar measurements". In: *Atmospheric Measurement Techniques* 15.10, pp. 3243–3260. DOI: 10.5194/amt-15-3243-2022.

Steinheuer, J., C. Detring, M. Kayser, and R. Leinweber (2021b). "Doppler wind lidar wind and gust data from FESTVAL 2019/2020". Version 01. In: *ICDC*. DOI: 10.25592/uhhfdm.9758.

Steinheuer, J. and P. Friederichs (2020). "Vertical profiles of wind gust statistics from a regional reanalysis using multivariate extreme value theory". In: *Nonlinear Processes in Geophysics* 27.2, pp. 239–252. DOI: 10.5194/npg-27-239-2020.

Steinheuer, J. and U. Löhnert (2023). "High-resolution profiling of wind gust patterns measured by Doppler wind lidars during the FESSTVaL campaign". In: *Preparation for Quarterly Journal of the Royal Meteorological Society*.

Stewart, R. W. (1979). *The atmospheric boundary layer*. World Meteorological Organization. ISBN: 978-9-263-10523-3.

Stone, M. (1974). "Cross-Validatory Choice and Assessment of Statistical Predictions". In: *Journal of the Royal Statistical Society: Series B (Methodological)* 36.2, pp. 111–133. DOI: 10.1111/j.2517-6161.1974.tb00994.x.

Suomi, I., S.-E. Gryning, R. Floors, T. Vihma, and C. Fortelius (2014). "On the vertical structure of wind gusts". In: *Quarterly Journal of the Royal Meteorological Society* 141.690, pp. 1658–1670. DOI: 10.1002/qj.2468.

Suomi, I., S.-E. Gryning, E. J. O'Connor, and T. Vihma (2017). "Methodology for obtaining wind gusts using Doppler lidar". In: *Quarterly Journal of the Royal Meteorological Society* 143.706, pp. 2061–2072. DOI: 10.1002/qj.3059.

Thorarinsdottir, T. L. and M. S. Johnson (2012). "Probabilistic Wind Gust Forecasting Using Nonhomogeneous Gaussian Regression". In: *Monthly Weather Revue* 140.3, pp. 889–897. DOI: 10.1175/MWR-D-11-00075.1.

Tibshirani, R. (1996). "Regression Shrinkage and Selection Via the Lasso". In: *Journal of the Royal Statistical Society: Series B (Methodological)* 58.1, pp. 267–288. DOI: 10.1111/j.2517-6161.1996.tb02080.x.

Vannitsem, S., J. B. Bremnes, J. Demaeyer, G. R. Evans, J. Flowerdew, S. Hemri, S. Lerch, N. Roberts, S. Theis, A. Atencia, Z. B. Bouallègue, J. Bhend, M. Dabernig, L. D. Cruz, L. Hieta, O. Mestre, L. Moret, I. O. Plenković, M. Schmeits, M. Taillardat, J. V. den Bergh, B. V. Schaeybroeck, K. Whan, and J. Ylhaisi (2021). "Statistical Postprocessing for Weather Forecasts: Review, Challenges, and Avenues in a Big Data World". In: *Bulletin of the American Meteorological Society* 102.3, E681–E699. DOI: 10.1175/bams-d-19-0308.1.

Vergara-Temprado, J., N. Ban, D. Panosetti, L. Schlemmer, and C. Schär (2020). "Climate Models Permit Convection at Much Coarser Resolutions Than Previously Considered". In: *Journal of Climate* 33.5, pp. 1915–1933. DOI: 10.1175/jcli-d-19-0286.1.

Weibull, W. (1951). "A Statistical Distribution Function of Wide Applicability". In: *Journal of Applied Mechanics* 18.3, pp. 293–297. DOI: 10.1115/1.4010337.

Weisman, M. L., W. C. Skamarock, and J. B. Klemp (1997). "The Resolution Dependence of Explicitly Modeled Convective Systems". In: *Monthly Weather Review* 125.4, pp. 527–548. DOI: 10.1175/1520-0493(1997)125<0527:trdoem>2.0.co;2.

Wernli, H., S. Dirren, M. A. Liniger, and M. Zillig (2002). "Dynamical aspects of the life cycle of the winter storm 'Lothar' (24–26 December 1999)". In: *Quarterly Journal of the Royal Meteorological Society* 128.580, pp. 405–429. DOI: 10.1256/003590002321042036.

Wilks, D. S. (2005). *Statistical methods in the atmospheric sciences: Volume 100*. 2nd ed. International Geophysics. San Diego, CA: Academic Press. ISBN: 978-0-12-751966-1.

World Meteorological Organization (2018). "Measurement of surface wind". In: *Guide to Meteorological Instruments and Methods of Observation* 8, pp. 196–213. URL: https://library.wmo.int/index.php?lvl=notice_display&id=12407#.YZz2hiVCdhF (visited on 11/25/2021).

Yano, J.-I., M. Z. Ziemiański, M. Cullen, P. Termonia, J. Onvlee, L. Bengtsson, A. Carrassi, R. Davy, A. Deluca, S. L. Gray, V. Homar, M. Köhler, S. Krichak, S. Michaelides, V. T. J. Phillips, P. M. M. Soares, and A. A. Wyszogrodzki (2018). "Scientific Challenges of Convective-Scale Numerical Weather Prediction". In: *Bulletin of the American Meteorological Society* 99.4, pp. 699–710. DOI: 10.1175/bams-d-17-0125.1.

Acronyms

ABL **A**tmospheric **b**oundary **l**ayer. 3, 4, 6, 20, 25, 31, 33, 39, 41, 43, 45, 47

agl **A**bove **g**round **l**evel. 3–6, 16, 17, 28, 32, 37, 38, 40, 41, 44, 46

APOLLO **A**utonomous Cold **Po**ol **lo**gger. 34, 41

CAPE **C**onvective **a**vailable **p**otential **e**nergy. 38, 44

CDF **C**umulative **d**istribution **f**unction. 11–17, 28

cGEV **C**ensored **g**eneralized **e**xtreme **v**alue. 15, 17, 37, 38

COSMO **Co**nsortium for **s**mall scale **mo**delling. vii, 4, 6, 9, 17, 37

CP **C**old **p**ool. 6, 8, 33, 34, 39, 41, 42, 45, 49

CSM **C**ontinuous **s**canning **m**ode. 23–25, 28–35, 39–41, 44, 46–48

DBS **D**oppler **b**eam **s**winging. 21–24, 39, 44

DOF **D**egree-**o**f-**f**reedom. 27, 28, 40

DWD German Weather Service; in german: **D**eutscher-**W**etter**d**ienst. 17, 33, 46

DWL **D**oppler **w**ind **l**idar. vii, 3, 4, 6–8, 19–24, 27, 29–35, 39–48, 50

EVT **E**xtreme **v**alue **t**heory. 6, 7, 11, 46

FESSTVaL **F**ield **e**xperiment on **s**ub-mesoscale **s**patio-**t**emporal **va**riability in **L**indenberg. vii, 6–8, 19, 22, 33, 34, 39, 41, 45–49, 127

GEV **G**eneralized **e**xtreme **v**alue. 6, 11–14, 16, 37, 38, 43, 46

HErZ Hans-Ertel Center for Weather Research; in german: **H**ans-**Er**tel **Z**entrum für Wettervorhersage. 17, 33, 127

ICON **Ico**sahedral **n**onhydrostatic. 2, 50

IFS **I**ntegrated **f**orecasting **s**ystem. 2

IOP **I**ntensive **o**bservation **p**eriod. 7, 34

LASSO **L**east-**a**bsolute-**s**hrinkage-and-**s**election-**o**perator. 15, 17, 38

lidar **Li**ght-**d**etection-**a**nd-**r**anging. 3, 7, 19

MLE **M**aximum **l**ikelihood **e**stimation. 14, 15, 38

MOL-RAO **M**eteorological **O**bservatory **L**indenberg – **R**ichard-**A**ßmann **O**bservatory. 34, 35, 40, 47

MOS **M**odel **o**utput **s**tatistics. 5

MRR **M**icro **r**ain **r**adar. 34, 41

MWR **M**icro**w**ave **r**adiometer. 34, 41

NWP **N**umerical **w**eather **p**rediction. vii, 1, 2, 4–6, 10, 14, 33, 37, 43, 45, 49

PDF **P**robability **d**ensity **f**unction. 14, 15, 26, 28

PPI **P**lan-**p**osition **i**ndicator. 47

radar **Ra**dio-**d**etection-**a**nd-**r**anging. 34, 41

RMSE **R**oot **m**ean **s**quared **e**rror. 40, 44

SNR **S**ignal-to-**n**oise-**r**atio. 20, 24, 25, 40, 44

TKE **T**urbulent **k**inetic **e**nergy. 23, 47

VAD **V**elocity-**a**zimuth **d**isplay. 21

WXT Weather station from *Vaisala* (Vantaa, Finnland) type ***WXT536***. 34, 41

Acknowledgements

I am very grateful to all the good people who have given me personal and professional support during the past years. A lot has happened during this time, the most important of which is the birth of my daughter Ida, who has turned Anna and my life upside down. I am incredibly grateful for that. I love the both of you! I want to thank my family, and my friends and colleagues, though some are certainly both, and all helpers. Hence, in alphabetical order, i.e., without having to go through the complicated procedure of creating a questionable and indefensible order, I wish to thank: Frank Beyrich, Armin Blanke, Steffen Böhmer, Karin Bossenkool, Sebastian Buschow, Susanne Crewell, Simon Dedenbach, Carola Detring, Johannes Diewald, Shashi Dixit, Leon Dörfler, Björn Fiege, Petra Friederichs, Alisa Henneke, Andreas Hense, Linh Ho, Dagmar Janzen, Markus Kayser, Christina Kelter, Matthias Kelter, Sophia Kelter, Ellen Kelter-Steinheuer, Felix Kleinert, Ronny Leinweber, Ulrich Löhnert, Kim Michelt, Daniel Morschhausen, Timon Netzel, Andreas Olzem, Lukas Pfitzenmaier, Celin Reece, Dennis Schreiber, Tobias Scharbach, Jan Schween, Johannes Steinheuer, Nuria Steinheuer, Martina Steinheuer, Svenja Szemkus, Henning Weber, and Nico Zipp.

Science benefits from the exchange in the community and therefore I am very grateful to participate in a big project and to be linked to two universities. Within HErZ, I was involved in the FESSTVaL campaign and benefited from the knowledge of many kind people. As a member of the *Exploiting-Observations-in-Meteorology group* led by Ulrich Löhnert in Cologne, and the *Working Group on Climate Dynamics* led by Andreas Hense, Petra Friederichs, and Leonie Esters in Bonn, I had an excellent background for my research. Both groups can be recommended as very fruitful working environments. It is left to thank the anonymous reviewers, the editors and the typesetters who helped to publish my articles. Finally, it remains to say that without free software packages, in my case in python and R, many things in research would not be possible. Thanks to everybody that contributes and takes the effort to create free knowledge.